

# **Crack propagation in rubber blends: Impact of blend morphology and energy dissipation mechanisms around the crack tip**

VON DER NATURWISSENSCHAFTLICHEN FAKULTÄT DER  
GOTTFRIED WILHELM LEIBNIZ UNIVERSITÄT HANNOVER

ZUR ERLANGUNG DES GRADES

**Doktor der Naturwissenschaften**  
**(Dr. rer. nat.)**

genehmigte Dissertation

von

Dipl.-Phys. Matthias Wunde

Erscheinungsjahr 2020

Referent: Prof. Dr. rer. nat. habil. Manfred Klüppel

Korreferent: Prof. Dr. rer. nat. Jürgen Caro

Tag der Promotion: 09. September 2020

# Preface

The presented thesis summarizes many results I have gathered during my occupation at the German Institute of Rubber Technology (DIK) between May 2013 and March 2019. Within this time I worked on several projects, both publicly and privately funded. The backbone of my occupation was a transfer project of the Deutsche Forschungsgemeinschaft (DFG) on crack propagation of truck tire treads (“Verbesserung der Laborvoraussagen zum Risswachstum und Verschleiß von Reifen-Lauflächen“) and its bilateral succession project under the same name.

The main results are written down in 5 publications, all of them authored by me as first author. In chapter 3 three articles about the influence of blend morphology on fatigue crack propagation are presented. The first two articles compare the blend morphology with crack growth measurements. The third publication deals with the influence of BR crystallization on the blend morphology. In this article also the blend morphology of triblend is shown. In chapter 4 two more articles are presented on the influence of energy dissipation around the crack tip on crack growth rates. The first of this two articles compares the tearing energy of unfilled and filled SBR at steady and dynamic tearing and relates it to viscoelasticity. The second publication deals with the J-Integral, a fracture mechanical quantity that determines the energy flow into a closed contour. This way could be shown that most energy is lost further away from the crack tip and only a fraction is available at the process zone around the crack tip.

# Acknowledgements

The writing of my thesis would not be possible without the help of many people and institutions. I would like to thank my supervisor Prof. Manfred Klüppel for his beneficial guidance and assistance during my research. Also he always took time for discussion when it was necessary.

The DFG is acknowledged to finance my most important project (grant KL 1409/9-1). The very good cooperation with the partners in this project, the IPF Dresden and the Continental AG, is appreciated.

I would also like to thank for the assistance and company of my former colleagues at the DIK. I appreciate the support of the colleagues of my department as well as of others, who helped me in my research. Special thanks go to my room mate Dr. Jan Plagge, who was a great help, especially but not only in programming related questions. He authored the model used to calculate stresses and energy density in the last publication, but also implemented his model in python code. Also in constructing the python code to calculate the J-Integral he was a great help. I appreciate him, Patrick Stratmann and Anuj Jain who have been my room mates for many years, as well as the other colleagues for the nice time I spent in the institute.

I would also like to thank my parents, my brother Sebastian and my girlfriend Ayde.

# Abstract

This work deals with crack growth investigations of tire tread compounds in laboratory. These measurements are usually performed with the Tear Fatigue Analyzer. In the Tear Fatigue Analyzer notched strip samples are loaded dynamically and the resulting crack growth rate  $dc/dn$  is measured. This way the crack growth rate  $dc/dn$  in dependence of tearing energy  $T$  can be determined for a compound under specific loading condition. The tearing energy  $T$  describes the energy available for crack growth and can be calculated for different sample geometries. This energy depends particularly on the stored energy density that is caused by straining the sample.

Thereby the crack growth rate depends on the used rubbers. Natural rubber, partially crystallizing under strain, shows clearly lower crack growth than the synthetic butadiene and styrene-butadiene rubbers. Using active fillers like carbon black leads to strongly decreased crack growth due to the multiple interactions between filler and polymer matrix. The crack growth in a polymer blend depends also on the morphology of the distinct polymer phases and the magnitude of the interphase. Also the filler distribution into the different polymer phases and the interphase is influencing the crack growth properties. The dynamic mechanical method used to determine the filler distribution is based on the increase of loss modulus due to the filler but the results are influenced by crystallization of the butadiene rubber.

The theoretic description of tearing energy in dependence of crack velocity was developed for steady tearing at constant crack velocity. It can be demonstrated that these concepts can be transferred to the dynamic crack growth of unfilled rubber, partially also to the dynamic crack growth of filled rubber.

When applying the tearing energy on elastomers it should be noticed that only a small fraction of this energy is reaching the process zone at the crack tip. The decrease of tearing energy towards the crack tip can be determined by the J-Integral. It turns out that the J-Integral decreases from its plateau value at large integration radii towards very small values for small integration radii. This decrease corresponds to the energy that is lost due to viscoelastic dissipation outside the crack tip and which is not available for crack growth.

Keywords: Crack growth, Tearing energy, Polymer blend, Viscoelasticity, J-Integral

# Kurzfassung

Diese Arbeit beschäftigt sich mit Risswachstumsuntersuchungen an Reifenlaufflächenmischungen im Labor. Diese Messungen werden gewöhnlich mit dem Tear Fatigue Analyzer durchgeführt. Der Tear Fatigue Analyzer belastet gekerbte Streifenproben dynamisch und misst die auftretende Risswachstumsrate  $dc/dn$ . Damit lässt sich für eine Mischung bei gegebener Belastungsart die Risswachstumsrate  $dc/dn$  in Abhängigkeit der Weiterreißenergie  $T$  bestimmen. Die Weiterreißenergie  $T$  beschreibt die für das Risswachstum zur Verfügung stehende Energie und kann für verschiedene Probenformen berechnet werden. Sie hängt insbesondere von der gespeicherten Energiedichte ab, die durch die Streckung der Probekörper verursacht wird.

Die Risswachstumsrate hängt dabei von den verwendeten Kautschuken ab. Naturkautschuk, der unter Dehnung teilweise kristallisiert, zeigt deutlich niedrigeres Risswachstum als die synthetischen Polybutadien- und Styrol-Butadien-Kautschuke. Die Verwendung von aktiven Füllstoffen wie Ruß führt durch die starke Wechselwirkung mit der Polymermatrix zu erheblich verringertem Risswachstum. Das Risswachstum in einem Polymerblend hängt dabei auch von der Morphologie der verschiedenen Polymerphasen und der Größe der Interphase ab. Ebenso beeinflussen die Verteilung des Füllstoffs in die verschiedenen Polymerphasen und die Interphase die Risswachstumseigenschaften. Die dynamisch mechanische Methode zur Bestimmung der Füllstoffverteilung basiert auf der Vergrößerung des Verlustmoduls durch den Füllstoff, aber die Ergebnisse werden dabei durch die Kristallisation des Polybutadiens beeinflusst.

Die theoretische Beschreibung der Weiterreißenergie in Abhängigkeit der Rissgeschwindigkeit wurde für stetiges Risswachstums bei konstanter Rissgeschwindigkeit entwickelt. Es zeigt sich, dass sich diese Konzepte auch für das dynamische Risswachstum von ungefülltem Kautschuk und zum Teil auch von gefülltem Kautschuk übertragen lassen.

Generell ist bei der Verwendung der Weiterreißenergie für Elastomere zu beachten, dass nur ein kleiner Teil dieser Energie die Prozesszone an der Rissspitze erreicht. Der Abfall der Weiterreißenergie zur Rissspitze hin, kann durch die Bestimmung des J-Integrals ermittelt werden. Es ergibt sich, dass das J-Integral von seinem Plateauwert für große Integrationsradien mit kleiner werdendem Integrationsradius auf sehr kleine Werte abnimmt. Diese Abnahme entspricht der außerhalb der Rissspitze durch viskoelastische Dissipation verlorenen Energie, die nicht für das Risswachstum zur Verfügung steht.

Stichwörter: Risswachstum, Weiterreißenergie, Polymerblend, Viskoelastizität, J-Integral

# Abbreviations

BR	Butadiene Rubber
CBS	N-cyclohexyl-2-benzothiazole sulfonamide
DFM	Dynamic Flocculation Model
DIK	Deutsches Institut für Kautschuktechnologie e.V.
DMA	Dynamic Mechanical Analysis
NR	Natural Rubber
SBR	Styrene Butadiene Rubber
SEN	Single Edge Notched
TFA	Tear Fatigue Analyzer
WLF	Williams-Landel-Ferry





# Contents

<b>1</b>	<b>INTRODUCTION</b>	<b>3</b>
1.1	Setting the scene	3
1.2	Elastomers	4
1.3	Elastomer blends	7
1.4	Crosslinking	8
1.5	Viscoelasticity	10
1.6	Reinforcing fillers	12
1.7	Filler network	13
1.8	Crystallization of elastomers	14
1.9	Modeling of elastomers	16
<b>2</b>	<b>FRACTURE MECHANICS</b>	<b>21</b>
2.1	Griffith criterion	21
2.2	Sample geometries	22
2.3	Tearing energy	24
2.4	Fatigue crack growth	25
2.5	Viscoelastic crack growth	27
2.6	The J-Integral	30
<b>3</b>	<b>INFLUENCE OF BLEND MORPHOLOGY ON FATIGUE CRACK PROPAGATION</b>	<b>33</b>
3.1	Introduction	33
3.2	Publication 1: Influence of phase morphology and filler distribution in NR/BR and NR/SBR blends on fracture mechanical properties	37
3.3	Publication 2: Impact of mixing procedure on phase morphology and fracture mechanical properties of carbon black filled NR/SBR blends	57
3.4	Publication 3: Thermally induced crystallization of polybutadiene in dynamic mechanical measurements	71
3.5	Supplementary information	83
3.6	Outlook	87

<b>4</b>	<b>INFLUENCE OF ENERGY DISSIPATION AROUND THE CRACK TIP ON STEADY AND DYNAMIC TEARING</b>	<b>89</b>
4.1	Introduction	89
4.2	Publication 4: Viscoelastic response during crack propagation of unfilled and filled SBR	93
4.3	Publication 5: The role of stress softening in crack propagation of filler reinforced elastomers as evaluated by the J-Integral	109
4.4	Supplementary information	123
4.5	Outlook	128
<b>5</b>	<b>SUMMARY AND CONCLUSIONS</b>	<b>131</b>
	<b>BIBLIOGRAPHY</b>	<b>133</b>
	<b>INDEX</b>	<b>141</b>
	<b>APPENDIX</b>	<b>143</b>
A.1	Curriculum vitae	143
A.2	Own literature	144
A.3	Contributions to Conferences	145

# 1 Introduction

## 1.1 Setting the Scene

The polymeric materials known as rubber can be extracted from natural sources or produced synthetically. Rubber from natural sources is called natural rubber and it is obtained from plants containing latex. Most commonly it is tapped from the rubber tree *Hevea brasiliensis* (Fig. 1.1). Natural rubber was already known 1000 B.C. in Central America.[1-3] However the first thorough scientific investigations of rubber were only done by Francois Fresneau in the late 1740s [1]. Vulcanization with sulfur, discovered by Charles Goodyear in 1839, was the first purposeful crosslinking of rubber. Although being used for special applications prior to this, many modern applications rely on the elasticity and improved thermal properties of crosslinked rubber that is formed by vulcanization. The first synthetic rubbers were developed in the beginning of the last century. Polybutadiene and styrene-butadiene rubber were invented in 1910 and 1929, respectively.[3]



Fig. 1.1: Latex dripping into a cup from a tapped rubber tree, Krabi, Thailand [4].

At latest the invention of the solid rubber tire by Thomas Hankook and the pneumatic tire by William Thomson, both in 1845, introduced rubber products, for which mechanical failure was a major issue. Mechanical fracture is nowadays an important or even the most important factor that governs the lifetime of many elastomer products and can be a great problem. Therefore the improvement and investigation of fracture mechanics of rubber is necessary. Due to the different rubbers and other ingredients used nowadays, a variety of rubber formulations exists. Therefore elastomers need to be evaluated regarding their crack growth

behavior in dependence of the compound recipe and the micromechanical compound morphology. The fracture resistance of elastomer compounds depends on the diverse micromechanical structure in the polymers and on its interaction with other components of the compounds, especially with fillers.

## 1.2 Elastomers

Polymers are large macromolecules composed of a huge number of repeatedly covalently bonded molecules, the monomers. Many polymers consist mainly of carbon and hydrogen atoms. The backbone of the polymer is then built as a chain of carbon atoms. A C-C double bond in the monomer can be used in the polymerization to build the bonding to the next monomer. If there is a second double bond in at least some of the monomers this C-C double bond remains in the polymer.[5-6] Vulcanized polymers with a glass transition temperature below service temperature (and that are elastically deformable above the glass transition temperature) are called elastomers due to their elastic behavior. All elastomers used in this study are composed solely of carbon and hydrogen atoms, have a glass transition temperature below 0°C and contain remaining C-C double bonds in the chain backbone.

Polymers differ not solely due to different monomers but also due to the arrangement of the monomers. In the arrangement of the monomers factors like the number of monomers in a polymer chain, the distribution of chain lengths and branching are important. But also for a single linear arrangement of the monomers, the polymer can vary in the carbon atoms of the monomer which create the bonds to the adjacent monomers. These carbon atoms are included in the name of the polymer. During polymerization monomers are usually arranged head-to-tail due to steric reasons. This means that one side of a monomer is bonded to the other side of the next monomer. In dependence of the geometrical arrangement also cis- and trans-isomers are distinguished [5,7]. For that the positions of two substituents regarding a double bond are considered. When both substituents are placed on one and on different sides of the double bond, the isomers are denoted by cis and trans, respectively. The structure of the polymer strongly influences crystallization which only appears for very regular arranged polymers.

GLASS TRANSITION. The glass transition can be seen as second order phase transition between a glassy state at low temperatures and an elastic state at higher temperatures [5,8] (compare Fig. 1.8). As the system is not in thermodynamic equilibrium some features of the glass transition can only be explained with a description as non-equilibrium state. In this

theory of free volume the chain mobility is described via the amount of a free volume. Below the glass transition temperature  $T_g$  the voids which form the free volume  $v_g$  are too small to allow processes of position change for movement of chain segments.[9] Above the glass transition temperature the free volume  $v_f = v_g + v_m\Delta\alpha(T - T_g)$  increases with the molecular volume  $v_m$  and the thermal expansion coefficient  $\alpha$  (Fig. 1.2). The glass transition temperature is determined by the structure of the polymer. Voluminous side chains impede the bond rotations of the backbone and lead to an increase of the glass transition temperature.[5] If the polymer behaves glassy depends not only on the temperature but also on the measurement velocity. For too high measurement velocities the polymer chains do not have enough time to flow in the free volume and the polymer behaves glassy. Important tire properties are directly related to the glass transition temperature of the elastomer: Wet skid of a tire tread is clearly improving with increasing glass transition temperature [10-11] but rolling resistance is usually better for compounds with low  $T_g$  [11].

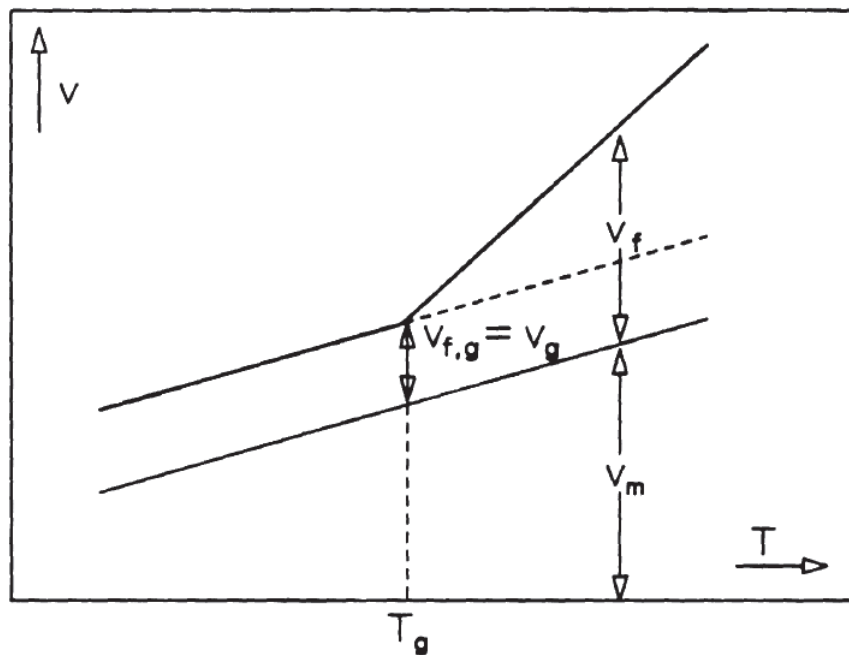


Fig. 1.2: Dependency of the free volume  $v_f$  on temperature  $T$ .  $v_m$  is the molecular volume.[9]

**NATURAL RUBBER (NR).** Natural rubber is produced biosynthetically in plants and consists of polyisoprene. Natural rubber contains a few percent of other constituents like proteins. For the production of NR nearly solely *Hevea brasiliensis* is used. The polyisoprene in natural rubber obtained from this plant is nearly completely cis-1,4-polyisoprene. The cis-1,4 content is >99.9%.[12] Cis-1,4-polyisoprene is a polymer consisting of isoprene monomers polymerized in head-to-tail configuration (Fig. 1.3). Natural rubber has a very high average

molecular weight between  $1 - 3 \cdot 10^6 \text{ g/mol}$ . Usually the molecular weight is reduced before processing by scission of polymer chains [3]. Natural rubber can crystallize, especially under strain it shows strong crystallizing behavior. This makes NR very fracture resistant in comparison to other rubbers. Therefore it is used in heavy duty articles like truck tires and conveyor belts.

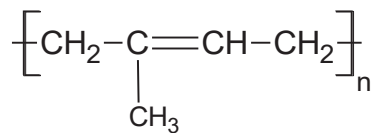


Fig. 1.3: Structure formula of cis-1,4 polyisoprene [3]

**BUTADIENE RUBBER (BR).** Butadiene rubber or Polybutadiene is a synthetically polymerized polymer consisting of butadiene monomers. Polymerization of the end atoms of the butadiene yields 1,4-polybutadiene (Fig. 1.4 a). When the butadiene is polymerized at the first two carbon atoms 1,2-polybutadiene is incorporated into the polymer chain. That way vinyl side chains are integrated into the polymer (Fig. 1.4 b). Due to the low amount of side chains high-cis BR with a large proportion of cis-1,4 polybutadiene has a very low glass transition temperature. The  $T_g$  increases linearly with vinyl content of the BR [13]. Regular arranged polybutadiene can crystallize at low temperatures. Due to its low glass transition BR lowers the rolling resistance of tires and crack initiation rates [3].



Fig. 1.4: Structure formula of 1,4-polybutadiene (a) und 1,2-vinyl-polybutadiene (b) [3]

**STYRENE BUTADIENE RUBBER (SBR).** Styrene-butadiene rubber is also produced synthetically. This rubber contains beside the polybutadiene monomers in Fig. 1.4 also styrene monomers (Fig 1.5). Due to the large benzol side groups SBR has a high  $T_g$ , strongly linearly dependent on styrene and vinyl content [13]. SBR is the most used polymer for automotive tires due to a good compromise between wet grip and rolling resistance [3].

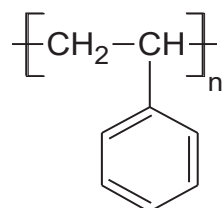


Fig. 1.5: Structure formula of polystyrene [3]

### 1.3 Elastomer blends

A compound with more than one dissimilar elastomer is called blend. Elastomer blends are used to fulfill conflicting demands on the material [14]. In general a blend combines the properties of the polymers. Nevertheless synergetic effects are possible, so that a blend can have superior properties compared to both polymers [14-16].

Polymers in a blend are miscible or immiscible. Two components mix with each other when the free energy  $F = U - TS$  is decreased due to mixing. Entropy always favors mixing but the entropy change for the mixing of two polymers is very small. The reason for that is the relatively low number of molecules due to their high molecular weights that leads to a low number of configurations the polymers can adapt. In the simplified lattice model known as Flory-Huggins theory both monomers are assumed to occupy the same lattice. Volume changes on mixing and chain connectivity are ignored. The entropy of changing per lattice site is  $\Delta\bar{S}_{mix} = k_B \left[ \frac{\phi_A}{N_A} \ln(\phi_A) + \frac{\phi_B}{N_B} \ln(\phi_B) \right]$ .  $N_A$  and  $N_B$  are the lattice sites occupied by monomer A and monomer B, respectively.  $\phi_A$  and  $\phi_B$  are their phase volume fractions. The energetic change can be described by comparing the interaction energies between monomers of the same polymer and between both polymers. The energy change on mixing per lattice site is  $\Delta\bar{U}_{mix} = \frac{z}{2}(2u_{AB} - u_{AA} - u_{BB})\phi(1 - \phi)$ .  $u_{AB}$  is the interaction energy between the different monomers and  $u_{AA}$  and  $u_{BB}$  are the interaction energies between the same monomers.  $z$  is the coordination number of the lattice. The net attraction between the species of the different non-polar polymers is given by the interaction parameter  $\chi = \frac{2u_{AB} - u_{AA} - u_{BB}}{k_B T}$ . The free energy of mixing per lattice site is then given by the Flory-Huggins equation:

$$\Delta\bar{F}_{mix} = k_B T \left[ \frac{\phi}{N_A} \ln(\phi) + \frac{1 - \phi}{N_B} \ln(1 - \phi) + \chi\phi(1 - \phi) \right] \quad (1.1)$$

Blends with  $\chi < 0$  are always miscible. But  $\chi$  is usually positive and it is related to the square of the difference in solubility parameters  $\delta$  of the polymers. The solubility parameters are defined as square root of the energy of vaporization divided by the monomer volume.[17-19] The solubility parameter is increasing linearly with the styrene content and decreasing linearly with the vinyl content [20]. As the entropy gain for large chains is very small and usually  $\chi > 0$ , polymer blends are mostly immiscible. In this case phase separation occurs and both polymers occupy separate domains [14]. In between both domains exists an area called interphase in which the polymers are mixing. Size of domains and interphase depend on how immiscible the polymers are, e.g. on the difference of solubility parameters. The volume of all

domains of a given phase in relation to the total volume is the respective phase volume fraction.

## 1.4 Crosslinking

Unvulcanized rubber is a very viscous liquid containing large polymer chains. Therefore it flows at sufficiently large time scales. Crosslinking the rubber connects the polymer chains via so called crosslinks. When sufficiently crosslinked, the polymer chains cannot flow past each other freely, as the crosslinks exert elastic forces on deformations. That way a soft but solid body is developed. The most common way of crosslinking is the crosslinking of rubbers that contain double bonds with sulfur at high temperatures. This is denoted as vulcanization. In the vulcanization process sulfur bridges between polymer chains are created. For this purpose usually accelerators, which reduce the vulcanization time drastically, are added to the compound. The sulfur bridge settles at the position of the allylic proton adjacent to the double bond which is transformed into a single bond.[6,21] Therefore for sulfur vulcanization double bonds remaining from polymerization are essential. On the other hand double bonds remaining after vulcanization are weak spots where ageing can take place more easily, as the dissociation energy of the C-C double bond is lower than a C-C single bond.

The amount of crosslinking is specified by the crosslink density. This denotes the number of polymer crosslinks per volume. The crosslink modulus  $G_c$  introduced in the models in chapter 1.9 is proportional to the crosslink density. The torque of a dynamically twisted elastomer increases with crosslink density. The increase of the torque during vulcanization at elevated temperatures is measured using a vulcameter. The evolution of the torque with time, the so called vulcameter curve (Fig. 1.6), enables the determination of vulcanization kinetics. After the induction period, in which no significant crosslinking occurs, the formation of crosslinks leads to a steep increase of the torque. First mainly polysulfidic sulfur bridges are built. With increasing vulcanization time the sulfur bridges are substituted by shorter di- and monosulfidic sulfur bridges [22-23]. After the placement of the sulfur into the polymer network the vulcameter curve flattens and ageing takes place. Optimal properties of the rubber are obtained shortly before. Although other properties are still improving the maximal tear resistance and resistance against dynamic crack growth are found at small under-cure [24]. The vulcanization is performed until the torque has increased by 90% of the torque difference between maximal and minimal value ( $t_{90}$ -time).



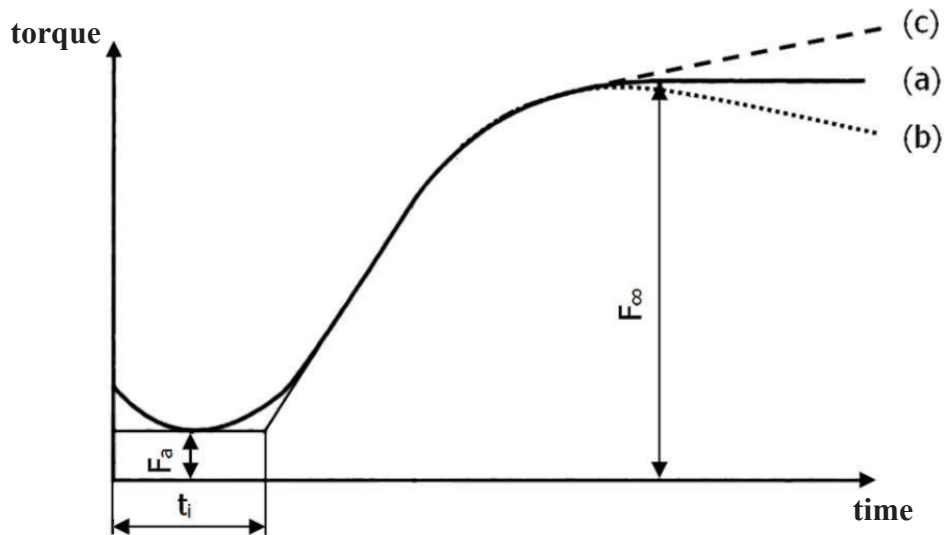


Fig. 1.6: Schematic vulcameter curve with induction time  $t_i$  and plateau (a), reversion (b) and marching modulus (c) [3].

Network formation and the dependency of various vulcanizate properties on crosslinking density are sketched in Fig. 1.7.

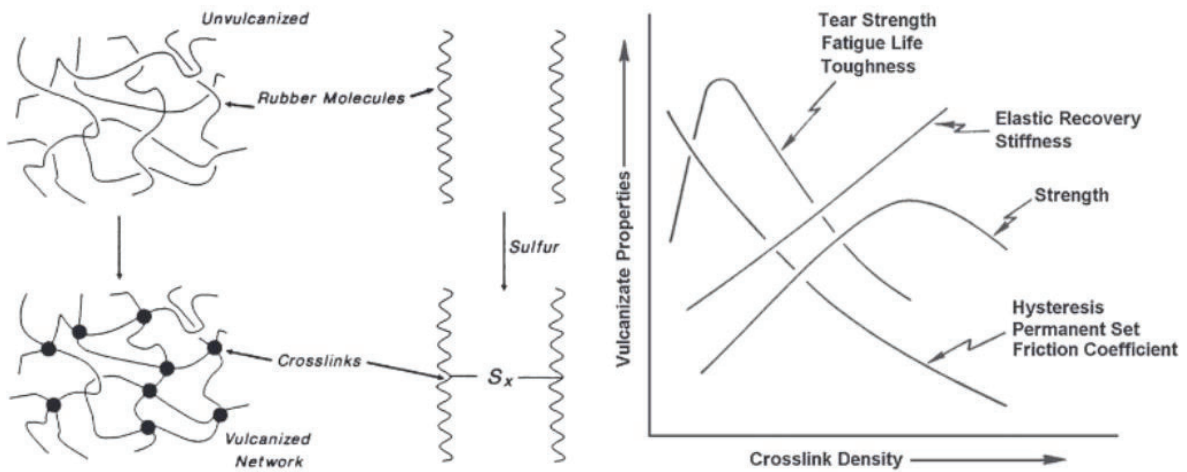


Fig. 1.7: Network formation (a) and dependency of vulcanizate properties on crosslink density (b) [21].

Vulcanization with sulfur is accelerated by adding accelerators. These polar organic substances open the  $S_8$ -rings of the sulfur and interact in the vulcanization process [3,24]. Zinc oxide is amplifying the effect of many accelerators [24]. The proportions of mono-, di and polysulfidic bridges depend not only on vulcanization time but also on the ratio of sulfur to accelerator. Conventional systems with larger amount of sulfur result in comparably long sulfur bridges. Efficient systems consist of more accelerator than sulfur so that mainly monosulfidic crosslinks are created. At semi-efficient systems with similar amounts of sulfur

and accelerator mostly mono- and disulfidic bridges are built. The crosslink structure depends also on the polymer, e.g. SBR reveals shorter sulfur bridges as equally vulcanized NR. Elongation at break, tensile strength and tear resistance increase with increasing length of the sulfur bridges but the thermal stability decreases.[3,5]

## 1.5 Viscoelasticity

**YOUNG'S MODULUS AND SHEAR MODULUS.** The Young's modulus  $E = \sigma/\varepsilon$  describes the resistance of a material to uniaxial stress  $\sigma$  at a small strain  $\varepsilon$ . The shear modulus  $G$  is defined as ratio between shear stress and shear strain.

**COMPLEX MODULI.** Crosslinked rubber is a viscoelastic material. For simplicity we consider now simple shear of a rectangular block specimen sheared between two perpendicular rigid surfaces with cross-section  $A$ . Applying a force  $f$  onto one of the rigid surfaces signifies applying the shear stress  $\sigma = f/A$ . The displacement  $\Delta x$  of the rigid surface implies a shear strain  $\gamma = \Delta x/d$ , where  $d$  is the distance between the two rigid surfaces. When oscillatory strain  $\gamma = \gamma_0 \sin(\omega t)$  is applied the stress  $\sigma = \sigma_0 \sin(\omega t + \delta)$  has the same frequency  $\omega$  but is preceding by a phase angle  $\delta$ . The complex modulus  $G^*(\omega) = \sigma^*/\gamma^*$  is the ratio of complex stress  $\sigma^*$  and complex strain  $\gamma^*$ .  $G^* = G' + iG''$  can be separated into a part  $G'$  in-phase and a part  $G''$  out-of-phase with the strain by  $\pi/2$ . The storage modulus  $G'$  corresponds to the energy being stored in the deformation and released under unloading. The loss modulus  $G''$  corresponds to the energy dissipated during deformation. The ratio of loss modulus and storage modulus yields the tangent of the phase angle  $\delta$ . [17]

The moduli are not only frequency but also temperature dependent.  $G'$  for rubber is comparably large ( $\sim 1$  GPa for unfilled polymer) for low temperatures clearly below the glass transition temperature  $T_g$  [17]. Around  $T_g$  the storage modulus drops by around three orders of magnitude. As  $G'$  and  $G''$  are real and imaginary part of a complex number, the Kramers-Kronig relations hold. These equations state that  $G'$  and  $G''$  can be calculated through an integration of the other part of the modulus, respectively. Therefore the loss modulus  $G''$  has a peak at  $T_g$ . Above the glass transition  $G'$  is decreasing more slowly. The behavior of storage modulus  $G'$  and loss modulus  $G''$  is shown for unfilled NR in Fig. 1.8.

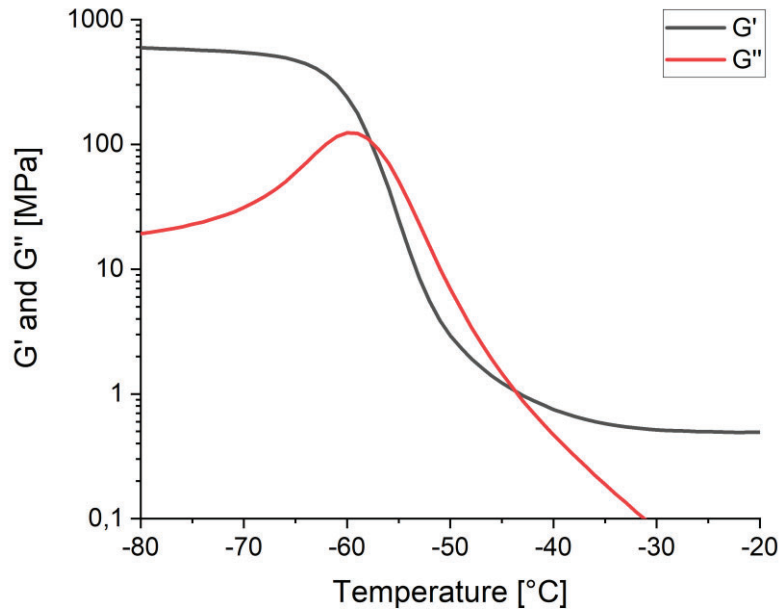


Fig. 1.8: Storage modulus  $G'$  and loss modulus  $G''$  for unfilled NR measured at various temperatures with a frequency of 1 Hz and 0.5% strain amplitude.

Equivalent behavior is also seen in the Young's modulus. The Young's modulus  $E_0$  at vanishing frequency or high temperatures is very low. The modulus  $E_\infty$  at high frequencies or low temperatures is around three magnitudes larger.

**TIME-TEMPERATURE SUPERPOSITION.** In the harmonic excitation of viscoelastic materials an increase of test frequency  $\omega$  has the same effect as decreasing the temperature  $T$ . With both changes the material is going into the glass transition. If all relaxation processes can be connected to a single relaxation process, e.g. the monomer relaxation, a material is called rheological simple. In these materials holds the time-temperature superposition principle  $G'(\omega, T_0) = G'(\omega/a_T, T)$ . It states that the modulus measured at temperature  $T$  is equivalent to the modulus at the reference temperature  $T_0$  when the frequency  $\omega$  is divided by horizontal shifting factors  $a_T$  which only depends on  $T$  and  $T_0$ . This way, out of measurements at different temperatures, so called master curves can be created. These master curves reflect the behavior of the material for a wider range of frequencies at the reference temperature  $T_0$ . The horizontal shifting factors  $a_T$  can be calculated by the WLF-equation

$$\log(a_T) = -\frac{C_1(T - T_0)}{C_2 + (T - T_0)} \quad (1.2)$$

The constants  $C_1$  and  $C_2$  are fitted. The WLF-equation is valid between the glass transition temperature  $T_g$  and approximately  $T_g+100^\circ\text{C}$ . [25-26] The WLF equation is derived from the

viscosity  $\eta$  decreasing proportional to  $e^{v^*/v_f}$  with increasing free volume  $v_f$ . The horizontal shift  $a_T$  is given by the ratio of  $\eta(T)/\eta(T_g)$ . [9]

## 1.6 Reinforcing fillers

Ingredients of a rubber compound which are insoluble in the polymer matrix and form a significant amount of the mixture are called filler. Inactive filler have a low surface area, therefore little interaction to the rubber matrix and essentially reduce the rubber content. Active fillers on the contrary have nanostructured morphology and therefore a high surface area that can interact with the rubber matrix. These fillers can reinforce the matrix, which means they are increasing the fracture energy of the compound [27]. Also other properties change due to the reinforcement. Viscosity and hardness increase and the stress-strain behavior changes significantly. This can be seen in higher stress values at given strain but also in a distinct form of the stress-strain curve. Not only the form of the stress-strain curve is changed but also the difference of the loading and unloading curve is greatly enhanced. The difference between the two curves is called hysteresis and the area in between the two curves corresponds to the dissipated energy. The permanent set is the remaining strain at zero stress which is also largely increased by the filler.

Fracture mechanical properties increase until they decrease at very high filler loadings [3,28]. Fracture mechanical properties and their dependence on filler loading are discussed more in Chapter 2. Active fillers are mainly reinforcing by the formation of a flexible filler-filler network and by strong polymer-filler couplings [29].

Technically most important fillers are carbon black and silica, both are active fillers. While carbon black is interacting with the polymer via van-der-Waals forces silica is bonding through silanes chemically with the polymer. Carbon black consist of small primary particles with cross-sectional dimensions of 5-100 nm. These primary particles are arranged in a fractal structure called aggregates. The aggregates form bigger agglomerates, which are broken when being mixed in a polymer compound. Due to and in dependence of their small particle size and structure carbon black has a high surface area between 10 and 200 m<sup>2</sup>/g. The surface area can be measured by gas adsorption or oil absorption.[29] The filler surface is covered by a layer of polymer that is decelerated in its motions by multiple van der Walls forces to the filler. This layer is denoted as bound rubber.

In small concentrations filler is only reinforcing due to hydrodynamic amplification. For freely dispersed, spherical particles, whose modulus is much higher than that of the rubber

matrix  $G_m$ , the modulus of the filled compound  $G$  is given by the Einstein-Smallwood formula  $G = G_m(1 + 2.5\phi)$  [30]. For higher filler concentrations a summand quadratic in the filler volume fraction appears. In branched aggregates a higher volume fraction  $\phi_{\text{eff}}$ , the effective filler volume fraction, has to be used, considering the occluded rubber that is trapped in the voids of the aggregates [31-32].

## 1.7 Filler network

During the induction period of vulcanization filled rubber compounds are subjected to elevated temperatures. This enables the filler to move in the polymer matrix. Due to depletion forces two filler aggregates that come close to each other tend to stay so that gradually a filler network is formed. The filler aggregates are surrounded by bound rubber. In the gap between two filler aggregates the bound rubber overlaps and the polymer is immobilized as it is bound to both sides. Due to its immobilization the polymer is behaving furthermore glassy. This glassy polymer in between the filler forms the filler-filler bonds which connect the aggregates into a network.[33-34] In Fig. 1.9 (a) a filler cluster is shown schematically. When a compound contains sufficient amount of filler the filler network becomes continuous. The critical filler content to build a continuous network is called percolation threshold. A compound with a continuous carbon black network has a largely increased electrical conductivity. This way the percolation threshold for SBR filled with the carbon black N339 is found at around 30 phr carbon black content [35].

**PAYNE EFFECT.** The filler network breaks down when filled rubber is deformed for the first time. The storage modulus has a comparably high constant value for very small deformations. Already at deformations larger than 0.2% the storage modulus is strongly decreasing. At large deformations a high amplitude plateau is reached, where the filler only acts by hydrodynamic interaction and polymer-filler interaction [36] (Fig. 1.9 (b)).

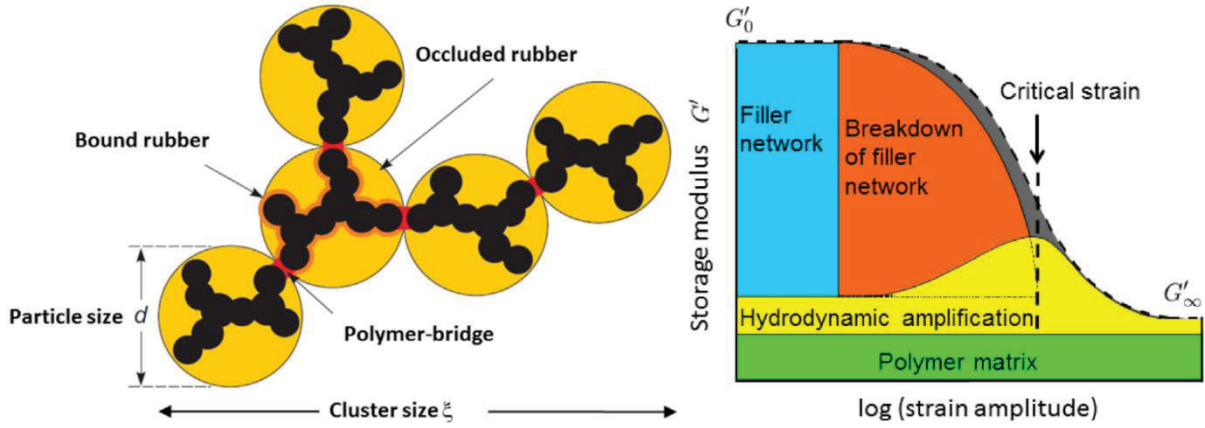


Fig. 1.9: Schematic diagram of a filler cluster with filler-filler bonds between aggregates. The effective filler volume fraction  $\phi_{\text{eff}}$  is greater than the actual filler volume fraction due to occluded rubber (a). Payne effect including the different contributions to the storage modulus  $G'$  (b).[37]

**MULLINS EFFECT.** Stress softening, which is often called Mullins effect, denotes the decrease of material stiffness measured in subsequent deformations in comparison to the stiffness measured at first deformation. When the strain is surmounting the previous deformation the stress is approaching the virgin stress-strain curve. Stress softening is already present for unfilled compounds but it is largely increased by filler. The increased stress softening for filled compounds is attributed to different phenomena, e.g. slippage of polymer segments on the filler surface. [38,29,3]

## 1.8 Crystallization of elastomers

Polymeric substances can be found in two states of matter, the liquid and the crystalline state. In the liquid or amorphous state the bonds connecting the polymer chain can rotate and therefore a single polymer molecule can adapt a large number of conformations  $\Omega$ . Then the entropy of the system  $S = k_B \ln(\Omega)$  is high. Under specific conditions the chains can order to form crystallites. This greatly decreases the entropy but the internal energy  $U$  is lowered. In elastomers no complete crystallization is realized but a semi-crystalline material is possible. The state of matter is adopted so that the free energy  $F = U - T \cdot S$  is minimized. As the entropic term, that favors the amorphous state, is proportional to the temperature  $T$  one possibility to crystallize is to reduce the temperature. Another possibility is to strain the material. In this case the number of configurations that the polymer chain can adopt is lower. Therefore the entropy loss during crystallization is reduced. Crystallization needs a very regular polymer configuration. A relatively low chain cross-section as in BR favors thermally induced crystallization and stiffer chains with higher cross-section as in NR favor strain-

induced crystallization [39]. Larger side groups as the benzol group in SBR are impeding crystallization.

**STRAIN INDUCED CRYSTALLIZATION.** NR is crystallizing under strain at room temperature while BR is not crystallizing under strain at room temperature for ordinary measuring times [40]. The crystallization in NR is expected to be explained by heterogeneous vulcanization. This leads to the existence of relative short chains that get fully stretched first and act as nucleation site for crystallites [41]. Surmounting a threshold strain value corresponding to the onset of crystallization the compound crystallizes. The crystallization leads to an increased strength. The reason for the reinforcement is still under discussion, but seems to be related to relaxation of the non-crystallizing rubber material [42]. The onset of crystallization seems to be independent of crosslink density [43-44]. Carbon black amplifies the local stretch of the polymer chains. This leads to a onset of crystallization at lower macroscopic strain values [44-45]. The crystallinity depends on crosslink density as the number of crystallites increases and the size of crystallites decreases with increasing crosslink density [43-44]. Strain-induced crystallization decreases with increasing temperature [46,44]. Due to the high local straining, crystallinity of NR is strongly increased in the vicinity of a crack tip [47-48]. This is seen as the reason for the large crack growth resistance of NR in comparison to other rubbers [44].

**THERMALLY INDUCED CRYSTALLIZATION.** Thermally induced crystallization denotes the property of some polymers to crystallize in contrast to strain induced crystallization without straining [49-50,9]. Vulcanization of the rubber and for vulcanized materials the crosslink density is strongly decreasing the crystallization rate as the crosslinks are hindering the diffusion of individual chain segments [49,9]. Some elastomers with regular composition as BR, NR, polyisoprene or polychloroprene show thermally induced crystallization [9,39]. This kind of crystallization is usually occurring at low temperatures but above the glass transition temperature  $T_g$ . The crystallization speed can be expressed via the half-life  $t_{1/2}$ , the time, half of the crystallizable material needs to crystallize [49,9,39]. The half-life strongly depends on the amount of regular ordered monomers and on temperature [51]. It is infinite for the glass transition temperature and the equilibrium melting temperature. The equilibrium melting temperature is the temperature at which an infinitely large solid and liquid have the same free energy. At higher temperatures the free energy of the crystal is higher so that crystallization is not occurring. In between these temperatures the logarithm of the half-life shows a parabolic dependency on temperature.[9,39] For BR the temperature of maximal crystallization rate is

between  $-55^{\circ}\text{C}$  and  $-56^{\circ}\text{C}$  [51] and for NR around  $-25^{\circ}\text{C}$  [50]. The maximal crystallization rate is in BR around three orders of magnitude faster than in NR [9,39] (Fig. 1.10). The low crystallization rate of NR is attributed to the methyl group [39].

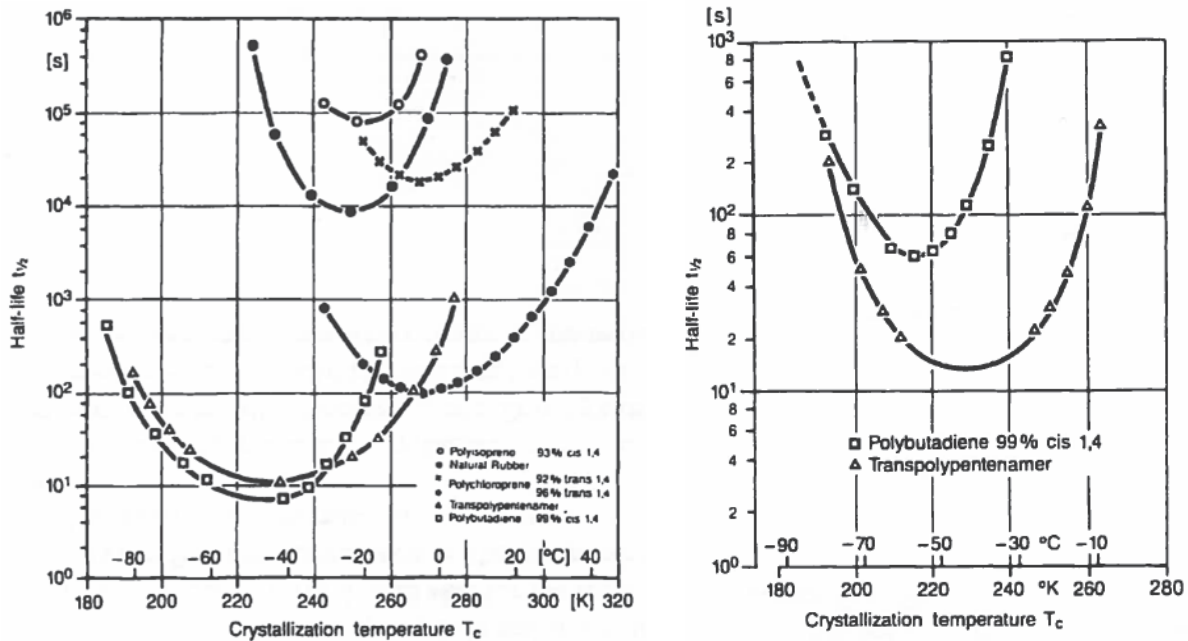


Fig. 1.10: Crystallization half-lives of different polymers in dependency of crystallization temperature: Uncrosslinked (a) and crosslinked (b).[9]

## 1.9 Modeling of elastomers

**STRESS TENSOR.** The stress in a material is given as tensor quantity. That means that the Cauchy stress tensor  $\sigma$  is given by a  $3 \times 3$  matrix with components  $\sigma_{ij}$  that represent the stress on the interface perpendicular to the direction  $i$  and acting in direction  $j$ . The Cauchy stress tensor  $\sigma$  is given in the actual configuration of the material. All models presented in this chapter are formulated with the Cauchy stress tensor. Situation in which all stress components involving the third component are zero are called plane stress conditions. These conditions typically occur in thin specimen in which the loading forces act parallel to the surface. The J-Integral for finite deformation (chapter 2.6) is using the 1. Piola Kirchhoff stress tensor  $\mathbf{P} = \det(\mathbf{F})\sigma(\mathbf{F}^T)^{-1}$ . [52] This stress tensor relates the actual forces with the undeformed areas.

**EXTENDED NON-AFFINE TUBE MODEL.** The elastomer matrix can be well described by the extended non-affine tube model. This model consists of a network of Gaussian chains interconnected by chemical crosslinks and entanglements. The entanglements around a specific chain are described by a virtual tube around that chain that restricts the fluctuation of



the chain. The tube radius is deforming non-affinely with the deformation with an exponent of 0.5. The chains in the model are not infinitely long, the model includes finite chain extensibility.[29] The energy density of the unfilled rubber in this model is given by

$$W_R = \frac{G_c}{2} \left[ \frac{\left(1 - \frac{1}{n}\right) \bar{I}_1}{1 - \frac{1}{n} \bar{I}_1} + \log \left(1 - \frac{1}{n} \bar{I}_1\right) \right] + 2G_e \bar{I}^* \quad (1.3)$$

The model has three fit parameters, the crosslink modulus  $G_c$ , the entanglement modulus  $G_e$  and the number of chain segments between two trapped entanglements  $n$ .  $I_1 = \lambda_1^2 + \lambda_2^2 + \lambda_3^2 - 3$  and  $\bar{I}^* = \lambda_1^{-1} + \lambda_2^{-1} + \lambda_3^{-1} - 3$  are the first invariant and a generalized invariant of the left Cauchy-Green Tensor, respectively.

**DYNAMIC FLOCCULATION MODEL.** The Dynamic Flocculation Model (DFM) [53] is established to model the quasistatic response in filled rubbers. These phenomena include stress softening, a largely increased hysteresis and permanent set. According to the model the filler interacts with the polymer matrix twofold: (i) The filler clusters increase the local strain in the polymer by hydrodynamic amplification and (ii) the strained and broken filler clusters contribute to the stress. The free energy density of the filled rubber can then be separated in two parts:

$$W(\varepsilon) = (1 - \phi_{\text{eff}})W_R(\varepsilon) + \phi_{\text{eff}}W_A(\varepsilon) \quad (1.4)$$

In this model the polymer matrix is still described by the extended non-affine tube model with energy density  $W_R$ , but the model is extended to include the interactions of the filler with the polymer. This effect is described by an amplification factor  $X_{\text{DFM}}$  that increases the local strain  $\lambda$  compared to the external strain  $\varepsilon$  in the following way:  $\lambda = 1 + X_{\text{DFM}}\varepsilon$ . The amplification factor  $X_{\text{DFM}}$  decreases with decreasing amount of rigid clusters that have never been broken and therefore with increasing maximal strain values.

When a critical cluster stress that depends on the cluster size is reached the cluster breaks into smaller aggregates which reaggregate under relaxation to softer clusters with damaged bonds. The energy density  $W_A$  stored in the deformation of the soft clusters which are breaking and reaggregating is added and causes hysteresis (Fig. 1.11). The energy density  $W_A$  is given by:

$$W_A = \sum_{\mu}^{\lambda_{\mu} > 0} \frac{1}{2} \int_{x_{\mu}(\lambda_{\text{max}})}^{x_{\mu}(\lambda)} G_A \varepsilon_A^2 \phi dx \quad (1.5)$$

Here,  $G_A$  is the elastic modulus and  $\varepsilon_A$  is the strain of the soft filler clusters and  $\phi$  is the cluster size distribution. The sum is taken over the three main axes  $\mu = 1,2,3$  in stretching direction ( $\dot{\lambda}_\mu > 0$ ). The integral is taken over the cluster sizes  $x$  that are soft but unbroken.

In addition to the three parameters of the extended non-affine tube model five new parameters are introduced: The filler volume fraction  $\phi_{\text{eff}}$  as introduced in Fig. 1.9 (a), the mean cluster size  $x_0$ , the tensile strength of virgin and damaged filler bonds  $s_v$  and  $s_d$  and the set stress  $\sigma_0$ .

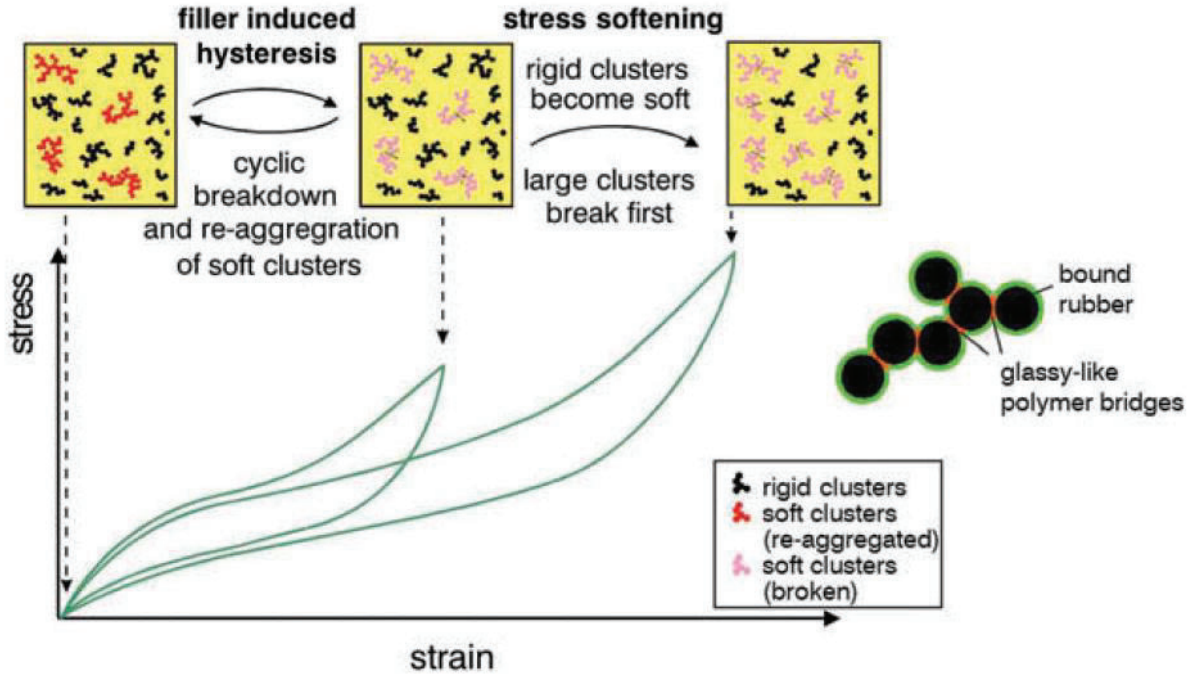


Fig. 1.11: Schematic drawing of micro-mechanical mechanisms giving rise to stress softening and filler-induced hysteresis as implemented in the DFM.[54]

**PHYSICALLY BASED MODEL OF STRESS SOFTENING AND HYSTERESIS.** A model proposed by J. Plagge and M. Klüppel describes also stresses and energy density of filled elastomers [55-56]. In this model the energy density is separated in two parts, an elastic part and a hysteretic part. The elastic part is based on the behavior of the unfilled elastomer matrix given by the extended non-affine tube model, but including hydrodynamic reinforcement of the filler. The hydrodynamic reinforcement is implemented via an amplification factor  $X$ , which describes the overstretching of the elastomer due to presence and rigidity of the filler. The elastic energy density is calculated as integration of the energy density  $W_R$  from the extended non-affine tube model multiplied by a distribution  $P_X(X) \sim X^{-X}$  of amplification factors:

$$W_X = \int_1^{X_{max}} P_X(X) W_R(X\bar{I}_1, X\bar{I}^*) dX \quad (1.6)$$

The distribution of amplification factors  $P_X(X)$  and the maximal amplification factor  $X_{\max}$  are shifting with increasing maximal strain to lower values as indicated by Fig. 1.12 (a). The elastic 1. Piola Kirchhoff stress  $\mathbf{P}_{el} = \det(\mathbf{F})\boldsymbol{\sigma}_{el}(\mathbf{F}^T)^{-1}$  is determined from the elastic stress  $\boldsymbol{\sigma}_{el}$  that is obtained as derivative of the elastic energy density  $W_X$  in eq. (1.6) with respect to the strain  $\lambda$ . The hysteretic stress  $\mathbf{P}_{hys}$  is determined by crossing an energy barrier to break the filler network. It is given by eq. (1.7):

$$\mathbf{P}_{hys} = \int_{-\infty}^{\zeta'} \frac{1}{1 + \frac{\zeta - \zeta'}{\sigma_c}} \frac{d\mathbf{P}_{el}}{d\zeta'} d\zeta' \quad (1.7)$$

Here,  $\sigma_c$  is the average critical stress to break rubber-filler structures and  $\zeta = \int_{-\infty}^t \dot{\mathbf{P}}_{el} dt'$  is an intrinsic time.

In addition to the three parameters of the extended non-affine tube model four new parameter are introduced: The filler volume fraction  $\phi_{eff}$ , the exponent  $\chi$  in the distribution of amplification factors, a parameter that determines the maximal amplification factor  $X_{\max,0}$  of the unstrained compound and the average critical stress  $\sigma_c$  to break rubber-filler structures (Fig. 1.12 (b)).

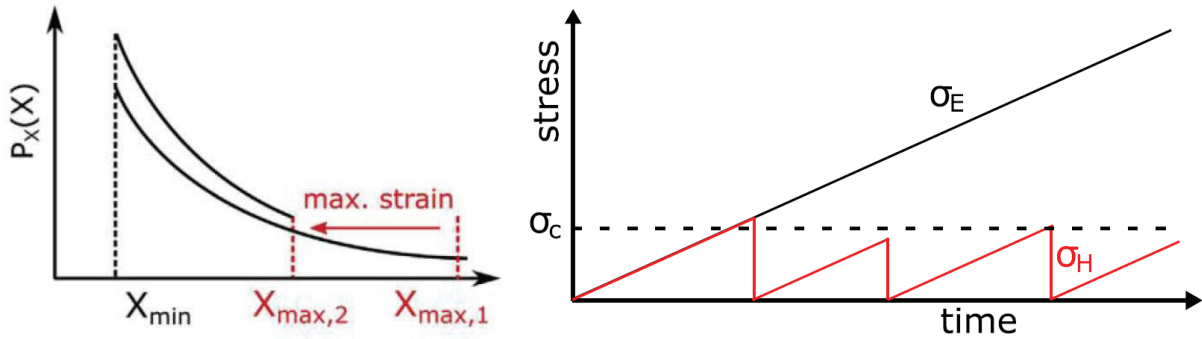


Fig. 1.12: Amplification factor distribution  $P_X(X)$  changes when  $X_{\max}$  is lowered due to increasing maximal strain (a). The hysteresis in this model is created by rubber-filler structures that are stretched up to a critical force  $\sigma_c$  at which they on average break down (b). [55]



## 2 Fracture mechanics

For the mechanical fracture of materials cracks need to initiate and to grow until final failure. Cracks are initiating at flaws in the material. In carbon black filled elastomers undispersed agglomerates act as flaws and their size is governing the fatigue life, because at larger agglomerates larger cracks are initiated.[57-58] Fracture mechanics deals not with crack initiation but studies the growth of existing cracks. The discipline started with Griffith work on glassy material [59] but after the second world war it was mainly developed on metals and later applied to all kind of materials [60].

So fracture mechanics of elastomers deals only with the propagation of existing cracks in elastomer compounds. It specifies how rapidly a present crack is growing under different loading conditions. The tear resistance determined during growth of existing cracks is strongly increased by active fillers and by strain-induced crystallization [3,39]. The improvement of crack growth resistance due to the filler increases with decreasing carbon black particle size [61]. For unfilled non-crystallizing elastomers the crack growth behavior is inferior and depends more on the type of cross-links than on the polymeric structure [62].

### 2.1 Griffith criterion

A crack in a solid does not grow by itself. To increase the crack from crack length  $c$  to  $c+dc$ , energy must be used against the cohesion energy between the molecules or to break the atomic bonds at the newly formed crack surface  $A = 2dc \cdot d$  (Fig. 2.1). Therefore the surface energy  $dS = 2dc \cdot d \cdot \gamma_0$  is necessary to grow the crack. Here,  $d$  is the thickness of the sample and  $\gamma_0$  is the specific surface energy.

When a sample is being deformed elastic strain energy  $W$  is stored. If a crack is growing the deformed material is partially relieved and some of the elastic strain energy is released. The Griffith criterion states that the crack is growing exactly than, when the surface energy  $dS$  is (over) compensated by the released elastic strain energy  $-dW$ :

$$-\frac{dW}{dc} \geq \frac{dS}{dc} \quad (2.1)$$

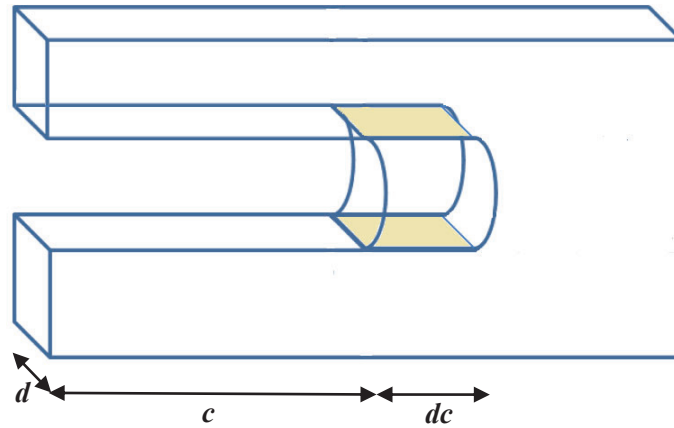


Fig. 2.1: Schematic drawing of a crack growing from length  $c$  to length  $c+dc$ . The newly formed crack surfaces  $A = 2dc \cdot d$  due to the crack growth are shown as colored surfaces.

Griffith calculated the released strain energy  $dW = -\sigma^2/2E \cdot \pi d c^2$  for an infinite half plate in uniaxial tension. Comparison of the surface energy increase with the elastic strain energy decrease yields crack growth for cracks exceeding a critical crack length  $c^*$ . [59]

## 2.2 Sample geometries

CRACK OPENING MODES. The types of forces exerted on the area around the crack tip are called crack opening modes. There are three different crack opening modes: In mode I the crack edges are separated by tensions perpendicular to the crack plane. Mode II and mode III denote shear stresses perpendicular and parallel to the crack front, respectively. Each mechanical load on the area around the crack tip is a combination of the three crack opening modes. The three modes are displayed in Fig. 2.2.

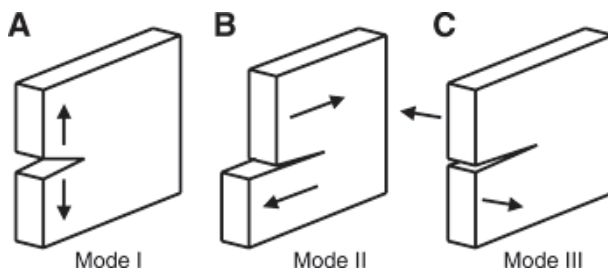


Fig. 2.2: Crack opening modes [63]

GEOMETRY OF SAMPLES. Different sample geometries can be tested (see Fig. 2.2). These geometries correspond to varying crack opening modes and deformation states. Unfilled elastomers possess a nearly constant volume: A sample being strained in one direction reduces its cross section so that the volume  $V = \lambda_1 \lambda_2 \lambda_3$  remains nearly constant. A constant

volume can be described by a Poisson's ratio  $\mu = -\ln(\lambda_2)/\ln(\lambda_1) = 0.5$ . Unfilled natural rubber has a Poisson's ratio of 0.4999 but it is clearly decreasing with carbon black content [64]. The Poisson's ratio is also decreasing at low temperatures and short measurement times. The decrease follows time-temperature superposition and is associated with the transition into the glass [65].

At uniaxial deformation the sample is strained in one direction  $\lambda_1 = \lambda$  and can contract in the two other directions. From volume constancy (assuming a Poisson's ratio of 0.5) follows  $\lambda_2 = \lambda_3 = 1/\sqrt{\lambda}$ . The single edge notched (SEN) sample is deformed uniaxially (Fig. 2.3 (b)). This strip sample with a single notch on one of the sides of the test-piece is used in the measurements with the Tear Fatigue Analyzer.

When the sample is strained in one direction  $\lambda_1 = \lambda$  and the deformation in a second direction is prevented ( $\lambda_2 = 1$ ), the sample can only contract in the third direction. From volume constancy (assuming again a Poisson's ratio of 0.5) follows  $\lambda_3 = 1/\lambda$ . A sufficiently broad test-piece which is clamped at its long sides can, due to the clamping, only contract marginally in this direction. This kind of specimen is called Pure Shear as the region far away from the edges is in a pure shear deformation state (Fig. 2.3 (c)). A crack can be inserted into one of the short sides of the Pure Shear sample. The crack should be sufficiently long so that effects due to the finite size of the specimen play a minor role.

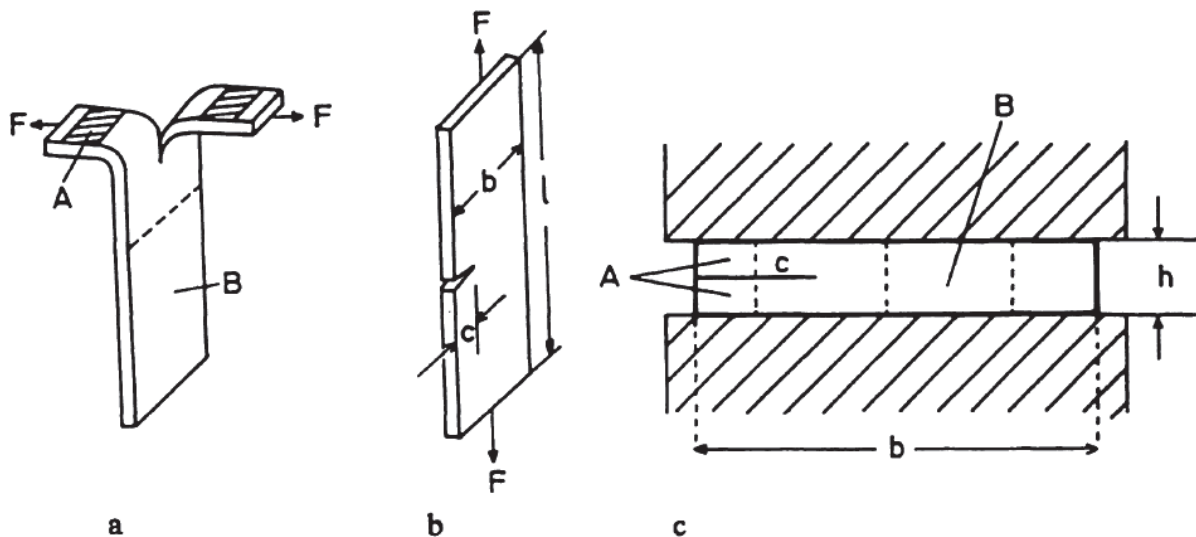


Fig. 2.3: Trousers sample with newly deformed volume indicated by A (a), Single edge notched sample (b) and Pure Shear sample (c) [9].

In these two test pieces the crack is loaded in mode I. On the contrary in the so called trousers sample the crack is loaded in mode III. This denotes a long specimen with a sufficient long crack inserted into the short side. The “trousers legs” created this way are clamped at different

sides and they are strained apart uniaxially (Fig. 2.3 (a)). When the tearing energy of the material is reached the specimen is cracking so that the legs are growing.

## 2.3 Tearing energy

The tearing energy  $T = -(dW/dS)_l$  denotes the characteristic energy of a material, which is necessary to increase the length of a crack. If a crack is growing depends not on the sample geometry or the forces which are applied at the specimen borders far away from the crack tip. Important for the crack growth is the state of deformation close to the crack tip. The state of deformation is determined by the shape of the cut and the strain at the crack tip. Therefore the tearing energy is independent of the sample geometry.[66]

TEARING ENERGY OF THE SINGLE EDGE NOTCHED SAMPLES. The tearing energy for SEN samples (Fig. 2.3(b)) is given by [66]

$$T = \frac{2\pi}{\sqrt{\lambda}} W_{el} c \quad (2.2)$$

Here,  $\lambda$  is the strain,  $W_{el}$  is the elastic energy density far away from the crack tip and  $c$  is the half crack contour length of the crack. The tearing energy is calculated from the energy difference  $dW$  between the notched sample in comparison to the unnotched one. The  $\sqrt{\lambda}$ -term in the denominator was added by Clapson and Lake [16] to account for the transversal contraction of rubber at larger strain. It has been shown [67] that the crack growth velocity for a specific material depends only on the tearing energy  $T$  not on the sample geometry, although for each geometry a distinct formula is used (eq. (2.2) – (2.4)).

TEARING ENERGY OF PURE SHEAR SAMPLES. In notched Pure Shear samples (Fig. 2.3 (c)) different regions can be distinguished:

- i. The crack tip region
- ii. The region in Pure Shear deformation far away in front of the crack tip (denoted by B in the figure)
- iii. The undeformed region at both sides of the crack (sufficiently far away from crack tip and the edges, denoted by A in the figure)
- iv. The regions at the edge of the sample. Their effect should be small for sufficiently broad specimen



For a sufficient long Pure Shear sample two states, which differ only in their crack length  $c$  and  $c+dc$ , simply differ in a volume  $hd\ dc$  being in region ii. and iii., respectively. Here,  $h$  and  $d$  are the height and the thickness of the undeformed sample, respectively. This yields a difference in strain energy  $dW = -W_{el}hd\ dc$ . The tearing energy of Pure-Shear samples is then

$$T = W_{el}h \quad (2.3)$$

The tearing energy for Pure Shear samples is thus independent of crack contour length  $c$ .

TEARING ENERGY OF TROUSERS SAMPLES. The tearing energy of trousers samples (Fig. 2.3 (c)) is

$$T = \frac{2\lambda F}{d} - 2bW_{el} \quad (2.4)$$

Here,  $F$  is the force,  $d$  is the sample thickness and  $b$  is the width of each leg of the trousers sample. The subtrahend  $-2bW_{el}$  considers the volume  $2bd\ dc$ , which the legs are growing due to the crack growth  $dc$  and therefore this volume is newly strained.

STRESS INTENSITY FACTORS. The stress intensity factors  $K$  are a measure for the stress field close to the crack tip. They depend on the loading as well as on the geometry of crack and sample. When the stress intensity factor reaches a critical value  $K_c$  so that under plane stress conditions  $T = K_c^2/E$  holds, the sample cracks. The stress and strain fields  $\sigma(r) \sim K/\sqrt{r}$  and  $u(r) \sim (K/E)\sqrt{r}$  vary with the distance  $r$  from the crack tip.[68]

## 2.4 Fatigue crack growth

In fatigue crack growth experiments a notched sample is loaded cyclically. The excitation can be harmonic or pulsed. The crack growth is measured as crack growth  $dc$  per loading cycle  $n$ . Also for dynamic crack growth the crack growth rate  $dc/dn$  of a crack in a material depends only on the tearing energy  $T$  not on the sample geometry [69]. In dependence of tearing energy different crack growth regions can be distinguished. Literature data are shown in Fig. 2.4.

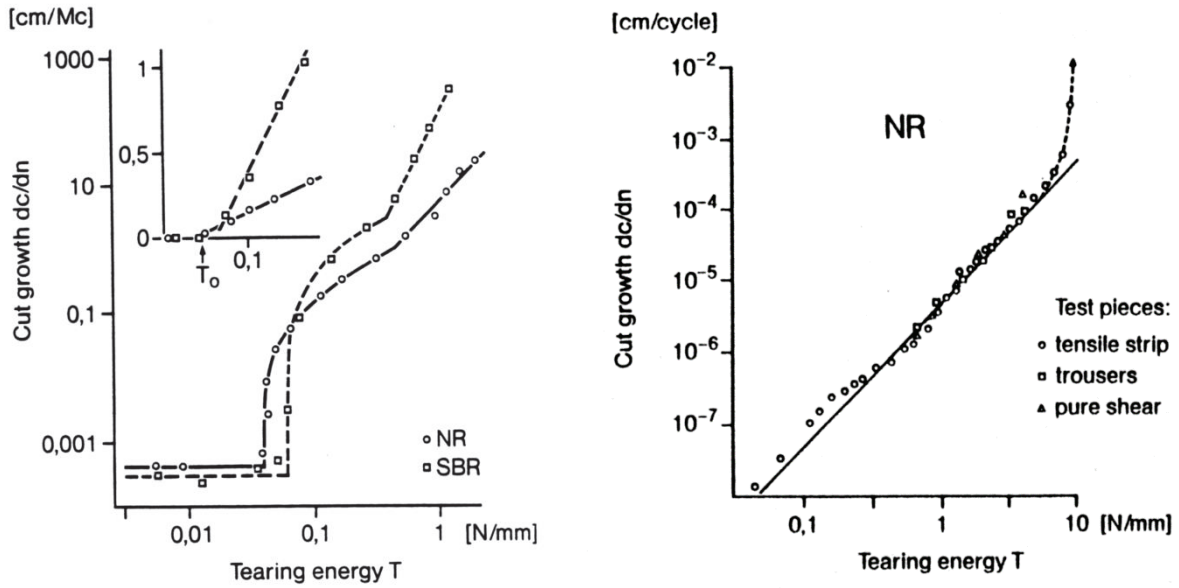


Fig. 2.4: Crack growth rate  $dc/dn$  in dependence of tearing energy for NR and SBR (a) [70] and for NR (b) [69]. In principle the theoretical behavior according to steady viscoelastic tearing is found (see Fig. 2.7). The crack growth rate  $dc/dn$  corresponds hereby to the crack growth velocity  $v$

**INTRINSIC STRENGTH.** Below the intrinsic strength  $T_0$  nearly vanishing crack propagation takes place. The crack growth rate  $dc/dn$  in this region is very low ( $\lesssim 10^{-8}$  mm/cycle) and independent of the tearing energy but depends on the ozone concentration. The intrinsic strength  $T_0$  is around 0.05 N/mm. This is in the order of magnitude to break the chain bonds. Just above  $T_0$  the crack growth rate increases linearly.[70]

**PARIS-ERDOGAN LAW.** In a range of intermediate tearing energies  $T$  the crack growth rate  $dc/dn$  follows a power law. This dependency is called Paris-Erdogan law [71-72]:

$$\frac{dc}{dn} = AT^B \quad (2.5)$$

The log-log plot of  $dc/dn$  in dependence of  $T$  is called Paris-plot. In this plot the prefactor  $A$  is given as the axis-intercept and the exponent  $B$  is given as the slope.  $A$  represents the crack growth rate at  $T=1$  N/mm and  $B$  describes how strong the crack growth is increasing with the tearing energy.

**CRITICAL TEARING ENERGY.** Close to the critical tearing energy  $T_c$  catastrophic tearing takes place and the crack growth rate  $dc/dn$  is increasing enormously. The critical tearing energy  $T_c$  is around 100-1000 times higher than the intrinsic strength  $T_0$ . The factor between  $T_c$  and  $T_0$  corresponds to the factor  $G'_\infty/G'_0$  from the theoretical description of steady tearing.

The crack propagation rate  $dc/dn$  in dynamic loading is measured by the Tear Fatigue Analyzer (TFA) [73]. In this machine the crack growths of 10 SEN-samples are measured simultaneously. The samples are stretched by a small preload and a usually dominating dynamic excitation (Fig. 2.5). The crack growth rates of filled SBR tested at moderate preload and the same strain amplitude are decreasing when the preload is increasing [74]. The dynamic excitation can be chosen, e.g. to be harmonic or pulsed. The tearing energy is regulated by the strain preset and calculated via eq. (2.2). The crack lengths are measured by evaluation of transmitted light images taken during the measurement. In these images the TFA-software determines the crack contour lengths by assessing the crack roughness.

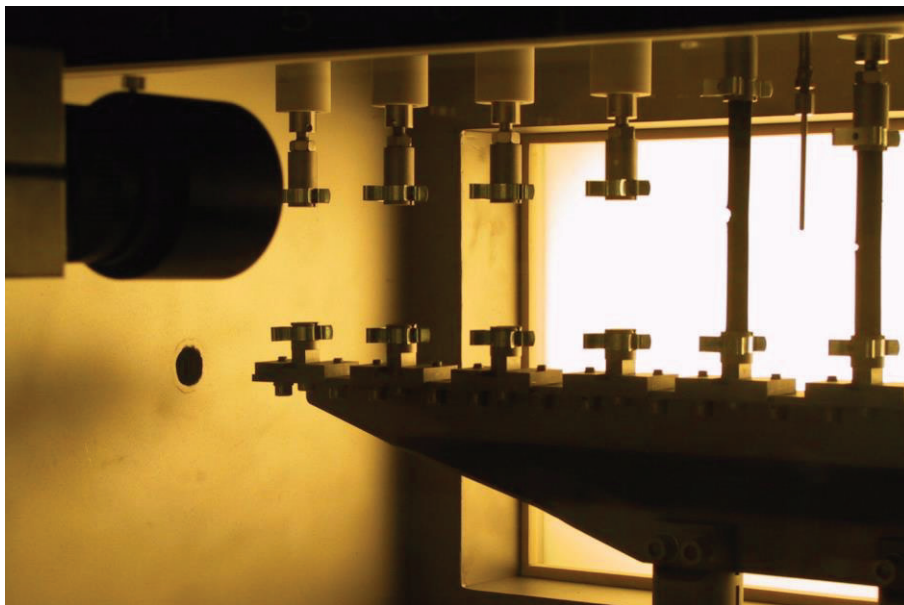


Fig. 2.5: Tear Fatigue Analyzer

## 2.5 Viscoelastic crack growth

**INTRINSIC STRENGTH.** The intrinsic strength  $T_0 = 2\gamma_0 = K_c^2/E_\infty$  is a threshold value below which no fracture occurs. Here,  $\gamma_0$  is the static surface energy and  $E_\infty$  is the Young's modulus at high frequencies and low temperatures. The intrinsic strength is connected to the fracture in the crack tip process zone. It can be measured at very low crack growth rates and high temperatures when viscous effects are minimized.

**VISCOUS EFFECTS.**

When tearing elastomers usually the viscoelastic properties are essential. Then a second contribution arises and these viscous effects are usually dominating the tearing energy [75-76]. The deformation rate compared to the bulk is increasing closer to the crack tip. Therefore

the material is approaching or even reaching the glass transition. At low crack velocities  $v$  or far away from the tip of the growing crack the excitation frequency is low so that the material is behaving elastically. The energy dissipation outside of the crack tip is in these cases low. Closer to the crack tip and with increasing crack velocity  $v$  the excitation frequency is increasing so that the elastomer is behaving more and more glassy. This leads to a strongly increasing energy dissipation. When the crack velocity is sufficiently high the vicinity of the crack tip is behaving glassy. The evolution of the different regions in dependence of crack velocity  $v$  is shown in Fig. 2.6.

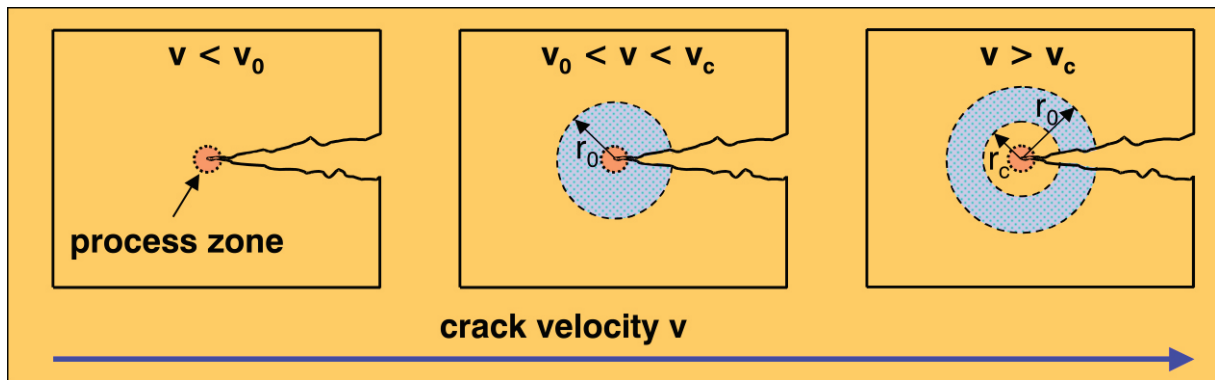


Fig. 2.6: Viscoelastic behavior close to a crack tip. The blue shaded area corresponds to the regions with high energy dissipation [77].

**TEARING ENERGY.** When the crack velocity  $v$  is increasing the excitation frequency increases so that the elastomer is behaving more and more glassy. Therefore faster crack growth needs a higher tearing energy. The surface energy  $\gamma_{\text{eff}}$  can be expressed semi-empirically as [78]

$$\gamma_{\text{eff}} = \gamma_0 \left( 1 + \frac{G'_{\infty}/G'_0}{(1 + v_c/v)^{\beta}} \right) \quad (2.6)$$

Here,  $G'_{\infty}$  and  $G'_0$  are the storage modulus in the glassy and rubbery state, respectively and  $v_c$  is a critical crack growth velocity. The tearing energy  $T = 2 \gamma_{\text{eff}}$  is given as twice the surface energy. For very low crack growth velocities  $v \ll v_c$  the tearing energy  $T$  is given by the intrinsic strength  $T_0$ . At higher crack growth velocities  $v < v_c$  the tearing energy follows a power law  $T \sim v^{\beta}$ . Above the critical crack velocity  $v_c$  a tearing energy  $T_c$  by a factor  $G'_{\infty}/G'_0$  higher than the intrinsic strength  $T_0$  is reached [79]. The qualitative curve progression is shown in Fig. 2.7. Eq. (2.6) was derived from a semi-empirical description of the shear stress in adhesion friction that has the same velocity dependency [80]. The critical velocity  $v_c$  increases systematically with decreasing glass transition temperature [81] and an equivalent increase of  $v_c$  with increasing sample temperature can be predicted.

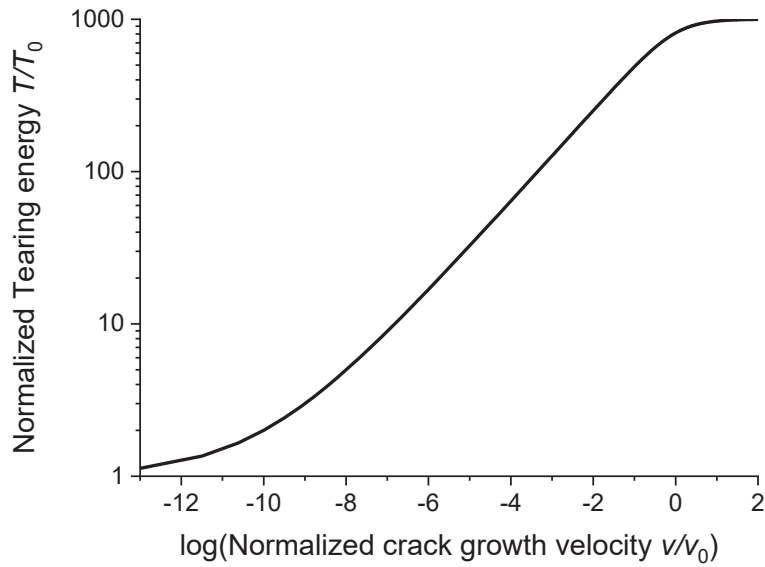


Fig. 2.7: Theoretical behavior of normalized tearing energy  $T/T_0 = \gamma_{\text{eff}}/\gamma_0$  in dependence of normalized crack growth velocity  $v/v_c$  according to eq. (2.6) for  $G'_{\infty}/G'_0 = 1000$  and  $\beta = 0.3$

**VISCOELASTIC CRACK OPENING MECHANISM.** At tearing energies that are sufficient high that the region close to the crack tip behaves glassy the crack contour takes a trumpet-like shape. This shape is created as in both, the soft solid region far away from the crack tip and the hard solid region in the vicinity of the crack tip, the displacement  $u(r)$  is increasing proportional to  $\sqrt{r}$ , but in the glass transition region the displacement is varying with  $r^{3/2}$  (Fig. 2.8).[79]

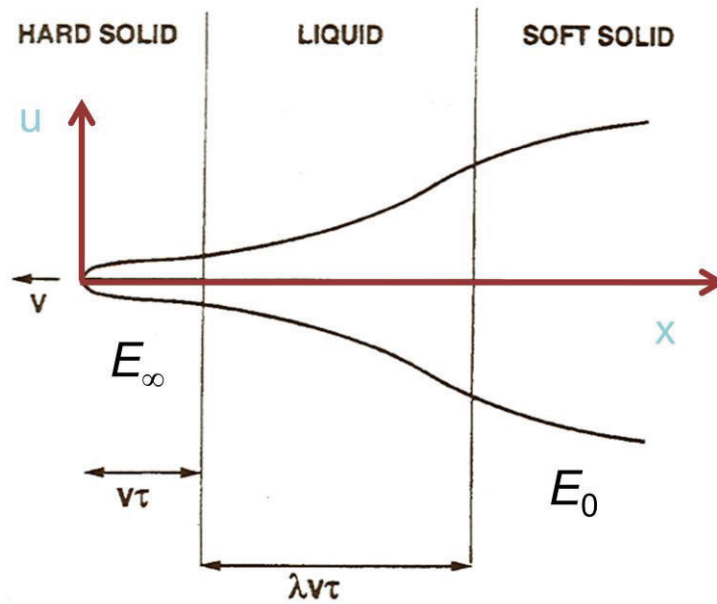


Fig. 2.8: Viscoelastic trumpet-like crack opening profile [79].

RELAXATION TIME SPECTRUM. The relaxation time spectrum  $H(\tau)$  can be determined from the course of the storage modulus  $G'$  (given by its smoothed master curve) using the approximation method of Ferry and Williams [82]. For larger relaxation times  $\tau$  a power law decrease with exponent  $m$  is found. This exponent  $m$  can be used to predict the exponent  $\beta = (1 - m)/(2 - m)$  of the power law increase of the tearing energy  $T \sim v^\beta$  with crack velocity  $v$  [76]. The exponent  $m$  in filled compounds is decreasing with the strength of polymer–filler interactions [78].

COMPARISON TO FATIGUE CRACK GROWTH. The exponent  $\beta^{-1} = (2 - m)/(1 - m)$  obtained from the relaxation time spectrum for viscoelastic crack growth roughly coincides with the exponent  $B$  in the Paris-Erdogan law (2.5) for fatigue crack growth [78].

## 2.6 The J-Integral

In contrast to the tearing energy, which is representing the global value of the energy available for surface growth of the propagating crack, the concept of J-Integral introduced by Cherepanov and Rice [83-84] delivers a local value. The J-Integral

$$J = \oint_{\Gamma} \left[ W_{el} N_1 - P_{ij} N_j \frac{\partial U_i}{\partial X_1} \right] d\Gamma \quad (2.7)$$

is based on a path integral taking into account the 1. Piola Kirchhoff stress tensor  $\mathbf{P}$ , the elastic energy density  $W_{el}$  and the displacement gradient  $\mathbf{H} = (\partial U_i / \partial x_j)_{ij}$  along a contour  $\Gamma$  around the crack tip (see Fig. 2.9). Here,  $\mathbf{U} = \mathbf{x} - \mathbf{X}$  is the displacement vector giving the difference between the deformed coordinates  $\mathbf{x}$  and the undeformed coordinates  $\mathbf{X}$ .  $\mathbf{F} = \mathbf{I} + \mathbf{H}$  is the deformation gradient and  $\mathbf{I}$  is the unity matrix. The 1. Piola Kirchhoff stress tensor is given by  $\mathbf{P} = \det(\mathbf{F}) \boldsymbol{\sigma} (\mathbf{F}^T)^{-1}$ . [52] Assuming incompressibility of the rubber leads to  $\det(\mathbf{F})=1$ . For small deformations the 1. Piola Kirchhoff stress converges into the Cauchy stress  $\boldsymbol{\sigma}$ . The J-Integral can be described in the framework of material forces [85] with the integrand of the J-Integral given by the Eshelby stress tensor [86].

For purely elastic materials the J-Integral over a closed path not containing voids or cracks is zero. In that case the J-Integral surrounding the crack tip is path-independent. The only sink of the energy flux is then the crack tip. In filled elastomers also significant energy dissipation occurs far away from the crack tip due to strong non-linearity and hysteresis. The J-Integral

can now capture the energy that is flowing into a small volume around the crack tip. In this region the energy is available for surface growth of the propagating crack [87-88].

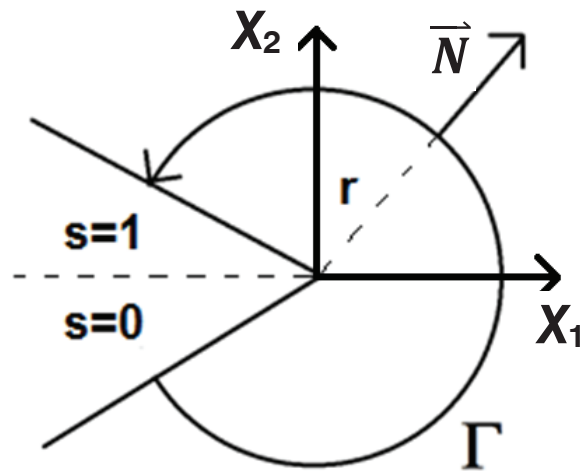


Fig. 2.9: Integration path of the J-Integral around the crack tip

The J-Integral is strictly only applicable on stationary cracks but the concept can be generalized to growing cracks [87,89]. One difference is that then the kinetic energy density is added to the elastic energy density  $W_{el}$  to build the total mechanical energy density. For nearly stationary conditions with very slowly moving cracks the kinetic energy density is very small and can be neglected. Freund [87] examined the energy flow into a body in the  $x_1, x_2, t$ -space and determined the instantaneous rate of energy flow  $F(I)$  through the integration path  $I$  which depends on the instantaneous crack tip velocity  $v_c$ . When the fields of all state variables within the contour  $I$  translate invariant with the moving crack this so called energy flux integral can be written as  $F(I) = J \cdot v_c$ .





# 3 Influence of blend morphology on crack propagation rate

## 3.1 Introduction

The fatigue crack growth behavior of filled elastomer blends under specified loading conditions depends not only on the polymers and fillers used, and their respective amounts in the compound, but also on the blend morphology and filler distribution. The influence of these morphological aspects on the crack propagation rate of blends measured by the Tear Fatigue Analyzer is presented in this chapter. The investigation was done on carbon black filled blends of NR with BR and/or SBR. For some blend systems the compound was mixed in two different ways: the standard mixing procedure in which the filler is added to the premixed blend and the batch mixing procedure in which the filler is added to the pure NR and then blended with the other rubbers.

The results are published in three papers. The *first paper* deals with NR/BR and NR/SBR blends mixed with the standard mixing procedure, as well as NR/BR blends mixed with the batch mixing procedure. The *second paper* focuses on NR/SBR blends, mixed with the standard and with the batch mixing procedure. *Both papers* compare the blend morphology with crack propagation measurements. The *third paper* investigates the influence of thermally-induced crystallization of the BR on the dynamic spectra and the blend morphology of NR/BR/SBR blends.

DETERMINATION OF BLEND MORPHOLOGY. The method used to determine the filler distribution in these blends relies on the increase of peak heights due to the filler incorporated into the respective polymer phases and on the additivity of dissipated energies so that the dissipated energy in the blend is given by the sum of the dissipated energy in the different polymer phases. The increase of the peak heights is hereby linear with the filler volume fraction  $\phi_F$ :  $G''(T_g) = G''_0(T_g) + \alpha\phi_F$ .  $G''_0$  is here the value of the unfilled polymer. The peak heights of the polymer phases in an unfilled blend in comparison to the peak heights of the pure polymers can be fitted by quadratic equations. The loss modulus of the blend  $G''_{\text{blend}}$  is then given by:  $G''_{\text{blend}} = \sum_i G''_{P,i}(a_i + b_i\phi_i + c_i\phi_i^2)$ .  $G''_{P,i}$  is here the loss modulus of the  $i$ -th phase. Combining the effect of the filler with the blend effect yields:

$$G''_{\text{blend}} = \sum_i \left( 1 + \alpha_i \frac{\phi_{F,i}}{\phi_{F,i} + \phi_i} \right) G''_{P,i} \left( a_i + b_i(\phi_{F,i} + \phi_i) + c_i(\phi_{F,i} + \phi_i)^2 \right) \quad (3.1)$$

This equation allows the determination of the filler volume fractions  $\phi_{F,i}$  in the different phases when the peak heights of filled and unfilled blends and the blend ratio are known.

The method has already been applied to a variety of polymer blends [90-95]. The peak heights of the different polymer phases with and without filler are compared. There are two causes for the change in peak height:

- I. Linear increase of peak height with filler volume fraction
- II. The change of phase volume fractions due to the filler in the different phases

The phase volume fraction has a non-linear effect on the peak height and is fitted by a quadratic function. In a blend the polymer with the lower glass transition has an over-proportional peak height compared to its phase volume fraction. The polymer with the higher glass transition has an under-proportional peak height and yields only a significant peak above a threshold value. At this threshold the polymer phase becomes continuous. Combining these two effects allows the determination of the filler distribution in the blend.

THE INTERPHASE. Besides the filling of the polymer phases also amount and filling of the interphase can be obtained. In the loss modulus  $G''$  the interphase can be seen as increased values between both glass transition peaks. For the calculation of interphase amount and filling the interphase is assumed to consist of the same amount of both polymers and all properties are the average of the properties of both polymers.

LIMITATIONS OF THE METHOD. The method cannot be used for any blend system. Besides the immiscibility which is obviously necessary to study the phase separated filler distribution, the glass transitions of both polymers should be well separated. The method relies on a clear attribution of filler responsible for increase of the loss modulus to the phase it is located. The blend ratio should be in such a way that both polymer peaks are clearly visible. This means that the content of the polymer with higher glass transition should not be too small. The NR is not miscible neither with the BR nor the SBR. That can be seen in two different glass transition peaks of the loss modulus  $G''$ . But the BR and SBR are miscible so that for a BR/SBR blend a single broad glass transition peak of  $G''$  is found.

The method can only be used if further compounds for the calibration are available. To quantify the filler amount in a phase one needs to know how strongly a polymer is increasing

the maximum of the loss modulus. For this reason single polymer compounds of each polymer unfilled and with varying filler volume are needed. The filler increases the volume fraction of a polymer phase and the peak height of the loss modulus increases non-linearly with the volume fraction of that phase. That makes it necessary to possess also the dynamic mechanical data of unfilled compounds with different blend ratios.

**PHASE NETWORK OF UNFILLED BLENDS.** In the second paper additionally the phase network of unfilled NR/SBR blends is analyzed. The storage modulus  $G'$  in between the glass transition temperatures of the SBR phase and the NR phase has only then highly increased values compared to the values found at room temperature if the phase volume fraction of the SBR surmounts a threshold value. This increased value is connected via the Kramers-Kronig relations to a visible peak around the  $T_g$  of the SBR. The threshold value could be identified with the phase volume fraction necessary to form a continuous phase of the SBR. At lower phase volume fractions the SBR domains are phase separated. In such a NR/SBR blend at temperatures in which only the SBR behaves glassy, these hard SBR domains only enhance the modulus by hydrodynamic amplification.

**FILLER DISTRIBUTION.** In NR/SBR blends the SBR has the higher affinity to carbon black so that the SBR phase is higher filled than the NR phase. In NR/BR blends the BR peak height is not increasing due to the filler, indicating very little amount of filler located in the BR phase. The NR phase has most of the carbon black then. The interphase in both blend systems is usually very high filled. In NR/BR/SBR blends the filler is concentrated in the NR phase. The thermally induced crystallization of the BR (see below) yields a second peak in the loss modulus  $G''$ , which is located in the same temperature range as the NR glass transition peak. This might hamper the calculation of the filler distribution in systems containing BR. The results of the filler distribution in blends are compared to previous findings [20,92-93, 96-101] which coincide for the NR/SBR blends fairly well.

**THERMALLY INDUCED CRYSTALLIZATION OF BR.** The temperature of maximal crystallization rate  $T_{\text{cryst}}$  is practically independent of temperature and lies between  $-55^\circ\text{C}$  and  $-56^\circ\text{C}$  [51]. In a temperature range between  $-70^\circ\text{C}$  and  $-40^\circ\text{C}$  crosslinked BR has a crystallization half-life around or below 100 s [9]. Then the time scale of crystallization is in the order of dynamic mechanical measurements. Therefore quicker measurements show less crystallization. In blends with unpolar rubbers the decrease of BR crystallization is larger for a larger difference in solubility parameter [102] so that blends crystallize less than the pure BR

and blends with NR show less crystallization than blends with SBR [103]. The decrease of crystallization in NR/SBR blends could be confirmed by DMA for BR/SBR blends. The decrease of crystallization with carbon black content [104] is not seen in the dynamic mechanical spectra. Instead the faster crystallization of filled compounds yields that the increase of the moduli due to crystallization is increasing with filler volume fraction. Additional Differential Scanning Calorimetry measurements support this picture.

**CRACK PROPAGATION.** The crack propagation of carbon black filled elastomers is much lower than that of unfilled compounds [90,105]. Due to the strengthening effect of strain-induced crystallization pure NR has the lowest crack propagation rates [106]. Increasing the SBR content leads to higher crack propagation for all loading intensities quantified by the tearing energy  $T$ . Increasing the BR content does not change the crack propagation at low tearing energies. But for high tearing energies the crack propagation rate  $dc/dn$  is strongly increasing with BR content. This may be a reason for the Chip & Cut effect denoting loss of tire tread material when trucks are driving on rough roads [107]. Chip & Cut can also be estimated by an instrumented Chip & Cut tester [108].

## INFLUENCE OF PHASE MORPHOLOGY AND FILLER DISTRIBUTION IN NR/BR AND NR/SBR BLENDS ON FRACTURE MECHANICAL PROPERTIES

MATTHIAS WUNDE, MANFRED KLÜPPEL\*

DEUTSCHES INSTITUT FÜR KAUTSCHUKTECHNOLOGIE E. V. (DIK), 30519 HANNOVER, GERMANY

RUBBER CHEMISTRY AND TECHNOLOGY, Vol. 89, No. 4, pp. 588–607 (2016)

### ABSTRACT

The filler distribution and the amount of interphase are determined for carbon black (CB) filled blends of natural rubber (NR) with butadiene rubber (BR) and styrene–butadiene rubber (SBR) and compared with fatigue crack propagation rates under pulsed excitation. A viscoelastic model is used to separate the contributions of the different polymer phases and the interphase to the total dissipated energy  $G''$  during dynamic straining. The filler amount in any phase can be calculated from the increase of the energy dissipation. For NR/SBR blends a higher filler load of the SBR phase and the interphase and a lower filling of the NR phase are identified. In contrast NR/BR blends show a very low filled BR phase and higher filling of the NR phase and the interphase. The carbon black distribution also depends on mixing procedures. Through a batch mixing procedure, in which the filler is previously mixed in the NR only and then blended with BR, the filler transfer from NR to BR increases the filling of the BR phase. The phase morphological results deliver information for a better understanding of crack propagation in CB filled NR/BR and NR/SBR blends. The fracture behavior differs significantly if NR is successively replaced by BR or SBR, respectively. A less pronounced effect is found for the variation of mixing procedure, although it seems that the more heterogeneous filler distribution with a high amount of CB in NR of the batched samples delivers slightly reduced crack propagation rates. [doi:10.5254/rct.16.83795]

### INTRODUCTION

#### FRACTURE MECHANICS OF RUBBER

High performance elastomer products like tires, conveyor belts, seals, air springs, and dampers are subjected to high dynamic loading conditions inducing crack propagation. The micro-mechanical mechanisms of crack initiation and propagation in elastomer materials are topics in current research, because it is still not known exactly how these processes start and how they proceed under quasi-static and dynamic loading conditions.<sup>1</sup> Recent research could establish a connection between flaw size and characteristics of crack initiation.<sup>2,3</sup> Most efforts in the quantitative characterization and physical understanding of crack propagation and tear resistance in viscoelastic solids are based on the fundamental work of Rivlin and Thomas.<sup>4</sup> Although recent efforts have been made,<sup>5–8</sup> there is still potential for the development of fracture mechanical methods and models of filler reinforced elastomers, especially due to the strongly nonlinear deformation behavior and stress softening effects.<sup>1,9,10</sup> In recent contributions knowledge about influencing parameters is extended, for example, in determining the heat buildup<sup>11</sup> and the influence of carbon black particle size.<sup>12</sup> Digital image correlation and finite element analysis were used to determine the strain distribution at the crack tip.<sup>12</sup> The fracture mechanical properties of tires and conveyor belts are characterized by the fatigue crack growth and the chip and cut behavior of the rubber compounds.<sup>13,14</sup> The fatigue crack growth determines the crack growth velocity under given loading conditions and is at present usually carried out using the tear fatigue analyzer.<sup>15,16</sup> Under the impact of harsh dynamic loading conditions the rubber can tear in such a way that pieces of rubber are removed. This so called chip and cut mechanism is measured by the weight change of a rotating wheel dynamically impacted by a sharp tool.<sup>13,14,17</sup>

\*Corresponding author. Ph: +49 5118420127; email: Manfred.Klueppel@DIKautschuk.de

## RUBBER BLENDS

Instead of using individual polymers for tire applications, often polymer blends are used. The blending can lead to a reduced compound cost and can improve the tire building or the tire performance.<sup>18</sup> Owing to their specific properties, carbon black (CB) filled blends of natural rubber (NR) with butadiene rubber (BR) and styrene–butadiene rubber (SBR) are used for the production of truck tires and conveyor belts. While pure natural rubber shows the highest tensile strength and resistance to catastrophic crack growth due to strain-crystallization,<sup>19,20</sup> BR provides a low rolling resistance and good resistance against crack initiation<sup>21,22</sup> and against abrasion.<sup>23,24</sup> SBR, especially compounds with high styrene content, has a good wet skid resistance.<sup>21</sup> By blending in general the properties of the individual polymers are combined, which sometimes delivers synergetic effects with improved properties. Indeed, in many cases a property in a blend has a far from linear behavior with the blend ratio and can be better than even both polymers.<sup>19,22,25</sup> Kim and Hamed<sup>19,20</sup> proved that the fracture properties of a NR/BR 50:50 blend are for a range of conditions, nearly those of the better polymer in each case. They attributed it to a co-continuity of the NR and BR phase. Clapson and Lake<sup>22</sup> showed improved groove cracking resistance of a NR/BR 70:30 blend compared with a pure NR. This improvement has been related to superior crack growth characteristics at low tearing energies.

## CARBON BLACK DISTRIBUTION IN BLENDS

So far there are still some open questions remaining, especially regarding the role of filler in rubber blends. The mechanical properties of the blends are not solely governed by the components used, but they depend also on the magnitude of the interphase connecting different polymer phases. Furthermore the distribution of the reinforcing filler into the different polymer phases and the interphase influences the mechanical and fracture mechanical properties.<sup>26,27</sup> This distribution of the carbon black in NR/BR and NR/SBR blends with varying proportions of the polymers is studied in this work by comparing the maxima of the loss moduli  $G''$  of the filled blend with those of an unfilled blend.

The carbon black affinity of different polymers has been studied extensively by different authors. For NR/SBR blends, consistently higher carbon black concentrations in the SBR phase are found, using a variety of techniques including inverse gas–liquid chromatography,<sup>28</sup> phase contrast optical microscopy,<sup>27,29</sup> combined static and dynamic modulus measurements,<sup>30</sup> thermogravimetry on the rubber–filler gel,<sup>31</sup> and analysis of bound rubber.<sup>32</sup> The higher carbon black loading in the SBR phase is attributed to a higher degree of carbon black polymer interaction.<sup>31,32</sup> Le et al.<sup>31</sup> investigated the kinetics of the filler distribution. They found out that, because of its higher affinity, the NR incorporates the CB more quickly. With increased mixing time the filler transfers to the SBR phase as a result of its stronger carbon black affinity.

The first two techniques have also been applied to NR/BR blends, revealing a higher carbon black amount in the BR phase.<sup>27–29</sup> By applying master batch technologies the filler distribution can be influenced and in particular be enriched in the interphase, leading to improved fracture mechanical properties.<sup>26,33</sup> Cotton and Murphy<sup>32</sup> showed that the carbon black dispersion is affected by the molecular weight of the polymers. The carbon black affinity increases with higher molecular weight, but the effect is weak for the immiscible NR/SBR blends. They also detected an increase of the loading in SBR with increasing surface area of the carbon black and with increased mixing time.

## EVALUATION OF FILLER DISTRIBUTION BY INCREASE OF LOSS MODULUS PEAKS

The method employed was used to study the filler distribution in elastomer blends. In contrast to this study, for NR/SBR blends higher filler concentrations in the SBR phase were found.<sup>34–36</sup> In

TABLE I  
RECIPES OF THE COMPOUNDS

Samples	NR	BR	SBR	CB	CBS	Sulfur	IPPD	ZnO	Stearic acid
NR	100	—	—	50	2.5	1.7	1.5	3	1
N85B15	85	15	—	50	2.5	1.7	1.5	3	1
N85S15	85	—	15	50	2.5	1.7	1.5	3	1
N70B30	70	30	—	50	2.5	1.7	1.5	3	1
N70B30Batch <sup>a</sup>	70	30	—	50	2.5	1.7	1.5	3	1
N70S30	70	—	30	50	2.5	1.7	1.5	3	1
N55B45	55	45	—	50	2.5	1.7	1.5	3	1
N55B45Batch <sup>a</sup>	55	45	—	50	2.5	1.7	1.5	3	1
N55S45	55	—	45	50	2.5	1.7	1.5	3	1

<sup>a</sup> “Batch” denotes samples mixed with the batching mixing procedure (carbon black blended first in NR only).

NR/BR blends a higher filling of the BR phase was found.<sup>35</sup> Furthermore carbon black filled EPDM/BR blends<sup>35–37</sup> and SBR/EPDM blends were investigated.<sup>34</sup> The method has also been applied to silica filled compounds.<sup>26,33</sup>

Following the principle of additivity of energy, the total stored or dissipated energy of a dynamically excited rubber blend is the sum of all energy contributions of the different phases. The maxima of the density of dissipated energy  $G''$  in the glass process is analyzed. By a fitting procedure it is possible to separate the contributions of the different polymer phases and also of the interphase to the total dissipated energy  $G''(T)$ .<sup>34,35,38</sup> As the carbon black located in one phase increases the energy dissipation in that phase, it is possible to determine the filler amount in the phases leading to the respective energy contributions.

In this work the above described method to obtain the filler distribution is applied to NR/BR and NR/SBR blends. Additionally crack propagation measurements with the tear fatigue analyzer are performed, so that the effect of the blend morphology on fracture mechanical properties can be analyzed.

## EXPERIMENTAL

### MATERIALS

The samples are composed of natural rubber (SVR CV 60) blended with butadiene rubber or styrene–butadiene rubber with varying proportions of polymers and filled with 50 phr carbon black (N339). The BR used is a high-cis butadiene rubber (Buna CB 24, Lanxess), and the SBR is a solution styrene–butadiene rubber (Buna VSL 4526, Lanxess) with 45 wt% vinyl and 26 wt% styrene groups. The samples were cross-linked semi-efficiently by sulfur together with the vulcanization accelerator *N*-cyclohexyl-2-benzothiazole sulfonamide (CBS). The samples were compounded with the processing and vulcanization additives stearic acid and ZnO and protected against aging by *N*-isopropyl-*N*-phenyl-*P*-phenylenediamine (IPPD). The full recipe is shown in Table I.

### SAMPLE PREPARATION

The composites are mixed in an industrial 5 L intermeshing mixer (Werner & Pfleiderer GK 5 E) at 40 rpm for 6 min. After 2 min mastication of the polymers the other ingredients are inserted. Leveling of the torque after mastication and after mixing indicates homogeneous mixtures. The

curing system is added on a roller mill, where the compounds are handled another 7 min. Vulcanization is performed at 150°C in a heat press up to 90% of the vulcameter torque maximum ( $t_{90}$  time). The carbon black dispersion is checked by optical dispersion analysis.

Two different mixing techniques are used. In the standard mixing procedure the polymers are mixed first, then the filler is added. The NR/BR blends are additionally mixed with a batching mixing procedure in which the filler is first blended with the NR only. The BR and the other ingredients are added in a second mixing stage. The specifics of both mixing stages match with the standard mixing procedure except a reduced time of 2 min on the roller mill after the first stage. The curing system is mixed in on the roller mill after the second mixing stage.

#### DYNAMIC-MECHANICAL ANALYSIS

The dynamic-mechanical measurements are carried out in the torsion-rectangular mode with strip specimen of 2 mm thickness on the dynamic analyzer advanced rheometric expansion system (ARES; Rheometric). The dynamic moduli are measured over a wide temperature range (−115°C to +20°C) at frequency of 1 Hz, 0.5% strain amplitude, and a heating rate of about 1°C/min.

#### TEAR FATIGUE ANALYZER

The fracture mechanical measurements are performed at notched strip samples on a tear fatigue analyzer (Coesfeld). This machine allows a fully automatic detection of crack length for investigating 10 specimens simultaneously. The crack propagation rates are measured under pulsed excitation (4 Hz, 30 ms pulse width) at 60°C. The 15 mm broad samples with a 1 mm deep crack are pre-strained by 2 N and excited by varying strain amplitudes between 10% and 30%. The graphic images for determination of the crack length are triggered between the pulses.

#### METHODOLOGY

##### MODEL OF ENERGY DISSIPATION TO OBTAIN FILLER DISTRIBUTION IN POLYMER BLENDS

Following the principle of additivity of energy, the total stored or dissipated energy  $G''_{\text{blend}}$  is the sum of all energy contributions of the different phases  $i$ :

$$G''_{\text{blend}} = \sum_i G''_{P,i} \phi_i \gamma_{0,i}^2 \quad (1)$$

Here,  $G''_{P,i}$  is the loss modulus of the  $i$ th blend fraction,  $\phi_i$  is the volume fraction of the  $i$ th phase, and  $\gamma_{0,i}$  is the strain amplitude of the  $i$ th phase.

The dissipated energy  $G''$  of a single polymer has a peak around its glass transition temperature  $T_g$ . Filling of a polymer with an active filler like carbon black leads to an increased dissipated energy. The maximum of the dissipated energy  $G''_{\text{max}}$  increases linearly with the filler volume fraction  $\phi_F$  (Figure 1):

$$G''_{\text{max}} = G''_0 + \alpha \phi_F \quad (2)$$

$G''_0$  denotes the maximum of the loss modulus of the unfilled polymer. In incompatible polymer blends the dissipated energy has several peaks (close to the  $T_g$  of the polymers) arising from the dissipation in the different polymer phases. Between the peaks the dissipated energy shows an enhanced signal, which is attributed to the interphase. The interphase is the area in which different polymers interconnect. The dissipated energy can be decomposed into the contributions from the different phases and the interphase. In an unfilled blend the dissipated energy of the phases,  $G''_{P,i}$ ,



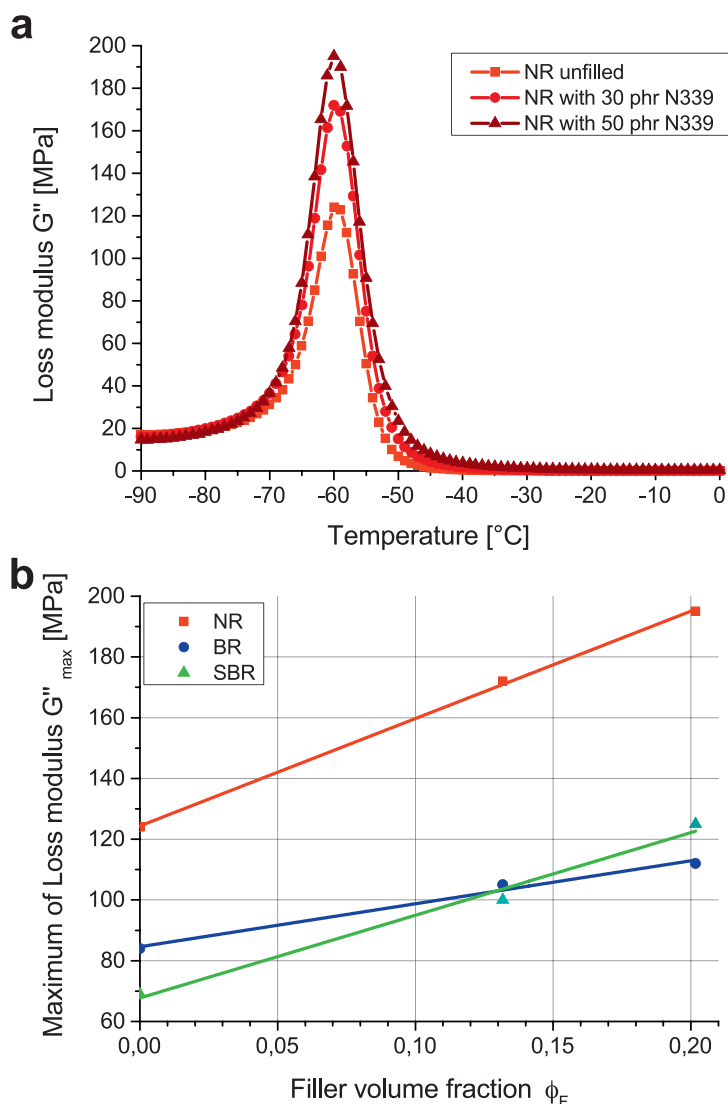


FIG. 1. — (a) Increase of the loss modulus  $G''$  in NR due to the filling with carbon black. (b) Linear increase of the maximum loss modulus  $G''_{\max}$  with filler volume fraction  $\phi_F$  in NR, BR, and SBR, respectively.

depends nonlinearly on their phase volume fractions,  $\phi_i$ , and are fitted by second order polynomials for the weight factor in terms of their volume fractions:

$$G''_{blend} = \sum_i G''_{P,i} (a_i + b_i \phi_i + c_i \phi_i^2) \quad (3)$$

The polymer A with the higher glass transition temperature only contributes significantly to the dissipated energy when its phase volume fraction exceeds  $\phi_c \approx 0.2$  (Figures 2 and 3). According to Klüppel et al.<sup>35</sup> this behavior can be explained by a percolation model: Below a critical volume fraction, the percolation threshold  $\phi_c$ , the domains of polymer A are separated. At temperatures below or around the glass transition temperature, these domains remain undeformed during

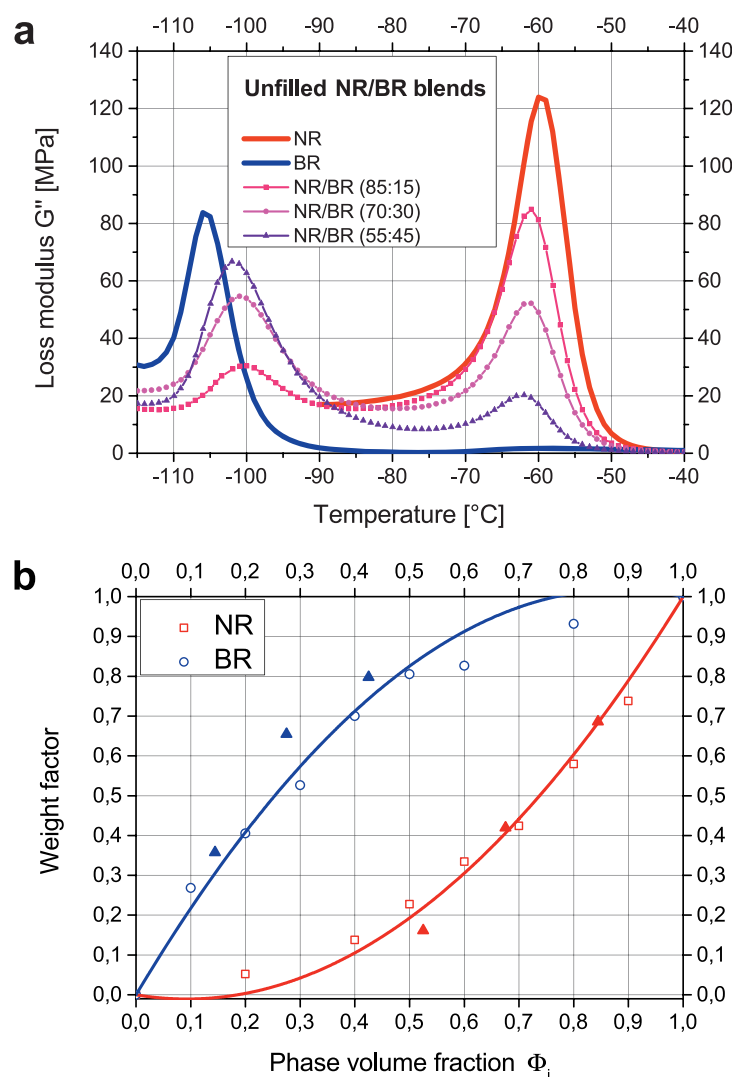


FIG. 2. — (a) Loss moduli of the unfilled NR/SBR blends in comparison with the pure unfilled NR and SBR, respectively. (b) The dissipated energy of the phases depends nonlinearly on their phase volume fraction  $\phi_i$ . The weight factor shows the ratio  $G''_{\max, \text{blend}}/G''_{\max, \text{polymer}}$ . The open symbols represent data taken from Schuster et al.<sup>37</sup> The full triangles, indicating the data from Figure 2a, fit well with the previous data. All values are fitted by a quadratic function.

dynamic excitation because of their large modulus compared with that of the other, continuous polymer. In this case the glassy domains of polymer A enhance the modulus only by hydrodynamic amplification. Above the percolation threshold the glassy domains of polymer A form a continuous phase network, where most energy is stored. In this region the storage modulus  $G'$  follows a power law with exponent  $\tau \approx 1.7$ . The smaller exponent than the theoretical value from percolation theory  $\tau \approx 3.6$  may result from coalescence implying a different loop structure.<sup>35</sup> The threshold can be calculated to  $\phi_c \approx 0.2\text{--}0.3$  depending on the structure assumed for the percolation model.

In a filled blend the effect of the filling (Eq. 2) is combined with the influence of the blend (Eq. 3). The filler located in any phase (or the interphase) increases the dissipated energy of that phase. From the increase of the maximum of the dissipated energies  $G''_{\max}$  in the different phases and the

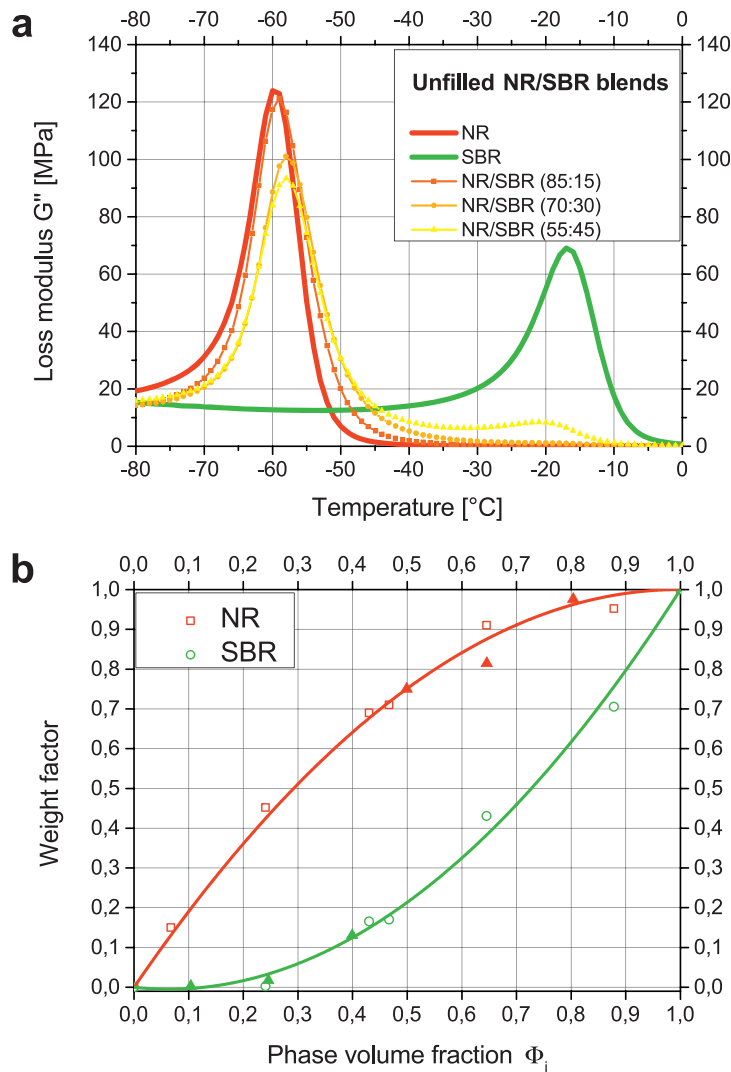


FIG. 3. — (a) Loss moduli of the unfilled NR/SBR blends in comparison with the pure unfilled NR and SBR, respectively. (b) The dissipated energy of the phases depends nonlinearly on their phase volume fraction  $\phi_i$ . The weight factor shows the ratio  $G''_{\max, \text{blend}}/G''_{\max, \text{polymer}}$ . The open symbols represent data taken from Schuster et al.<sup>37</sup> The full triangles, indicating the data from Figure 3a, fit well with the previous data. All values are fitted by a quadratic function.

interphase, the filler volume fraction  $\phi_{F,i}$  of each phase  $i$  can be calculated:

$$G''_{\text{blend}}(T) = \sum_i \left( 1 + \alpha_i \frac{\phi_{F,i}}{\phi_{F,i} + \phi_i} \right) \left( a_i + b_i(\phi_{F,i} + \phi_i) + c_i(\phi_{F,i} + \phi_i)^2 \right) G''_{P,i}(T) \quad (4)$$

#### FITTING PROCEDURE TO OBTAIN FILLER DISTRIBUTION

The filler distribution is obtained by comparing the loss modulus  $G''(T)$  of the filled blend with that of an unfilled blend. The unfilled blend is fitted by the unfilled single polymer peaks in the

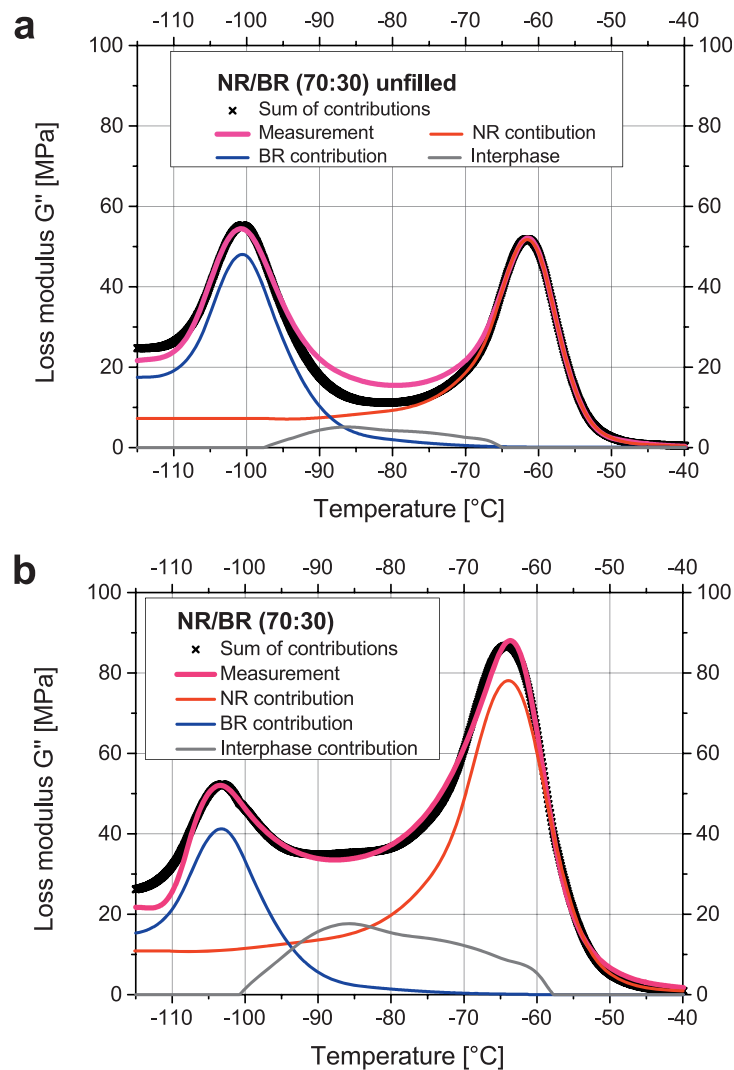


FIG. 4. — Fit of the loss modulus of the unfilled NR/BR (70:30) blend with the single polymer peaks. (a) The interphase is obtained as fit difference. (b) Fit of the loss modulus of the filled NR/BR (70:30) blend with the single polymers and the interphase. The filling of the phases and the interphase is obtained from the increase of the maxima of the contributions using Eq. 4.

region around the glass transition temperatures. Between the glass transition temperatures the sum of both single polymers does not account for the measured loss modulus. This difference is attributed to the interphase (Figures 4a and 5a). In a second fitting procedure the filled blend is fitted by the single polymer peaks and the interphase peak obtained in the fit of the unfilled blend (Figures 4b and 5b). In both fitting routines the amplitude and broadness of the peak and a shift of the glass transition temperature are used as fitting parameters. From the increase of the amplitude of the peaks in the filled blend compared with the unfilled blend, the filling of the phases and interphases can be calculated. For that the filler amount in the different phases and the interphase is determined from Eq. 4, so that the maximal modulus in each phase corresponds to the peak heights of the fits.

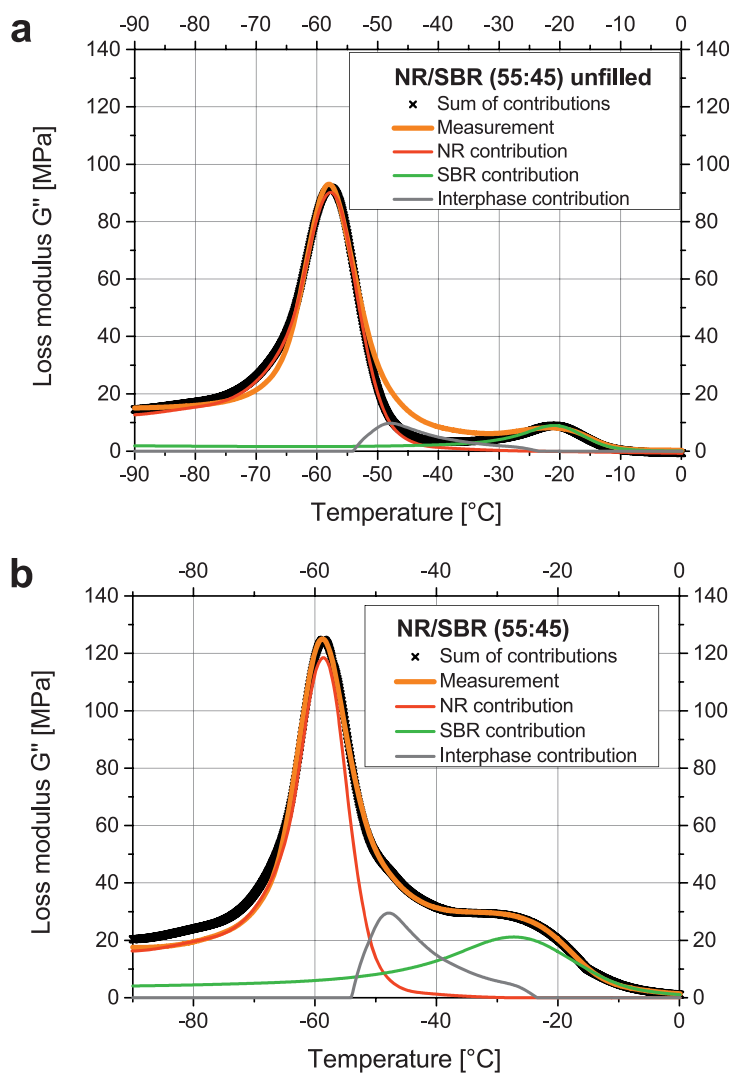


FIG. 5. — Fit of the loss modulus of the unfilled NR/SBR (55:45) blend with the single polymer peaks. (a) The interphase is obtained as fit difference. (b) Fit of the loss modulus of the filled NR/SBR (55:45) blend with the single polymers and the interphase. The filling of the phases and the interphase is obtained from the increase of the maxima of the contributions using Eq. 4.

#### ACCURACY OF CALCULATED FILLER VOLUME FRACTIONS

The accuracy of the calculated filler volume fractions  $\phi_{F,i}$  is governed by the following points: The errors of dynamic-mechanical analysis (DMA) measurements are small. The effect of sample variation (5%) on the reproducibility is larger than the error of the dynamic analyzer ARES (2%). Nevertheless small peaks in the dynamic spectrum are subject to higher inaccuracies when calculating the filler loading of the corresponding phase. This is especially the case for blend systems where the minor component has the higher glass transition temperature. For a reasonable evaluation of the spectrum the glass transition temperatures  $T_g$  of the polymers should be clearly distinct. The smaller the  $T_g$ -difference of the polymers is, the stronger the overlap of the loss

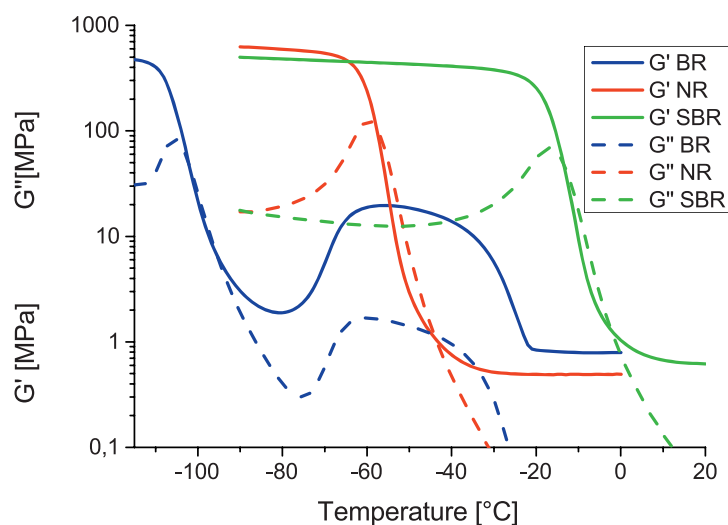


FIG. 6. — Logarithmic plot of storage modulus  $G'$  and loss modulus  $G''$  of the unfilled BR, NR, and SBR. The broad peaks of the BR at about  $-50^{\circ}\text{C}$  are attributed to the crystallization of the BR. For NR no such effect is visible.

modulus peaks from the different polymers and the overlap of these peaks with the interphase signal is.

Crystallization can have an effect on the dynamic spectra, but not all crystallizing polymers seem to be affected. In Figure 6 the modulus of the unfilled BR, NR, and SBR is shown in a logarithmic plot. The BR reveals not only the decline of the storage modulus and peak of the loss modulus attributed to the glass transition, but another peak around  $-50^{\circ}\text{C}$  due to crystallization. The NR does not reveal such behavior. The difference can be explained by different crystallization kinetics. The crystallization time of high-cis BR is quite short and has its minimum around  $-50^{\circ}\text{C}$  with less than 100 s for cross-linked BR.<sup>39</sup> The crystallization time for NR is around three orders of magnitude larger than that of BR<sup>39</sup> and therefore beyond our measuring times. Differential scanning calorimetry data may suggest that NR facilitates BR crystallization.<sup>32</sup> BR crystallization is also increased by carbon black load or by blending with SBR.<sup>40</sup>

Also for compounds in which the above problems do not arise, the standard deviation of the filler volume fractions  $\tilde{\phi}_{F,i}$  can hardly be given, but the errors can be estimated. Considering the measurement errors and the uncertainties of the fitting procedure, the error of the filler volume fractions  $\tilde{\phi}_{F,i}$  is roughly estimated to be 0.05. From the theory the sum of the local filler volume fraction  $\sum_i \tilde{\phi}_{F,i}$  should equal the overall concentration of the filler  $\phi_F$ . Regarding this condition, the sum of the calculated filler has a standard deviation of about 10% from the filler amount in the samples.

## RESULTS AND DISCUSSION

### PHASE MORPHOLOGY OF NR/BR BLENDS

In the NR/BR blends a very low filled BR phase, but a highly filled NR phase and a very highly filled interphase, is found (Figure 7a; Table II). This is in contrast to previous findings indicating a higher carbon black loading in the BR phase.<sup>28,29,31</sup> The results for the NR/BR blends could be strongly influenced by the crystallization of the BR. Effects of the crystallization can already be seen for measurements of the pure BR, unfilled and with various filler content. Therefore the

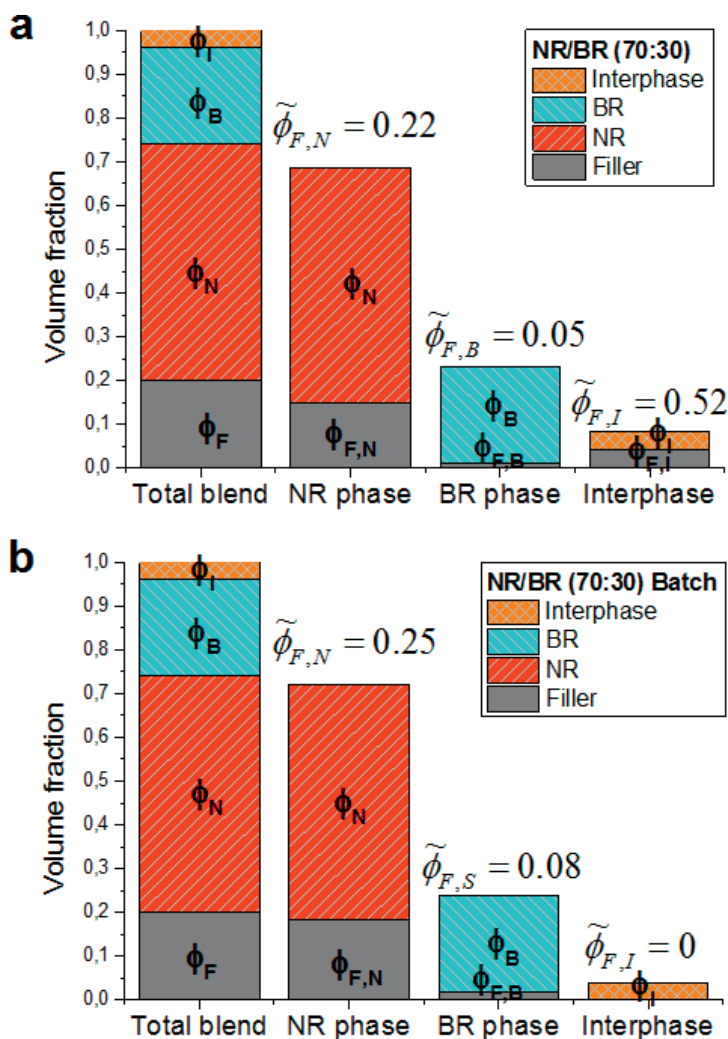


FIG. 7. — Carbon black distribution in NR/BR blends: (a) Standard 70:30 and (b) Batch mixing 70:30. The left column shows the phase proportion in the complete blend. The other columns show the amount of filler in the phases  $\phi_{F,i}$ , and the filler volume fraction is given above the columns.

dependency of the loss modulus peak with filler content may be uncertain for the BR (see Figure 1b). In the measurements of the unfilled and filled NR/BR blends the crystallization is covered (Figures 2 and 4), but the influence of the crystallization on the peak heights may not be negligible. In the batch mixing procedure the carbon black is first mixed with NR only. Then the BR is added. The analysis of the DMA curves reveals a higher filling of the NR as well as the BR phase compared with that of the standard mixing procedure, but surprisingly the interphase is almost depleted from carbon black (Figure 7b; Table III). The carbon black, preferring to be in the NR, seems to stay in the NR phase. Therefore there may only be little carbon black transfer between the phases and a small amount of filler gets stuck in the interphase.

The differences in the filler distribution in the NR/BR blends mixed with the different mixing procedures are inspected by transmission electron microscopy (TEM; Figure 8). In both cases dark filler particles can be seen scattered in a brighter two colored polymer matrix. Owing to the lower

TABLE II  
PROPORTION OF THE DIFFERENT PHASES IN THE NR/BR BLENDS, INCLUDING BATCHES, CONSISTING OF CARBON BLACK

Filler volume fraction	N85B15	N70B30	N70B30 Batch	N55B45	N55B45 Batch
$\tilde{\Phi}_{FN}$	0.21	0.22	0.25	0.20	0.26
$\tilde{\Phi}_{FB}$	0	0.05	0.08	0.11	0.14
$\tilde{\Phi}_{FI}$	0.70	0.52	0	0.60	0.06

density and lower molecular weight the BR appears brighter than the NR. In contrast to the standard mixed sample, the NR/BR batch shows bright BR domains free of filler particles. This indicates that the filler accumulates in the NR phase as shown by filler distribution results. Optical dispersion analysis verifies good dispersion for all NR/BR samples besides the N55B45 batch. As for this sample the NR is premixed with nearly the same amount of filler; there are still a few big agglomerates detectable.

#### PHASE MORPHOLOGY OF NR/SBR BLENDS

In the NR/SBR blends a higher filler load of the SBR phase and the interphase and a lower filling of the NR phase are found. Figure 9 exemplifies for the 55:45 blend how the carbon black is distributed among the different phases. Table III summarizes the proportion of the phases consisting of carbon black. For all blend ratios the highest carbon black concentration is found in the interphase, followed by the SBR phase.

The SBR is supposed to be filled higher than the interphase only in the 85:15 blend. The unfilled 85:15 blend has a very low SBR peak. Since the filling of the SBR is determined by the increase of the SBR peak, this result is imprecise. All NR/SBR blends showed good dispersion in optical dispersion analysis.

Table IV shows how much of the carbon black is distributed into the different phases. This can be compared with previous results for NR/SBR blends. Cotton and Murphy<sup>32</sup> found for a similar 50:50 blend that 31.1% of the carbon black is found in the SBR phase and 58.9% in the NR phase. Their compound contains a solution of SBR with a similar amount of 25% styrene and 45 phr of N339. Keeping in mind that they did not study carbon black in the interphase, both results coincide fairly well. Callan et al. found in a NR/SBR 50:50 blend using emulsion SBR, an even higher carbon black loading in the SBR.<sup>30</sup> Other studies did state a preferred carbon black affinity of the SBR but did not quantify the filler distribution in the blends.<sup>28,29</sup>

Previous measurements using our technique have been made on NR/SBR blends: Using 50:50 blends with a solution SBR with 25% styrene and 60 phr N234, 51% of the filler is found in the SBR, and 12% and 37% are found in the NR phase and interphase, respectively.<sup>14</sup> For 70:30 blends with a solution SBR with 40% styrene a lower carbon black amount in the SBR is identified.<sup>35</sup>

TABLE III  
PROPORTION OF THE DIFFERENT PHASES IN THE NR/SBR BLENDS CONSISTING OF CARBON BLACK

Filler volume fraction	N85S15	N70S30	N55S45
$\tilde{\Phi}_{FN}$	0.11	0.12	0.11
$\tilde{\Phi}_{FS}$	0.50	0.25	0.24
$\tilde{\Phi}_{FI}$	0.34	0.43	0.37



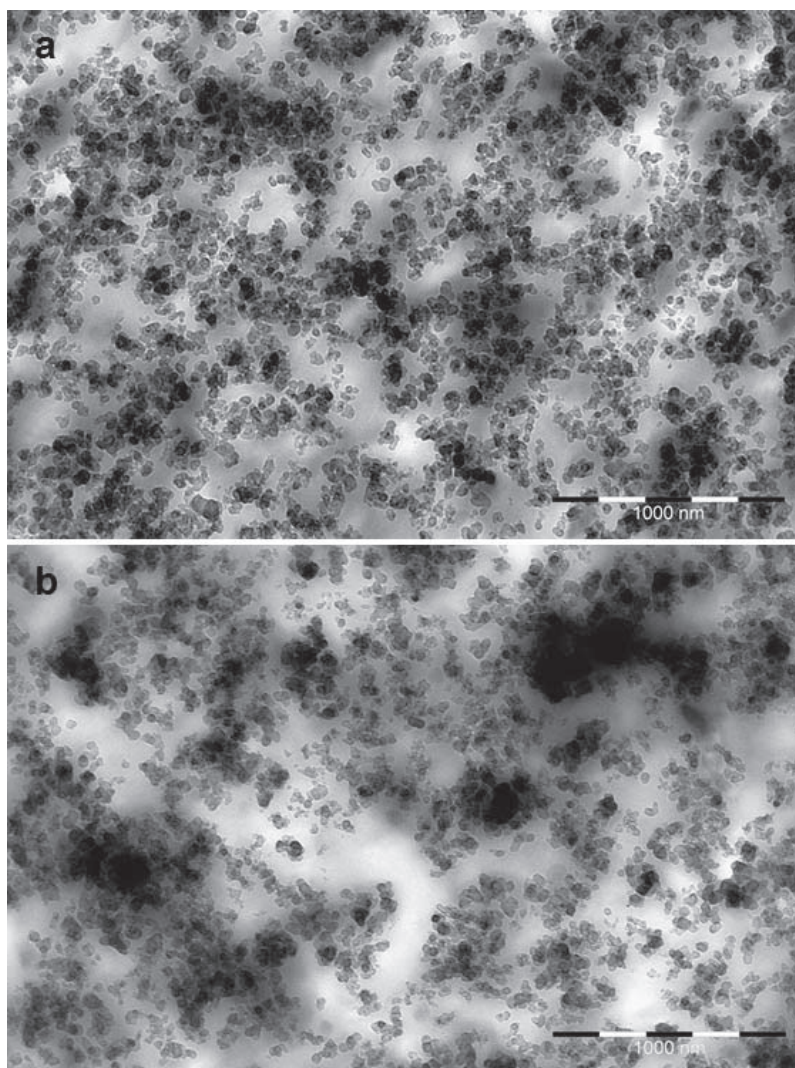


FIG. 8. — TEM images of (a) the NR/BR Standard 70:30 blend and (b) the batch mixing 70:30. Carbon black particles appear dark, and the bright domains reveal BR (images by D. Jugan and J. Lacayo-Pineda, Continental Reifen Deutschland GmbH).

Table IV summarizes for the NR/SBR blends and also for the NR/BR blends how much of the carbon black is found in the different phases and the interphase. Owing to its smaller volume fraction  $\phi_f$ , not that much filler is found in the interphase, although it is highly filled. In the NR/BR blends most of the filler is found in the NR. In the NR/SBR the filler is more evenly split up between the NR and the SBR. The general trends follow the interplay between carbon black affinity and the amount of the specific phases.

The separated peaks of the loss modulus at the different glass transition temperatures show that the NR/BR blends and NR/SBR blends are immiscible. The relatively high volume fraction of the interphase [around 5% for the NR/BR blends (Figure 7) and 10% for the NR/SBR blends (Figure 9)] indicates that the polymers in the blends are not completely incompatible. These results fit with

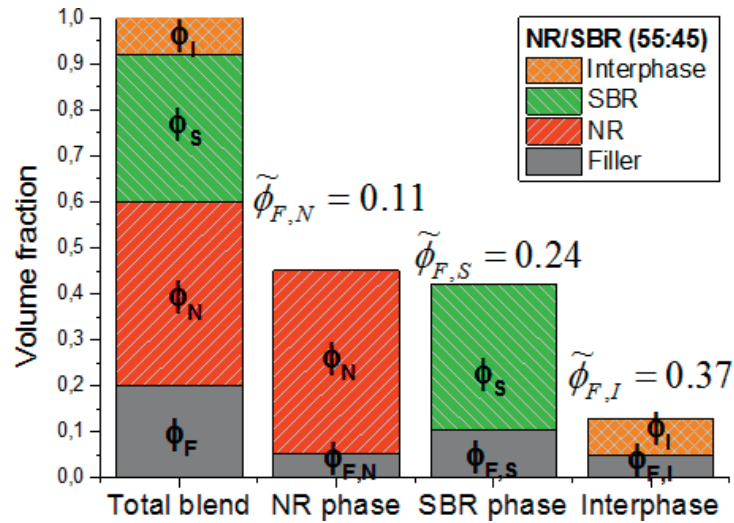


FIG. 9. — Carbon black distribution in NR/SBR 55:45 blend. The left column shows the phase proportion in the complete blend. The other columns show the amount of filler in the phases  $\phi_{F,i}$ , and the filler volume fraction is given above the columns.

the literature, where there is disunity if the blends are compatible or not.<sup>41,42</sup> The solubility parameters of the polymers following the results of Schuster et al.<sup>28</sup> measured by gas-liquid chromatography are 16.6 (NR), 17.2 (BR), and 17.6 (J/cm<sup>3</sup>)<sup>1/2</sup> (SBR) indicating blend incompatibility.

#### EVALUATION OF TEARING ENERGY AND CRACK PROPAGATION RATES

According to the Griffith criteria, the energy  $dS$  needed to increase crack surfaces has to be (over) compensated by the release of elastic energy  $-dW$ .<sup>43</sup> The elastic energy release rate  $T = -dW/dS$ , called tearing energy, is controlling the crack propagation under fixed conditions. The tearing energy in the measurements performed with the tear fatigue analyzer (TFA) is regulated by the strain preset. Paris and Erdogan found a constitutive power law characterizing the crack propagation rate per cycle  $dc/dn$  in dependence of  $T$ :<sup>44,45</sup>

$$\frac{dc}{dn} = AT^B \quad (5)$$

For the evaluation of the tear fatigue measurements, the crack contour length  $c_{\text{contour}}$  is evaluated in a region of stable crack growth. For some samples a second stable region is analyzed

TABLE IV  
RATIO  $\phi_{F,i}/\phi_F$  (%) OF THE CARBON BLACK DISTRIBUTED INTO THE DIFFERENT PHASES OF THE NR/SBR AND NR/BR BLENDS

Carbon black portion in	N85S15	N70S30	N55S45	N55B15	N70B30	N55B45
NR phase	41	36	26	90	74	51
SBR phase	41	32	51	—	—	—
BR phase	—	—	—	0	5	20
Interphase	19	32	24	10	10	29

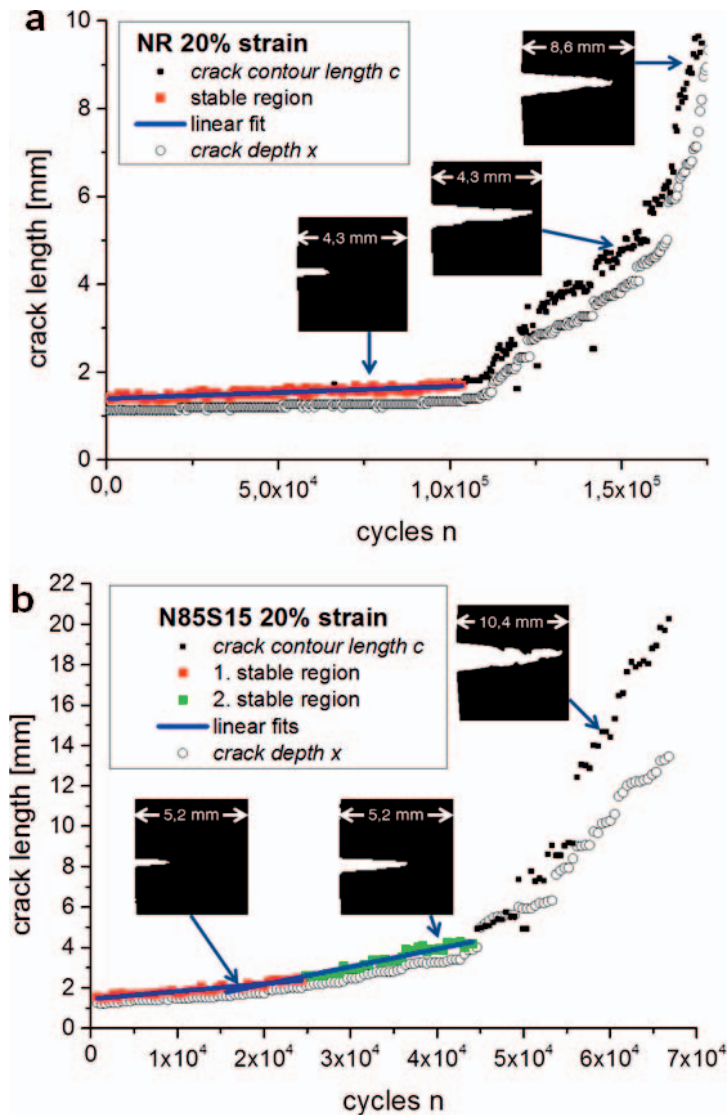


FIG. 10. — Tear fatigue analyzer measurements of (a) NR and (b) N85S15: (Half) crack contour length  $c$  (solid squares) in comparison with the crack depth  $x$  (open circles). One and two linear regions of stable crack growth, which are evaluated using the crack contour length, are shown in red and green, respectively. Additionally, three crack images at different crack lengths are shown. The first two images have twice the magnification as the image at catastrophic crack growth.

(Figure 10b). The crack growth rate  $dc/dn$  is obtained as the slope in the stable regions. The tearing energy of a single edge notched strip sample can be calculated via<sup>30</sup>

$$T = \frac{2\pi}{\sqrt{\langle\lambda\rangle}} \langle w_{el} \rangle \langle c \rangle \quad (6)$$

where  $\langle\lambda\rangle$  is the average elongation and  $\langle w_{el} \rangle$  is the average elastic energy density. When evaluating TFA measurements the crack depth  $x$  could be taken. This is the perpendicular distance of the crack tip in relation to the crack opening. The half crack contour length  $c$  in the stable regions is often

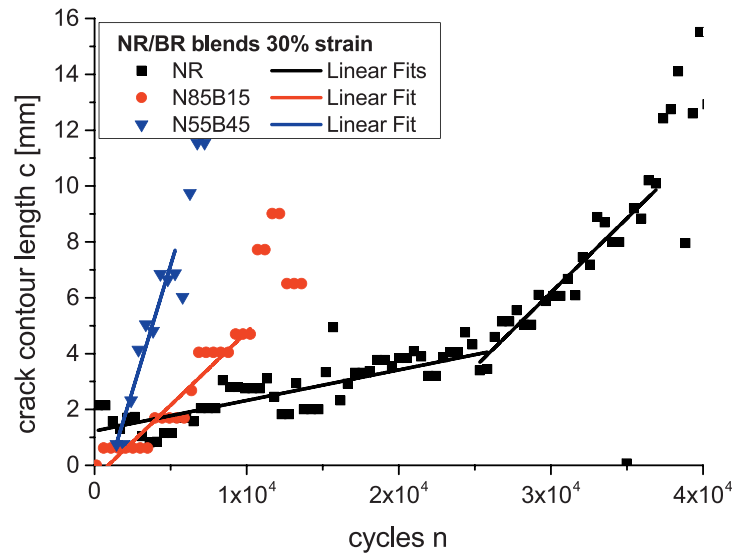


FIG. 11. — (Half) crack contour length of exemplary measurements with the tear fatigue analyzer on the NR/BR blends with 30% strain. For this high load a larger BR content leads to a faster crack growth.

larger by a factor somewhat above 1 than the crack depth. This factor depends mainly on the roughness of the crack contour being recognized by the TFA software. While the crack depth is more easily accessible and scatters less, it is, in contrast to the crack contour length, not directly related to the increase of crack surfaces and hence to the tearing energy. According to finite element method simulations<sup>46</sup> Eq. 6 is valid only for crack depths smaller than 20% of the sample width. The error for substantially longer cracks is small. However, Lorenz et al.<sup>34</sup> showed that Eq. 6 can be used to describe the crack length versus cycle number even up to crack depths of 40% of the sample width provided the crack remains perpendicular to the stretching direction and does not turn.

The crack contour length and the crack depth are exemplarily contrasted in Figure 10. Other measurements often show more scattered data. In Figure 10a, a long very linear growing crack is detected, as can be followed in the added crack images. In Eq. 6 the average energy  $\langle w_{el} \rangle$  and  $\langle c \rangle$  is entering, corresponding to the region of linear increase of crack length.  $T$  is calculated with the elastic density relating to the cross section area,  $w_{el,Rest}$ . The constituents of  $T$  are averaged over the region in which the crack propagation rate is determined. Log–log plots of  $dc/dn$  versus  $T$  yield so called Paris–Erdogan plots. Different crack growth rates  $dc/dn$  in the Paris plots displayed in the next section are directly related to diverse crack contour length progresses. The largest effect on the crack growth relates to the strain preset. But also the effects of varying mixtures can already be followed in the crack growth curves. This is shown in Figure 11 where crack growth curves of NR/BR blends with different BR contents are compared at 30% strain.

#### PARIS–ERDOGAN PLOTS

The pure polymers used have different crack growth rates largely depending on the crystallizing behavior of the polymers.<sup>47,48</sup> NR, showing pronounced strain-induced crystallization, has the highest crack resistance. BR, although crystallizing faster than NR in the unstrained state, reaches only two-thirds of its final degree of crystallization.<sup>47,48</sup> Additionally, the melting temperature of the BR crystallization is less raised on stretching than the crystallization of NR. At the 60°C measurement temperature the BR does not crystallize quickly enough to decrease crack

propagation.<sup>47</sup> SBR, formed by random copolymerization of two different monomers, cannot crystallize<sup>48</sup> and has a higher crack propagation rate than NR.<sup>34</sup> Both polymers, BR and SBR, have a similar, low tensile strength at 60°C.<sup>46</sup> The Paris–Erdogan plots resulting from the fracture mechanical measurements are shown in Figure 12. Here, every symbol corresponds to a separate measurement, that is, an (initial) slope (solid lines in Figure 10) and the corresponding tearing energy obtained with Eq. 5.

For the NR/BR blends, increasing the BR content leads to faster crack growth  $dc/dn$  at high tearing energies  $T$  (Figures 11 and 12a). The faster crack growth depends mainly on the lower NR content. For high tearing energies a crack growth larger than 1  $\mu\text{m}/\text{cycle}$  is observed, leading to 1 mm crack propagation in only 1000 cycles. The low crack growth resistance of BR compounds may result in chip and cut, the removal of pieces of the tire tread, which is a critical tire property for hot climate and bad roads. Cutting denotes penetration or cut of the surface by sharp objects striking the tire tread. Chipping causes tearing perpendicular to the load direction and is induced by forces on rough surfaces.<sup>17</sup> Therefore when NR is the dominant component in the blends, the change of filler loading in BR may not affect the crack propagation of the whole blend.

Batching of the NR/BR blends leads to improved fracture mechanical properties with slightly lower crack growth rates (Figure 12b). For samples with 30% BR both mixing procedures do not differ significantly, but for samples with 45% BR, the samples mixed in the batch process have decreased crack propagation rates for high tearing energies. This may be related to the somewhat higher filler loading of the NR phase shown in Figure 6 and Table II. The low amount of the interphase in the batches seems not to play a crucial role, here. The higher filler loading in the NR may result in more pronounced strain-induced crystallization at a given strain. This would result in increased reinforcement of the NR and a higher crack growth resistance of the NR/BR batches compared with the standard mixing procedure.

The fracture mechanical properties of the NR/SBR blends do not depend much on the SBR content (Figure 12c). Although increasing the SBR content leads to a faster crack growth rate  $dc/dn$  for all measured tearing energies, the effect is considerably smaller than the effect for the NR/BR blends. It appears that a fair distribution of the filler into the different polymer phases and the interphase is important for the improved performance compared with NR/BR. Based on the morphological data in Table III it becomes clear that a more homogeneous carbon black distribution in the NR/SBR blends is realized compared with the distribution of the NR/BR blends listed in Table II. In addition, the high amount of interphase in the NR/SBR blends shown in Figure 9 may support the crack growth resistance in these systems.

## CONCLUSIONS

The carbon black distribution in blends can be determined by the increase of the loss modulus peaks in a filled blend in comparison with an unfilled blend. With this method the filler loading of the different phases, including the interphase, can be obtained easily and reliably, as shown by the NR/SBR blends. As several other studies affirm,<sup>27–32</sup> the SBR has a higher affinity to carbon black than the NR. The quantitative filler amount in the phases attained lies midway in the literature data for NR/SBR blends and quite close to data for similar compounds.<sup>27–32</sup>

Nevertheless several issues can induce difficulties: For a reasonable evaluation the loss modulus peaks in the unfilled blends should be significantly separable and not vanishingly small. Apparently also the crystallization of the BR creates difficulties. This may be the reason in the NR/BR blends that most filler seems to be in the NR phase, although other studies say the converse. For the NR/BR blends mixed with the masterbatch procedure, dynamic-mechanical data as well as TEM images suggest a higher filler concentration in the NR compared with the standard mixing procedure.

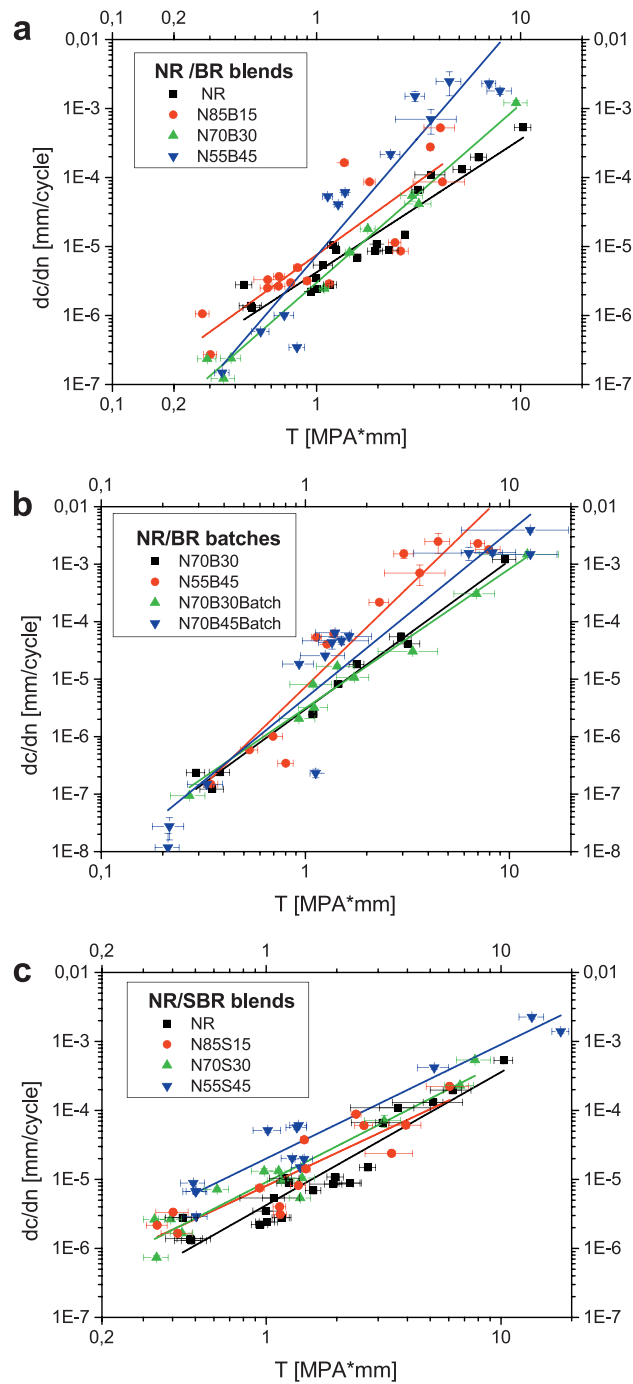


FIG. 12. — Tear fatigue analyzer results (Paris–Erdogan plots) at 60°C: (a) crack growth rate  $dc/dn$  in dependence of tearing energy  $T$  for the NR/BR blends, (b) the NR/BR blends mixed with the batch mixing procedures in comparison with the standard mixed blends, and (c) the NR/SBR blends.

Owing to the strain-induced crystallization of the NR, the crack resistance increases with the NR content. The fracture mechanical measurements indicate that blends containing BR have lower crack growth resistance at high tearing energies, possibly resulting in chip and cut. Batching of the NR/BR blends seems to result in slightly improved fracture mechanical properties, which may be related to the more heterogeneous filler distribution with high amounts of CB in NR. It seems that a high filler loading of NR improves crack resistance due to a more pronounced strain-induced crystallization at fixed strain level. For the NR/SBR blends a faster crack growth rate  $dc/dn$  is found upon increasing the SBR content. But the behavior is not so critical for high tearing energies  $T$  possibly because of the higher filling of the SBR phase compared with the low BR filling in the NR/BR blends.

#### ACKNOWLEDGEMENTS

We would like to thank the Deutsche Forschungsgemeinschaft (DFG) for financial support (grant KL1409/9-1) and our project partners IPF Dresden and Continental AG for very good cooperation. J. Lacayo-Pineda, MSc, and D. Jugan (both from Continental Reifen Deutschland GmbH) are appreciated for providing the TEM images.

#### REFERENCES

- <sup>1</sup>A. N. Gent, *Engineering with Rubber*, Hanser, Munich, Vienna, 2001.
- <sup>2</sup>B. Huneau, I. Masquelier, Y. Marco, V. Le Saux, S. Noizet, C. Schiel, and P. Charrier, *RUBBER CHEM. TECHNOL.* **89**, 126 (2016).
- <sup>3</sup>M. Ludwig, T. Alshuth, M. El Yaagoubi, and D. Juhre, *Constitutive Models for Rubber IX*, B. Marvalová, I. Petříková, Eds., Taylor & Francis, London, 2015, pp. 445–448.
- <sup>4</sup>R. S. Rivlin and A. G. Thomas, *J. Polym. Sci.* **10**, 291 (1953).
- <sup>5</sup>B. N. J. Persson, O. Ahlbor, G. Heinrich, and H. Ueba, *J. Phys.: Cond. Matter* **17**, R1071 (2005).
- <sup>6</sup>B. N. J. Persson and E. A. Brener, *Phys. Rev. E* **71**, 036123 (2005).
- <sup>7</sup>M. Klüppel, *J. Phys: Cond. Matter* **21**, 035104 (2009).
- <sup>8</sup>K. Reinke, M. Klüppel, and W. Grellmann, *Kautschuk Gummi Kunststoffe* **62**, 246 (2009).
- <sup>9</sup>A. R. Payne, *RUBBER CHEM. TECHNOL.* **36**, 432 (1963).
- <sup>10</sup>J. D. Ferry, *Viscoelastic Properties of Polymers*, 3rd ed., Wiley, New York, 1980.
- <sup>11</sup>R. Behnke, M. Kaliske, and M. Klüppel, *RUBBER CHEM. TECHNOL.* **89**, 154 (2016).
- <sup>12</sup>C. Liu, B. Dong, L.-Q. Zhang, Q. Zheng, and Y.-P. Wu, *RUBBER CHEM. TECHNOL.* **88**, 276 (2015).
- <sup>13</sup>R. Stoczek, R. Kipscholl, E. Euchler, and G. Heinrich, *Kautschuk Gummi Kunststoffe* **4**, 26 (2014).
- <sup>14</sup>R. Stoczek, P. Ghosh, R. Mukhopadhyay, R. Kipscholl, and G. Heinrich, *Constitutive Models for Rubber VIII*, N. Gil-Negrete and A. Alonso, Eds., Taylor & Francis, London, 2013, pp. 323–328.
- <sup>15</sup>U. Eisele, S. A. Kelbch, and H.-W. Engels, *Kautschuk Gummi Kunststoffe* **45**, 1064 (1992).
- <sup>16</sup>R. Stoczek, G. Heinrich, M. Gehde, and R. Kipscholl, *Lecture Notes Appl. Comput. Mech.* **70**, 269 (2013).
- <sup>17</sup>J. R. Beatty and B. J. Miksch, *RUBBER CHEM. TECHNOL.* **55**, 1531 (1982).
- <sup>18</sup>W. M. Hess, C. R. Herd, and P. C. Vegvari, *RUBBER CHEM. TECHNOL.* **66**, 329 (1993).
- <sup>19</sup>H. J. Kim and G. R. Hamed, *RUBBER CHEM. TECHNOL.* **73**, 743 (2000).
- <sup>20</sup>G. R. Hamed, H. J. Kim, and A. N. Gent, *RUBBER CHEM. TECHNOL.* **69**, 807 (1996).
- <sup>21</sup>H. Takino, R. Nakayama, and Y. Yamada, *RUBBER CHEM. TECHNOL.* **70**, 584 (1997).
- <sup>22</sup>B. E. Clapson and G. J. Lake, *Rubber J.* **152**, 36 (1970).
- <sup>23</sup>F. Röhemyer and F. Sommer, *Kautschuktechnologie*, Hanser, Munich, Vienna, 2001, pp. 77–89.

- <sup>24</sup>C. Marano, S. H. Mohammadpoor, and M. Rink, *Constitutive Models for Rubber VIII*, N. Gil-Negrete, and A. Alonso, Eds., Taylor & Francis, London, 2013, pp. 491–496.
- <sup>25</sup>D. Mangaraj, *RUBBER CHEM. TECHNOL.* **75**, 365 (2002).
- <sup>26</sup>J. G. Meier, M. Klüppel, H. Geisler, and R. H. Schuster, *Kautschuk Gummi Kunststoffe* **58**, 587 (2005).
- <sup>27</sup>W. M. Hess, C. E. Scott, and J. E. Callan, *RUBBER CHEM. TECHNOL.* **40**, 371 (1967).
- <sup>28</sup>R. H. Schuster, H. M. Issel, and V. Peterseim, *RUBBER CHEM. TECHNOL.* **69**, 769 (1996).
- <sup>29</sup>J. A. Ayala, W. M. Hess, F. D. Kistler, and G. A. Joyce, *RUBBER CHEM. TECHNOL.* **64**, 19 (1991).
- <sup>30</sup>J. E. Callan, W. M. Hess, and C. E. Scott, *RUBBER CHEM. TECHNOL.* **44**, 814 (1971).
- <sup>31</sup>H. H. Le, S. Ilisch, G. R. Kasaliwal, and H.-J. Radusch, *Kautschuk Gummi Kunststoffe* **60**, 241 (2007).
- <sup>32</sup>G. R. Cotton and L. J. Murphy, *RUBBER CHEM. TECHNOL.* **61**, 609 (1988).
- <sup>33</sup>J. F. Meier, M. Klüppel, and R. H. Schuster, *Kautschuk Gummi Kunststoffe* **58**, 82 (2005).
- <sup>34</sup>H. Lorenz, D. Steinhauser, and M. Klüppel, *Lecture Notes Appl. Comput. Mech.* **70**, 81 (2013).
- <sup>35</sup>M. Klüppel, R. H. Schuster, and J. Schaper, *RUBBER CHEM. TECHNOL.* **72**, 91 (1999).
- <sup>36</sup>M. Klüppel, R. H. Schuster, and J. Schaper, *GAK—Gummi Fasern Kunststoffe* **51**, 508 (1998).
- <sup>37</sup>R. H. Schuster, J. Meier, and M. Klüppel, *Kautschuk Gummi Kunststoffe* **53**, 663 (2000).
- <sup>38</sup>M. Wunde and M. Klüppel, Carbon black distribution in NR/BR and NR/SBR blends. *Proceedings, 14th International Seminar on Elastomers*, Bratislava, Slovakia, Aug 24–28, 2014, Librix.eu, Bratislava, 2014, p. 68.
- <sup>39</sup>U. Eisele, *Introduction to Polymer Physics*, Springer, Berlin, Heidelberg, New York, 1990, pp. 87–92.
- <sup>40</sup>A. K. Sircar and T. G. Lamond, *RUBBER CHEM. TECHNOL.* **45**, 178 (1972).
- <sup>41</sup>A. L. G. Saad and S. El Sabbagh, *J. Appl. Polym. Sci.* **79**, 60 (2000).
- <sup>42</sup>S. C. George, K. N. Ninan, G. Groeninckx, and S. Thomas, *J. Appl. Polym. Sci.* **78**, 1280 (2000).
- <sup>43</sup>A. A. Griffith, *Philos. Trans. R. Soc. London A*, **221**, 163 (1921).
- <sup>44</sup>P. C. Paris, M. P. Gomez, and W. E. Anderson, *Trend Eng.* **13**, 9 (1961).
- <sup>45</sup>P. Paris and F. Erdogan, *J. Basic Eng.* **528** (1963).
- <sup>46</sup>C. Timbrell, M. Wiehahn, G. Cook, and A. H. Muhr, *Constitutive Models for Rubber III*, J. J. C. Busfield and A. H. Muhr, Eds., Swets Zeitlinger, Lisse, the Netherlands, 2003, pp. 11–20.
- <sup>47</sup>A. N. Gent and L. Q. Zhang, *J. Polym. Sci., Part B* **39**, 811 (2001).
- <sup>48</sup>L. R. G. Treloar, *The Physics of Rubber Elasticity*, 3rd ed., Clarendon, Oxford, 1975, pp. 16–23.

[Received February 2016, Revised April 2016]



Matthias Wunde · Manfred Klüppel

# Impact of mixing procedure on phase morphology and fracture mechanical properties of carbon black-filled NR/SBR blends

Received: 30 September 2016 / Accepted: 7 March 2017 / Published online: 30 March 2017  
© Springer-Verlag Berlin Heidelberg 2017

**Abstract** Based on a viscoelastic model, the filler distribution and the amount of interphase of carbon black-filled blends of natural rubber (NR) with styrene-butadiene rubber (SBR) are evaluated. Hereby, the total dissipated energy  $G''$  during dynamical straining is decomposed into the contributions of the different polymer phases and the interphase. For the NR/SBR blends, we find a higher filling of the SBR phase and the interphase and a lower filling of the NR phase. The filler distribution itself depends not only on the affinity of the polymer to the filler but also on the mixing procedure. This is investigated by studying NR/SBR blends prepared by two different mixing procedures. In the standard mixing procedure, the polymers are mixed first, and then, the filler is added. In the batch mixing procedure, the filler is previously mixed in the NR only and then blended with SBR. Batch mixing is resulting in an increase in the filling of the interphase due to filler transfer from NR to SBR. The results for the filler distribution are compared to fatigue crack propagation rates under pulsed excitation. The crack propagation is accelerated when substituting NR with SBR. The batched samples show higher crack propagation rates at higher tearing energies due to a worse dispersion of the carbon black and/or higher filler loading of the interphase.

**Keywords** Filled rubber blends · Filler distribution · Phase morphology · Interphase · Fracture mechanics · Viscoelastic model

## 1 Introduction

### 1.1 Filler distribution in rubber blends

The material used for tires, conveyor belts and other high-performance elastomer products needs to fulfill certain properties. Among the requirements for tires are the rolling resistance, the wet skid resistance and service life. Natural rubber has the highest durability due to strain-induced crystallization. This is reflected by the highest tensile strength and resistance to catastrophic crack growth [1,2]. SBR compounds show a good wet skid resistance, especially those with high styrene content [3]. Blending usually combines the properties of the individual polymers. But also synergetic effects are possible so that a blend can have a better property than both polymers [1,4,5]. Using polymer blends can result in a reduced compound cost, improve the building or the performance [6].

---

Communicated by Johlitz, Laiarinandrasana and Marco.

Matthias Wunde · Manfred Klüppel (✉)  
Deutsches Institut für Kautschuktechnologie e. V. (DIK), 30519 Hannover, Germany  
E-mail: Manfred.Klueppel@DIKautschuk.de

Besides on the components of the blend, the fracture mechanical properties depend on the distribution of the reinforcing filler into the different polymer phases [7]. Using master batches changes the filler distribution and can lead to enhanced reinforcement in silica-filled NR/BR/SBR blends [8]. The affinity of carbon black to NR and SBR in NR/SBR blends has been studied by several authors using different techniques [9–14], all of them detecting a higher affinity of the SBR to CB. The higher carbon black loading in the SBR phase is explained by stronger carbon black polymer interactions [9, 10]. Le et al. [9] studied the kinetics of the filler distribution with thermogravimetry on the rubber–filler gel [9]. The NR bonds to the CB more quickly, but with increased mixing time the filler transfers to the SBR phase due to the stronger SBR-CB bonds. Cotton and Murphy [10] showed by analysis of bound rubber that the molecular weight of the polymers is affecting the carbon black dispersion. The carbon black affinity increases with higher molecular weight, but the effect is weak for the immiscible NR/SBR blends. Also, higher carbon black loadings in the SBR with increasing surface area of the carbon black and with increased mixing time are revealed. Other techniques applied to study the carbon black affinity include, phase contrast optical microscopy [11, 12], inverse gas liquid chromatography [13], and combined measurements of the static and dynamic modulus [14]. Differences in the carbon black distribution measured by the different techniques are caused, not only but also, from different ingredients used in the compounds. The rubbers are not identical, e.g., varying in styrene content of the SBR and different molecular weights of the NR. The CB also differs in grade and content. The previously mentioned techniques do not state information about the interphase and the interphase filling. But both the magnitude of the interphase connecting different polymer phases and the filler amount in the interphase are influencing the fracture mechanical properties of the blend.

## 1.2 Evaluation of filler distribution based on viscoelastic spectra

By the evaluation of the increase in the loss modulus peaks, the filler distribution not only in the two polymer phases but also in the interphase can be obtained. A fitting procedure separating the contributions of the different polymer phases and also of the interphase to the temperature-dependent total dissipated energy  $G''$  during dynamical straining is presented [15–19]. Due to the filler located in a specific phase, the energy dissipation in that phase is increased. From the increase of energy dissipation in the different phases, it is possible to determine the carbon black amount in the phases.

This method was already used to study the filler distribution in elastomer blends. The results of this study are within the range of previous results of NR/SBR blends using this technique [15–17]. All studies agree in a higher affinity of CB to SBR, but there are differences in the extent of the affinity toward the SBR. The differences may be caused by material variation. In NR/BR blends, contradictory results have been reported. A higher filling of the BR phase [15] as well a very low filling of the BR phase [18] were found. Also, studies on carbon black-filled EPDM/BR blends [15, 16, 20] and SBR/EPDM blends were performed [17]. Furthermore, silica-filled compounds have been studied [8, 21, 22].

## 1.3 Fracture mechanics of rubbers

Elastomer products made of NR/SBR blends like tires often need to sustain high dynamic loading conditions inducing crack propagation. Micro-mechanical mechanisms of crack initiation and propagation occurring under quasi-static and dynamic loading conditions are in current investigation [7]. The characteristics of crack initiation could be recently connected to the flaw size in the rubber [23, 24]. Fracture mechanical methods and models for viscoelastic solids are based on the fundamental work of Rivlin and Thomas [25]. Although recent efforts have been made [26–29], there is still potential, especially due to the strongly nonlinear deformation behavior and stress softening effects [7, 30, 31]. The fracture mechanical properties of tires and conveyor belts can be characterized by the Fatigue Crack Growth and the Chip & Cut behavior of the rubber composites [32, 33]. The Fatigue Crack Growth is at present usually carried out using the tear fatigue analyzer and evaluates the crack growth velocity under given loading conditions [34, 35]. The Chip & Cut behavior is described by the tearing of rubber under harsh loading conditions that lead to a removal of rubber pieces. This effect is measured by the weight change in a rotating wheel dynamically impacted by a sharp tool [32, 33, 36].

**Table 1** Recipes of the compounds (in phr)

Samples	NR	SBR	CB	CBS	Sulfur	IPPD	ZnO	Stearic acid
NR	100	–	50	2.5	1.7	1.5	3	1
N85S15	85	15	50	2.5	1.7	1.5	3	1
N70S30	70	30	50	2.5	1.7	1.5	3	1
N70S30Batch	70	30	50	2.5	1.7	1.5	3	1
N55S45	55	45	50	2.5	1.7	1.5	3	1
N55S45Batch	55	45	50	2.5	1.7	1.5	3	1

Batch denotes samples mixed with the batching mixing procedure (carbon black blended first in NR only)

## 2 Experimental

### 2.1 Materials

The investigation is carried out on polymer blends based on natural rubber (SVR CV 60) blended with styrene-butadiene rubber (Buna VSL 4526, Lanxess) with 45 wt% vinyl and 26 wt% styrene groups with varying proportion of the polymers. As filler, 50 phr (parts per hundred rubber) of carbon black (N339) are used. The samples are cross-linked semi-efficiently by sulfur and the vulcanization accelerator *N*-cyclohexyl-2-benzothiazole sulfonamide (CBS). The samples are compounded with the processing and vulcanization additives stearic acid and zinc oxide and protected against aging by *N*-isopropyl-*N'*-phenyl-*p*-phenyldiamine (IPPD). The full recipe is shown in Table 1.

### 2.2 Sample preparation

The compounds are mixed in an industrial 5-liter intermeshing mixer (Werner & Pfleiderer GK 5 E) at 40 rpm for 6 min. After 2-min mastication of the polymers, the other ingredients are inserted. The homogeneity of the mixtures is indicated by leveling of the torque after mastication and after mixing. The composites are handled another 7 min on a roller mill where the curing system is added. Vulcanization is performed at 150 °C in a heat press up to 90% of the vulcameter torque maximum ( $t_{90}$  time).

Two different mixing techniques are used. In the standard mixing procedure, the polymers are mixed first, and then, the filler is added. In the batch mixing procedure, the filler is first blended with the NR only and the SBR and the other ingredients are added in a second mixing stage. After the second mixing stage, the curing system is mixed in the roller mill.

### 2.3 Optical dispersion analysis

The carbon black dispersion is checked by optical dispersion analysis. As non-dispersed filler scatters the light diffusely, a computer-aided evaluation [Dispersions Index Analysis System (DIAS), developed at DIK] can determine the agglomerate size distribution of the filler from reflected-light microscope images. The images are taken on fresh elastomer surfaces at 150 times magnification. For each compound, five images are evaluated. The degree of dispersion is estimated by the portion of non-dispersed carbon black in the observed surface. In the estimation of dispersion grade, the medialia factor  $v$  representing the volume fraction of carbon black in the agglomerates is taken into account [37,38].

### 2.4 Dynamic-mechanical analysis

The dynamic-mechanical properties are measured in the torsion-rectangular mode on an ARES rheometer (Rheometric) with strip specimen of 2 mm thickness. The dynamic moduli are measured over a wide temperature range (−90 to +20 °C) in steps of 1 °C at a frequency of 1 Hz and 0.5% strain amplitude.

## 2.5 Tear fatigue analyzer

The fracture mechanical measurements are performed on a tear fatigue analyzer (Coesfeld) at notched strip samples. This machine can detect the crack length of 10 specimens simultaneously. The crack propagation rates are measured under pulsed excitation (4 Hz, 30 ms pulse width) at 60 °C. The 15 mm broad samples with a 1-mm-deep crack are pre-strained by 2 N and excited by varying strain amplitudes between 10 and 30%. The graphical images for determination of the crack length are triggered between the pulses.

## 3 Viscoelastic response of filled rubber blends

### 3.1 Effect of fillers in homo-polymers

A single polymer shows a peak of the dissipated energy  $G''$ . The peak, centered around the glass transition temperature  $T_g$  of the polymer, is increased by filling with an active filler. Previous investigations have shown that the maximum of the dissipated energy  $G''_{\max}$  increases almost linearly with the filler volume fraction  $\phi_F$  [15, 16, 22]:

$$G''_{\max}(\phi_F) = G''_{\max,0} + \alpha\phi_F \quad (1)$$

Here,  $G''_{\max,0}$  is the maximum of the loss modulus of the unfilled polymer.

Storage and loss modulus  $G'$  and  $G''$  are real and imaginary part of a complex function  $G^*$ , and both moduli have a connection analogous to Kramers–Kronig relations. This connection links the linear increase in the maximum of dissipated energy  $G''_{\max}$  given in Eq. (1) with a linear increase in the step height of the storage modulus  $G'$ . The step height itself is dominated by the value of  $T_g$  in the glass, as  $G'$  in the rubber is 2–3 orders of magnitude lower (Fig. 1a). Accordingly, a similar linear relation as Eq. (1) holds for the storage modulus in the glassy regime:

$$G'_{\text{glass}}(\phi_F) = G'_{\text{glass},0} + \alpha'\phi_F \quad (2)$$

with  $\alpha' \approx \alpha$ . Here,  $G'_{\text{glass}}$  is the storage modulus of the filled rubber in the glass and  $G'_{\text{glass},0}$  is the storage modulus of the unfilled rubber in the glass. In Fig. 1b, the linear increase in  $G''_{\max}$  and in  $G'$  at  $-90$  °C is shown. Above the glass transition, hydrodynamic amplification plays a role and an additional quadratic term enters, presuming very stiff filler compared to the stiffness of the polymer [39]. In Fig. 1b, no quadratic behavior can be seen for the NR, while for the SBR a very small quadratic term is possible. The linearity in Fig. 1b valid for NR/SBR blends seems to be a general characteristic in the glassy regime where the stiffness of the filler and the polymer is in the same order [15–17, 20, 22].

Ziegler and Schuster [22] studied the influence of silanization in BR and NBR on the slope of  $G''$  with the filler volume fraction  $\phi_F$ . They found that the front factor  $\alpha$  of Eq. (1) increases systematically with the rubber–filler interaction strength. The polar silica interacts strongly with the polar NBR but only weakly with the non-polar BR. The silanization decreases the polarity of the silica surface and the intensity of rubber–filler interactions with the NBR decreases but with the BR increases. The change in the strength of interactions correlates with a decrease in the slope of  $G''(\phi_F)$  in NBR and an increase in the slope in BR.

A linear dependency of  $G'$  in the glass can be explained by a parallel coupling of the pure rubber and of the rubber–filler structures consisting of the filler network including strongly bounded, immobilized rubber:

$$G'_{\text{glass}}(\phi_F) = (1 - \phi_F)G'_{\text{glass},0} + \phi_F G'_{\text{CB}} \quad (2')$$

This parallel coupling requires that the strain of both components is almost the same. The storage modulus of the rubber–filler structures at  $-90$  °C yields  $G'_{\text{CB}} = 2260$  MPa for NR and  $G'_{\text{CB}} = 2480$  MPa for SBR, indicating that the rubber–filler structure of NR is softer than that of SBR. This can be related to (immobilized) polymer bridges between the filler particles that transmit the stress similar as in the rubber elastic regime well above  $T_g$  [39, 40].

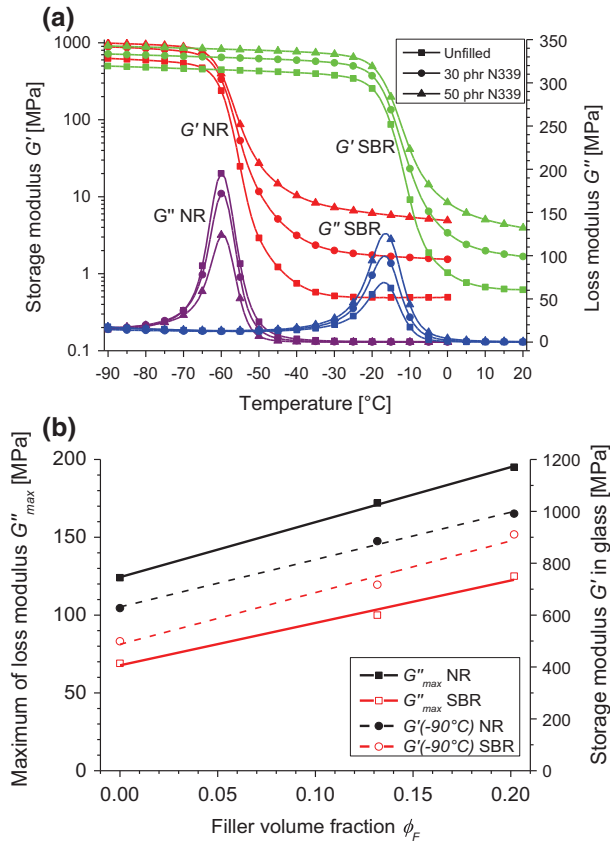


**Fig. 1** Temperature-dependent moduli  $G'$  (logarithmic scale) and  $G''$  for unfilled and differently filled NR and SBR compounds (a). Linear increase in the maximum loss modulus  $G''_{max}$  and of the storage modulus  $G'$  in the glass at  $-90^\circ\text{C}$  with filler volume fraction  $\phi_F$  in NR and SBR, respectively (b)

### 3.2 Phase network of unfilled blends

The mechanical response of the phase network of unfilled blend systems with one phase glassy and the other not, can be described by percolation theory [15]. In percolation theory, there exists a critical concentration  $\phi_c$ , at which the initially separated domains grow together to form an infinite cluster. Then, the largest phase domain of the glassy polymer becomes infinite large, leading to a phase transition at  $\phi_c$  [41].  $\phi_c$  depends on the assumed lattice structure. The correlation length  $\xi$  for this polymers is given by the mean distance between two sites on the same polymer domain for polymer concentrations  $\phi < \phi_c$  and between two empty sites of the same hole (corresponding to two sites on the same domain of the other polymer) for  $\phi > \phi_c$ , respectively. When  $\phi$  is approaching the threshold  $\phi_c$ , the correlation length increases as:

$$\xi \cong a |\phi - \phi_c|^{-\nu} \quad (3)$$

with the same exponent  $\nu$  below and above  $\phi_c$ . Here,  $a$  is the characteristic size of the domains [41]. The situation below and above the threshold  $\phi_c$  is exemplified on phase contrasted TEM images of EPDM/NR blends (Fig. 2). Images of this blend show better contrast than NR/SBR blends due to staining by osmium tetroxide so that the bright dispersed EPDM phase below  $\phi_c$  and the interpenetrating phase network above  $\phi_c$  can be seen.

Other quantities associated with the percolation transition show a similar power-law behavior with other critical exponents. The storage modulus of the glassy phase is given by:

$$G'_{\text{glass}} \cong E \left( \frac{a}{\xi} \right)^3 / N_1(\xi) \quad (4)$$

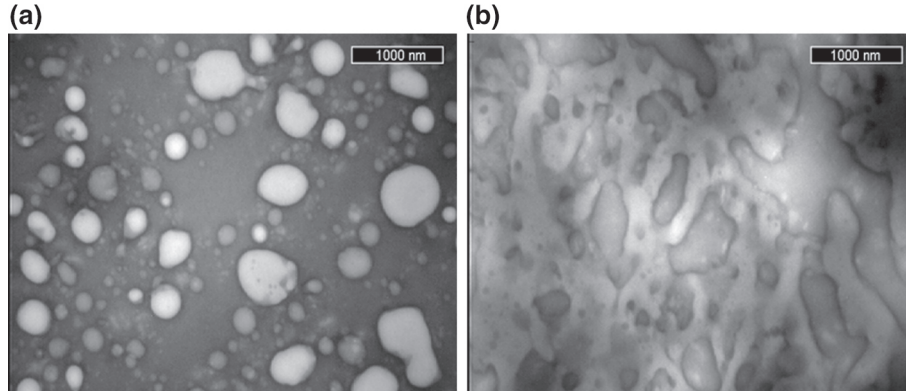


**Fig. 2** Phase morphology of phase-contrasted EPDM/NR blends: dispersed phase morphology of the EPDM/NR (20:80) blend (a) and interpenetrating phase network in the EPDM/NR (60:40) blend (b)

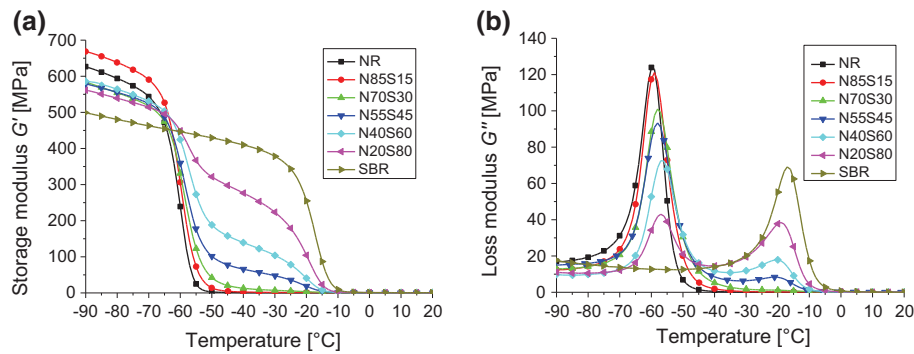


**Fig. 3** Storage modulus  $G'$  (a) and loss modulus  $G''$  (b) of unfilled NR/SBR blends

where  $E$  is the elastic modulus of the glassy phase and  $N_1(\xi)$  is the number of singly connected bonds of the phase network. With Eq. (3) and  $N_1(\xi) = \left(\frac{\xi}{a}\right)^{\frac{1}{\nu}}$  [15,41], it follows:

$$G'_{\text{glass}} \cong E (\phi - \phi_c)^{3\nu+1} \sim (\phi - \phi_c)^\tau \quad (5)$$

The shear modulus  $G'$  of the polymer phase increases above  $\phi_c$  with the critical exponent  $\tau = 3\nu + 1 \approx 3.6$  [42]. The exponents  $\nu$  and  $\tau$  are universal and do not depend on details of the percolation [15]. Based on this approach, the filler network and the Payne effect have also been described [43].

When the temperature in an unfilled blend is chosen in-between both glass transition temperatures, the elastic modulus is dominated by the harder glassy phase, when this phase is above the threshold  $\phi_c$  [15]. Below  $\phi_c$ , the glassy domains remain undeformed during dynamic excitation because of their large modulus compared to that of the continuous NR. Then, the glassy domains of the SBR enhance the modulus only by hydrodynamic amplification. Above the percolation threshold, the glassy domains of the SBR form a continuous phase network, where most energy is stored. The percolation behavior of the glassy SBR phase is shown in Fig. 3 for the NR/SBR blends in the temperature range around  $-40^\circ\text{C}$ . Below the threshold  $\phi_c$ , the storage modulus  $G'$  shown in Fig. 3a at temperatures around  $-40^\circ\text{C}$  is very small and increases substantially above  $\phi_c$ . An analogous increase can be seen for the local maximum of the loss modulus  $G''$  in Fig. 3b.

Figure 4a shows a fit of  $G'$  at different temperatures in-between both glass transitions and of  $G''_{\text{max}}$  according to the power law Eq. (5) for different SBR contents above the critical SBR concentration  $\phi_c$ . The value of  $\phi_c = 0.22$  has been fitted to get a minimum variance. The slope is found as  $\tau = 1.34$  for  $G'(-45^\circ\text{C})$ ,  $\tau = 1.53$  for  $G'(-40^\circ\text{C})$ ,  $\tau = 1.65$  for  $G'(-35^\circ\text{C})$ ,  $\tau = 1.73$  for  $G'(-30^\circ\text{C})$  and  $\tau = 1.76$  for  $G''_{\text{max}}$ . This differs significantly from the theoretical value  $\tau \approx 3.6$ , which can be related to coalescence effects that alter the phase network structure.

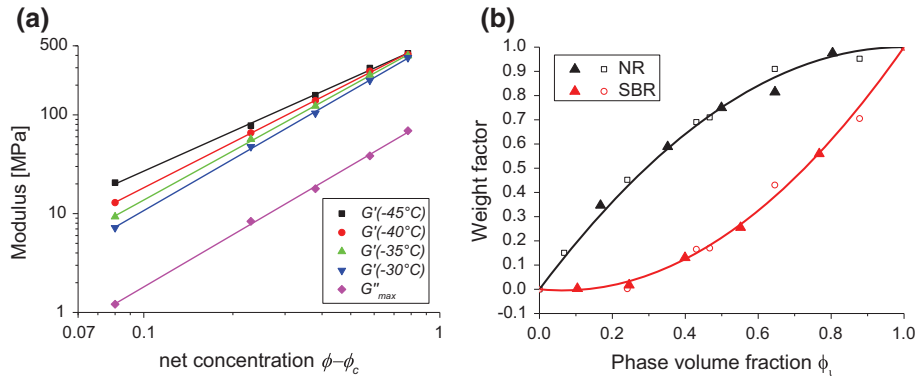


**Fig. 4** Increase in the storage modulus of unfilled NR/SBR blends at temperatures between  $-45$  and  $-30^\circ\text{C}$  and the maximum of the loss modulus with increasing SBR content. A power-law behavior according to Eq. 5 above  $\phi_c = 0.22$  can be identified (a). Weight factor  $G''_{\text{max,blend}}/G''_{\text{max,polymer}}$  (b). The *open symbols* represent data taken from Schuster et al. [16]. The *full triangles*, indicating own data, fit well with the previous data. All values are fitted by Eq. 7

### 3.3 Energy dissipation in filled rubber blends

The total dissipated energy  $G''_{\text{blend}}$  is due to the additivity of energy the sum of all energy contributions of the different phases  $i$ :

$$G''_{\text{blend}} = \sum_i G''_{P,i} \phi_i \gamma_{0,i}^2 \quad (6)$$

$G''_{P,i}$  denotes the loss modulus,  $\phi_i$  the volume fraction and  $\gamma_{0,i}$  the strain amplitude of the  $i$ th phase.

In an unfilled blend, the dissipated energies of the phases depend nonlinearly on their phase volume fractions. The weight factors in term of their volume fractions are fitted by quadratic functions (Fig. 4b):

$$G''_{\text{blend}} = \sum_i G''_{P,i} (a_i + b_i \phi_i + c_i \phi_i^2) \quad (7)$$

The quadratic increase in the weight factor of the SBR in Fig. 4b correlates with the power law increase with linear slope of the log-log plot of  $G''_{\text{max}}$  in Fig. 4a.

In incompatible polymer blends, each polymer phase causes dissipation around its glass transition temperature. Besides the NR and the SBR phase, areas exist in which both polymers coexist. This so-called interphase leads to an enhanced signal of  $G''$  between the pure polymer peaks. The dissipated energy in unfilled, as well as filled blends, can be decomposed into the contributions from the different phases and the interphase. For this decomposition, a fitting routine is used. The amplitude and broadness of the peaks as well as the glass transition temperature are used as fitting parameters. The increase in the peaks with increasing filler content is due to the specific filler loading of the phases.

For the unfilled blends, the dynamic spectrum is fitted with the unfilled NR and SBR peaks so that the sum of both contributions coincides best with the measured curve in the two areas around both glass transition temperatures (Fig. 5). The interphase signal is received as the difference between the viscoelastic spectrum of the unfilled blend compared to the sum of the unfilled polymers.

In a filled blend, the filler effect (Eq. (1)) and the blend effect (Eq. (7)) are combined. The filler located in any phase (or the interphase) increases the dissipated energy of that phase. From the increase in the maximum of the dissipated energies  $G''_{\text{max}}$  in the different phases and the interphase, the filler volume fractions  $\phi_{F,i}$  of the different phases  $i$  can be calculated:

$$G''_{\text{blend}} = \sum_i \left( 1 + \alpha_i \frac{\phi_{F,i}}{\phi_{F,i} + \phi_i} \right) \left( a_i + b_i (\phi_{F,i} + \phi_i) + c_i (\phi_{F,i} + \phi_i)^2 \right) G''_{P,i} \quad (8)$$

The dynamic spectra of the filled blends are fitted with the unfilled NR and SBR peaks and the interphase peak so that the sum of all three curves corresponds best with the measurements (Fig. 6). The filler volume fractions in the phases and interphases  $\phi_{F,i}$  are obtained from the increase in the maximum values of  $G''$  using Eq. (8).

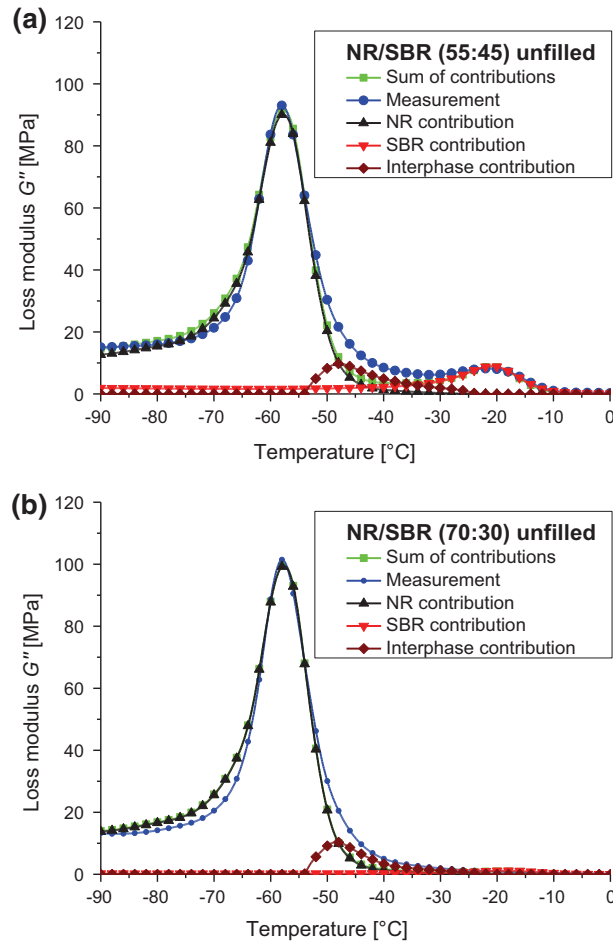


**Fig. 5** Fit of the loss modulus of the unfilled NR/SBR blends with the single polymer peaks. The interphase is obtained as fit difference: unfilled NR/SBR (55:45) blend (a) and unfilled NR/SBR (70:30) blend (b)

When calculating the filler volume fractions  $\phi_{F,i}$  with Eq. (8), there is no intrinsic reason why the calculated sum  $\sum_i \phi_{F,i}$  should exactly match the overall filler concentration  $\phi_F$ . Therefore, the sum of the calculated filler has a standard deviation of about 10% from the filler content in the samples. Nevertheless, all compounds should contain the same filler amount  $\phi_F = 0.2017$ . That is why for every compound the filler volume fraction is corrected by a factor around 1 so that

$$\sum_i \phi_{F,i} = \phi_F \quad (9)$$

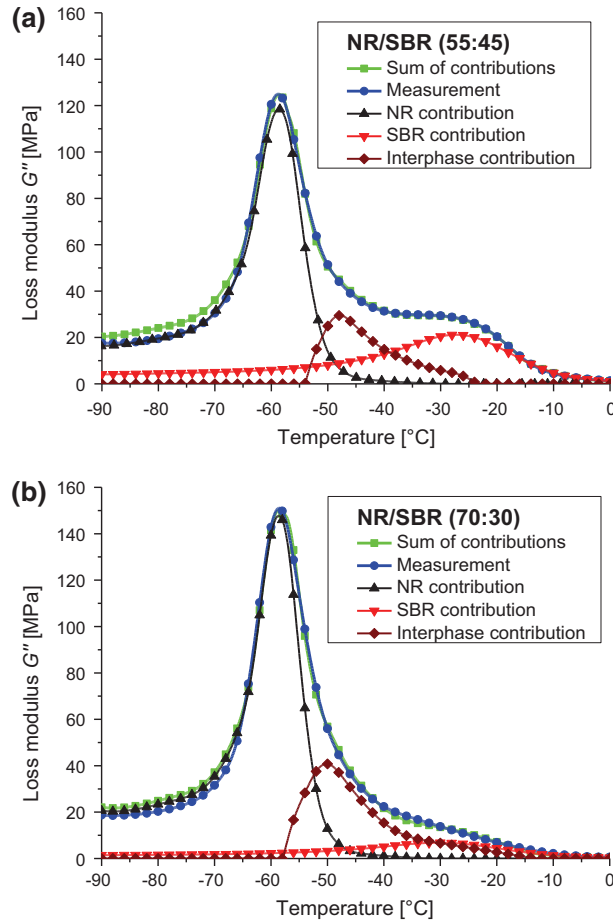
is fulfilled. If the correction factor deviates strongly from unity, it is a sign for unreliable results and the reasons for that should be understood. For the compound with only 15 phr SBR, the dynamic spectrum is dominated by the NR peak. The very small SBR peak of the unfilled compound does not allow a reliable calculation of the filler volume fraction  $\phi_{F,S}$  in the filled sample.

## 4 Phase morphology of filled blends

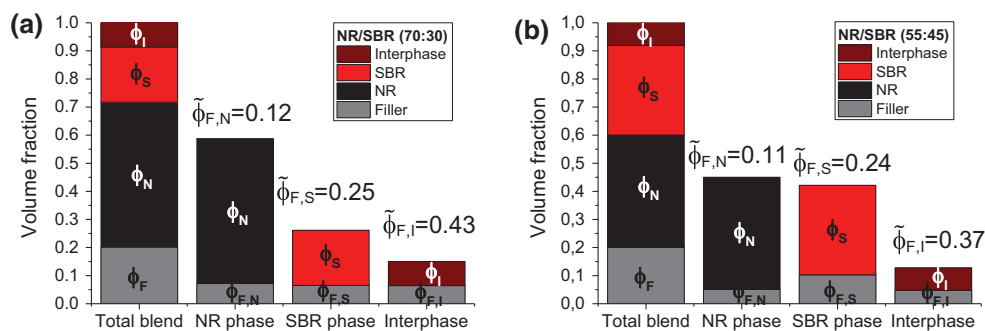
### 4.1 Carbon black distribution

Figure 7 shows the calculated carbon black distribution in the NR/SBR blends. A higher filling of the SBR phase and the interphase is found, while the NR phase is lower filled. These results are obtained for all blends with varying proportion of the polymers.





**Fig. 6** Fit of the loss modulus of the filled NR/SBR blends with the single polymers and the interphase. The filling of the phases and the interphase is obtained from the increase in the maxima of the contributions using Eq. (7): filled NR/SBR (55:45) blend (a) and filled NR/SBR (70:30) blend (b)



**Fig. 7** Carbon black distribution in NR/SBR blends: NR/SBR (70:30) (a) and NR/SBR (55:45) (b) (from Ref. [18]).  $\tilde{\phi}_{F,i}$  denotes the relative filler volume fraction in phase  $i$

Figure 8 shows the carbon black distribution in the NR/SBR blends mixed with the batching mixing procedure. In the batch, the whole amount of filler is mixed into the NR, but as the SBR has the higher affinity to carbon black, the filler needs to transfer from the NR to the SBR phase. Because of this transfer, more carbon black gets stuck in the interphase, leading to a higher filling of the interphase compared to the standard mixing procedure. Batching also seems to lead to a slightly higher filling of the NR phase and a lower filling of the SBR phase.

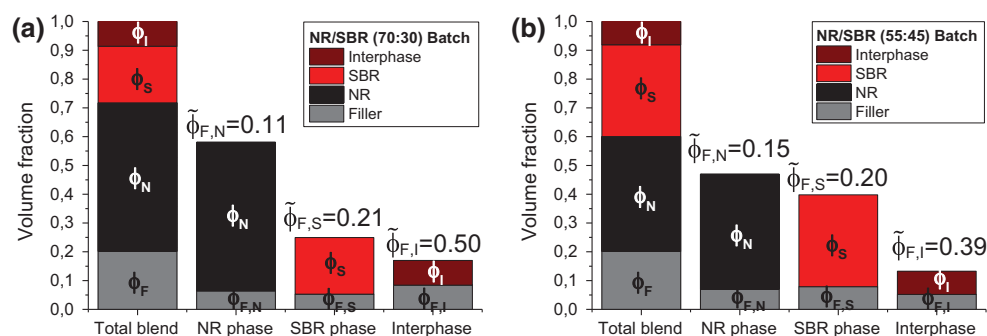


**Fig. 8** Carbon black distribution in NR/SBR blends mixed with the batch mixing procedure (CB first mixed into NR only): NR/SBR (70:30) batch (a) and NR/SBR (55:45) batch (b).  $\tilde{\phi}_{F,i}$  denotes the relative filler volume fraction in phase  $i$

**Table 2** Proportion of carbon black  $\tilde{\phi}_{F,i} = \phi_{F,i}/(\phi_i + \phi_{F,i})$  of the different phases in the NR/SBR blends

Filler volume fraction	N70S30	N70S30 Batch	N55S45	N55S45 Batch
$\tilde{\phi}_{F,N}$	0.12	0.11	0.11	0.15
$\tilde{\phi}_{F,S}$	0.25	0.21	0.24	0.20
$\tilde{\phi}_{F,I}$	0.43	0.50	0.37	0.39

**Table 3** Ratio  $\phi_{F,i}/\phi_F$  of the carbon black distributed into the different phases of the NR/SBR blends

Carbon black portion in	N70S30 (%)	N70S30 Batch (%)	N55S45 (%)	N55S45 Batch (%)
NR phase	36	32	26	35
SBR phase	32	26	51	39
Interphase	32	42	24	26

Table 2 summarizes what proportion of the different phases and the interphase consists of carbon black. The filler volume fractions in the NR  $\tilde{\phi}_{F,N}$  as well as in the interphase  $\tilde{\phi}_{F,I}$  seem to increase slightly with increasing NR content in the blend, while the proportion of the SBR seem to stay constant. It is no contradiction that no proportion is falling because the amount of the lowly filled NR phase is obviously rising with NR content.

In Table 3, it is shown how much of the filler is distributed in the different phases and the interphase. Due to its higher volume fraction  $\phi_{F,N}$ , a significant amount of the filler is found in the NR phase, although it is low filled. The interplay between carbon black affinity and the amount of the specific phases leads for many of the studied compounds to filler distributions with similar amount of carbon black in the different phases and interphases.

The proportions given in Table 3 can be compared with literature data. Cotten and Murphy [10] discovered for a similar 50:50 blend that 31.1% of the carbon black is found in the SBR phase and 58.9% in the NR phase. The SBR used is also solution polymerized with similar amount of 25% styrene. The compounds are filled with 45 phr of the same carbon black N339. When considering that they did not distinguish the carbon black located in the interphase, both results fit fairly well. Callan et al. [14] detected in a NR/SBR 50:50 blend using emulsion SBR, an even higher carbon black loading in the SBR. Also, other studies measured a preferred carbon black affinity of the SBR, but did not quantify the filler distribution in the blends [12, 13]. Previous measurements using our technique on NR/SBR blends have been made: In a 50:50 blends containing a solution SBR with 25% styrene and 60 phr N234, 51% of the filler is found in the SBR and 12 and 37% are found in the NR phase and interphase, respectively [17]. That is a lower NR filling and a higher interphase filling. In a 70:30 blend using a solution SBR with 40% styrene, a higher carbon black amount in the NR and a lower amount in the interphase is found [15]. On the contrary for NR/SBR (40:60) blends, a lower NR filling and a higher interphase filling are found [16]. When studying the filler distribution of NR/SBR blends using different techniques, the preference of the carbon black to the SBR is clearly resulting. But even using a single technique, the quantitative filler distribution seems to be strongly influenced by material variation. Also, the mixing is influencing the filler distribution as can be seen by comparing the results for the standard and the batch mixing procedure.

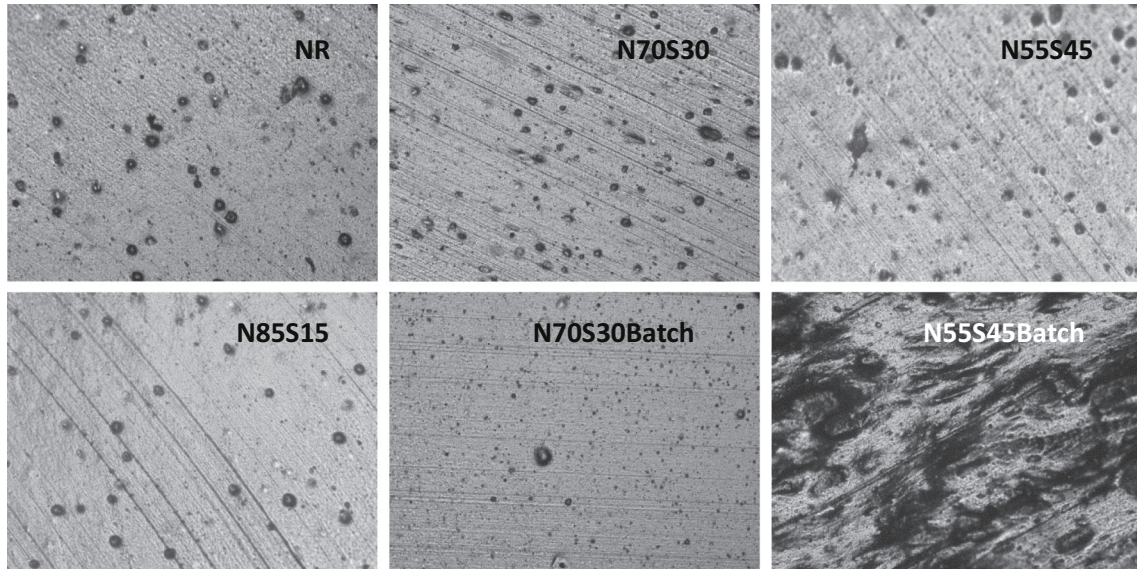


**Fig. 9** Exemplary optical dispersion images of the compounds

#### 4.2 Optical dispersion analysis

In Fig. 9, images for different compounds are shown. In the images, not dispersed filler is appearing dark because the light is scattered diffusely. All compounds show a good dispersion of around 90%. Only the compound with 55 phr NR mixed with the batch mixing technique N55S45Batch has a very bad dispersion. In this mixture, 50 phr CB need to be premixed in only 55 phr NR. This is equivalent to a compound with 91 phr CB. Therefore, the carbon black could not be incorporated well. Also, in the second mixing step after addition of the SBR no good dispersion could be achieved.

### 5 Fracture mechanical properties

#### 5.1 Evaluation of tearing energy and crack propagation rates

The energy  $dS$  needed to increase crack surfaces cannot exceed the release of elastic energy  $-dW$  (Griffith criteria) [44]. The elastic energy release rate  $T = -dW/dS$  is called tearing energy. The tearing energy regulates the crack propagation under fixed conditions. Using the tear fatigue analyzer, the tearing energy is adjusted by the strain preset (and slightly by the initial crack length). The crack propagation rate per cycle  $dc/dn$  in dependence of  $T$  is characterized by the power law from Paris and Erdogan [45,46]:

$$\frac{dc}{dn} = AT^B \quad (10)$$

The Paris–Erdogan law is applied to the tear fatigue measurements. Therefore, the crack contour length  $c_{contour}$  is evaluated in a region of stable crack growth. The crack contour length is in contrast to the crack depth  $x$  directly related to the crack surface and therefore to the tearing energy. For some samples, a second stable region is evaluated. The crack growth rate  $dc/dn$  is obtained as the slope in the stable regions. The tearing energy of a single-edge notched (SEN) strip sample is given by [17]:

$$T = \frac{2\pi}{\sqrt{\langle\lambda\rangle}} \langle w_{el} \rangle \langle c \rangle \quad (11)$$

where  $\langle\lambda\rangle$  is the average elongation and  $\langle w_{el} \rangle$  is the average elastic energy density. Equation (11) is no exact formula. FEM simulations [47] show that the linear dependency on crack length is valid only for crack depths smaller than 20% of the sample width. However, the error for crack lengths substantially longer is small. Lorenz et al. [17] showed that Eq. (11) can be used to describe  $c(n)$  even up to crack depths of 40% of the

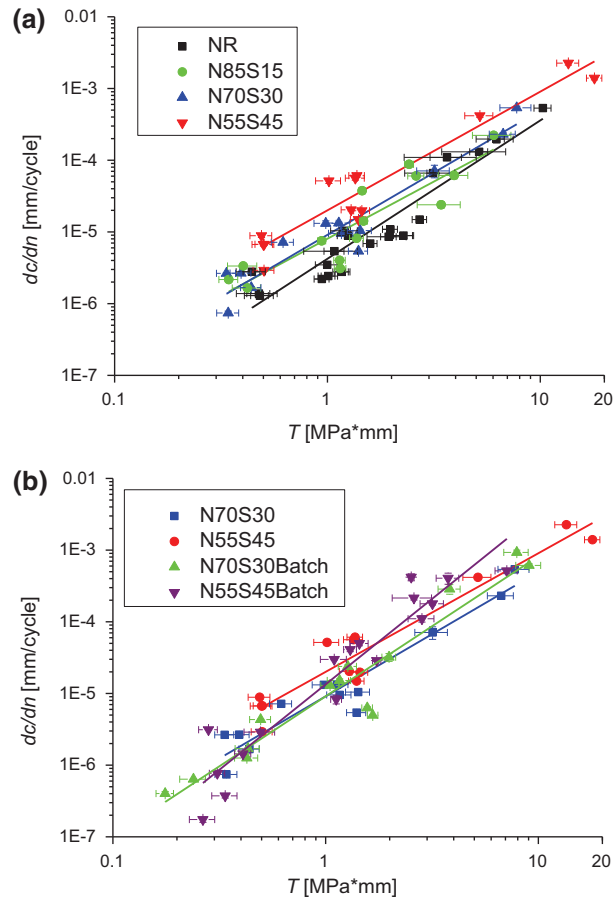


**Fig. 10** Crack propagation per cycle  $dc/dn$  versus tearing energy  $T$  for **a** NR/SBR blends (standard mixing procedure) and **b** NR/SBR blends (standard vs. batch mixing procedure)

sample width provided the crack remains perpendicular to the stretching direction and does not turn.  $T$  is calculated with the elastic density relating to the cross-sectional area,  $w_{el,Rest}$ .

Because filled rubbers show strong nonlinear behavior and hysteresis, energy is not only dissipated at the process zone at the crack tip but also far away from the crack tip. In fact, the crack growth does not depend on the global tearing energy  $T$  but on the energy available at the process zone. This energy can be evaluated using the concept of  $J$ -integral. By the  $J$ -integral

$$J = \int_{\Gamma} (W * \vec{n} - \vec{\sigma} * \vec{n} * \nabla \vec{u}) \quad (12)$$

the energy flow into a small volume around the crack tip can be accessed. Here,  $\Gamma$  is a path surrounding that volume,  $\vec{n}$  is the normal vector of that path,  $W$  is the energy density,  $\vec{\sigma}$  is the stress tensor and  $\nabla \vec{u}$  is the displacement gradient. An investigation dealing with the analytic determination of the  $J$ -integral based on an advanced material model was recently proposed [48]. Here, we will use Eq. (11) for the evaluation of the tearing energy.

## 5.2 Crack propagation under pulsed loading

Figure 10a shows the fracture mechanical properties of the NR/SBR blends prepared by normal mixing. The crack propagation of NR/SBR blends increases slightly, but in clear order, with increasing SBR content. The crack growth rate at fixed tearing energy increases almost linearly with the SBR content. The compounds N70S30 and N70S30Batch, with 70 phr NR and 30 phr SBR, show a similar crack growth behavior with a

slightly worse crack growth resistance of the batch at high tearing energies (Fig. 10b). This is possibly related to the higher filler loading of the interphase accompanied by the lower filling of the SBR phase (compare Figs. 7, 8). However, the differences of the two compounds in the NR loading as well as in the crack growth results are within the error range of the measurements. The differences in the carbon black distribution of the compounds N55S45 and N55S45Batch, with 55 phr NR and 45 phr SBR, are as expected. In the batch compound, in which all filler is mixed with the NR first, more filler is found in the NR phase and in the interphase and less filler is detected in the SBR. As shown in Fig. 9, the compound N55S45Batch has a very bad dispersion. The bad dispersion is expected to be responsible for the higher slope in the Paris–Erdogan plot, and the influence of dispersion is covering possible effects due to the difference in filler distribution.

## 6 Conclusions

The carbon black distribution into the different phases and interphases of NR/SBR blends has been analyzed by referring to a viscoelastic model of energy dissipation in the glass transition process. Throughout the entire study, the SBR shows a higher carbon black affinity than the NR. The filler amount calculated lies midway in the literature data and quite close to data for similar compounds [9–14]. But in contrast to other techniques also statements about the interphase are possible. A high interphase filling for all compounds is found. By the batch mixing procedure of the NR/SBR blend a higher interphase filling and a lower SBR filling is obtained. Crack propagation rates increase slightly with increasing SBR content. The effect of batch mixing procedure on filler distribution was analyzed delivering a higher filling of the interphase and lower filling of the SBR phase. The crack propagation rates are slightly increased for the batched sample with 70% NR and 30% SBR (N70S30Batch). The crack propagation of the N55S45Batch sample, with 55% NR and 45% SBR prepared by batch mixing, is worse at high tearing energies which probably results from the bad carbon black dispersion.

**Acknowledgements** We thank the Deutsche Forschungsgemeinschaft (DFG) for financial support (Grant No. KL1409/9-1) and our project partners IPF Dresden and Continental AG for the very fruitful cooperation.

## References

1. Kim, H.J., Hamed, G.R.: On the reason that passenger tire sidewalls are based on blends of natural rubber and *cis*-polybutadiene. *Rubber Chem. Technol.* **73**, 743 (2000)
2. Hamed, G.R., Kim, H.J., Gent, A.N.: Cut growth in vulcanizates of natural rubber, *cis*-polybutadiene, and a 50/50 blend during single and repeated extension. *Rubber Chem. Technol.* **69**, 807 (1996)
3. Takino, H., Nakayama, R., Yamada, Y.: Viscoelastic properties of elastomers and tire wet skid resistance. *Rubber Chem. Technol.* **70**, 584 (1997)
4. Clapson, B.E., Lake, G.J.: Truck tire groove cracking theory and practice. *Rubber J.* **152**, 36 (1970)
5. Mangaraj, D.: Elastomer blends. *Rubber Chem. Technol.* **75**, 365 (2002)
6. Hess, W.M., Herd, C.R., Vegvari, P.C.: Characterization of immiscible elastomer blends. *Rubber Chem. Technol.* **66**, 329 (1993)
7. Gent, A.N.: *Engineering with rubber*. Hanser, Munich (2001)
8. Meier, J.G., Klüppel, M., Geisler, H., Schuster, R.H.: Kieselsäuregefüllte Elastomerblends durch Masterbatchtechnologie. *Kautsch. Gummi Kunstst.* **58**, 587 (2005)
9. Le, H.H., Ilisch, S., Kasaliwal, G.R., Radusch, H.-J.: Thermogravimetrischer Analyse an Kautschuk-Füllstoff-Gel: Bestimmung der phasenspezifischen Füllstoffverteilung in Kautschukblends. *Kautsch. Gummi Kunstst.* **60**, 241 (2007)
10. Cotten, G.R., Murphy, L.J.: Mixing of carbon black with rubber. VI. Analysis of NR/SBR blends. *Rubber Chem. Technol.* **61**, 609 (1988)
11. Hess, W.M., Scott, C.E., Callan, J.E.: Carbon black distribution in elastomer blends. *Rubber Chem. Technol.* **40**, 371 (1967)
12. Ayala, J.A., Hess, W.M., Kistler, F.D., Joyce, G.A.: Carbon-black–elastomer interaction. *Rubber Chem. Technol.* **64**, 19 (1991)
13. Schuster, R.H., Issel, H.M., Peterseim, V.: Selective interactions in elastomers, a base for compatibility and polymer–filler interactions. *Rubber Chem. Technol.* **69**, 769 (1996)
14. Callan, J.E., Hess, W.M., Scott, C.E.: Elastomer blends. Compatibility and relative response to fillers. *Rubber Chem. Technol.* **44**, 814 (1971)
15. Klüppel, M., Schuster, R.H., Schaper, J.: Carbon black distribution in rubber blends: a dynamic-mechanical analysis. *Rubber Chem. Technol.* **72**, 91 (1999)
16. Schuster, R.H., Meier, J., Klüppel, M.: The role of interphase in filler partition in rubber blends. *Kautsch. Gummi Kunstst.* **53**, 663 (2000)
17. Lorenz, H., Steinhauser, D., Klüppel, M.: Morphology and micro-mechanics of filled elastomer blends: impact on dynamic crack propagation. *Lect. Notes Appl. Comput. Mech.* **70**, 81 (2013)
18. Wunde, M., Klüppel, M.: Influence of phase morphology and filler distribution in NR/BR and NR/SBR blends on fracture mechanical properties. *Rubber Chem. Technol.* **89**, 588 (2016)

19. Wunde, M., Klüppel, M.: Carbon black distribution in blends of natural rubber with polybutadiene rubber and styrene-butadiene rubber. In: Proceedings of the 14th International Seminar on Elastomers, Bratislava, Slovakia, Aug 24–28, p. 68. Librix.eu, Bratislava (2014)
20. Klüppel, M., Schuster, R.H., Schaper, J.: Dynamischer Glasübergang in füllstoffverstärkten Kautschukblends. *GAK Gummi Fasern Kunststoffe* **51**, 508 (1998)
21. Meier, J.F., Klüppel, M., Schuster, R.H.: Steuerung der physikalischen Eigenschaften von Elastomeren. *Kautsch. Gummi Kunstst.* **58**, 82 (2005)
22. Ziegler, J., Schuster, R.H.: Dynamisch-mechanische Eigenschaften und Verteilung von Kieselsäure in NBR/BR-Verschnitten. *Kautsch. Gummi Kunstst.* **56**, 159 (2003)
23. Huneau, B., Masquelier, L., Marco, Y., Le Saux, V., Noizet, S., Schiel, C., Charrier, P.: Fatigue crack initiation in a carbon black-filled natural rubber. *Rubber Chem. Technol.* **89**, 126 (2016)
24. Ludwig, M., Alshuth, T., El Yaagoubi, M., Juhre, D.: Lifetime prediction of elastomers based on statistical occurrence of material defects. In: Marvalová, B., Petříková, I. (eds.) *Constitutive Models for Rubber IX*, pp. 445–448. Taylor & Francis, London (2015)
25. Rivlin, R.S., Thomas, A.G.: Rupture of rubber. I. Characteristic energy for tearing. *J. Polym. Sci.* **10**, 291 (1953)
26. Persson, B.N.J., Ahlbor, O., Heinrich, G., Ueba, H.: Crack propagation in rubber-like materials. *J. Phys. Cond. Matter.* **17**, R1071 (2005)
27. Persson, B.N.J., Brener, E.A.: Crack propagation in viscoelastic solids. *Phys. Rev. E* **71**, 036123 (2005)
28. Klüppel, M.: Evaluation of viscoelastic master curves of filled elastomers and applications to fracture mechanics. *J. Phys. Cond. Matter* **21**, 035104 (2009). (10pp)
29. Reinke, K., Grellmann, W., Klüppel, M.: Investigation of fracture mechanical properties of filler-reinforced styrene-butadiene elastomers. *Kautsch. Gummi Kunstst.* **62**, 246 (2009)
30. Payne, A.R.: The dynamic properties of carbon black-loaded natural rubber vulcanizates. Part I. *Rubber Chem. Technol.* **36**, 432 (1963)
31. Ferry, J.D.: *Viscoelastic Properties of Polymers*, 3rd edn. Wiley, New York (1980)
32. Stoczek, R., Kipscholl, R., Euchler, E., Heinrich, G.: Study of the relationship between fatigue crack growth and dynamic chip & cut behaviour of reinforced rubber materials. *Kautsch. Gummi Kunstst.* **4**, 26 (2014)
33. Stoczek, R., Ghosh, P., Mukhopadhyay, R., Kipscholl, R., Heinrich, G.: Fracture behaviour of rubber-like materials under classical fatigue crack growth vs. chip & cut analysis. In: Gil-Negrete, N., Alonso, A. (eds.) *Constitutive Models for Rubber VIII*, pp. 323–328. Taylor & Francis, London (2013)
34. Eisele, U., Kelbch, S.A., Engels, H.-W.: The tear analyzer—a new tool for quantitative measurements of the dynamic crack growth of elastomers. *Kautsch. Gummi Kunstst.* **1992**, 45 (1064)
35. Stoczek, R., Heinrich, G., Gehde, M., Kipscholl, R.: Analysis of dynamic crack propagation in elastomers by simultaneous tensile- and pure-shear-mode testing. *Lect. Notes Appl. Comput. Mech.* **70**, 269 (2013)
36. Beatty, J.R., Miksch, B.J.: A laboratory cutting and chipping tester for evaluating off-the-road and heavy-duty tire treads. *Rubber Chem. Technol.* **55**, 1531 (1982)
37. Medalia, A.I.: Microscopic estimation of carbon black dispersion. *Rubber Age* **97**, 82 (1965)
38. Medalia, A.I.: Dispersion of carbon black in rubber: revised calculation procedure. *Rubber Chem. Technol.* **34**, 1134 (1961)
39. Vilgis, T.A., Heinrich, G., Klüppel, M.: Hydrodynamic reinforcement of elastomers. *Reinforcement of Polymer Nano-Composites*, Chapter 8
40. Klüppel, M.: The role of disorder in filler reinforcement of elastomers on various length scales. *Adv. Polym. Sci.* **164**, 1–86 (2003)
41. Bunde, A., Havlin, S. (eds.): *Fractals and Disordered Systems*, 2nd edn. Springer, Berlin (1996)
42. Kantor, Y., Webman, I.: Elastic properties of random percolating systems. *Phys. Rev. Lett.* **52**(21), 1891 (1984)
43. Lin, C.-R., Lee, Y.-D.: Strain-dependent dynamic properties of filled rubber network systems. *Macromol. Theory Simul.* **5**, 1075–1104 (1996)
44. Griffith, A.A.: The phenomena of rupture and flow in solids. *Philos. Trans. R. Soc. Lond. A* **221**, 163 (1921)
45. Paris, P.C., Gomez, M.P., Anderson, W.E.: A rational analytic theory of failure. *Trend Eng.* **13**, 9 (1961)
46. Paris, P., Erdogan, F.: A critical analysis of crack propagation laws. *J. Basic Eng.* **85**, 528 (1963)
47. Timbrell, C., Wiehahn, M., Cook, G., Muhr, A.H.: Simulation of crack propagation in rubber. In: Busfield, J.J.C., Muhr, A.H. (eds.) *Constitutive Models for Rubber III*, pp. 11–20. Swets Zeitlinger, Lisse (2003)
48. Wunde, M., Plagge, J., Klüppel, M.: Tearing energy in filler reinforced elastomers for tire treads. In: Proceedings, 12th Rubber Fall Colloquium, Hannover, Germany, Nov 22–24 (2016)

# Effect of filler and blending with SBR and NR on thermally induced crystallization of high-cis BR as evaluated by dynamic mechanical analysis

M. Wunde, M. Klüppel\*

Deutsches Institut für Kautschuktechnologie e. V., Eupener Straße 33, 30519 Hannover, Germany

Received 8 May 2019; accepted in revised form 2 September 2019

**Abstract.** The effect of thermally induced crystallization of high-cis polybutadiene (BR) on dynamic mechanical spectra is analyzed under different heating and cooling conditions. It is studied how the addition of carbon black and the blending with styrene-butadiene rubber (SBR) and natural rubber (NR) is affecting the crystallization. For unfilled BR an increased heating rate after fast cooling delivers less crystallization demonstrating that crystal formation requires time. With rising carbon black (CB) loading, a pronounced increase of crystallization speed is found indicating that CB supports nucleation and growth of BR crystals. In BR/SBR blends, which are detected as a single phase in dynamic mechanical spectra, crystallization is reduced for low SBR amounts and seems to disappear totally for 50/50 blends. In blends of BR, SBR, and NR the filler distribution is determined by comparing the peak heights in the loss modulus  $G''$  of unfilled and filled compounds. The filler located in each phase is determined from the increase of the peak height corresponding to the respective phase. It is found that the filler is mainly located in the NR phase.

**Keywords:** rubber, dynamic mechanical analysis, thermal crystallization, high-cis polybutadiene, elastomer blends

## 1. Introduction

Thermally induced crystallization denotes the property of some polymers to crystallize in contrast to strain-induced crystallization without the need for straining. Some elastomers as polybutadiene (BR), natural rubber (NR), polyisoprene or polychloroprene, with regular composition show thermally induced crystallization [1]. This kind of crystallization is usually occurring at low temperatures but above the glass transition temperature  $T_g$ . The crystallization speed can be expressed via the half-life  $t_{1/2}$ , the time, half of the crystallizable material needs to crystallize. The half-life strongly depends on the amount of regularly ordered monomers. For BR this is the cis-1,4 content. BR with 97% cis-1,4 content crystallizes more than 10 times faster than BR with 90% cis-1,4 [2]. Crystallization rates are depending on

crosslinking as the crosslinks are hindering the diffusion of individual chain segments [1, 2]. The crystallization half-life depends strongly on temperature. It is infinite for the glass transition temperature and the equilibrium melting temperature. The equilibrium melting temperature is the temperature at which an infinitely large solid and liquid have the same free energy. At higher temperatures, the free energy of the crystal is higher so that crystallization is not occurring. In between these temperatures, the logarithm of the half-life shows a parabolic dependence on temperature [1]. For BR the temperature of maximal crystallization rate  $T_{\text{cryst}}$  is between  $-55$  and  $-56^\circ\text{C}$  and does practically not depend on the microstructure [3]. For crosslinked BR between  $-70$  and  $-40^\circ\text{C}$  a half-life around or smaller than 100 s is reported [1]. In this temperature interval, the time

\*Corresponding author, e-mail: [Manfred.Klueppel@DIKautschuk.de](mailto:Manfred.Klueppel@DIKautschuk.de)  
© BME-PT

scale of crystallization is in the order of dynamic mechanical measurements. Melting of the crystallites depends on the crystallization temperature and occurs a few dozen degrees above the temperature the crystallites are formed [4]. This means that in dynamic mechanical measurements during heating crystallites start to form. At higher temperatures the formation of more stable crystallites and the melting of existing crystals occur simultaneously until finally all crystals are melted. The temperature process-dependent kinetics and the caloric behavior of crystallizable polymers can be simulated by a recently developed thermodynamic model [5]. This model shows that increasing the cooling or heating rate of measurement reduces the maximum level of crystallization.

Crystallization of elastomers can be observed e.g. by X-ray diffraction, calorimetry and stress relaxation. Methods for crystalline studies are reviewed in [3]. BR crystallization is decreased by carbon black loading or by blending with SBR [6]. The larger the difference in  $\delta$ -parameter in blends of BR with non-polar rubbers, the higher is the decrease of BR crystallization [7], leading to a smaller decrease of BR crystallization in a blend with SBR compared with the decrease in crystallization in a blend with NR [8]. The crystallization rate of NR is about three orders of magnitude smaller than for BR and therefore, for crosslinked NR, beyond our measuring times [1]. The increase of the storage and loss modulus in a temperature range where the crystallization speed is sufficiently fast can be seen as an effect of crystallization. Crystallization, also the partial crystallization found in the BR, increases the storage modulus as the material is more difficult to strain. This increase in storage modulus is decreasing when the crystallites melt. At least for small deformations, the decrease of storage modulus due to the melting is directly related to a peak in the loss modulus through the Kramers-Kronig relations.

The filler distribution can be evaluated by comparing the dynamic mechanical spectra of unfilled and filled immiscible elastomer blends [9–14]. The main idea is that filler increases the loss modulus peak of the respective polymer phase and so the filler distribution can be calculated from the increase of the different glass transition peaks. The height of the loss modulus peaks can thereby be influenced if one of the polymers is crystallizing during measurement. This is the case for blends with high-cis BR. High-cis BR is

blended in tire tread compounds, especially to improve the rolling resistance of the tire.

This study is a supplement to previous works [13, 14] on the blend morphology and its influence on fracture mechanics within the collaboration in a fracture mechanical project. It has been found that the calculated filler distribution in NR/BR blends is affected by the crystallization of the BR [13]. The main idea for this study is to understand and possibly to subtract this effect. Therefore especially dynamic mechanical measurements have been done. A few differential scanning calorimetry measurements giving direct information on crystallization have been added. X-ray diffracting as the standard method to investigate crystallization behavior is usually involving large synchrotron radiation facilities. Additionally, the filler distribution of triple blends is shown.

## 2. Experimental

### 2.1. Materials

The samples contain a high-cis butadiene rubber (Buna CB 24, Arlanxeo, Dormagen (Germany),  $T_g \approx -109^\circ\text{C}$ ) with min. 96% cis-1,4 content. Some compounds are blends with styrene-butadiene rubber (Buna VSL 4526, Arlanxeo, Port Jérôme (France),  $T_g \approx -22^\circ\text{C}$ ) and some of the blends also contain natural rubber (SVR CV 60, Vietnam,  $T_g \approx -60^\circ\text{C}$ ). The compounds are unfilled or filled with up to 50 phr carbon black N339 (Corax, Orion Engineered Carbons, Cologne (Germany)). The SBR is a solution styrene-butadiene rubber with 45 wt% vinyl and 26 wt% styrene groups. The samples are cross-linked semi-efficiently by sulfur together with the vulcanization accelerator *N*-cyclohexyl-2-benzothiazole sulfonamide (CBS (Vulkacit CZ, Lanxess)). The samples were compounded with the processing and vulcanization additives stearic acid and ZnO (Rotsiegel, Grillo, Goslar (Germany)) and protected against aging by *N*-isopropyl-*N*-phenyl-*P*-phenylenediamine (IPPD (Vulkanox 4010, Lanxess)). The full recipes are shown in Table 1.

### 2.2. Sample preparation

The unfilled composites are mixed in a laboratory Haake mixer at 50 rpm for 10 minutes, the filled compound for 20 minutes. After 5 minutes mastication of the polymers, the other ingredients are added. Leveling of the torque after mastication and after mixing indicates homogeneous mixtures. In mixtures with a



**Table 1.** Recipes of the compounds.

Samples	BR	SBR	NR	CB	CBS	Sulfur	IPPD	ZnO	Stearic acid
BR_0	100	–	–	–	2,5	1,7	1,5	3	1
BR_15	100	–	–	15	2,5	1,7	1,5	3	1
BR_30	100	–	–	30	2,5	1,7	1,5	3	1
BR_50	100	–	–	50	2,5	1,7	1,5	3	1
B90S10_0	90	10	–	–	2,5	1,7	1,5	3	1
B90S10_30	90	10	–	30	2,5	1,7	1,5	3	1
B90S10_50	90	10	–	50	2,5	1,7	1,5	3	1
B50S50_0	50	50	–	–	2,5	1,7	1,5	3	1
B50S50_30	50	50	–	30	2,5	1,7	1,5	3	1
B50S50_50	50	50	–	50	2,5	1,7	1,5	3	1
N55B23S23_0	22.5	22.5	55	–	2,5	1,7	1,5	3	1
N55B23S23_50	22.5	22.5	55	50	2,5	1,7	1,5	3	1
N70B15S15_0	15	15	70	–	2,5	1,7	1,5	3	1
N70B15S15_50	15	15	70	50	2,5	1,7	1,5	3	1

higher amount of carbon black the rotor speed is lowered to keep the temperature below 120 °C. The curing system is added at 80% of the mixing time. Afterward, the compounds are handled on a roller mill. Vulcanization is performed at 150 °C in a heat press up to 90% of the vulcameter torque maximum ( $t_{90}$  time).

### 2.3. Dynamic mechanical analysis (DMA)

The dynamic-mechanical measurements are carried out in the torsion-rectangular mode with a strip specimen of 2 mm thickness on the dynamic analyzer ARES (Rheometric). This means that torsion is applied to a rectangular specimen. The width of the sample is 10 mm and the distance between the two clamps is around 30 mm. The dynamic moduli are measured over a wide temperature range (–115C to +20 °C) at a frequency of 1 Hz and 0.5% strain amplitude. All samples besides the unfilled BR are only measured

with the standard measurement procedure. In this procedure the sample is first quickly cooled to –115 °C (cooling rate ~10 °C/minute) and then measured while heating. In the heating process, the chamber temperature is increased successively by 1 °C. When this temperature is reached in the chamber it is kept for 45 s before storage and loss moduli are measured. This enables the sample to roughly adopt the temperature of the chamber. This procedure corresponds to a heating rate of around 1 °C/minute.

The unfilled BR is also measured with the cooling procedure. In this case, the chamber temperature is decreased successively by 1°, again with 45 s waiting time. In another measurement procedure, the chamber temperature is decreased and increased continuously with a cooling rate of 5 °C/minute and varying heating rates of 1, 2 and 5 °C/minute. The schematic temperature profiles in the chamber are shown in Figure 1.

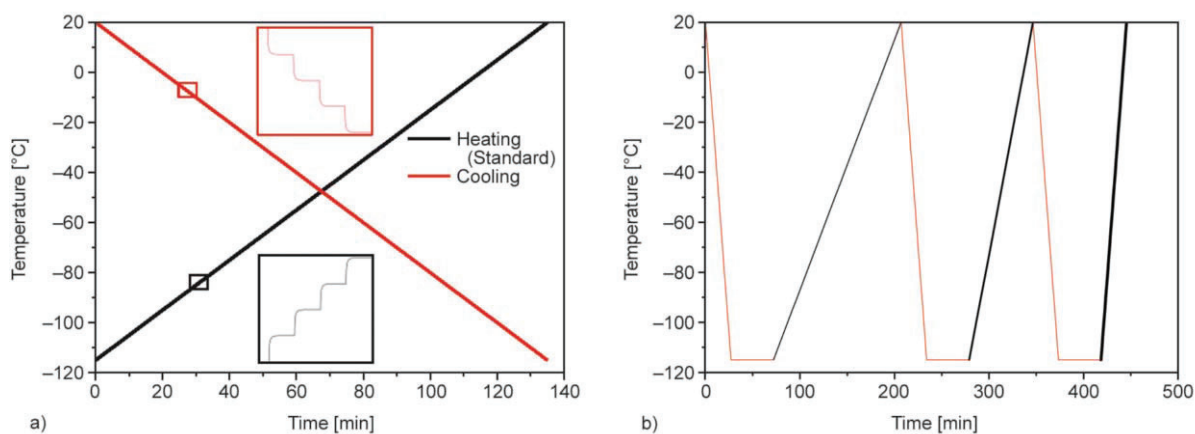


**Figure 1.** DMA-measurement procedures (schematic): Heating (Standard) and cooling measurement (a) and temperature ramp measurement (b).

## 2.4. Differential scanning calorimetry (DSC)

The differential scanning calorimetry measurements were performed with a heat flux DSC 2920CE (TA-Instruments) at a constant heating rate of 10 °C/min and sample weights of approximately 10 mg. The sample in a pan and an empty pan are quickly cooled by liquid nitrogen down to –150 °C. During the following heating up to 100 °C, the heat fluxes between both pans and the machine are measured and subtracted to get the heat flow of the sample only.

## 3. Results and discussion

### 3.1. Unfilled BR

The effect of crystallization on the dynamic mechanical spectrum can be seen by comparing the measurement while heating after quick cooling (standard measurement procedure) with the same measurement while cooling the sample (Figure 2a). During the cooling the effect of crystallization can be seen in an increase of the storage modulus  $G'$  and the loss modulus  $G''$  below –40 °C. During the heating, the crystallization appears as broad peaks in the storage and loss modulus between –80 and –20 °C. The local maximum of  $G'$  is found close to the temperature of maximal crystallization rate  $T_{\text{cryst}} \approx -55$  °C. For the heating (standard) measurement, representing crystallization at lower temperatures, smaller crystallites are expected than during cooling. Furthermore, recrystallization processes take place and lead to an increase in crystal size [15]. The non-equilibrium at measurement can be seen by a small shift of the glass transition temperature given by the maximum of the loss modulus.

The effect of measurement duration can be seen in Figure 2b. This measurement was done with uniformly changing chamber temperatures at different rates of heating (temperature profile shown in Figure 1b). The heating rate depending shift of the glass transition can be seen at the global maximum of  $G''(T)$  around –100 °C. The crystallization can be observed in a second local maximum around the temperature of maximal crystallization  $T_{\text{cryst}}$  of the BR. Due to the lower measuring times at the particular temperature interval, the crystallization observed as an increase of the moduli is decreasing with the heating rate. The form of the crystallization peak of  $G'$  might also give a hint whether the maximal crystallization speed is completed or not. In a ‘round’ peak (as in the 5 °C/min curve) the most rapid crystallization is not completed when the increasing temperature starts to melt the crystallites. When in the slower measurements the most rapid crystallization has occurred, kind of plateaus with slightly decreasing values are formed. In this temperature range only some crystallization occurs but melting does not have started to a significant degree yet. The decrease of crystallization with increasing heating rate agrees with the expectations from thermodynamic considerations [5].

The crystallization behavior at the temperature of maximal crystallization rate  $T_{\text{cryst}}$  seen in the dynamic mechanical analysis is displayed in Figure 3. In this measurement the sample is heated with a temperature ramp of 5 °C/minute from –90 °C to  $T_{\text{cryst}} \approx -55.5$  °C. At this temperature, the sample is kept for 10 000 s. In the heating period, the moduli are

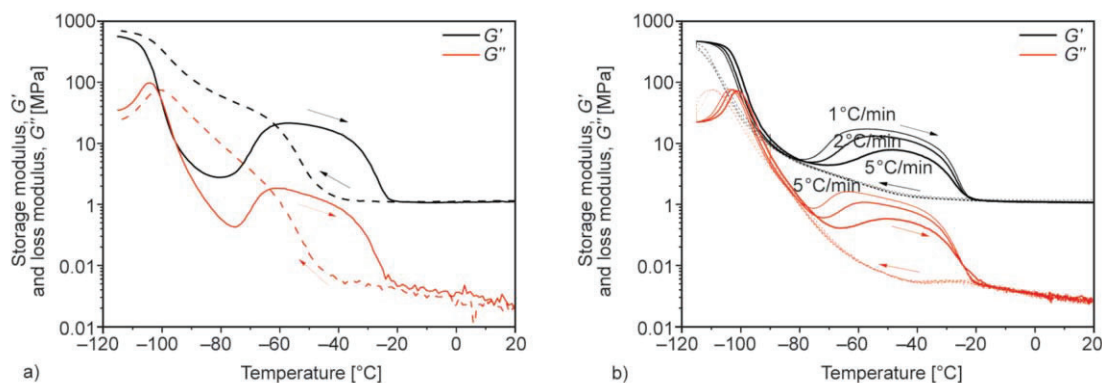


**Figure 2.** DMA-measurements of unfilled BR: Heating and cooling measurement where the heating is given as full lines and the cooling as dashed lines (a). Heating and cooling are stepwise according to Figure 1a with a heating rate of around 1 °C/min, for the heating measurement the sample was cooled down quickly before (cooling rate  $\sim 10$  °C/min). Temperature ramp measurement according to Figure 1b measuring different heating rates of 1, 2 and 5 °C/min as indicated (b). The cooling is performed at a rate of 5 °C/min.

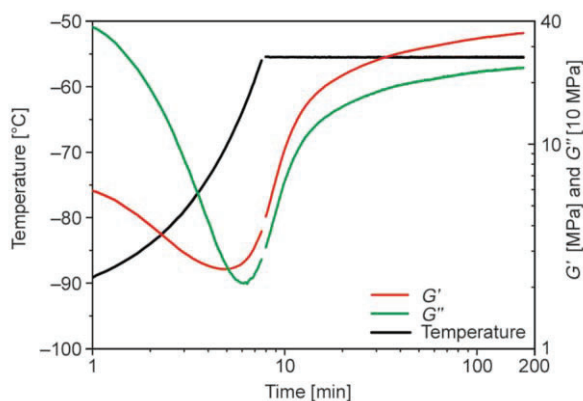


**Figure 3.** DMA-measurements of unfilled BR: Moduli measured during a temperature ramp of 5 °C/min from –90 °C to the temperature of maximal crystallization rate  $T_{\text{cryst}} \approx -55.5$  °C and keeping this temperature for 10 000 s. Previously the compound was cooled quickly to –90 °C.

primarily decreasing as the compound is departing from the glass transition. Closer to  $T_{\text{cryst}}$  the moduli are increasing as the effect of crystallization dominates. The increase of the modulus is the strongest in the first minutes after reaching  $T_{\text{cryst}}$ . Afterward, the moduli are leveling out when the crystallization is nearly completed. It should be noted that in the first minutes of the measurement the sample temperature is not given by the chamber temperature and that no direct statements about the crystallization kinetics are possible from the increase of the moduli. Nevertheless, the time period until which most crystallization has appeared and which increase of the moduli this crystallization generates can be estimated.

### 3.2. Filled BR

The effect of carbon black on the crystallization seen in the dynamic mechanical spectra is shown in Figure 4. Again, fast cooling down to –115 °C was

applied followed by heating according to Figure 1a. At moderate filler loading (15 phr) the crystallization peak in storage and loss modulus is enhanced by a factor of nearly two. This is more than expected by hydrodynamic amplification of the filler and indicates that a higher amount of crystallization is reached during the measurement. At higher filler loading the moduli at  $T_{\text{cryst}} \approx -55$  °C reach values that seem to be nearly independent of filler loading. The moduli at this temperature are 5 or 6 times higher than those of the unfilled compound. This suggests that for 30 phr an even higher degree of crystallinity is reached, that is not further increased by higher filler loadings. The reason for this could be that in these compounds the most pronounced increase of the moduli due to crystallization has already occurred at lower temperatures. For unfilled BR at  $T_{\text{cryst}}$  the most pronounced increase happens within 20 minutes (see Figure 3), for the filled compounds it seems to be less. For the higher filler loadings also a pronounced increase of the modulus in the intermediate temperature range between glass transition and crystallization is seen. This indicates that the crystallization speed due to the presence of the filler increases substantially so that the crystallization already at temperatures of around –90 °C is sufficiently fast to yield the strongly increased moduli compared to the lower filled and unfilled sample. The crystallization is so fast that the moduli of the BR are not decreasing to ordinary values of rubbers above their glass transition ( $G'$  of a few MPa) before crystallization sets in. Instead for a long temperature interval intermediate values of  $G'$  around 100 MPa are measured until the crystallites melt significantly. In all cases, crystallization plateaus are formed indicating that a higher portion of final crystallization degree is reached. These results seem

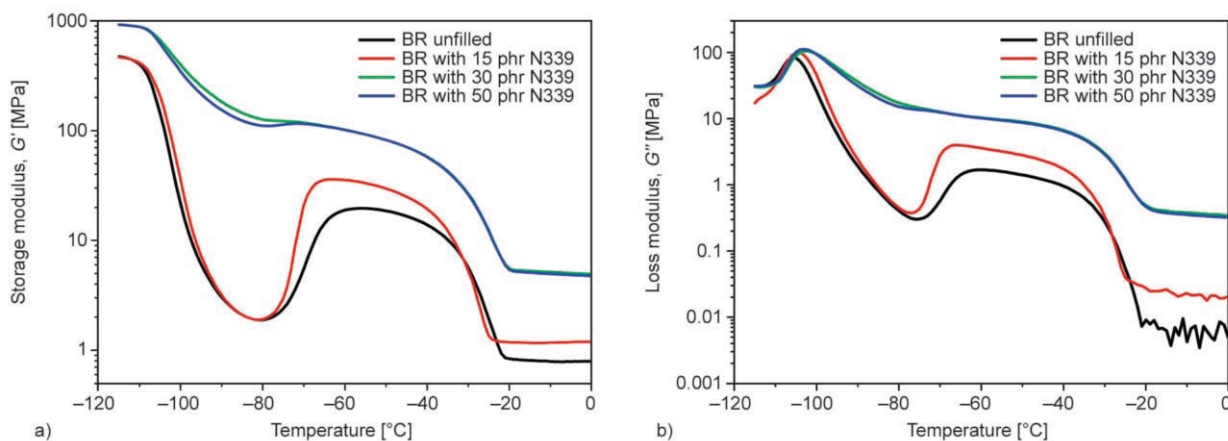


**Figure 4.** DMA-measurements of BR filled with different amount of carbon black: Storage modulus (a) and loss modulus (b).

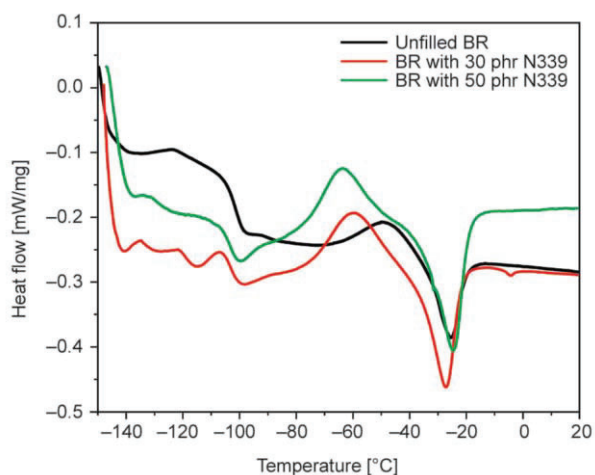


**Figure 5.** Heat flows measured by DSC of unfilled BR and filled BR with 30 and 50 phr carbon black.

to contradict previous findings where the carbon black content decreases BR crystallization [5]. The main reason for that discrepancy is that from the analysis of the moduli the crystallization speed can be compared, not the level of final crystallization. A possible explanation of the increased moduli in filled BR could be synergetic reinforcement of filler and crystallites that lead to higher moduli, although less crystallization could be present compared to the unfilled BR. Another possibility could be increased nucleation due to the presence of carbon black.

Figure 5 shows DSC measurements of the unfilled and filled BR compounds. The glass transition can be seen as a step-like decrease of heat flow for all samples at around  $-100\text{ }^{\circ}\text{C}$ . The unfilled sample starts to crystallize at around  $-70\text{ }^{\circ}\text{C}$  and crystallization reaches a maximum at around  $-50\text{ }^{\circ}\text{C}$ , indicated by the flat peak of the heat flow. Contrary, the filled compounds are starting to crystallize directly after the glass transition and the maximum crystallization is reached earlier at around  $-65\text{ }^{\circ}\text{C}$ . All compounds are melting at around  $-25\text{ }^{\circ}\text{C}$ . These observations are in line with the DMA measurements and confirm the results and interpretations of Figure 4.

### 3.3. BR/SBR blends

Mixing entropy is very small for polymers because of the small number of molecules involved due to their high molecular weight. Therefore most polymer blends are not miscible. The miscibility of two polymers can be predicted by the comparison of their solubility parameters  $\delta$ . The  $\delta$ -parameter is defined as the square root of the energy of vaporization per volume and is related to the cohesion energy be-

tween identical monomers. Only for very small differences of  $\delta$ , it is expected that the two polymers form a common phase. In that case, only one glass transition in between both polymer glass transitions occurs. Already for small differences of the solubility parameter, the very low mixing entropy of long polymer chains is surmounted so that the phases separate. A very broad glass transition indicates micro phases with different content of the two polymers [16–18].

The miscibility of BR and SBR depends on the composition of the polymers. Cis 1,4-polybutadiene, as the polymer with the least voluminous side groups, has the lowest glass transition temperature and both, the addition of vinyl and styrene units is increasing the volume of side groups and therefore increasing  $T_g$ . But the solubility parameter which is connected to the vaporization energy is increasing linearly with the styrene content and decreasing linearly with the vinyl content [19]. The SBR used here has a high vinyl content of 45% which nearly counterbalances the decrease in  $\delta$  due to the styrene content of 26%. This makes the BR and the SBR used in this study at least partially miscible. The storage and loss moduli of the BR/SBR blends are shown in Figure 6. The glass transition is seen in a single broad peak in the loss modulus  $G''$  indicating a global mixture with locally varying polymer concentrations. Such a mixture we will call in the following a mixed phase. In a 50:50 blend the BR and the SBR form a mixed phase which can be seen as broad peak of the loss modulus in between the glass transition temperatures of the polymers but closer to the glass transition of the BR (Figure 6d) ( $T_g \sim -86\text{ }^{\circ}\text{C}$ ). Crystallization can be seen neither in the storage modulus (Figure 6c) nor in the loss modulus, even not for the filled compounds. Nevertheless, a low amount of crystallization which is not directly visible in DMA is possible. For a 90:10 blend the glass transition peak in the loss modulus shifts due to the higher amount of BR to lower temperatures close to  $-100\text{ }^{\circ}\text{C}$  (Figure 6b) ( $T_g \sim -102\text{ }^{\circ}\text{C}$ ). A crystallization peak is visible in storage modulus (Figure 6) and loss modulus. These peaks are increasing with filler volume fraction. The crystallization rate is clearly smaller compared to the pure BR. This can be seen in lower local maxima around  $T_{\text{cryst}}$  and in more curved shape of these peaks indicating that the most rapid crystallization is not finished. The results agree with the known hindrance of SBR on BR crystallization [6–8].

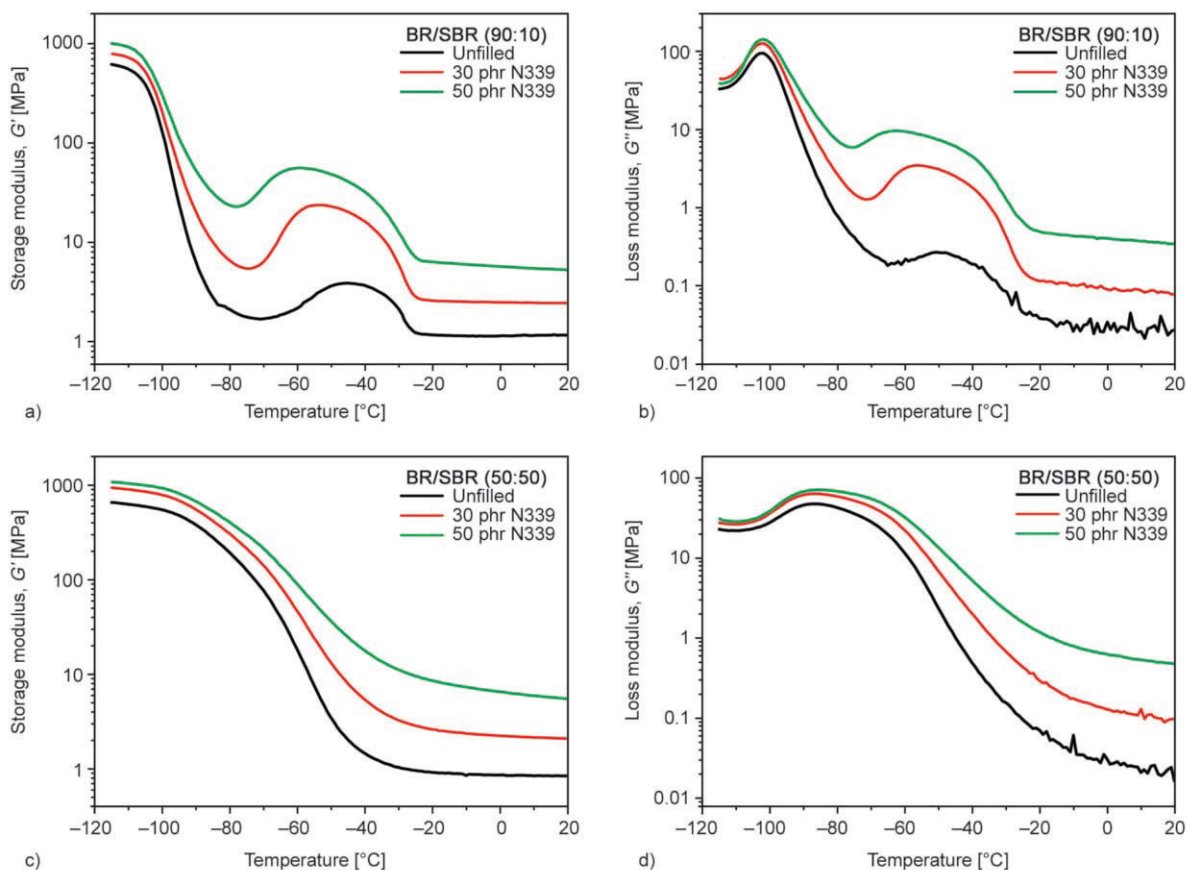


**Figure 6.** DMA-measurements of BR/SBR blends with different blend ratio and amount of carbon black: Storage modulus  $G'$  (a) and loss modulus  $G''$  (b) of (90:10) blend, storage modulus  $G'$  (c) and loss modulus  $G''$  (d) of (50:50) blend.

### 3.4. NR/BR/SBR blends

NR is miscible neither with the BR nor with the SBR. In the NR/BR/SBR blends two glass transitions can be observed (Figures 7 and 8): The glass transition of the NR is at around  $-60^{\circ}\text{C}$  and the glass transition of the BR/SBR mixed phase at lower temperatures. The loss modulus  $G''$  of the mixed BR/SBR phase, as discussed in the previous chapter, is

maximal between  $-80$  and  $-90^{\circ}\text{C}$  or around  $-100^{\circ}\text{C}$ , depending on the composition of the mixed BR/SBR phase (compare with Figure 6). A possible crystallization especially of the compounds with high BR content is not visible as the glass transition of the NR around  $-60^{\circ}\text{C}$  is hiding possible effects of BR crystallization occurring in a similar temperature range.

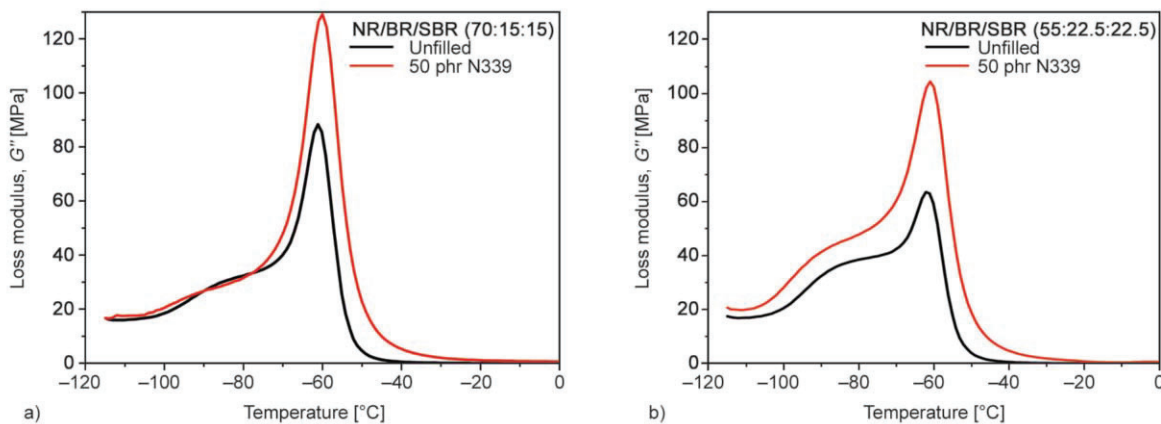


**Figure 7.** Loss modulus  $G''$  of NR/BR/SBR blends (equal amount of BR and SBR): Unfilled and filled blends with 70 phr NR (a) and with 55 phr NR (b).

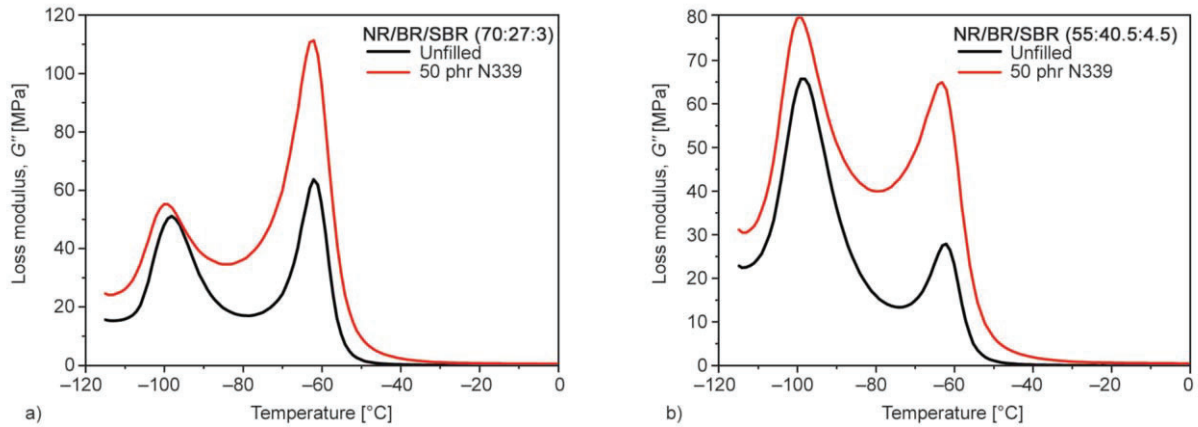


**Figure 8.** Loss modulus  $G''$  of NR/BR/SBR blends (very small amount of SBR): Unfilled and filled blends with 70 phr NR (a) and with 55 phr NR (b).

### 3.5. Filler distribution in NR/BR/SBR blends

The dissipated energy  $\Delta E$  of a harmonic strained rubber with amplitude  $\gamma_0$  is directly related to the loss modulus  $G''$  [9], as shown by Equation (1):

$$\Delta E = \pi G'' \gamma_0^2 \quad (1)$$

Due to the additivity of dissipated energy the dissipated energy in a polymer blend  $\Delta E_{\text{blend}}$  equals the sum of the dissipated energies  $\Delta E_i$  in the different polymer phases  $i$ . According to the different stiffness, the phases are strained with their specific amplitude  $\gamma_{0,i}$  see Equation (2):

$$\Delta E_{\text{blend}} = \sum_i \Delta E_i = \sum_i \pi \phi_i G''_{P,i} \gamma_{0,i}^2 \quad (2)$$

where,  $\phi_i$  and  $G''_{P,i}$  are the volume fraction and the loss modulus of the  $i$ -th phase, respectively. For the loss modulus of the blend see Equation (3):

$$G''_{\text{blend}} = \sum_i G''_{P,i} \phi_i \frac{\gamma_{0,i}^2}{\gamma_{0,i}^2} \quad (3)$$

We consider a polymer blend with different phases and sufficiently separated glass transition temperatures of the phases. In the temperature range just below the glass transition temperature of the higher  $T_g$  phase this phase is in a glassy state and exhibits a high stiffness while all other phases are soft. In ref. [9] the mechanical response of the glassy phase network was modeled as a percolation network: Below a critical concentration  $\phi_c$  the glassy polymer phase builds a hard dispersed phase with spatially separated domains within one or more soft continuous phases. In this case, the glassy polymer phase increases the stiffness of the composite only by hydrodynamic amplification. At the critical concentration  $\phi_c$  the separated glassy domains form a co-continuous phase

network which is dominating the elastic modulus at concentrations  $\phi_i > \phi_c$ . In a percolation network, only the singly connected links which are not building close loops are deformed under external strain. Therefore, the elastic modulus of the composite is strongly affected by the distribution of singly connected links. This also determines the deformation  $\gamma_{0,i}$  of the glassy phase which shows power-law behavior above the percolation threshold  $\phi_c$ . The expression  $\phi_i(\gamma_{0,i}^2/\gamma_0^2)$  in Equation (3) is the amplitude height of the polymer phase in an unfilled blend compared to the pure polymer and can be written as power-law increase with elasticity exponent  $\tau$  if only one phase is in the glassy state [9], as shown by Equation (4):

$$\phi_i \frac{\gamma_{0,i}^2}{\gamma_0^2} = \left( \frac{\phi_i - \phi_c}{1 - \phi_c} \right)^\tau \quad (4)$$

Lower values than the theoretical value of  $\tau \approx 3.6$  were found and explained by coalescence phenomena on small length scales [9].

Semi-empirically the term  $\phi_i(\gamma_{0,i}^2/\gamma_0^2)$  in Equation (3) can also be fitted by quadratic equations, so that the loss modulus of the blend  $G''_{\text{blend}}$  is given by Equation (5) [12]:

$$G''_{\text{blend}} = \sum_i G''_{P,i} (a_i + b_i \phi_i + c_i \phi_i^2) \quad (5)$$

The lower branch is adopted by the polymer with the higher glass transition temperature  $T_g$  and the higher branch by the polymer with the lower  $T_g$ . In Figure 9 these ratios are shown for the unfilled NR/BR/SBR blends. In this case, the NR is found on the lower branch and the BR/SBR mixed phase on the upper branch. For lower contents of BR and SBR in the blend the evaluation becomes difficult as the broad BR/SBR peak gets covered by the low-temperature

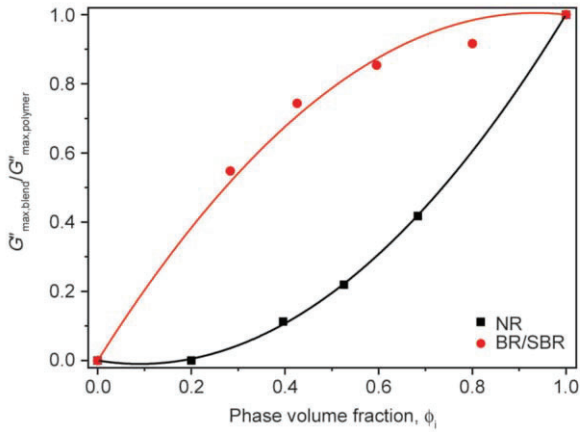


**Figure 9.** Amplitude height  $G''_{\max,\text{blend}}$  of a polymer phase in an unfilled blend compared to the amplitude height of the pure polymer  $G''_{\max,\text{polymer}}$  fitted by quadratic equations.

tail of the NR. The quadratic function for the NR phase of the NR/BR/SBR blends is quite close to the quadratic function found for the NR phase in NR/BR blends [13].

In this method, it is assumed that the loss modulus  $G''$  of the compound is the sum of the loss moduli of the different polymer phases. In fact, the complex modulus is formed in different ways that dependent on the blend morphology. There are quite different results obtained, e.g. when the phases are ordered in parallel or in series. For the case of spherical inclusions in a matrix, the Olroyd-Palierne model [20] or self-consistent models [21] can be used. For most blend ratios studied here, the different phases build separate continuous networks for which these models cannot be used.

Neglecting hydrodynamic effects of the filler particles the loss modulus of a filled polymer at the glass transition temperature  $G''(T_g)$  is expected to

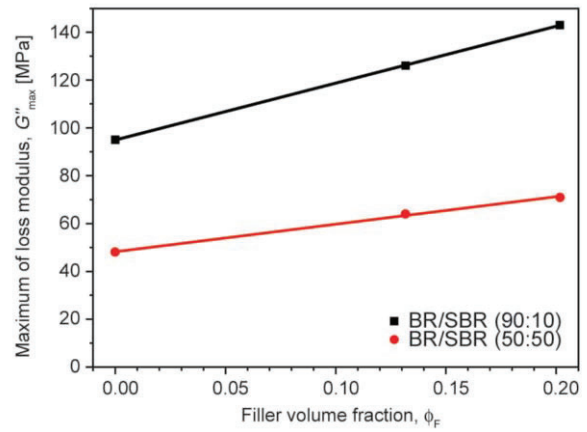


**Figure 10.** Linear increase of the maximum of loss modulus  $G''$  (glass transition of BR/SBR weights) with filler volume fraction.

be linearly increasing with filler volume fraction  $\phi_F$ , see Equation (6) [9]:

$$G''(T_g) = G''_0(T_g) + \alpha\phi_F \quad (6)$$

where,  $G''_0(T_g)$  is the loss modulus of the unfilled polymer at the glass transition temperature and  $\alpha$  is the slope of loss modulus with filler volume fraction. In fact, this linear behavior is found for a variety of polymer blends [9–12]. Linear increase with filler volume fraction was also already found for all three polymer compounds used here [13–14].

The maximum loss modulus  $G''(T_g)$  of the filled compounds can also be measured for the mixed BR/SBR phase. Also, the maximum of the mixed phase is increasing linearly with the filler volume fraction (Figure 10).

Combining the effect of the filler (Equation (4)) with the blend effect (Equation (3)) yields the formula for the loss modulus of the filled blend, see Equation (7) [12]:

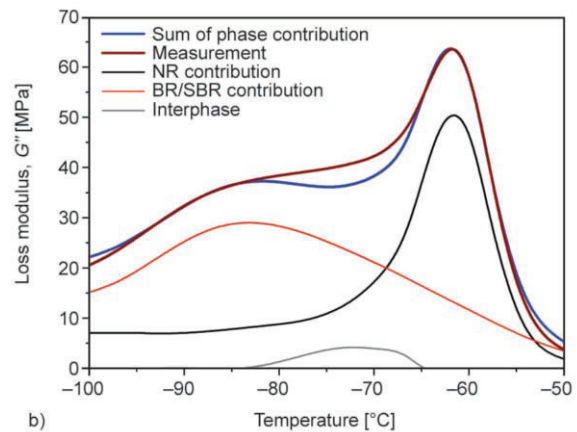
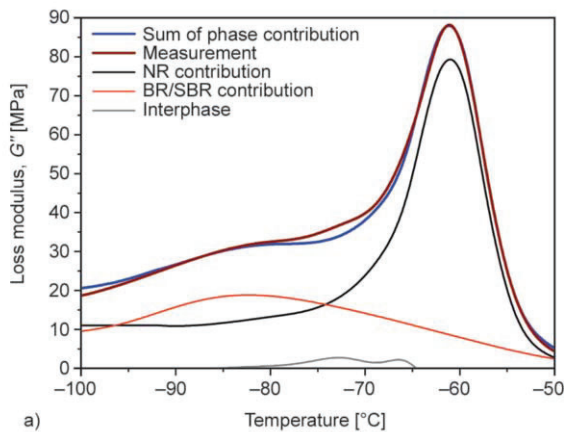


**Figure 11.** Separation of the unfilled NR/BR/SBR (70:15:15) (a) and (55:22.5:22.5) (b) blend into the contributions of the NR phase, the BR/SBR mixed phase and the interphase.

$$G''_{\text{blend}} = \sum_i \left( 1 + \alpha_i \frac{\phi_i}{\phi_{F,i} + \phi_i} \right) G''_{P,i} \left( a_i + b_i (\phi_{F,i} + \phi_i) + c_i (\phi_{F,i} + \phi_i)^2 \right) \quad (7)$$

This equation allows estimating the peak heights of the polymer phases in blends when knowing the peak heights of the unfilled blend, the blend ratio of the polymers and the filler volume fractions in the polymer phases. Otherwise, the filler volume fractions in the polymer phases can be determined when the peak heights of filled and unfilled blends and the blend ratio are known. Therefore the unfilled blend is decomposed into the contributions of the different phases (Figure 11). The interphase is obtained as a difference between the measurement and the sum of phase contributions between both polymer phases.

The filled NR/BR/SBR blends are displayed in Figure 12. In the filled blends the filler increases the loss modulus of the phase in which the filler is located. For the NR/BR/SBR blends all filler is ascribed to the NR phase as the peak heights in the BR/SBR mixed-phase and the interphase are not increasing due to the filling. The calculated filler amount in the NR coincides well with the filler amount mixed into the compounds. A problem occurring in these blends is the overlap of the different phase contributions which makes a clear separation difficult. In addition, the BR/SBR mixed-phase itself is no pure polymer phase. Possibly differently composed mixed phases with distinct glass transitions and filler affinities could be assumed. The phases with higher glass transition, containing more SBR do then superimpose with the NR phase.

#### 4. Conclusions

Polybutadiene with a high *cis*-1,4 content is crystallizing at low temperatures. As the crystallization

speed in a temperature range between  $-70$  and  $-40$  °C is sufficiently high, the crystallization can be seen in and it is influencing dynamic mechanical measurements. This effect depends on the measurement procedure, e.g. the temperature history of the sample and the heating rate. Filling with carbon black increases the effect of crystallization seen in the dynamic spectra. Blending with SBR which cannot crystallize is decreasing the effect. In this case BR and SBR are building a mixed phase.

The comparison of the dynamic spectra of unfilled and filled blends can yield the filler distribution in different phases of a blend. For NR/BR/SBR blends the filler seems to be located in the NR only. Thereby should be considered that due to the broadness of the BR/SBR mixed peak a clear separation of the phase contributions is not guaranteed.

#### Acknowledgements

We would like to thank the Deutsche Forschungsgemeinschaft (DFG) for financial support (grant KL1409/9-1) and our project partners IPF Dresden and Continental AG for the very good cooperation.

#### References

- [1] Eisele U.: Introduction to polymer physics. Springer, Berlin (1990).
- [2] Bekkedahl N., Wood L. A.: Crystallization of vulcanized rubber. *Industrial and Engineering Chemistry*, **33**, 381–384 (1941).  
<https://doi.org/10.1021/ie50375a023>

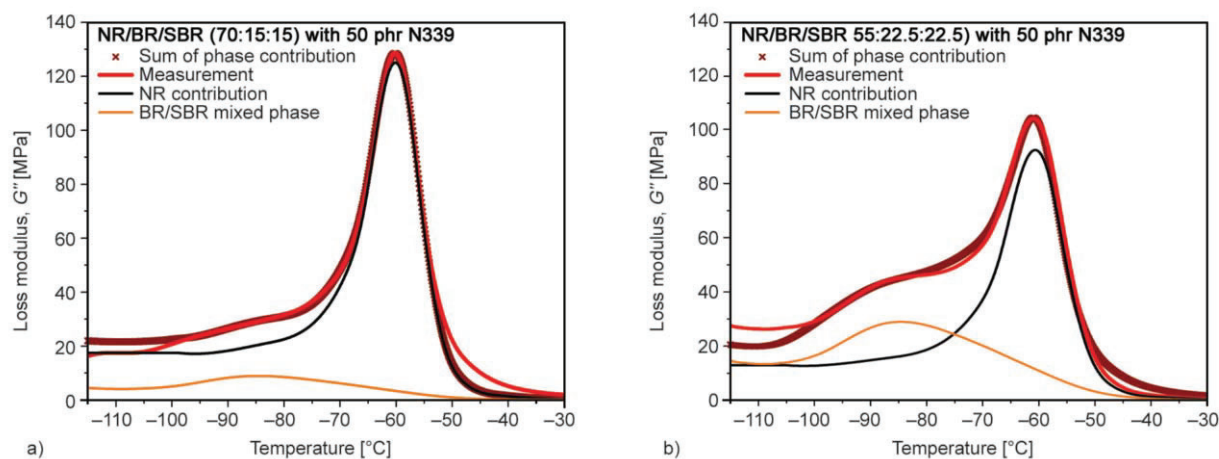


**Figure 12.** Separation of the filled NR/BR/SBR (70:15:15) (a) and (55:22.5:22.5) (b) blend into the contributions of the NR phase, the BR/SBR mixed phase and the interphase. Filler in the respective phases increases the peak amplitudes.



- [3] Bukhina K.: Low-temperature behaviour of elastomers. Koninklijke Brill, Leiden (2007).  
<https://doi.org/10.1201/b12239>
- [4] Wood L. A., Bekkedahl N.: Crystallization of unvulcanized rubber at different temperatures. *Journal of Applied Physics*, **17**, 362–375 (1946).  
<https://doi.org/10.1063/1.1707725>
- [5] Lion A., Jöhlitz M.: A thermodynamic approach to model the caloric properties of semicrystalline polymers. *Continuum Mechanics and Thermodynamics*, **28**, 799–819 (2016).  
<https://doi.org/10.1007/s00161-015-0415-8>
- [6] Sircar A. K., Lammond T. G.: Carbon black transfer in blends of cis-poly(butadiene) with other elastomers. *Rubber Chemistry and Technology*, **46**, 178–191 (1973).  
<https://doi.org/10.5254/1.3545009>
- [7] Schuster R. H.: Beziehung zwischen Verschnittmorphologie und physikalischen Eigenschaften von Elastomeren (in German). *Gummi Fasern Kunststoffe*, **49**, 966–974 (1996).
- [8] Morris M. C.: Rates of crystallization of cis-1,4-polybutadiene in elastomer blends. *Rubber Chemistry and Technology*, **40**, 341–349 (1967).  
<https://doi.org/10.5254/1.3539050>
- [9] Klüppel M., Schuster R. H., Schaper J.: Carbon black distribution in rubber blends: A dynamic-mechanical analysis. *Rubber Chemistry and Technology*, **72**, 91–108 (1999).  
<https://doi.org/10.5254/1.3538797>
- [10] Schuster R. H., Meier J., Klüppel M.: The role of interphase in filler partition in rubber blends. *Kautschuk Gummi Kunststoffe*, **53**, 663–674 (2000).
- [11] Meier J. G., Klüppel M., Geisler H., Schuster R. H.: Kieselsäuregefüllte Elastomerblends durch Masterbatchtechnologie (in German). *Kautschuk Gummi Kunststoffe*, **58**, 587–594 (2005).
- [12] Lorenz H., Steinhauser D., Klüppel M.: Morphology and micro-mechanics of filled elastomer blends: Impact on dynamic crack propagation. in ‘Fracture mechanics and statistical mechanics of reinforced elastomeric blends’ (eds.: Grellmann W., Heinrich G., Kaliske M., Klüppel M., Schneider K., Vilgis T.) Springer, Berlin, 81–128 (2013).  
[https://doi.org/10.1007/978-3-642-37910-9\\_3](https://doi.org/10.1007/978-3-642-37910-9_3)
- [13] Wunde M., Klüppel M.: Influence of phase morphology and filler distribution in NR/BR and NR/SBR blends on fracture mechanical properties. *Rubber Chemistry and Technology*, **89**, 588–607 (2016).  
<https://doi.org/10.5254/rct.16.83795>
- [14] Wunde M., Klüppel M.: Impact of mixing procedure on phase morphology and fracture mechanical properties of carbon black-filled NR/SBR blends. *Continuum Mechanics and Thermodynamics*, **29**, 1135–1148 (2017).  
<https://doi.org/10.1007/s00161-017-0562-1>
- [15] Strobl G.: Crystallization and melting of bulk polymers: New observations, conclusions and a thermodynamic scheme. *Progress in Polymer Science*, **31**, 398–442 (2006).  
<https://doi.org/10.1016/j.progpolymsci.2006.01.001>
- [16] Rubinstein M., Colby R. H.: *Polymer physics*. Oxford University Press, New York (2003).
- [17] Schuster R. H.: *Verträglichkeit von Kautschuken in Verschnitten. Teil 1. Theorie und Methoden* (in German). Wirtschaftsverband der deutschen Kautschukindustrie, Frankfurt (1992).
- [18] Schuster R. H.: *Verträglichkeit von Kautschuken. Ein altes und ein aktuelles Problem* (in German). *Die Angewandte Molekulare Chemie*, **202**, 159–185 (1992).  
<https://doi.org/10.1002/apmc.1992.052020110>
- [19] Schuster R. H., Issel H. M., Peterseim V.: Selective interactions in elastomers, a base for compatibility and polymer-filler interactions. *Rubber Chemistry and Technology*, **69**, 769–780 (1996).  
<https://doi.org/10.5254/1.3538400>
- [20] Palièrne J. F.: Linear rheology of viscoelastic emulsions with interfacial tension. *Rheologica Acta*, **29**, 204–214 (1990).  
<https://doi.org/10.1007/BF01331356>
- [21] Shi P., Schach R., Munch E., Montes H., Lequeux F.: Glass transition distribution in miscible polymer blends: From calorimetry to rheology. *Macromolecules*, **46**, 3611–3620 (2013).  
<https://doi.org/10.1021/ma400417f>



### 3.5 Supplementary information

CRACK PROPAGATION OF NR/BR/SBR BLENDS. The crack growth rates of the filled NR/BR/SBR triblend presented in the third publication (Chapter 3.4) have also been measured. In the triblend the crack propagation rate for low tearing energies is very low as in the NR and the NR/BR blends (Fig. 3.1). At high tearing energies the crack growth is increased but not as strong as in the NR/BR blends.

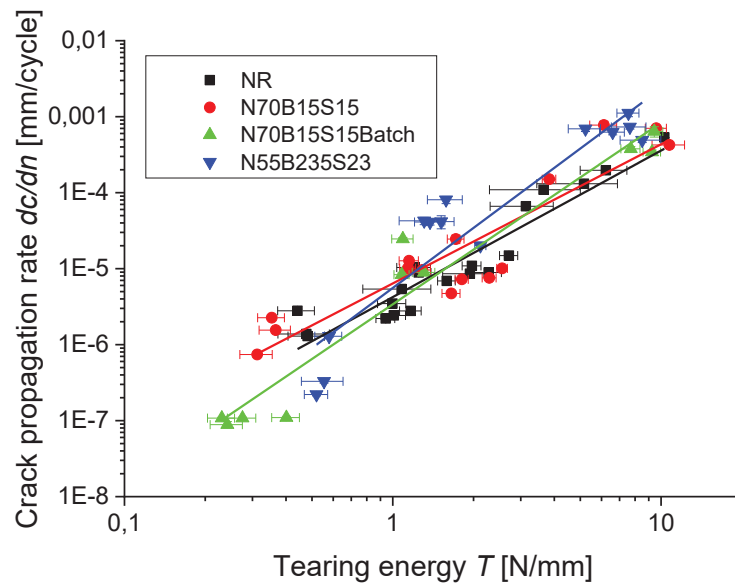


Fig. 3.1: Crack growth rate  $dc/dn$  in dependence of tearing energy  $T$  for the NR/BR/SBR blends

COMPARISON OF LABORATORIES. The crack propagation rates of the compounds have not only been measured and evaluated at the German Institute of Rubber Technology (DIK) but also by the project partners with other Tear Fatigue Analyzers located at Continental and Technische Universität Chemnitz [109]. The machines at the different locations differ in construction year and details. All results for the pure NR and for 55 phr NR mixed with 45 phr BR (N55B45), 45 phr SBR (N55S45) and 22.5 phr BR and SBR (N55B23S23), respectively, are compared in Fig. 3.2. Blending with BR leads in comparison with the pure filled NR to lower crack growth rates at low tearing energies and higher crack growth rates at higher tearing energies. That means that a crack in the compound N55B45 primarily increases very slowly but with increasing tearing energy the crack growth rate strongly increases. Blending with SBR leads to higher crack growth rates. The differences of the measurements at different laboratories were discussed in detail. Important aspects are not only the loading history but also the moment of image acquisition and the evaluation procedure. The

comparison of laboratories for identical samples shows quantitative differences but the trends are given by all laboratories.

To obtain the reasons behind the differences between the laboratories some TFA measurements performed at DIK and Continental were evaluated by both sides. It has been demonstrated that different results are yielded when two different persons are evaluating the same measurement. Reasons for this disparity are different length of evaluation regimes and a deviating interpretation of leaps in the measured crack length. The leap can be seen as time interval with strongly increased crack growth. It can also be argued that the crack length before the leap in reality was larger than measured. This could be explained for instance by a crack that does not go through the whole sample thickness and therefore appears smaller in the transmitted light images. But even stronger differences appear when an equivalent measurement is performed at different locations but evaluated by the same person. In this case the moment of image acquisition plays a big role. In this case a congruent acquisition was not possible as it was defined in time at the TFA of the DIK and as a traverse distance at Continentals TFA. Therefore for compound development it is strongly recommended that rubber compounds are compared using results obtained at one location and evaluated by one person.[109]

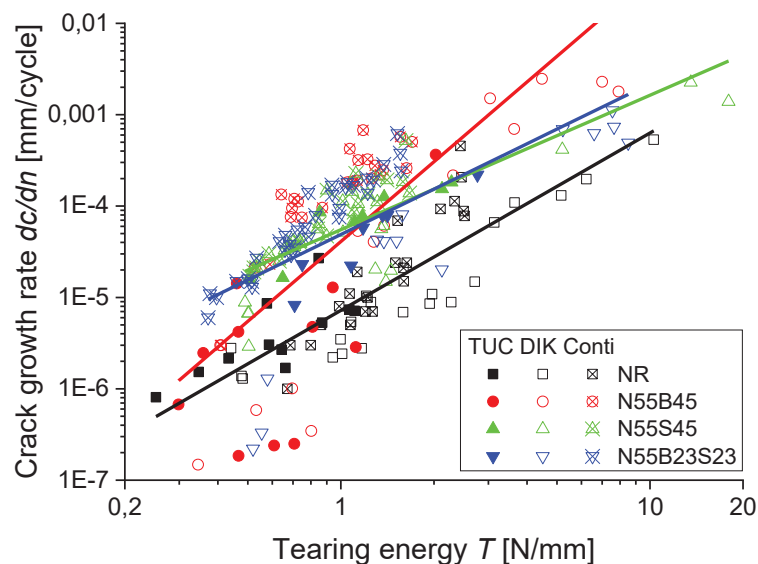


Fig. 3.2: Crack growth rate  $dc/dn$  in dependence of tearing energy  $T$  measured at Technische Universität Chemnitz (TUC), Continental (Conti) and my previous shown results measured at the German Institute of Rubber Technology (DIK) [109].

STRESS-STRAIN MEASUREMENTS. The stress-strain behavior of the unfilled polymers as well as with different filler loading is compared in Fig. 3.3. All polymers are strongly

reinforced by the filler. Due to strain-induced crystallization the NR is more stable than the two synthetic polymers. This is especially obvious for the unfilled compounds. For the compounds filled with 50 phr carbon black it can be seen that the stress-strain curve of all polymers have a similar curve (Fig. 3.3 (d)). The higher strength of the NR due to the crystallization leads to higher reached strains with higher stresses. This is expressed as higher tensile strength and elongation at break.

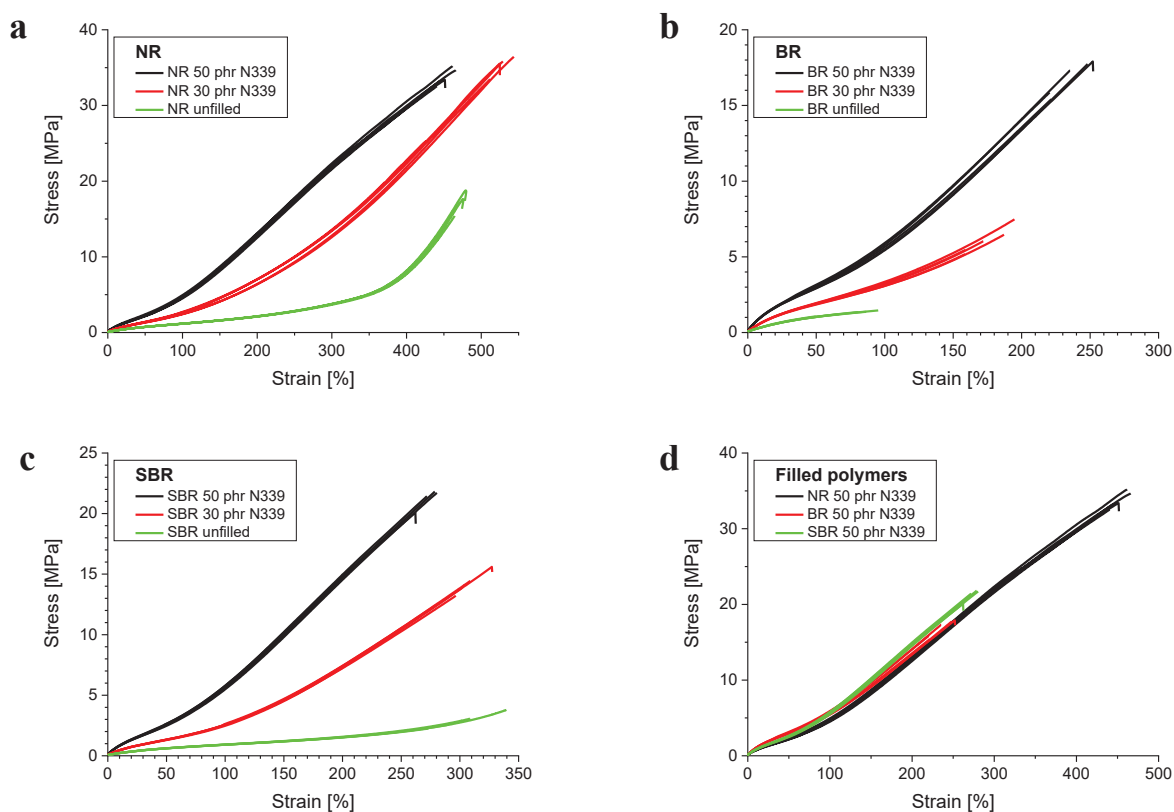


Fig. 3.3: Stress-strain behavior of homopolymers: NR (a), BR (b) and SBR (c) unfilled and with varying filler concentration. Comparison of filled polymers (d).

In addition to the compounds presented so far four additional compounds were produced in industrial style at Continental. These compounds RNR, RN55B45, RN55S45 and RN55B23S23 are the pure filled NR and 55 phr NR blended with BR and / or SBR. The recipes of these compounds are given in the last publication of chapter 4 (chapter 4.3). Using these materials test truck tires were produced at Continental. Therefore these compounds are called tire compounds in contrast to the previously presented laboratory compounds. The main difference is a lower amount of the accelerator N-cyclohexyl-2-benzothiazole sulfonamide (CBS). Therefore the expected crosslink density is lower.

In Fig. 3.4 are shown the stress-strain curves of the filled NR/BR and NR/SBR blends. The resulting tensile strength and elongation at break are summarized in dependency of the NR

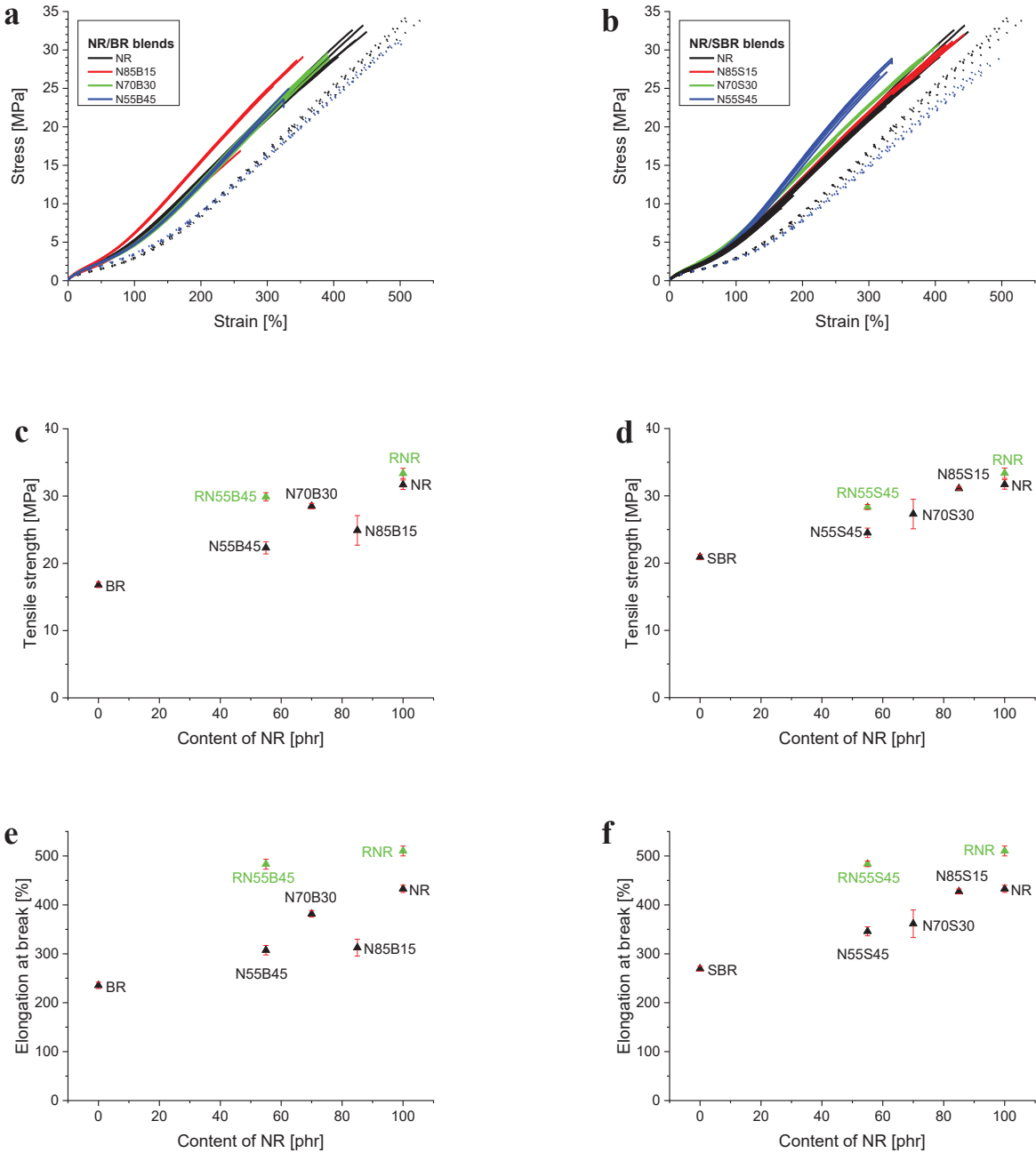


Fig. 3.4: Stress-strain behavior of filled NR/BR blends (a) and NR/SBR blends (b), tensile strength of the filled NR/BR blends (c) and NR/SBR blends (d) and elongation at break of the filled NR/BR blends (e) and NR/SBR blends (f). The tire compounds are shown in the figures (a) and (b) as dotted lines in the color of the corresponding laboratory compound and in the figures (c) – (f) in green.

content. It can be seen that tensile strength and elongation at break are increasing with the NR content. Fig 3.5 displays the stress strain curves, tensile strength and elongation at break for the triblend. These blends show the same dependency on NR content. In all cases the higher

stability of compounds with a large NR fraction is directly connected to strain-induced crystallization of NR. Due to their lower crosslink density the tire compounds behave softer, i. e. they show lower stresses at given strain. The tensile strength is slightly increased in comparison with the laboratory compounds but the enhancement of elongation at break is more pronounced. The decrease of tensile strength and elongation at break with decreasing NR content is less pronounced for the tire compounds.

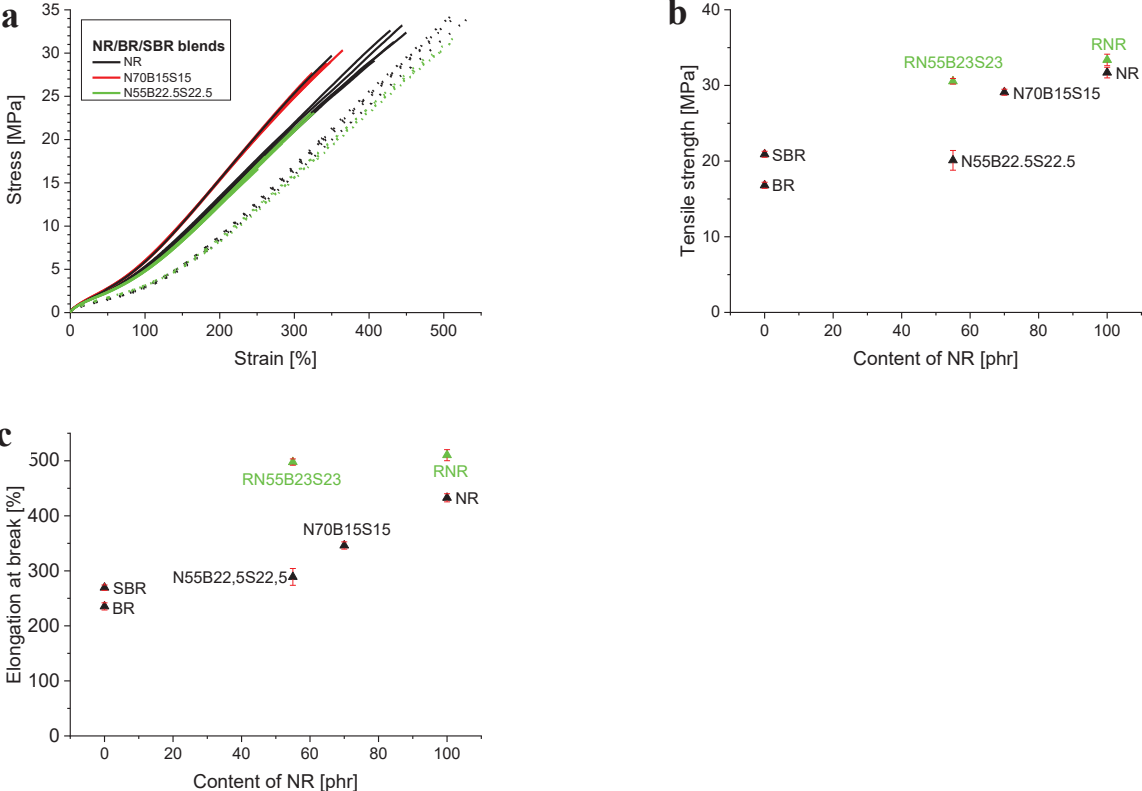


Fig. 3.5: Filled NR/BR/SBR blends: Stress-strain behavior (a), tensile strength (b) and elongation at break (c). The tire compounds are shown in the figures (a) and (b) as dotted lines in the color of the corresponding laboratory compound and in the figures (c) – (f) in green.

### 3.6 Outlook

The impact of polymer and filler concentration on crack growth is well known, but the influence of blend morphology and filler distribution remains uncertain. This is strongly connected to the small differences in crack growth rates that are often covered in the large scattering of the fracture mechanical measurements. Due to lower scattering in the crack growth rates the connection between crack growth behavior and blend morphology can be studied easier on unfilled blends. It should be noticed that the unfilled blends will crack much

more rapidly, especially those with lower NR fraction. Therefore considerably lower strain amplitudes must be used.

In this study the measurements have been done on blends with NR that have a high technical importance in truck tire treads. Due to the strain-induced crystallization the blends with higher NR content have better fracture mechanical properties independent of other effects. Many blends contain also BR that shows thermally induced crystallization that is fast enough to hamper the DMA measurements from which the filler distribution is calculated. Although probably technically of lower importance a study on a blend system that avoids these effects could be used to focus on the effect that blend morphology and filler distribution have on the crack growth behavior. Apart from using different combinations of polymers also different filler systems could be studied.

To understand the behavior of compounds containing BR it is also important to know the crystallization behavior in measurements at low temperatures. For this reason further direct measurements of crystallinity on the studied compounds by Differential Scanning Calorimetry or X-ray Diffraction can give more quantitative information.

The comparison of laboratories shows strong deviations between TFA measurements performed at different laboratories. In this respect the interlaboratory test is not satisfying. The test demonstrates that until now TFA measurements are only suitable for comparative studies. To obtain reliable quantitative data uniform guidelines and a standardized measuring method are necessary.

In this context it should be studied in which situations leaps in the measured crack length occur and what kind of crack morphology is observed before, during and after the leaps. This knowledge would help to formulate regulations to choose appropriate and consistent evaluation regimes in the course of the crack length.



# 4 Influence of energy dissipation around the crack tip on steady and dynamic tearing

## 4.1 Introduction

The energy needed to increase the crack length of an elastomer sample is much higher than the energy to break the respective polymer bonds in the new created crack surfaces. The energy to break the bonds can be connected to the intrinsic strength  $T_0$ . The under usual conditions large difference between the energy necessary to break the sample and the energy to break the bonds is attributed to energy dissipation around the crack tip. A consistent theoretical description was formulated for unfilled elastomers at steady tearing. By comparing the tearing energy in steady and dynamic tearing in unfilled and filled compounds it can be seen in how far viscoelastic effects are also dominating in other circumstances. Then the viscoelastic crack growth theory can also be applied in these cases. The J-Integral can locate the energy dissipation due to stress softening as the difference in the J-Integral of two different contours corresponds to the energy dissipation in between these contours. The results of this chapter are presented in two papers.

In the *first paper* the influence of energy dissipation around the crack tip on steady and dynamic tearing of elastomers is compared. Dynamic tearing was performed with the Tear Fatigue Analyzer. Steady tearing was investigated at different crack growth rates on trousers samples in crack opening mode III. Both investigations were done for different temperatures. Results were obtained for unfilled and filled SBR. The *second paper* compares the locally determined J-Integral with the global tearing energy  $T$  of notched Pure Shear samples. This investigation was done on NR and NR blended with BR and/or SBR. The use of digital image correlation enables the determination of the strain fields in a region around the crack tip. For this experimental technique a random pattern is painted on the specimen surface. During deformation a sequence of images is taken and the strain fields are calculated from the movements of the pattern. Using a physically based model of stress softening and hysteresis (Chapter 1.9) allows the calculation of stress and energy density fields [55-56]. In this context the evolution of the model and its implementation into python code has been done by Dr. J. Plagge. The J-Integral (eq. 2.7) can then be calculated for circular integration paths around the crack tip and compared to the tearing energy (eq. 2.3).

**STEADY TEARING.** The tearing energy for steady tearing measured on trousers samples is yielded using eq. (2.4). In the unfilled compound the tearing energy is increasing with crack growth rate and decreasing with temperature. The fatigue life in unfilled SBR increases by a factor of about  $10^4$  when the temperature decreases from  $100^\circ\text{C}$  to  $0^\circ\text{C}$  [110-111]. Using the WLF-equation (1.2) with the parameter obtained by creating a master curve for the dynamic moduli, a master curve for the tearing energy in steady tearing can be created [112-113]. The master curve is given by a power law increase with exponent  $\beta$ . This exponent is coinciding with the exponent  $\beta = (1 - m)/(2 - m)$  obtained from the exponent  $m$  of the relaxation time spectrum. The exponent  $m$  in filled compounds is decreasing with the strength of polymer–filler interactions [32,59]. For higher crack growth rates and temperatures the measured tearing energy is lower than predicted by the master curve. The difference is attributed to flash temperature effects close to the crack tip. Flash temperature denotes the increased temperature due to energy dissipation.

In the filled compounds at lower temperatures the tearing energy is decreasing with crack growth rate indicating that contributions of the filler network dominate.

**DYNAMIC TEARING.** The tearing energy for the dynamic tearing of the SBR compounds is calculated with eq. (2.2). Creating master curves is possible also for the filled compound. In the calculation of tearing energy a master curve is only achieved, if only the dynamic part of the energy density is used. For both, the unfilled and the filled compound, two distinct slopes are found at high and low crack growth rates. Two distinct slopes were also reported by M. Ludwig who demonstrated that the higher slope at lower tearing energies should be used for lifetime predictions [114].

**PARAMETER FITTING.** To identify the parameters of the physically based model multihysteresis measurements on dumbbell samples are performed. As the hysteretic contribution of the model is not formulated as energy functional the hysteretic contributions are not considered and the J-Integral is evaluated at the end of the cycle only. There the hysteretic contribution vanishes.

**POWER LAW BEHAVIOR.** Stress, strain and energy density show a power law decline towards the values far away from the crack tip. The exponents clearly differ from the exponents expected from linear elastic fracture mechanics [60].

COMPONENTS OF THE J-INTEGRAL. The J-Integral in eq. (2.7) is an integration on a path  $\Gamma$  over an integrand. The integrand is a sum of two contributions. Both contributions depend on the integration path and the normal vector of this path. One contribution,  $idw$  only depends else on the energy density distribution. The other contribution,  $idp$  depends on the 1. Piola Kirchhoff stress tensor and the displacement gradients. Due to the tensor character of the stress tensor this contribution is a summation of four terms representing the four tensor components in the visible plane. By choosing a circular contour for  $\Gamma$  the different contributions can be visualized and their influence on the J-Integral becomes clear. The separation of the integrand yields that the far field is dominated by  $idw$ , but close to the crack tip  $idp$  gives the largest contributions lateral to the crack tip.

THE J-INTEGRAL. The J-Integral is determined for four compounds and for different strain levels in dependence of the distance from the crack tip. The value of the J-Integral is increasing from very low values close to the crack tip until a plateau at higher distances is reached. The difference between the J-Integral for two different radii is interpreted as dissipated energy in the region in-between both integration paths. The plateau value coincides with the global tearing energy well, but for higher strains the J-Integral is surmounting the tearing energy. There are only slight differences in the compounds due to the varying stiffness of the compounds.

CRACK DEVIATION AND STRAIN-INDUCED CRYSTALLIZATION. A J-Integral vector can be defined with components  $J_k = \oint_{\Gamma} \left[ W_{el} N_k - P_{ij} N_j \frac{\partial u_i}{\partial x_k} \right] d\Gamma$ . The first component is given by the J-Integral. The ratio  $J_2/J_1$  is a measure for the crack to deviate from straight crack grow direction [115]. The values calculated for  $J_2$  are much lower than the values for  $J_1$ . Nevertheless NR shows sideways cracks [116-117] possibly being favored by strain-induced crystallization of NR.



## VISCOELASTIC RESPONSE DURING CRACK PROPAGATION OF UNFILLED AND FILLED SBR

MATTHIAS WUNDE, MANFRED KLÜPPEL\*

DEUTSCHES INSTITUT FÜR KAUSCHUKTECHNOLOGIE E. V. (DIK), HANNOVER 30519, GERMANY

RUBBER CHEMISTRY AND TECHNOLOGY, Vol. 91, No. 4, pp. 668–682 (2018)

### ABSTRACT

The crack propagation behavior of unfilled and filled styrene–butadiene rubber (SBR) in steady and dynamic tearing was investigated using tensile tests on trousers samples and tear fatigue measurements on single edge notched tension (SENT) samples, respectively. For the unfilled sample, both types of measurements indicated that the tearing energy is dominated by the viscoelastic response of the polymer. This was demonstrated by the creation of crack growth master curves using the horizontal shift factors obtained from mastering the complex modulus. The tearing energy increased with increasing crack velocity and decreasing temperature as required by the time-temperature superposition principle. The crack growth master curves followed a power law with the same exponent for steady and dynamic tearing. This exponent agrees fairly well with the exponent predicted by linear viscoelastic crack propagation theory. For steady tearing at high crack propagation rates, systematic deviations from the master curves appeared, which were attributed to flash temperature effects. For the filled SBR, which contained 50 phr carbon black, only dynamic tearing was found to be dominated by the viscoelastic response of the polymer. For steady tearing, filler networking seemed to alter crack propagation rates significantly, so that the viscoelastic fingerprint was no longer visible. For the filled sample, additional measurements with a high preload were conducted. It was demonstrated that a single master curve can be constructed, only if the (static) preload contribution is neglected and the dynamic contribution of the energy density is used for the evaluation of the tearing energy. This master curve showed two distinct slopes at high and low crack velocities. It is argued that the higher slope at low crack speeds is relevant for lifetime predictions based on the integration of the Paris–Erdogan power law. Under conditions in which the viscoelastic crack propagation holds, very slow crack growth rates can be explored at reasonable testing times by measurements at elevated temperatures. [doi:10.5254/rct.18.81537]

### INTRODUCTION

Passenger tires and other elastomer products made of styrene–butadiene rubber (SBR) often encounter high dynamic loading conditions inducing crack propagation. The micro-mechanical mechanisms of crack initiation and propagation occurring under steady and dynamic loading conditions are not exactly known.<sup>1</sup> Recently, the characteristics of crack initiation were connected to the flaw size in the rubber.<sup>2,3</sup> Physical understanding of crack propagation in viscoelastic materials is still under development, especially because of the strongly nonlinear deformation behavior and stress-softening effects.<sup>1,4,5</sup> The foundation for this understanding originates from the fundamental work of Rivlin and Thomas.<sup>6</sup> Recent efforts have been made<sup>7–10</sup> to develop fracture mechanical methods and models of filler-reinforced elastomers. Fatigue crack growth as well as chip and cut behavior characterize the fracture mechanical properties of rubber compounds for tires and conveyor belts.<sup>11,12</sup> Fatigue crack growth determines the crack growth velocity under given loading conditions. Early measurements made by Lake and Lindley<sup>13,14</sup> showed that the fatigue life in unfilled SBR decreases by a factor of about  $10^4$  when the temperature increases from 0 to 100 °C. At present, fatigue crack growth is usually carried out using a tear fatigue analyzer (TFA).<sup>15,16</sup> Chip and cut describes rubber tearing under harsh loading conditions in such a manner that pieces of rubber are removed. This mechanism is measured by the weight change of a rotating wheel that is dynamically impacted by a sharp tool.<sup>11,12,17</sup>

Previous measurements of the crack growth behavior of carbon black (CB)–filled SBR using a TFA were performed at room temperature with pulsed excitation<sup>10</sup> and with harmonic excitation at

\*Corresponding author. Email: Manfred.Kluppel@DIKautschuk.de

TABLE I  
RECIPES OF THE COMPOUNDS

Compound	SBR	CB	CBS	Sulfur	6PPD	ZnO	Stearic acid
Unfilled SBR	100	—	2	1.2	2	3	1.5
Filled SBR	100	50	2	1.2	2	3	1.5

4 Hz.<sup>9</sup> TFA measurements of CB-filled natural rubber (NR)/SBR blends showed lower crack growth rates than filled SBR because of the strain-induced crystallization of the NR.<sup>18–20</sup> Abraham<sup>21</sup> showed that for filled SBR tested at moderate preload for the same strain amplitude, the crack growth rate decreased when the preload was increased. No studies have been performed of the effect of temperature on SBR crack growth. In this work, TFA measurements of CB-filled and unfilled SBR compounds at different temperatures were done. Furthermore, measurements of the filled compounds were performed for a moderate preload and a very high preload value.

Because of the viscoelastic nature of elastomers, dynamic moduli depend on both temperature and frequency. In a thermo-rheological simple material with only one fundamental relaxation time, all relaxation processes can be connected to a single relaxation process with a specific relaxation time (e.g., describing the relaxation of a single polymer segment). In these materials, the connection between time and temperature is associated with the time-temperature superposition principle. This means that the dynamic modulus at a given temperature and frequency is equivalent to the modulus of a higher frequency and lower temperature and vice versa. Using the Williams-Landel-Ferry (WLF) equation, the modulus measured at different temperatures and frequencies can be combined into a single master curve. The master curve displays data in a wide frequency range, which is not accessible by direct measurement. In general, master curves of unfilled polymers show good agreement with direct measurements. Because of the polymer–filler interaction, filled systems have separate relaxation processes, and without further modifications, the master curves deviate from the direct measurement. The concept of master curves has been applied not only to fracture mechanics<sup>9</sup> but also to investigation of the network structure<sup>22</sup> and to friction of rubber on rough surfaces.<sup>23,24</sup>

Gent and colleagues<sup>25,26</sup> measured steady tearing energy at different tear rates and temperatures on trousers samples. They showed that the tearing energy can be divided in an intrinsic strength of about 0.05–0.08 N/mm and that the increased tear strength by internal energy losses depends on the tear rate and temperature. With regard to internal energy losses, time-temperature superposition can be applied to obtain a crack growth master curve. For high speeds and low temperatures, these viscoelastic losses surmount the intrinsic strength by a factor of about 1000. The intrinsic strength depends on the crosslink-density, as Gent showed by peeling partially crosslinked interfaces.

## EXPERIMENTAL

### MATERIALS

The compounds consisted of solution SBR (SLR 4502, Styron) with 53 wt% vinyl and 20 wt% styrene groups with and without 50 phr CB N330 as filler. They were cross-linked semiefficiently by sulfur, together with the vulcanization accelerator N-cyclohexyl-2-benzothiazole sulfonamide (CBS). The samples were compounded with the processing and vulcanization additives stearic acid and ZnO and protected against aging by 6PPD. The full recipes are shown in Table I.

## SAMPLE PREPARATION

The compounds were mixed in an industrial 1.5 L intermeshing mixer (Werner & Pfleiderer GK 1.5 E). A homogeneous mixture was indicated by leveling of the torque after mastication and after mixing. The curing system was added to a roller mill. The composites were vulcanized at 160 °C in a heat press up to 90% of the vulcameter torque maximum ( $t_{90}$  time).

## DYNAMIC MECHANICAL MEASUREMENTS

The dynamic moduli were measured on the dynamic analyzer ARES (Rheometric). The measurements on 2 mm thick strip samples were performed in the torsion-rectangular mode at temperatures  $\theta$  between  $-80$  and  $60$  °C and frequencies between 0.01 and 10 Hz. The measurement was performed in the linear region at 0.2% strain amplitude. The data of different temperatures were shifted toward each other to best fit to the WLF equation, indicating the validity of the time-temperature superposition principle.

## TEAR TESTS

The tear strength  $F/d$  was measured on a universal test machine (Zwick 1445) using trousers samples at 0, 23, 60, and 100 °C. Here,  $F$  is the measured force and  $d$  is the thickness of the sample. The velocity of the traverse  $v_t$  varied over  $4^{1/2}$  decades from 0.001 to 33.3 mm/s. The samples were 100 mm long, 15 mm broad, and had a 40 mm long cut forming the two legs, which were gripped by the clamps. The preload was 0.5 and 1 N for the unfilled and filled samples, respectively. The tear strength in dependence of the traverse path was recorded until complete tear, and the peaks  $>0.1$  N were analyzed. The median of the peak values of tear strength was evaluated.

## TEAR-FATIGUE ANALYZER

Crack propagation was measured using the TFA (Coesfeld) with notched strip samples. This machine allows for fully automatic detection of crack length and can investigate 10 specimens simultaneously. The crack propagation rates of the unfilled SBR were measured under harmonic excitation (2.5 Hz) at 23 and 60 °C. The 15 mm broad samples with a 1 mm deep crack were prestrained by 0.09 MPa and excited by varying strain amplitudes between 5 and 28%. The filled SBR was measured at 23, 60, and 100 °C with 0.09 and 1 MPa preload, respectively. The strain amplitudes were varied between 10 and 40%.

## VISCOELASTIC MASTER CURVES

Viscoelastic master curves were obtained by shifting the frequency-dependent dynamical mechanical data of different temperatures (see Figure 1) toward each other. Hereby, the measured frequency  $\omega$  was replaced with the horizontally shifted frequency  $a_T\omega$ . When the time-temperature superposition principle was valid, the horizontal shifting factors  $a_T$  delivered a smooth master curve of the different frequency branches (Figure 2). In the temperature range between  $T_g$  and  $T_g+100$  °C, they are well fitted by the WLF equation<sup>5,27</sup>:

$$\log(a_T) = -\frac{C_1(\theta - \theta_{ref})}{C_2 + (\theta - \theta_{ref})} \quad (1)$$

where  $C_1$  and  $C_2$  are constants and  $\theta_{ref}$  is the reference temperature where the shifting factor is unity (Figure 3). We used the arbitrary reference temperature  $\theta_{ref}=20$  °C and obtained the constants  $C_1$

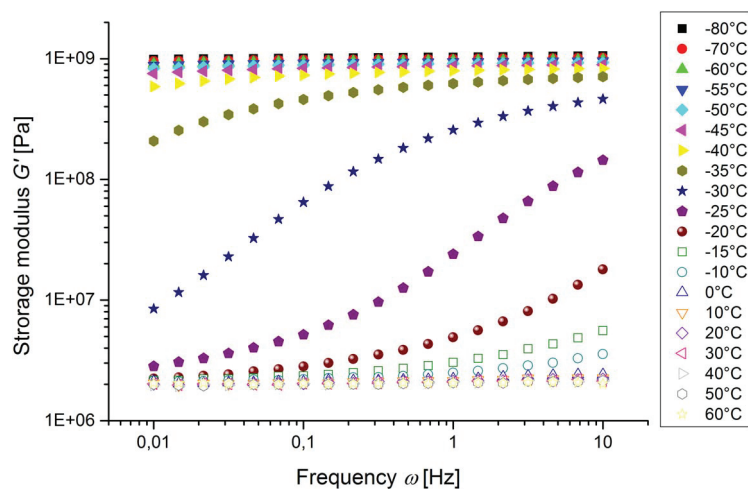


FIG. 1. — Frequency sweeps of the storage modulus  $G'$  at different temperatures.

and  $C_2$ , for which the branches of the moduli at different temperatures fit best to form the master curves.

For the unfilled sample, we obtained  $C_1 = 3.58$  and  $C_2 = 77.07$ . Using Eq. 1, the temperature dependence of the horizontal shifting factors  $a_T$  were calculated and shown in Figure 3.

The relaxation time spectrum  $H(\tau)$  of the unfilled compound was calculated from the storage moduli  $G'$  with the approximation method of Williams and Ferry.<sup>28</sup>  $H(\tau) = AG' / d \log G' / d \log \omega$  with  $A = (2 - p)/2\Gamma(2 - p/2)\Gamma(1 + p/2)$  was proportional to  $G'$  and to the slope in the double logarithmic plot of  $G'(\omega)$  at  $\omega = 1/\tau$ . Here,  $p$  is the slope at  $\tau = 1/\omega$  and  $\Gamma$  is the gamma function. To get smooth data for the slope, the modulus was interpolated. The relaxation time spectrum in Figure 4 follows in the glass transition regime a power law  $H(\tau) \sim \tau^{-m}$  with  $m = 0.54$ . The exponent  $m$  in filled compounds decreased with the strength of polymer–filler interactions.<sup>9,22</sup>

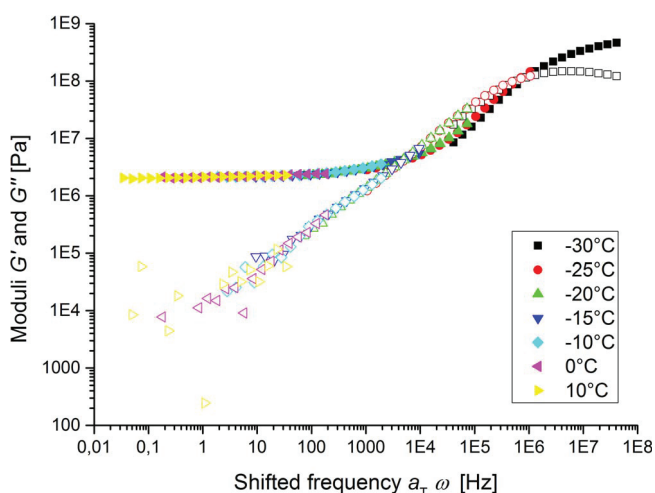


FIG. 2. — Branches of the moduli at different temperatures of Figure 1 are shifted simultaneously to yield master curves of  $G'$  (full symbols) and  $G''$  (open symbols). The resulting shifting factors  $a_T$  are displayed in Figure 3.



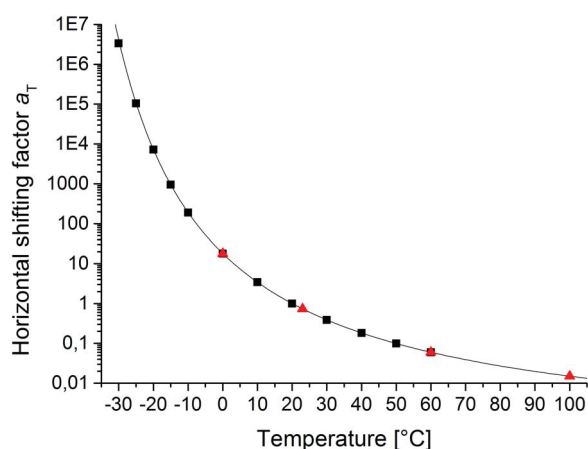


FIG. 3. — Horizontal shifting factors  $a_T$  (symbols) and fit to Eq. 1 (line). The values of  $a_T$  for the temperatures of Figure 2 are marked by squares. The temperatures at which tear tests are performed are marked by red triangles.

According to a theory of crack propagation in viscoelastic solids,<sup>7,8</sup> the increase of the tearing energy at low temperatures and/or high tear rates can be explained. Close to the crack tip, the deformation rate increases and the material approaches the glass transition, and at very high deformation rates, it even has a glassy behavior. The surface energy  $\gamma_{eff}$  can be approximated by the semi-empirical expression<sup>9</sup>

$$\gamma_{eff} = \gamma_0 \left( \frac{G'_\infty / G'_0}{1 + (v_c / v)^\beta} \right) \quad (2)$$

Here,  $\gamma_0$  is the static surface energy and  $G'_\infty$  and  $G'_0$  are the storage modulus in the glassy and rubbery state, respectively. For velocities  $v$  considerably below the critical velocity  $v_c$ , the tearing energy  $T$  follows a power law:  $T \sim v^\beta$ . The exponent  $\beta$  is connected to the power law exponent  $m$  of the relaxation time spectrum<sup>8</sup>:

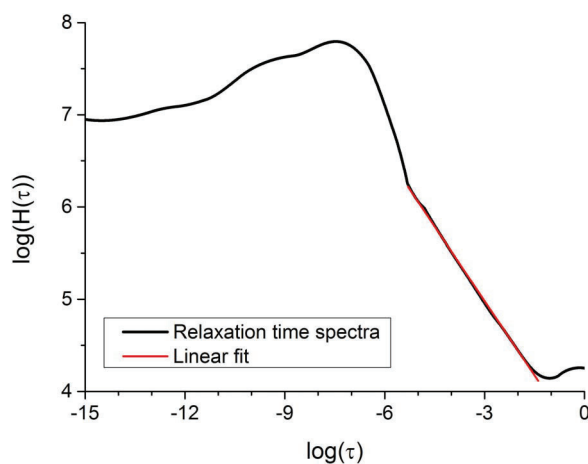


FIG. 4. — Relaxation time spectrum  $H(\tau)$  of the unfilled SBR.

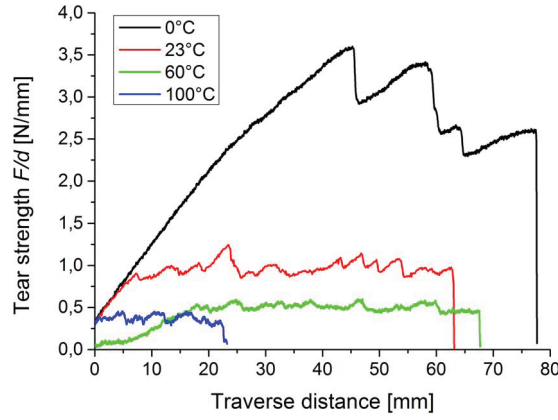


FIG. 5. — Tear strength  $F/d$  of the unfilled SBR measured at a traverse velocity  $v_t = 1$  mm/s for different temperatures.

$$\beta = \frac{1 - m}{2 - m} \quad (3)$$

With  $m = 0.54$  follows  $\beta = 0.32$  for the unfilled SBR. This exponent coincides roughly with the exponent found from the data of Gent,<sup>24</sup>  $\beta = 0.26$ .

#### STEADY TEARING

The tear strength  $F/d$  is given by the quotient of necessary force to tear  $F$  and the thickness of the sample  $d$ . The tear strength is plotted against the traverse distance in Figure 5 for a traverse velocity of  $v_t = 1$  mm/s at 0, 23, 60, and 100 °C. Obviously, the tear strength decreases significantly with increasing temperature. In addition, it increases with increasing traverse velocity (see below). Following the findings of Gent and Lai,<sup>25,26</sup> this indicates that the crack-opening mechanisms during tearing are governed by the viscoelastic material behavior.

The steady tearing energy  $T_c$  can be calculated from the tear strength  $F/d$  by considering that to increase the crack length by  $dc$ , the traverse needs to be separated by  $2\lambda dc$ . The factor 2 arises from the fact that in a stiff material, both legs grow half the amount compared with the change in the traverse distance. The factor  $\lambda$  respects the strain  $\lambda$  in the legs of the sample at given stress  $\sigma = F/db$ , where  $b$  is the leg width.  $\lambda$  is determined from stress–strain measurements on S2-samples, resulting from the given stress  $\sigma$ . In the tear tests the recently created leg volumes are strained and contribute to the elastic energy by  $2w_0 A_0 dc$ . Here,  $w_0$  is the energy density and  $A_0 = db$  is the cross-section area of each leg. The energy density  $w_0$  is calculated by integrating the stress–strain curves until  $\lambda$ . The steady tearing energy  $T_c = -(\partial W/\partial A)_l$  is therefore given by<sup>6</sup>

$$T_c = 2\lambda \frac{F}{d} - 2bw_0 \quad (4)$$

The crack growth velocity  $v$  is calculated from the traverse velocity  $v_t$  by  $v = v_t/2\lambda$ . The tearing energy  $T_c$  is in a good approximation twice the tear strength  $F/d$ :  $T_c \approx 2F/d$ . The crack growth velocity  $v$  is approximately half the traverse velocity  $v_t$ :  $v \approx v_t/2$ .

Figure 6a displays the tearing energy  $T_c$  in dependence of the crack growth velocity  $v$ . Hereby, we set  $T_c = 2F/d$  and  $v = v_t/2$ , in agreement with Gent and Lai.<sup>25,26</sup> The tearing energy of the unfilled SBR increases with increasing crack growth speed. An increase in temperature leads to a reduction of tearing energy because of the higher mobility of the polymer chains. The tearing

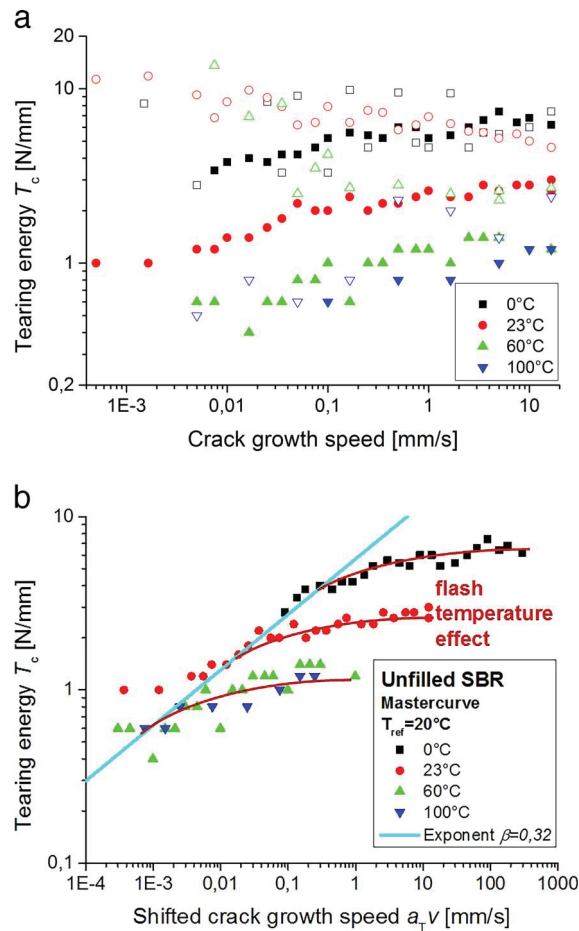


FIG. 6. — Tearing energy  $T_c \approx 2F/d$  of the unfilled SBR (full symbols) and filled SBR (open symbols) measured at different tear rates  $v \approx v_t/2$  and temperatures (a). The tearing energy  $T_c$  for the unfilled SBR is mastered by multiplying the tear rate  $v$  by the horizontal shifting factors  $a_T$  (b).

energy of the filled SBR decreases with crack growth speed for all temperatures up to 60 °C. In these cases, the tearing energy shows clearly nonviscoelastic behavior due to the filler network. Creating a master curve is therefore not possible for the filled SBR. For 100 °C, the filler network seems to play a minor role, so that nearly the unfilled behavior is obtained.

Figure 6b shows a master curve for steady tearing of the unfilled SBR by applying the horizontal shifting factors  $a_T$  depicted in Figure 3. Although there is substantial scattering, the time-temperature superposition seems to work for the branches at small crack speeds. This is indicated by the solid line with exponent  $\beta = 0.32$ , which is calculated using Eq. 3 from the exponent  $m$  of the relaxation time spectrum. This mastering behavior compares with the results of Gent and Lai<sup>25,26</sup> obtained for steady tearing of unfilled SBR with a higher styrene content of 48% and crosslinked by dicumyl peroxide, although the exponent  $\beta = 0.26$  is somewhat smaller. For higher values of  $a_T v$ , the power law behavior is not further followed, and a clear difference in the tear strength of the unfilled compound measured at different temperatures is visible. This difference is attributed to flash temperature effects (i.e., a significant increase in temperature in the vicinity of the crack tip). For the same value of  $a_T v$ , temperature effects are more pronounced at higher measuring

temperatures because these measurements are performed at higher tearing rates. For the same tear rate, the measurements at lower temperatures are more sensitive to heat buildup as the compound is closer to the glass transition and reacts more strongly to temperature differences. Therefore, the shift to lower values of  $a_{TV}$  should be higher for lower temperature measurements.

The measurements are performed with traverse velocities  $v_t$  between 0.01 (0.001 mm/s for room temperature) and 33.3 mm/s at temperatures between 0 and 100 °C. Gent and Lai<sup>25,26</sup> used a smaller velocity range of between 0.008 and 8 mm/s but a larger temperature range of between –20 and 130 °C. Their data do not show a clear flash temperature effect. This can be only partially explained by the higher velocities used in our study, which led to an increased flash temperature effect. For traverse velocities larger than 2 mm/s, clear deviations from the power law are already obvious (Figure 6b). The differences in the flash temperature effect should be attributed to the differences caused by sulfur and peroxide crosslinking. Results from Gent and Lai<sup>26</sup> for conventional sulfur-cured polybutadiene indicate that this system shows similar characteristics to our semiefficiently sulfur-cured SBR.

#### EVALUATION OF TEARING ENERGY AND CRACK PROPAGATION RATES

The energy  $S dA$  needed to increase the crack surfaces cannot exceed the release of elastic energy  $-dW$  (Griffith criteria).<sup>29</sup> Here,  $S$  is the surface energy and  $dA$  the newly formed surface area. The elastic energy release rate, called the tearing energy, is adjusted in the tear fatigue analyzer by the strain preset. The crack propagation rate per cycle  $dc/dn$  depends on the tearing energy  $T$  following a power law from Paris and Erdogan.<sup>30,31</sup>

$$\frac{dc}{dn} = AT^B \quad (5)$$

The crack growth rate at 1 N/mm,  $A$ , and the exponent  $B$  are fitting parameters. Although Eq. 2 is deviated for steady crack propagation, the typical viscoelastic effects should also appear under dynamic loading. By identifying the crack velocity  $v$  with the crack propagation rate  $dc/dn$ , a correlation between the exponents  $B \approx \beta^{-1}$  was obtained by Klüppel.<sup>9</sup>

The tearing energy of a single-edge notched (SEN) strip sample is given by<sup>6</sup>

$$T = \frac{2\pi}{\sqrt{\lambda}} \langle w_{el} \rangle \langle c \rangle \quad (6)$$

where  $\lambda$  is the sample elongation,  $\langle w_{el} \rangle$  is the average elastic energy density far away from the crack tip, and  $\langle c \rangle$  is the average (half) contour length of the crack. Equation 6 is based on the linear elastic fracture criterion formulated by Griffith,<sup>29</sup> who approximated the elastic energy available for crack growth by  $W_{el} \approx -\pi \langle c \rangle^2 d \langle w_{el} \rangle$ , with  $d$  being the sample thickness.<sup>32</sup> This reflects the reduced strain energy of an SEN strip sample with crack of length  $\langle c \rangle$  compared with the unnotched one. The definition of the tearing energy  $T = -(\partial W_{el} / \partial A)_l$  delivers Eq. 6 without the  $\sqrt{\lambda}$  term in the denominator. This was introduced by Lake and Clapson<sup>33</sup> to account for the transversal contraction of the rubber at larger strain (see also Gent<sup>1</sup>). By referring to experimental and numerical data, an empirical test of Eq. 6 was provided by Lindley<sup>34</sup> to confirm the  $\sqrt{\lambda}$  term but with a front factor a bit smaller than  $\pi$ . Recently, Eq. 6 was shown to agree fairly well with experimental evaluations by applying the Landes–Begley method for unfilled and filled SBR and EPDM, respectively, although the front factor was found to be systematically smaller and weakly dependent on crack length.<sup>35</sup> We point out that the crack contour length must be measured in the reference configuration at small strain (relaxed state). For higher preloads, this can hardly be realized, implying that the measured crack contour length is a bit larger than the one in the reference configuration.

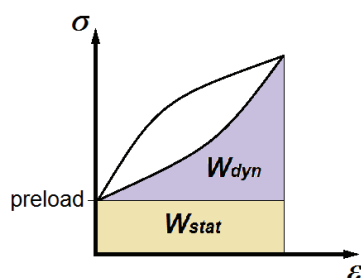


FIG. 7. — Static and dynamic part of the elastic energy density  $w_{el}$ .

The validity of Eq. 6 is ensured only for small crack depths. In finite element method simulations,<sup>36</sup> this formula is accurate for crack depths smaller than 20% of the sample width, and the error for crack lengths substantially longer is small. Lorenz et al.<sup>37</sup> showed that the equation can be used to describe the crack length versus cycle number even up to crack depths of 40% of the sample width, provided the crack remains perpendicular to the stretching direction and does not turn.

The elastic energy density  $w_{el}$  consists of a static part  $w_{stat}$  and a dynamic part  $w_{dyn}$  (Figure 7). The static part is given by the preload multiplied by the elongation  $\lambda$ . In common TFA measurements, the preload is small, and therefore, the static contribution  $w_{stat}$  to the energy density is small compared with the dynamic contribution. So far, it has not been specified in the literature whether the static part should be omitted when calculating the tearing energy via Eq. 6. For high preloads,  $w_{stat}$  generates a significant amount of the tearing energy.

Figure 8 shows exemplary crack growth curves, and the added crack images display the corresponding crack morphology. The crack growth curve shows the half crack contour length  $c$  versus the cycle number  $n$ . The crack growth rate  $dc/dn$  is evaluated in a linear region of stable crack growth. The crack morphology at high preloads (added images in Figure 8b) reveals a huge crack opening. This results from the high preload straining the samples, which is also applied when the images are taken. Because of this effect, for the same crack, a higher crack contour length  $c$  is measured with high preload than with lower preload. This leads to higher measured crack growth rates  $dc/dn$  and higher measured tearing energies  $T$ .

According to Eq. 6, the tearing energy is proportional to  $\langle w_{el} \rangle$  and  $\langle c \rangle$ . These values are averaged over the same region in which the crack propagation rate is determined. Log-log plots of  $dc/dn$  versus  $T$  yield so-called Paris–Erdogan plots. Different crack growth rates  $dc/dn$  in the Paris plots presented in the next section are directly related to the slope in the crack growth curves. The largest effects on the crack growth relate to the strain preset, the preload, and the temperature.

#### PARIS-ERDOGAN PLOTS

SBR, formed by random copolymerization of two different monomers, cannot crystallize<sup>38</sup> and has a higher crack propagation rate than NR.<sup>37</sup> The Paris–Erdogan plots for the unfilled SBR measured at 23 and 60 °C are displayed in Figure 9a. Here, every symbol is obtained by a separate measurement, leading to a slope  $dc/dn$  (solid lines in Figure 1) and the corresponding tearing energy  $T$  following from Eq. 6. The crack growth  $dc/dn$  shows clearly the power law increase with the tearing energy  $T$  as stated by Eq. 5. The exponent  $B$  for both temperatures coincides with the inverse exponent  $\beta^{-1}$  calculated according to Eq. 3. In Eq. 3,  $\beta$  is determined from the exponent  $m=0.54$  of the relaxation time spectrum  $H(\tau)$ . On the crack growth rate  $dc/dn$ , the horizontal shifting factors  $a_T$  can be applied, and a master curve is obtained (Figure 9b).

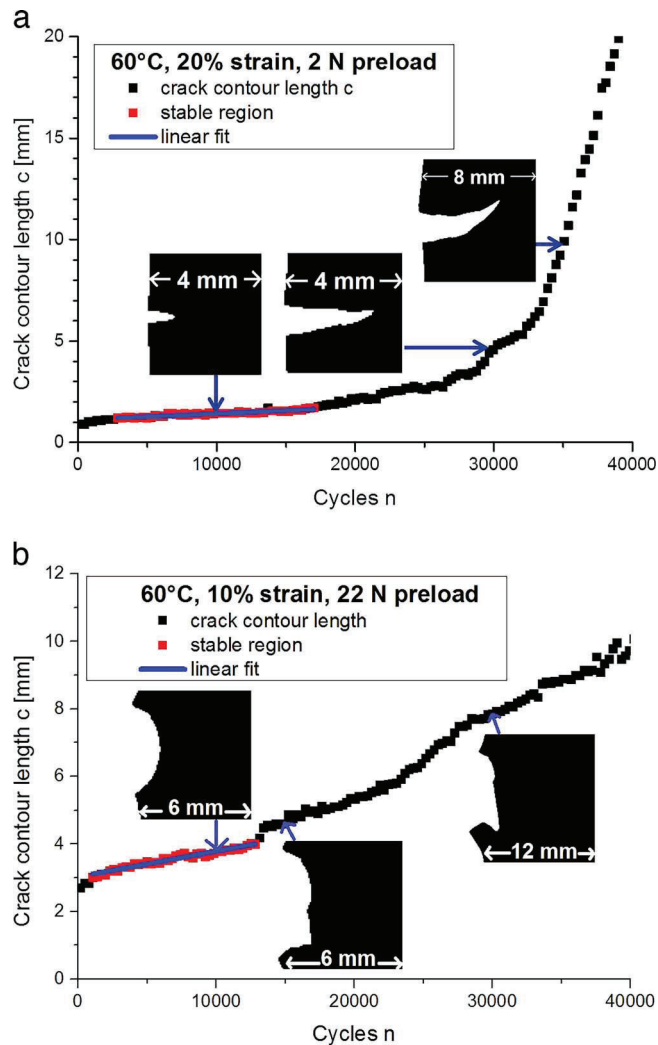


FIG. 8. — Crack contour length of filled SBR at 60 °C and 20% strain with (a) 0.09 MPa (2 N) and (b) 1 MPa (22 N) preload. The linear region of stable crack growth, which is evaluated, is shown in red. In addition, three crack images at different crack lengths are shown. The first two images have twice the magnification of the image at catastrophic crack growth.

For the lowest strain amplitude, the crack growth is smaller than given by the power law. For such small tearing energies, a transition to the intrinsic strength  $T_0$  is expected. Accordingly, the crack growth rate  $dc/dn$  drops to a very low value, which depends only on the ozone concentration. The value of  $T_0 \sim 0.05$  N/mm and crack growth rates somewhat below  $10^{-8}$  mm/cycle for  $T < T_0$  coincide with literature data for room temperature.<sup>21</sup> Nevertheless, a fit in the low tearing energy range up to 1 N/mm with a higher exponent  $\beta^{-1} = 6$  shows fair agreement. In absence of ozone, the curve should transfer into a vertical line when approaching  $T_0$ . A higher exponent at lower rates would correspond to a higher exponent  $m$  for larger times  $\tau$  in the relaxation time spectrum (Figure 4). Such a higher slope is not found.

In conclusion, the results of the unfilled SBR for steady as well as dynamic tearing demonstrate that viscoelasticity dominates the tearing energy necessary for crack propagation.

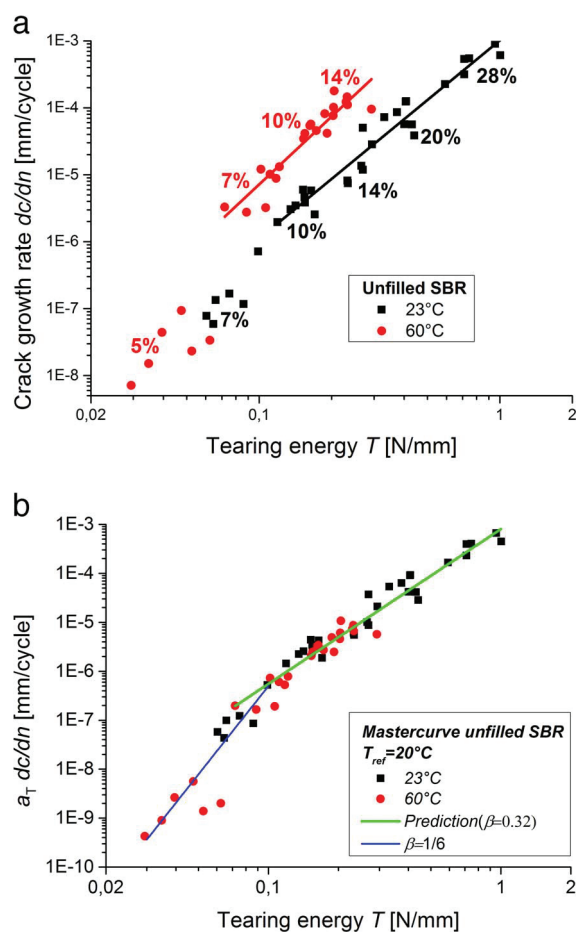


FIG. 9. — Tear fatigue analyzer results (Paris–Erdogan plots) of the unfilled SBR: crack growth rate  $dc/dn$  in dependence of tearing energy  $T$  at temperatures of 23 and 60 °C for a preload of 0.09 MPa (2 N) (a) and the master curve obtained by multiplying the crack growth rate  $dc/dn$  by the horizontal shifting factors  $a_T$  (b).

In filled SBR, the filler networking alters crack propagation, and the tearing energy cannot be derived from viscoelastic reasoning alone. The filled SBR has a strongly reduced crack growth rate compared with the unfilled SBR. Therefore, higher strain amplitudes are tested at 23, 60, and 100 °C. The measurements on the tear analyzer are performed not only with the common preload of 0.09 MPa but also with a significantly higher preload of 1 MPa. The resulting Paris–Erdogan plot is shown in Figure 10. For both preloads, the crack growth rate increases with increasing temperature. At 0.09 MPa preload, both the axis intercept and the slope increase with temperature. For the high preload of 1 MPa, the axis intercept increases more strongly than at 0.09 MPa preload with increasing temperature. However, the slope decreases with increasing temperature. At 1 MPa preload and 100 °C, the crack growth rate does not change much between 5 and 15% excitation amplitude. Under these conditions, the samples tear almost evenly without any dynamic load, implying that the slope (green dashed line) is very small.

Different slopes for measurements at the same preload but different temperatures suggest that the time-temperature superposition is not holding and that the Paris–Erdogan plots cannot be mastered. Nevertheless, the crack growth rates  $dc/dn$  can be shifted using the horizontal shifting

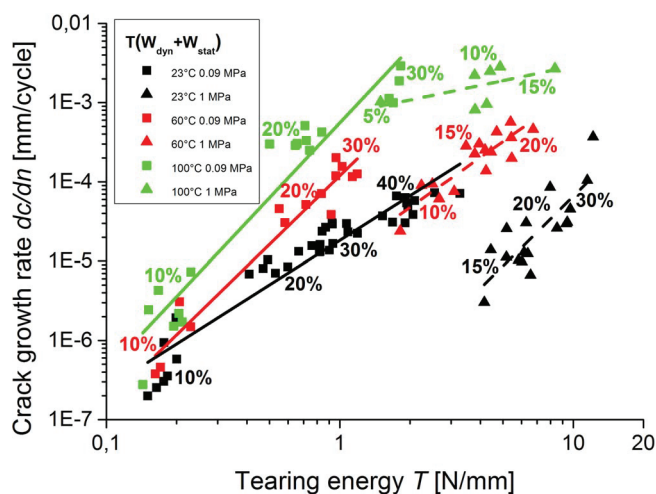


FIG. 10. — Tear fatigue analyzer results (Paris–Erdogan plots) of the filled SBR: crack growth rate  $dc/dn$  in dependence of tearing energy  $T$  at temperatures of 23, 60, and 100 °C, for preloads of 0.09 MPa (2 N) and 1 MPa (22 N), respectively.

factors  $a_T$ . This is shown in Figure 11 for two different evaluations of the tearing energy. In Figure 11a, the tearing energy is calculated with the sum of the static and dynamic part of the energy density; in Figure 11b, it is evaluated with the dynamic part of the energy density only. The results of the lowest strain rates measured at the moderate preload of 0.09 MPa seem to follow roughly a power law with an exponent of 2.98 (Figure 10a). The other measurements at this preload can also be fitted with a power law with a low exponent of 1.50. The experiments performed at a high preload of 1 MPa result in higher tearing energies and a slightly higher exponent of 1.56. For the same tearing energy  $T$ , the measurements measured with the high preload show a slower crack growth than the measurements with the moderate preload. This indicates that the dynamically stored energy density has a larger effect on crack growth than the static part. When the tearing energy is calculated with the dynamic part of the energy density only, the results for both preloads roughly coincide, and an exponent of 0.98 is found (Figure 11b). For the measurements at 100 °C and the high preload of 1 MPa, the static energy density surmounts the dynamic part clearly, especially for low amplitudes. Under these conditions, the static load plays a significant role. Therefore, these measurements are found at too low tearing energies in Figure 11b. When using the dynamic energy density only, the lowest strain rates at 0.09 MPa preload have an exponent of 3.68. These results suggest using the dynamic energy density for calculating the tearing energy and dividing the measured tearing energy range into two regions with different exponents: a higher exponent at low tearing energies and a lower exponent at higher tearing energies. The lower exponents for the higher tearing energy region in Figure 11 in comparison to Figure 10 arise from the separation of the region of low tearing energies.

In conclusion, we can say that also for the filled SBR, dynamic tearing seems to be dominated by viscoelastic crack-opening mechanisms, although steady tearing is not. This becomes apparent when two different scaling laws for the tearing energy versus crack propagation rate at small and large crack velocities are taken into account.

It is striking that that the crack growth master curves of the unfilled as well as filled SBR in both Figures 8b and 10b show two distinct slopes at high and low crack velocities. Similar results were recently reported by Ludwig<sup>39</sup> for filled EPDM and NR compounds. He demonstrated that the



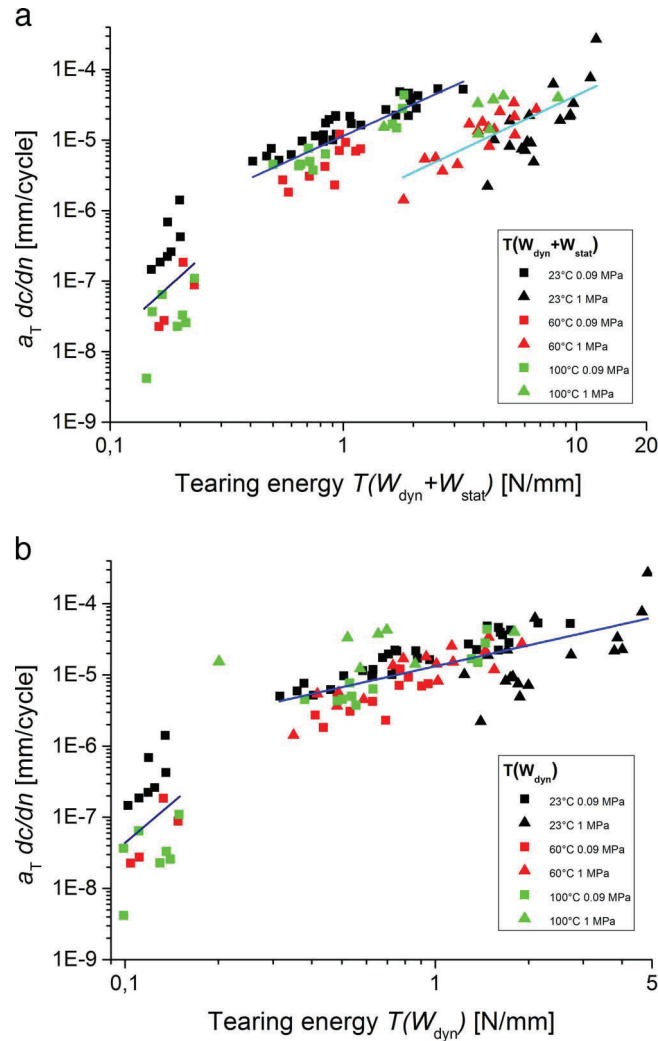


FIG. 11. — Master curve for the crack growth rate for the filled SBR in dependence of tearing energy  $T$  measured at temperatures of 23, 60, and 100 °C for a preload of 0.09 MPa (2 N) and 1 MPa: the tearing energy in Eq. 6 is calculated using the energy density  $W_e$ , the static and dynamic part  $W_{stat} + W_{dyn}$  (a), and the dynamic part  $W_{dyn}$  only (b). Linear fits are shown in blue.

higher slope at very small crack velocities found for these systems should be used for lifetime predictions based on the integration of the Paris–Erdogan power law. Indeed, fair agreement between predicted and experimental lifetime data at moderate loadings could be achieved if the initial slope at low crack speeds was considered, indicating that the low crack propagation rates around small cracks appearing at the beginning of a lifetime cycle test dominate the long-time fatigue behavior. A similar conclusion was drawn in 1970s by Clamroth and Eisele,<sup>40</sup> who found systematic larger slopes for the lifetime data (log-log plots of cycle number vs. energy) compared with the predicted slope obtained from the integration of the Paris–Erdogan power law (log-log plots of crack growth rate vs. tearing energy).

## SUMMARY AND CONCLUSIONS

The unfilled SBR, a noncrystallizing polymer, behaves predominantly viscoelastically. The increase in tearing energy with increasing frequency and decreasing temperature corresponds to an approach to the glass transition. Because of the time-temperature superposition principle, master curves of the tearing energy in steady and dynamic tearing of unfilled SBR can be created. The master curves show very low crack propagation rates at small tearing energies (high temperatures), indicating a transition to the intrinsic strength  $T_0$ . For larger tearing energies, the master curves follow a power law. The exponents coincide for steady and dynamic tearing. By referring to viscoelastic crack-opening mechanisms, these exponents can be derived from the exponent of the relaxation time spectrum. For high steady tear rates, the increase in tearing energy is less pronounced than according to the power law. This is attributed to flash temperature effects.

Filling of the SBR with CB clearly increases the crack growth resistance of the compound. The tearing energy is increased because of the reinforcing CB filler network. The filler network alters the viscoelastic behavior so that the viscoelastic fingerprint might disappear. For steady tearing, the time-temperature superposition is no longer fulfilled, and the tearing energy decreases with crack speed. However, the construction of master curves for dynamic tearing of filled SBR is possible in the frame of experimental errors, indicating that fatigue crack growth is still dominated by the viscoelastic response of the polymer. Measurements with a high preload demonstrate that a single master curve can be constructed roughly if the (static) preload contribution is disregarded and the dynamic contribution of the energy density is used for the evaluation of the tearing energy only. Calculation of the tearing energy by using the static and dynamic part of the energy density leads to different master curves for different preloads.

The crack growth master curves for both unfilled and filled SBR show two distinct slopes at high and low crack velocities. The higher slope at low crack speed is expected to be relevant for the durability or lifetime of the samples, if predicted from the integration of the Paris–Erdogan power law.

The viscoelastic response during static and dynamic tearing of unfilled samples or dynamic tearing of filled samples allows for the evaluation of very slow crack growth rates by measurements at elevated temperatures. This is of some practical importance, since long testing times can be avoided. This is not possible for steady tearing of filled samples.

## REFERENCES

- <sup>1</sup>A. N. Gent, *Engineering with Rubber*, Hanser, Munich, Vienna, 2001.
- <sup>2</sup>B. Huneau, I. Masquelier, Y. Marco, V. Le Saux, S. Noizet, C. Schiel, and P. Charrier, *RUBBER CHEM. TECHNOL.* **89**, 126 (2016).
- <sup>3</sup>M. Ludwig, T. Alshuth, M. El Yaagoubi, and D. Juhre, *Constitutive Models for Rubber IX*, B. Marvalová and I. Petříková, Eds., Taylor & Francis, London, 2015.
- <sup>4</sup>A. R. Payne, *RUBBER CHEM. TECHNOL.* **36**, 432 (1963).
- <sup>5</sup>J. D. Ferry, *Viscoelastic Properties of Polymers*, 3rd ed., Wiley, New York, 1980.
- <sup>6</sup>R. S. Rivlin and A. G. Thomas, *J. Polym. Sci.* **10**, 291 (1953).
- <sup>7</sup>B. N. J. Persson, O. Ahlbor, G. Heinrich, and H. Ueba, *J. Phys.: Cond. Matter* **17**, R1071 (2005).
- <sup>8</sup>B. N. J. Persson and E. A. Brener, *Phys. Rev. E* **71**, 036123 (2005).
- <sup>9</sup>M. Klüppel, *J. Phys.: Cond. Matter* **21**, 035104 (2009).
- <sup>10</sup>K. Reinke, M. Klüppel, and W. Grellmann, *Kautschuk Gummi Kunstst.* **62**, 246 (2009).
- <sup>11</sup>R. Stocck, R. Kipscholl, E. Euchler, and G. Heinrich, *Kautschuk Gummi Kunstst.* **4**, 26 (2014).

- <sup>12</sup>R. Stoczek, P. Ghosh, R. Mukhopadhyay, R. Kipscholl, and G. Heinrich, *Constitutive Models for Rubber VIII*, N. Gil-Negrete and A. Alonso, Eds., Taylor & Francis, London, 2013.
- <sup>13</sup>G. J. Lake and P. B. Lindley, *Rubber J.* **146**, 10 (1964).
- <sup>14</sup>G. J. Lake and P. B. Lindley, *Rubber J.* **146**, 11 (1964).
- <sup>15</sup>U. Eisele, S. A. Kelbch, and H.-W. Engels, *Kautschuk Gummi Kunstst.* **45**, 1064 (1992).
- <sup>16</sup>R. Stoczek, G. Heinrich, M. Gehde, and R. Kipscholl, *Lecture Notes Appl. Comput. Mech.* **70**, 269 (2013).
- <sup>17</sup>J. R. Beatty and B. J. Miksch, *RUBBER CHEM. TECHNOL.* **55**, 1531 (1982).
- <sup>18</sup>M. Wunde and M. Klüppel, *RUBBER CHEM. TECHNOL.* **89**, 588 (2016).
- <sup>19</sup>M. Wunde and M. Klüppel, *Contin. Mech. Thermodyn.* **29**, 1135 (2017).
- <sup>20</sup>P. Ghosh, R. Mukhopadhyay, and R. Stoczek, *Kautschuk Gummi Kunstst.* **6**, 53 (2016).
- <sup>21</sup>F. Abraham, “The Influence of Minimum Stress on the Fatigue Life of Non Strain-Crystallising Elastomers,” Ph.D. Thesis, Coventry University and Deutsches Institut für Kautschuktechnologie e.V., 2002.
- <sup>22</sup>J. Fritzsche and M. Klüppel, *J. Phys. Condens. Matter* **23**, 035104 (2011).
- <sup>23</sup>A. Le Gal, X. Yang, and M. Klüppel, *J. Chem. Phys.* **123**, 014704 (2005).
- <sup>24</sup>A. Le Gal and M. Klüppel, *J. Phys. Condens. Matter* **20**, 015007 (2008).
- <sup>25</sup>A. N. Gent, *Langmuir* **12**, 4492 (1996).
- <sup>26</sup>A. N. Gent and S.-M. Lai, *J. Polym. Sci. Pol. Phys.* **32**, 1543 (1994).
- <sup>27</sup>M. L. Williams, R. F. Landel, and J. D. Ferry, *J. Am. Chem. Soc.* **77**, 3701 (1955).
- <sup>28</sup>M. L. Williams and J. D. Ferry, *J. Polym. Sci.* **11**, 169 (1953).
- <sup>29</sup>A. A. Griffith, *Philos. Trans. R. Soc. London A* **221**, 163 (1921).
- <sup>30</sup>P. C. Paris, M. P. Gomez, and W. E. Anderson, *Trend Eng.* **13**, 9 (1961).
- <sup>31</sup>P. Paris and F. Erdogan, *J. Basic Eng.* 528 (1963).
- <sup>32</sup>M. F. Ashby and D. R. H. Jones, *Engineering Materials: An Introduction to Properties, Applications and Design*, Elsevier Butterworth-Heinemann, Oxford, UK, 2005.
- <sup>33</sup>G. J. Lake and B. E. Clapson, *Rubber J.* **153**, 36 (1970).
- <sup>34</sup>P. B. Lindley, *J. Strain Anal.* **7**, 132 (1972).
- <sup>35</sup>M. Klüppel, G. Huang, and B. Bandow, *Kautschuk Gummi Kunstst.* **61**, 656 (2008).
- <sup>36</sup>C. Timbrell, M. Wiehahn, G. Cook, and A. H. Muhr, *Constitutive Models for Rubber III*, J. J. C. Busfield and A. H. Muhr, Eds., Swets Zeitlinger, Lisse, France, 2003.
- <sup>37</sup>H. Lorenz, D. Steinhauser, and M. Klüppel, *Lecture Notes Appl. Comput. Mech.* **70**, 81 (2013).
- <sup>38</sup>L. R. G. Treloar, *The Physics of Rubber Elasticity*, 3rd ed., Clarendon, Oxford, UK, 1975.
- <sup>39</sup>M. Ludwig, “Entwicklung eines Lebensdauer-Vorhersagekonzepts für Elastomerwerkstoffe unter Berücksichtigung der Fehlstellenstatistik”, Ph.D. Thesis, Leibniz University, Hannover, Germany, 2017.
- <sup>40</sup>R. Clamroth and E. Eisele, *Kautschuk Gummi Kunstst.* **8**, 433 (1975).

[Received March 2018, Revised August 2018]





Contents lists available at ScienceDirect

## Engineering Fracture Mechanics

journal homepage: [www.elsevier.com/locate/engfracmech](http://www.elsevier.com/locate/engfracmech)



# The role of stress softening in crack propagation of filler reinforced elastomers as evaluated by the J-Integral



Matthias Wunde, Jan Plagge, Manfred Klüppel\*

Deutsches Institut für Kautschuktechnologie e.V., Eupener Strasse 33, D-30519 Hannover, Germany

### ARTICLE INFO

#### Keywords:

Fracture mechanics  
Tearing energy  
J-Integral  
Stress softening  
Filler reinforced rubbers

### ABSTRACT

A recently developed micromechanical model of stress softening and hysteresis of filled rubber is used to calculate the energy density- and stress distribution around the crack tip for a given displacement field, which is determined by digital image correlation. This allows for a quantitative evaluation of stress-softening influences on the J-Integral,  $J_1$ . In addition, the gradients of stress, strain and energy close to the crack tip are evaluated and compared to predictions of purely elastic material behaviour. The J-Integral is determined for carbon black filled truck tire tread compounds based on natural rubber (NR) and phase separated blends of NR with butadiene rubber (BR) and/or styrene-butadiene rubber (SBR). Dependent on the compound used,  $J_1$  is found to decrease significantly with decreasing contour radius  $r$ , indicating that most of the energy flux into the crack tip is dissipated due to stress softening and is not available for crack growth. For larger distances  $r$ , when the energy field becomes isotropic, plateau values are obtained for the J-Integral, which coincide with global tearing energies calculated by simple thermodynamics.

## 1. Introduction

In the development of rubber materials for high performance elastomer products like tires, conveyor belts, air springs and dampers the durability of the materials is one key feature. Therefore fracture mechanics and crack propagation in elastomers are of great technical importance. The addition of active fillers like carbon black or silica leads to a significant reinforcement of mechanical properties [28] which improves crack propagation properties, significantly [6,17]. In contrast to the purely elastic behaviour of unfilled elastomers, the addition of filler leads to a pronounced hysteresis and stress-softening effects, which result from filler networking and/or the interaction between polymer and filler. Different authors [11,21,29,30] investigated fracture mechanical properties of elastomer blends and showed that they are not only linked to the polymers used and the amount and activity of fillers, but also on filler distribution and the amount of filler in the interphase. A theory for crack propagation in viscoelastic solids [22,23] connects the surface energy with the viscoelastic properties of the material. As one approaches the crack tip, the rubber is excited with increasing frequency and therefore dissipates more energy if the glass transition frequency of the rubber is reached (comp. Fig. 1a)). With increasing crack velocity the crack tip passes through the glass transition and the surface energy increases according to a power law with an exponent determined by the exponent of the relaxation time spectrum. The predicted exponent was shown to agree fairly well with measured exponents between crack propagation rate and tearing energy for various filled and unfilled rubbers [13,31]. For the crack growth rate also transient effects were found to be important [8].

The concept of the J-Integral was introduced by Cherepanov and Rice in the late 1960th [26,2]. Accordingly, the elastic energy

\* Corresponding author.

E-mail address: [Manfred.Klueppel@DIKautschuk.de](mailto:Manfred.Klueppel@DIKautschuk.de) (M. Klüppel).

<https://doi.org/10.1016/j.engfracmech.2019.04.025>

Received 27 August 2018; Received in revised form 18 April 2019; Accepted 20 April 2019

Available online 25 April 2019

0013-7944/ © 2019 Elsevier Ltd. All rights reserved.

Nomenclature			
$A$	area	$W_{el}$	elastic energy density
$\mathbf{b}^{(n)}$	Eigenvectors of the left Cauchy-Green Tensor $\mathbf{B}$	$W_H$	hysteretic contribution to the energy density
$\mathbf{B}$	Left Cauchy-Green Tensor	$W_X$	amplified elastic energy density
$f_{ij}(\theta)$	weak function of planar angle $\theta$	$W_{tot}$	total energy density
$F_{ij}$	components of the deformation gradient	$W_\infty$	elastic energy density far away from the crack tip
$\mathbf{F}^T$	transpose of the deformation gradient	$x_i$	$i$ -th component of the deformed coordinates
$G_c$	cross-linking modulus	$X$	amplification factor
$G_e$	entanglement modulus	$X_i$	$i$ -th component of the undeformed coordinates
$h$	height of a Pure Shear sample	$X_{max}$	maximum amplification factor
$H_{ij}$	component of the displacement gradient	$\alpha$	exponent of $\Delta P_{22}$ vs. $r$
$\bar{I}_1$	first invariant of the left Cauchy-Green Tensor $\mathbf{B}$	$\beta$	exponent of $\Delta \epsilon_{22}$ vs. $r$
$\bar{I}^*$	generalized invariant of the left Cauchy-Green Tensor $\mathbf{B}$	$\chi$	exponent of the distribution of amplification factors $P_X(X)$
$id_p$	part of the integrand depending on the 1. Piola-Kirchhoff stress $\mathbf{P}$ and the displacement gradient	$\delta$	exponent of $\Delta W_{el}$ vs. $r$
$id_{p22}$	part of $id_p$ depending on $P_{22}$	$\delta_{ij}$	Kronecker $\delta$ ; 1 for $i = j$ , 0 otherwise
$id_w$	part of the integrand depending on the energy density $W_{el}$	$\Delta P_{22}$	increase of $P_{22}$ at $x_2 = 0$ close to the crack tip
$J_k$	$k$ -th component of the J-Integral	$\Delta W_{el}$	increase of $W_{el}$ at $x_2 = 0$ close to the crack tip
$k$	factor in tearing energy of single edge notched samples due to stress increase close to the crack tip	$\Delta \epsilon_{22}$	increase of $\epsilon_{22}$ at $x_2 = 0$ close to the crack tip
$K$	stress intensity factor	$\epsilon_{22}$	strain component $du_2/dx_2$
$n$	average number of segments between trapped entanglements	$\epsilon_\infty$	value of $du_2/dx_2$ far away from the crack tip
$N_i$	$i$ -th component of the normal vector	$\phi_{eff}$	effective filler volume fraction
$\mathbf{P}_{el}$	Elastic 1. Piola-Kirchhoff stress	$\gamma$	parameter determining the maximum amplification factor $X_{max}$
$\mathbf{P}_H$	Hysteretic 1. Piola-Kirchhoff stress	$\Gamma$	contour of integration path
$P_{ij}$	components of the 1. Piola-Kirchhoff stress tensor	$\zeta$	intrinsic time
$P_X(X)$	distribution of amplification factors $X$	$\theta$	planar angle
$P_\infty$	value of $P_{22}$ far away from the crack tip	$\lambda_i$	principal strains
$r$	radius of contour $\Gamma$	$\boldsymbol{\sigma}$	Cauchy stress tensor
$r_0$	radius of energy dissipation regime	$\sigma_c$	critical fracture stress of rubber-filler structures
$s$	running variable	$\tau_R$	Rouse relaxation time
$U_i$	$i$ -th component of displacement vector	$\omega_0$	onset-frequency of the viscoelastic dissipation regime
$T$	tearing energy	BR	butadiene rubber
$v$	crack growth velocity	CB	carbon black
$v_s$	sound velocity	CBS	N-cyclohexyl-2-benzothiazole sulphonamide
$W$	energy density of the non-affined tube model	IPPD	N-isopropyl-N-phenyl-P-phenylenediamine
		NR	natural rubber
		phr	per hundred rubber
		SBR	styrene-butadiene rubber
		ZnO	zinc oxide

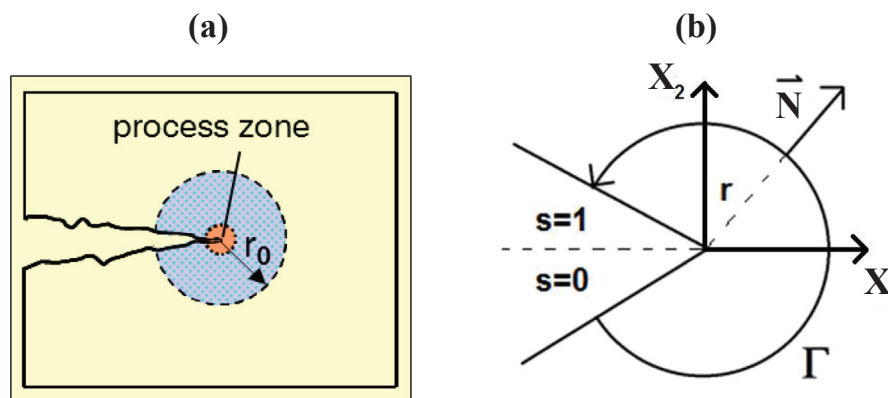


Fig. 1. Schematic drawing of crack growth in rubber materials showing the process zone (orange) and a pronounced energy dissipation regime of size  $r_0$  (blue) (a); Graphical illustration of the circular contour  $\Gamma$  around the crack tip used for calculation of the J-Integral  $J_1$  in spatial direction  $X_1$  (b). (For interpretation of the references to colour in this figure legend, the reader is referred to the web version of this article.)

release rate due to propagating cracks can be evaluated based on a line integral  $J$  taking into account the energy, stress and strain fields along a contour  $\Gamma$  around the crack tip. This path integral refers to the energy flux into the crack tip under deformation, which, according to the famous Griffith Criteria [7], determines the available energy for surface growth of the propagating crack [4,32]. The J-Integral describes the tearing energy available for crack growth by integrating the energy flux into the crack tip through closed contours around the crack tip, here chosen as circular paths with varying radius  $r$ . It can be described in the framework of material forces [20]. The integrand of  $J$  is given by the Eshelby stress tensor and the sources of this tensor are the material forces acting on the crack tip. The J-Integral  $J_1$ , pointing into crack growth direction perpendicular to the stretching direction as well as the J-Integral  $J_2$ , for crack growth in stretching direction, consists of several additive terms, which are analysed in detail in this paper for getting a better understanding of the dominant contributions. The energy release  $W_{el}$  per change of surface area  $A$  due to crack growth is specified by the global tearing energy  $T = -dW_{el}/dA$  [27]. For Pure Shear samples the tearing energy is given by  $T = W_{\infty} h$ , where  $W_{\infty}$  is the elastic energy density far away from the crack tip and  $h$  is the height of the sample. For an infinite long Pure Shear sample with a contour surrounding the edge of the sample, one can show that  $J_1 = W_{\infty} h$  [26], which coincides with the global value of the tearing energy  $T$ . For purely elastic materials the J-Integral is independent of the selected contour but this is no longer true for viscoelastic materials like filled elastomers showing pronounced stress softening and hysteresis. Recently, the tearing energy and the analytical energy release rate of carbon black-filled elastomers in mode III trousers samples were compared with finite element simulations of the J-Integral [3]. They found comparable results using the hyperelastic Ogden-model that neglects hysteresis and stress-softening effects. Other authors [16] used digital image correlation and finite element analysis of carbon black-filled SBR. They could correlate a decreasing carbon black particle size with an increasing strain at the crack tip delivering improved fracture properties.

Filled elastomers show pronounced stress softening and filler-induced hysteresis, which is not considered in hyperelastic models. The stress softening effect, also denoted Mullins effect, appears as a stress decrease due to previous deformation (Mullins and Tobin, 1965). After several cycles repeated straining a steady-state cycle is reached, which can be explained by interaction and restructuring of the filler and polymer network [28]. A micro-mechanical model relating stress softening to hydrodynamic strain amplification due to the presence of fillers is the Dynamic Flocculation Model [14,28]. According to this model the rubber matrix is reinforced by rigid filler clusters, which are broken successively in the conditioning cycles with increasing maximum strain. Although the filler clusters re-aggregate when the rubber is relaxed, these re-aggregated clusters are softer than the initial ones. The difference in stiffness of the clusters after deformation leads to stress softening, while the repeated stretching and breakdown of re-aggregated clusters implies filler-induced hysteresis. In a similar physically motivated model [24,25] different domains amplified by the filler coexist, which are described by a distribution of amplification factors. After deformation the amplification factors are shifted towards lower values yielding the stress softening effect of the rubber. This analytical model, being recapitulated in Chapter 3.3, will be used in the following evaluations.

In the present paper we use a combined experimental and theoretical approach for the evaluation of the J-Integral analysed for several strain amplitudes varying between 10% and 60%. On the one side, digital image correlation by evaluating the displacements of an airbrushed pattern sprayed around the crack tip of a notched rubber sample will be applied for evaluating the displacement field around the crack tip of carbon black filled truck tire tread compounds. On the other side, the above analytical model of stress softening is used to calculate the energy density- and stress distribution around the crack tip from the measured displacement fields. All three quantities are required for the calculation of the J-Integral, which is done in some detail for circular paths of different radius  $r$  around the crack tip. Thereby, the effect of energy dissipation due to stress softening on the available energy for crack propagation is analysed.

## 2. Experimental

### 2.1. Materials

In this study, truck tire tread compounds based on natural rubber (NR) and phase-separated blends consisting of 55 wt% NR and 45 wt% butadiene rubber (BR) or styrene-butadiene rubber (SBR) as well as a tri-blend of all three rubbers are used. All compounds are filled with 50 phr carbon black (CB, N339). The samples are cross-linked semi-efficiently by sulphur in combination with the vulcanization accelerator N-cyclohexyl-2-benzothiazole sulphonamide (CBS). The compounds include the processing and vulcanization additives stearic acid and ZnO. The composites are protected against aging by N-isopropyl-N-phenyl-P-phenylenediamine (IPPD). The full recipes are shown in Table 1.

**Table 1**  
Composition in [phr] of the truck tire tread compounds used in this study.

Compound	NR	BR	SBR	N339	CBS	Sulfur	IPPD	ZnO	Stearic acid
NR	100	–	–	50	1.1	1.8	1.8	3	1
N55B45	55	45	–	50	1.1	1.8	1.8	3	1
N55S45	55	–	45	50	1.1	1.8	1.8	3	1
N55BS23	55	22.5	22.5	50	1.1	1.8	1.8	3	1

[phr]: per hundred rubber.

## 2.2. Sample preparation

Mixing of the compounds was done at Continental AG at industrial scale. Vulcanization was performed at 150 °C in a heat press up to 90% of the vulcameter torque maximum ( $t_{90}$  time). Pure Shear samples with a height of 27.5 mm and width of 200 mm were prepared. A 50 mm long cut was inserted at the short edge. Due to the bulges at the long edges Pure Shear samples possess a restricted deformation in crack growth direction. The Pure Shear geometry is called this way as the region of the specimen far away from the crack tip and the edges is in a pure shear deformation state.

## 2.3. Digital image correlation

The displacement fields were determined by digital image correlation using the ARAMIS software from GOM. By airbrushing the samples gently with white paint a fine black and white pattern was created. The change of the pattern when the samples are deformed was calculated into the evolution of the displacement field. The stretching of the composites was performed in a Zwick Universal Testing machine 1445 at a speed of 20 mm/minute. The notched Pure Shear samples were strained five times to the same maximum strain value varying between 10% and 60%. A camera recorded 1 image per second of the last deformation cycle. The spot size was approximately 20 mm × 20 mm. The image at the start of the cycle showing the smallest deformation was taken as reference configuration. For the following images the displacement field towards the reference was calculated. Only the displacement field of the image with the highest deformation was evaluated.

## 3. Computation of the J-Integral

### 3.1. Energy flux integrals

In the following we will restrict ourselves to plane stress conditions in order to simplify the issue. In this frame, crack propagation of materials can be characterized by energy flux integrals, which quantify the amount of energy flowing into the crack tip [4]. The J-Integral is a vector that describes the energy flow available for crack growth in spatial direction  $k$ :

$$J_k = \oint_{\Gamma} \left[ W_{el} N_k - P_{ij} N_j \frac{\partial U_i}{\partial X_k} \right] d \quad (1)$$

Here,  $\Gamma$  is the integration path,  $W_{el}$  is elastic energy density,  $\mathbf{P}$  is the first Piola-Kirchhoff stress tensor,  $\mathbf{U} = \mathbf{x} - \mathbf{X}$  is the displacement vector giving the difference between the deformed coordinates  $\mathbf{x}$  and the undeformed coordinates  $\mathbf{X}$  and  $\mathbf{N}$  is the normal vector. For small deformations the first Piola-Kirchhoff stress tensor  $\mathbf{P}$  coincides with the Cauchy stress tensor  $\boldsymbol{\sigma}$  given in spatial coordinates. It should be noted that the calculations yield  $\oint_{\Gamma} P_{ij} N_j d\Gamma \neq 0$ , not satisfying conservation of momentum. A closer analysis of this discrepancy shows that the second component  $F_2 = P_{21} N_1 + P_{22} N_2$  of the integrand has opposing signs above and below the crack plane ( $X_2 = 0$ ), so that the contributions to the integral in both half planes roughly compensate each other. The first component  $F_1 = P_{11} N_1 + P_{12} N_2$  of the integrand has opposing signs in front ( $X_1 > 0$ ) and behind ( $X_1 < 0$ ) the crack tip. In this case the contributions in front of the crack tip surmount those behind the crack tip. The reason for this is expected to be connected to the insufficient resolution of the displacement fields very close to the crack tip and the crack edges.

The first component  $J_1$  is pointing into the direction of the crack  $X_1$  perpendicular to the stretching direction (Fig. 1b).

$$J_1 = \oint_{\Gamma} \left[ W_{el} N_1 - P_{ij} N_j \frac{\partial U_i}{\partial X_1} \right] d\Gamma \quad (2)$$

In the following the component  $J_1$  in spatial direction  $X_1$  is attributed as “the J-Integral”.

The J-Integral allows for the consideration of energy dissipation mechanisms close to the crack tip that lower the available energy for crack growth. One origin of pronounced energy dissipation can be viscoelastic losses due to increasing deformation rates when approaching the crack tip [22,13], which refers to viscoelastic crack opening mechanisms. This is depicted schematically in Fig. 1a) by the blue area of size  $r_0$ , which increases with increasing crack velocity  $v$  ( $r_0 \approx v/\omega_0$ ). Here,  $\omega_0$  is the onset-frequency of the viscoelastic dissipation regime, which can be identified with the inverse Rouse relaxation time  $\tau_R$  ( $\tau_R = 1/\omega_0$ ). The inner region, shown in orange, is the so called Barenblatt process zone where chain rupture, pull-out of chains, cavitation and crack like defects appear. The typical size of the process zone lies between 100 nm and 1  $\mu\text{m}$ , as determined by roughness measurements of the fracture surface [10]. The size  $r_0$  of the viscoelastic dissipation regime can become significantly larger with increasing crack velocity, reaching a maximum value of  $r_0 \approx 10$  mm at the sound velocity  $v_s \approx 10^3$  m/s, if a typical value of  $\tau_R \approx 10^{-5}$  s is assumed. We point out that in these theoretical evaluations the crack velocity is considered to be constant, which is realized in our cyclic stretching experiments in an infinite small time interval, only. However, due to the small extension rates the samples are almost in equilibrium and the recorded images reflect the deformation state for a fixed but unknown small crack velocity. In [13] it was demonstrated that the theory of viscoelastic crack growth with constant crack speed [22] seems to work even for cyclic fatigue crack growth experiments at relatively high strain rate (4 Hz), demonstrating that such theory can also be applied approximately for pulsed crack propagation by referring to an averaged crack velocity.

A second origin of pronounced energy dissipation can be stress softening of filled rubbers, which also appears in a circular area of size  $r_0$  around the crack tip (Fig. 1a)). This effect can be measured at quasi-static conditions, implying that it appears already at very



small crack velocities. The size  $r_0$  typically lies in the mm- to cm-range depending on filler amount and applied strain (see below). In the following the dissipated energy between two circular contours  $\Gamma_1$  and  $\Gamma_2$  of different size  $r$  around the crack tip will be evaluated by referring to the J-Integral Eq. (2). Although, integration over a rectangular paths looks more simple, the spherical geometry of the energy dissipation regime implies that circular paths with radius  $r$  around the crack tip should be chosen for getting reasonable results. The parametrization of this path is specified in Fig. 1b). Accordingly, the integration path  $\Gamma$  and the normal vector  $\mathbf{N}$  on this path are given by:

$$\Gamma(s) = r \begin{pmatrix} -\cos(2\pi s) \\ -\sin(2\pi s) \\ 0 \end{pmatrix} \text{ and } \mathbf{N}(s) = \begin{pmatrix} -\cos(2\pi s) \\ -\sin(2\pi s) \\ 0 \end{pmatrix}, \quad s \in (0, 1) \tag{3}$$

where  $s$  is a running variable (see Fig. 1b). The first coordinate is in direction of the crack, the second coordinate is in stretching

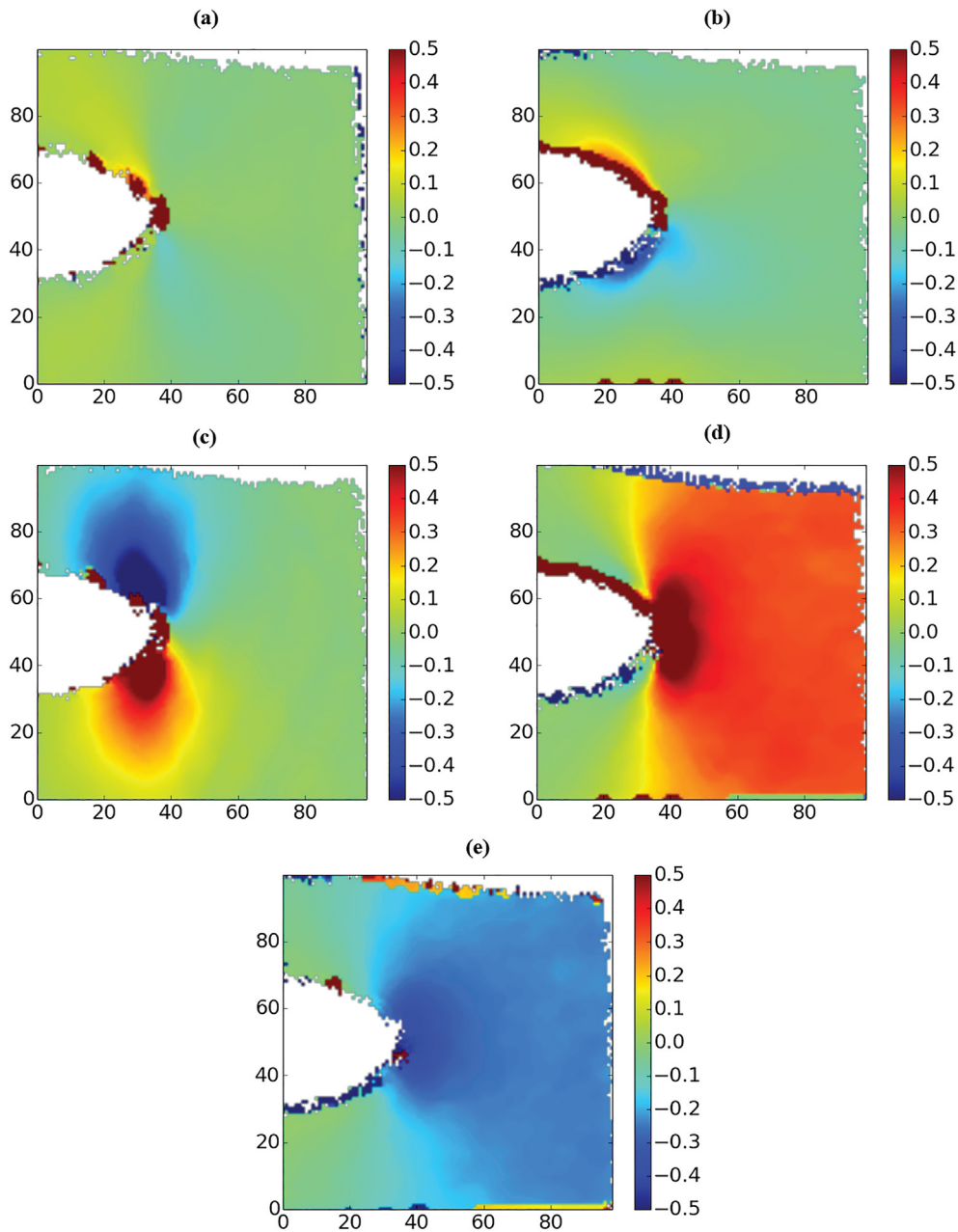


Fig. 2. Components of the displacement gradient  $(H)_{ij} = (F)_{ij} - \delta_{ij}$  for NR elongated by 40%:  $\partial U_1/\partial X_1$  (a),  $\partial U_1/\partial X_2$  (b),  $\partial U_2/\partial X_1$  (c),  $\partial U_2/\partial X_2$  (d) and finally  $\partial U_3/\partial X_3$  (e), which is calculated using incompressibility condition.

direction and the third coordinate is pointing perpendicular to the rubber surface. Using the definition of line integrals we obtain

$$J_1 = \int_0^1 \left[ -W_{el} \cos(2\pi s) - P_{ij} N_j \frac{\partial U_i}{\partial X_1} \right] 2\pi r ds = \int_0^1 (id_W + id_P) 2\pi r ds \tag{4}$$

The integrand in Eq. (4) consists of two parts: One part only depends on the energy density  $W_{el}$  and we denote it by  $id_W = -W_{el} \cos(\theta)$  with  $\theta = 2\pi s$ . The other part does not depend on the energy density but on the 1. Piola-Kirchhoff stress tensor  $P$  and the displacement gradient. This part, denoted  $id_P$  in the following, consists of four contributions representing the four in-plane components of the 1. Piola-Kirchhoff stress tensor.

### 3.2. Evaluation of the displacement fields

The evaluation of the displacement fields is performed using the programming language python. From the digital image correlation system ARAMIS we obtain for a mesh of undeformed coordinates  $X_j$  in the reference image the respective values of the coordinates after deformation  $x_i$ . With a mesh size of about 0.2 mm the resolution of this method is approximately 0.5 mm. For the derivative used to form the deformation gradient  $(F)_{ij} = dx_i/dX_j$  as well as later in the calculation of the line integral of  $J$  continuous values are needed. Therefore the deformed coordinates are interpolated with a spline function. This way we obtain the deformation gradient for all undeformed coordinates. The deformation gradient measures the change of the original coordinates to the new coordinates due to deformation [12]. The transfer to the deformation gradient for all deformed coordinates leads to some artefacts showing undefined values. For this reason and to smooth the data an averaging algorithm is used. This algorithm sets for an undefined value a reasonable average value of neighbouring points followed by small scale median filters. The components of the displacement gradient  $(H)_{ij} = (F)_{ij} - \delta_{ij}$  for NR elongated by 40% are shown in Fig. 2. The averaging algorithm is executed after each of the following calculation steps. From the deformation gradient the eigenvalues and eigenvectors  $b^{(n)}$  of the left Cauchy-Green Tensor  $B = F^T F$  are calculated. The principal strains  $\lambda_1$  and  $\lambda_2$  are obtained as square root of the eigenvalues. The third principal strain  $\lambda_3 = 1/(\lambda_1 \lambda_2)$  perpendicular to the sample surface is received from incompressibility condition.

### 3.3. Micromechanical modelling of stress softening and hysteresis

The energy density  $W_X$  and stress distribution  $P_{ij}$  are calculated using a recently proposed micromechanical model of stress softening and hysteresis [24]. The model can be applied to any deformations and is built on physical principles. The total energy density  $W_{tot}$  is the weighted sum of an elastic contribution  $W_{el} = (1 - \phi_{eff})W_X$  and a hysteretic one  $W_H$

$$W_{tot} = (1 - \phi_{eff}) W_X + \phi_{eff} W_H \tag{5}$$

where  $\phi_{eff}$  is the effective filler volume fraction. The effective filler volume exceeds the actual filler volume fraction because of occluded rubber. This part of the rubber is entrapped in the voids of the filler clusters and cannot follow the elastic deformation.

#### 3.3.1. Elastic contribution

The hyperelastic rubber matrix is implemented in this model by the extended non-affine tube model [9,14]

$$W(\bar{I}_1, \bar{I}^*) = \frac{G_c}{2} \left[ \frac{\left(1 - \frac{1}{n}\right) \bar{I}_1}{1 - \frac{1}{n} \bar{I}_1} + \log\left(1 - \frac{1}{n} \bar{I}_1\right) \right] + 2G_e \bar{I}^* \tag{6}$$

where  $G_c$  and  $G_e$  are the crosslinking-modulus and entanglement-modulus, respectively, and  $n$  is the average number of segments between trapped entanglements.  $\bar{I}_1 = \lambda_1^2 + \lambda_2^2 + \lambda_3^2 - 3$  and  $\bar{I}^* = \lambda_1^{-1} + \lambda_2^{-1} + \lambda_3^{-1} - 3$  are the first invariant and a generalized invariant of the left Cauchy-Green Tensor  $B$ , respectively. The elastic contribution  $W_X$  is given by the energy density  $W$  of the non-affine tube model in Eq. (6) but enhanced by amplification factors  $X$  representing the hydrodynamic amplification of the rubber matrix due to the presence of the filler

$$W_X(\bar{I}_1, \bar{I}^*, X_{max}) = \int_1^{X_{max}} P_X(X) W(X\bar{I}_1, X\bar{I}^*) dX \tag{7}$$

where  $X_{max}$  is the maximum amplification factor that varies with the maximum value of the first deformation invariant

$$X_{max} = \frac{n}{\bar{I}_1 + \gamma} \geq 1 \tag{8}$$

Here,  $\gamma$  is a free parameter that determines the maximum amplification factor  $X_{max} = n/\gamma$  before any deformation when the first deformation invariant is zero.  $P_X(X)$  is a normalized power law distribution of amplification factors given by:

$$P_X(X) = X^{-\chi} \frac{\chi - 1}{1 - X_{max}^{1-\chi}} \tag{9}$$

with  $\chi$  being the power law exponent. Stress softening is described by decreasing hydrodynamic amplification of the rubber matrix. When the maximal strain in the deformation history, and thereby the maximum value of the first invariant  $\bar{I}_1$ , is increasing,

the value of  $X_{\max}$  decreases and the normalized distribution  $P_X(X)$  is shifted to smaller amplification factors  $X$ . As the distribution  $P_X(X)$  changes during the first loading cycle the material law is not elastic in the sense that the material after the cycle is in the same state as before. Looking at the red lines in Fig. 2b shows that after the first cycle the material is at vanishing stress and strain, but the lower stress measured in the next cycle shows the inelasticity of Eq. (7). Nevertheless the material law is elastic when it is not the first time the material is subjected to the respective loading condition. Therefore we keep calling the quantities neglecting hysteretic contributions elastic. The elastic Cauchy stress  $\sigma_{el}$  is calculated from the amplified energy density  $W_X$  using the assumption of an incompressible material via

$$\sigma_{el} = \sum_{n=1}^3 \lambda_n \frac{\partial W_X}{\partial \lambda_n} \mathbf{b}^{(n)} \otimes \mathbf{b}^{(n)} - p \mathbf{1} \tag{10}$$

where  $p$  is a Lagrange multiplier ensuring the incompressibility constraint. With the boundary condition  $(\sigma_{el})_{33} = 0$  (no stress outside sample plane) its value is easily determined to be  $p = \lambda_3 \frac{\partial W_X}{\partial \lambda_3}$ . This tensor reflects the elastic stress required for the calculation of the J-Integral, Eq. (2), whereby the principal strains  $\lambda_n$  are taken from the digital image correlation measurements.

### 3.3.2. Hysteretic contribution

For fitting purposes the hysteretic part of the 1. Piola Kirchhoff stress  $\mathbf{P}_H$  is required. Rubber-filler structures are assumed to be stretched similar to the rubber matrix but break down and immediately re-aggregate at a critical fracture stress  $\sigma_c$ :

$$(\mathbf{P}_H)_{11} = \int_{-\infty}^{\zeta} \frac{1}{1 + \frac{\zeta - \zeta'}{\sigma_c}} \frac{d(\mathbf{P}_{el})_{11}(\zeta')}{d\zeta'} d\zeta' \quad \text{with} \quad \zeta = \int_{-\infty}^t |(\dot{\mathbf{P}}_{el})_{11}(t')| dt' \tag{11}$$

with  $\mathbf{P}_{el} = \sqrt{\det(\mathbf{B})} \sigma_{el} \mathbf{F}^{-T}$ . The critical stress corresponds to an energy barrier that has to be overcome to break a rubber-filler structure. The crossing of the energy barrier, which can be identified with a filler-filler or monomer-filler bonding energy, is driven by an external force. It is determined by the Kramer's escape rate, which may depend on temperature, time and deformation rate of the sample. More details of the model are found in [24,25].

## 4. Results and discussion

### 4.1. Parameter fitting

Multihysteresis measurements on dumbbell samples were done to obtain the material parameters. The dumbbells were elongated successively from 10% up to 100%, five times for each strain value. The measurement as well as the fits of the 5th cycle with the full and reduced model for the NR compound are displayed in Fig. 3a) and b), respectively. The full model shows good agreement with the measured 5th cycle and the fitting parameters appear reasonable. Regarding the polymer network we find  $G_c = 0.18$  MPa for the crosslinking modulus,  $G_e = 0.58$  MPa for the entanglement modulus and  $n = 40$  for the average number of statistical segments between trapped entanglements. The filler network is characterized by the effective filler volume fraction  $\phi_{eff} = 0.44$ , the finite extensibility parameter  $\gamma = 0.29$ , the power law exponent  $\chi = 2.35$  and the critical fracture stress  $\sigma_c = 0.066$  MPa.

In the evaluation of the displacement fields, entering the J-Integral, we only compare the start point of an equilibrium cycle with the point in that cycle at maximal strain. In these points the loading and the unloading curve coincide. This corresponds to unstressed rubber-filler structures and a vanishing hysteretic stress  $P_H$ . The calculation of the J-Integral for other points in the cycle would require considering the hysteretic contribution. In this case the separate handling of loading and unloading would be necessary.

Therefore it is convenient to perform a reduced fitting procedure that considers stress-softening, because the hysteresis

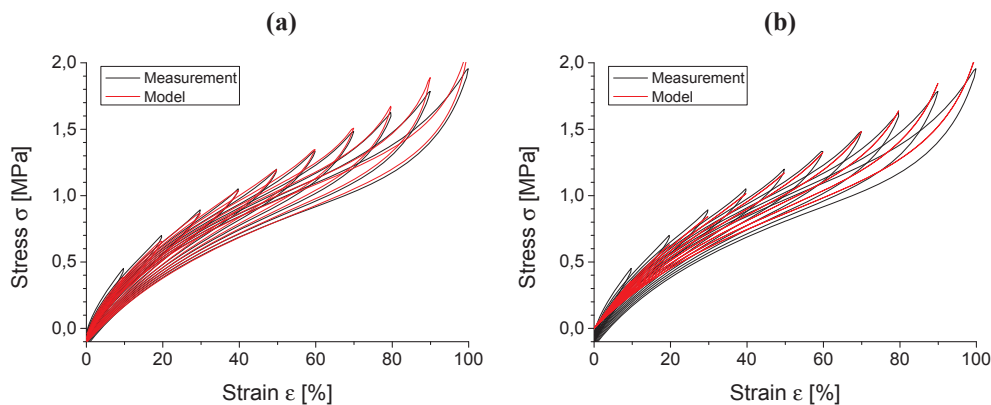


Fig. 3. Multihysteresis measurement of the NR compound performed with a dumbbell sample and fitting obtained with the micromechanical model (a); reduced fitting procedure with the pure stress-softening model without hysteresis (b).

contribution is not formulated as energy functional. This means that the free energy entering the J-integral can only be reconstructed by a complex numerical integration of the stress fields. Therefore, the critical fracture stress  $\sigma_c$  is set to zero so that hysteretic contributions are not considered. Then, the stress-strain behaviour of the model is lying in between the loading and unloading curves. The parameters  $n$  and  $\phi_{\text{eff}}$  are set to the fixed values as determined above, because they can hardly be fitted. The first parameter requires larger strain values, which have to be avoided due to strain-induced crystallization effects not considered by the model. The second parameter is not determined if hysteresis contributions are neglected (Eq. (5)). A fit of the 5th cycle by using the reduced fitting procedure with  $\sigma_c = 0$  is shown in Fig. 3b), whereby the stress-strain curves are fitted to the average between loading and unloading curve. Obviously, the quality of the fit is worse, but the basic features of stress softening are reflected well. The parameters of the reduced fitting procedure for all compounds are listed in Table 2.

#### 4.2. Power law behaviour

At  $X_2 = 0$  stress, strain and energy density increase significantly when approaching the crack tip, which is exemplified for the NR compound in Fig. 4. In particular, Fig. 4a) shows that  $\Delta P_{22} = P_{22} - P_\infty$  vs.  $r$  follows power law behaviour at  $X_2 = 0$  for distances greater than approximately 1 mm in front of the crack tip. Here,  $P_\infty$  is the value of  $P_{22}$  far away from the crack tip, just below the lowest value of  $P_{22}$ . The exponent  $\alpha$  and the value at infinite distance from the crack tip  $P_\infty$  can be found by minimizing the error of a power law fit function with variable start point at  $r < 2$  mm and fixed end point at  $r = 8$  mm. The determination is very rough as the exponents depend strongly on the values of  $P_\infty$ . Closer to the crack tip the stress increase deviates from this power law behaviour as the underlying strain fields does (see below). The exponent of  $\Delta P_{22}$  vs.  $r$  is changing from  $\alpha = -0.58$  for the low strain to  $\alpha = -0.22$  for the highly strained sample. The decay of the exponent  $\alpha$  with increasing strain is due to the blunting of the crack tip. These exponents differ from  $\alpha = -0.5$  as expected from linear elastic fracture mechanics [1]:

$$P_{ij} = \frac{K}{\sqrt{2\pi r}} f_{ij}(\theta) r^\alpha \quad (12)$$

Here,  $K$  is the stress intensity factor and  $f_{ij}(\theta) \approx 1$  is a weak function of the planar angle  $\theta$ . It must be noted that the exponent  $\alpha = -0.5$  is calculated without any geometrical constraints. In our experiments with pure shear samples this is not the case and the restricted deformation in crack growth direction might affect the exponent.

Evaluating the displacement fields with the ARAMIS software delivers reasonable strain fields up to the distance of ca. 0.5 mm. Fig. 4b) displays power law behaviour also for  $\Delta \epsilon_{22} = \epsilon_{22} - \epsilon_\infty$  vs.  $r$  at  $X_2 = 0$  in front of the crack tip. Here,  $\epsilon_{22}$  is  $dU_2/dX_2$  and  $\epsilon_\infty$  is the value of  $dU_2/dX_2$  far away from the crack tip, which is set appropriately, just below the lowest value of  $dU_2/dX_2$ . Closer than approximately 1–1.5 mm to the crack tip the measured strains are no longer following this power law but increase well pronounced. The region where the modelled stress fields show reasonable results coincides with the region of suitable strain fields. The exponent of  $\Delta \epsilon_{22}$  vs.  $r$  varies between  $\beta = -2.0$  and  $\beta = -0.9$  with a decreasing slope for the higher strained sample. The exponent  $\beta$  also strongly deviates from  $\beta = -0.5$  as expected from linear elasticity [1]. Accordingly, stress softening modifies the stress and strain fields around the crack tip significantly.

In Fig. 4c) a similar power law behaviour of the energy density  $\Delta W_{\text{el}} = W_{\text{el}} - W_\infty$  vs.  $r$  at  $X_2 = 0$  is shown.  $W_\infty$  denotes the energy density far away from the crack tip. As the strain and stress fields are underrated closer than 1–1.5 mm from the crack tip, the same is true for the energy density  $W_{\text{el}}$ . The exponent varies from  $\delta = -2.4$  for low straining to  $\delta = -1.0$  for higher straining.

The change of the three exponents  $\alpha, \beta$  and  $\delta$  with strain is summarized in Fig. 4d). At small strain values, the obtained exponents for strain are almost four times larger than the elastic reference value  $-0.5$ , indicating a more pronounced singular behaviour due to strong stress softening effects. At higher strain amplitudes this is less pronounced since the level of stress and strain is larger far away from the crack tip. This implies that less stress softening can appear when approaching the crack tip.

#### 4.3. Components of the J-Integral

As specified in Eq. (4),  $J_1$  consists of several components. These components are analysed in this chapter in more detail exemplarily for the NR compound strained to 20%. For circles around the crack tip the integrand can be displayed graphically (Fig. 7) and we yield  $J_1$  simply as integration over the integrand on a circular path. The integrand consist of two parts, one part  $id_w$  only depends on the energy density  $W_{\text{el}}$ , the other part  $id_p$  depends on the 1. Piola-Kirchhoff stress tensor  $\mathbf{P}$  and the deformation gradient  $dU_i/dX_1$ . Both terms again are formed by multiplication of different terms. The energy density distribution  $W_{\text{el}}$  is exemplified for the NR at 20% strain in Fig. 5a).

The energy density component is given by  $id_w = -W_{\text{el}} \cos(\theta)$ , whereby the trigonometric function  $\cos(\theta)$  is maximal for  $\theta = \pi$  (in

**Table 2**

Fitting parameters of the four truck tire tread compounds with the pure stress-softening model without hysteresis.

Compound	$G_c$ [MPa]	$G_e$ [MPa]	$n$	$\phi_{\text{eff}}$	$\chi$	$\gamma$
NR	0.166	0.458	40	0.44	2.10	0.408
N55B45	0.224	0.547	40	0.44	2.09	0.437
N55S45	0.215	0.297	40	0.44	1.89	0.732
N55BS23	0.221	0.467	40	0.44	2.09	0.474

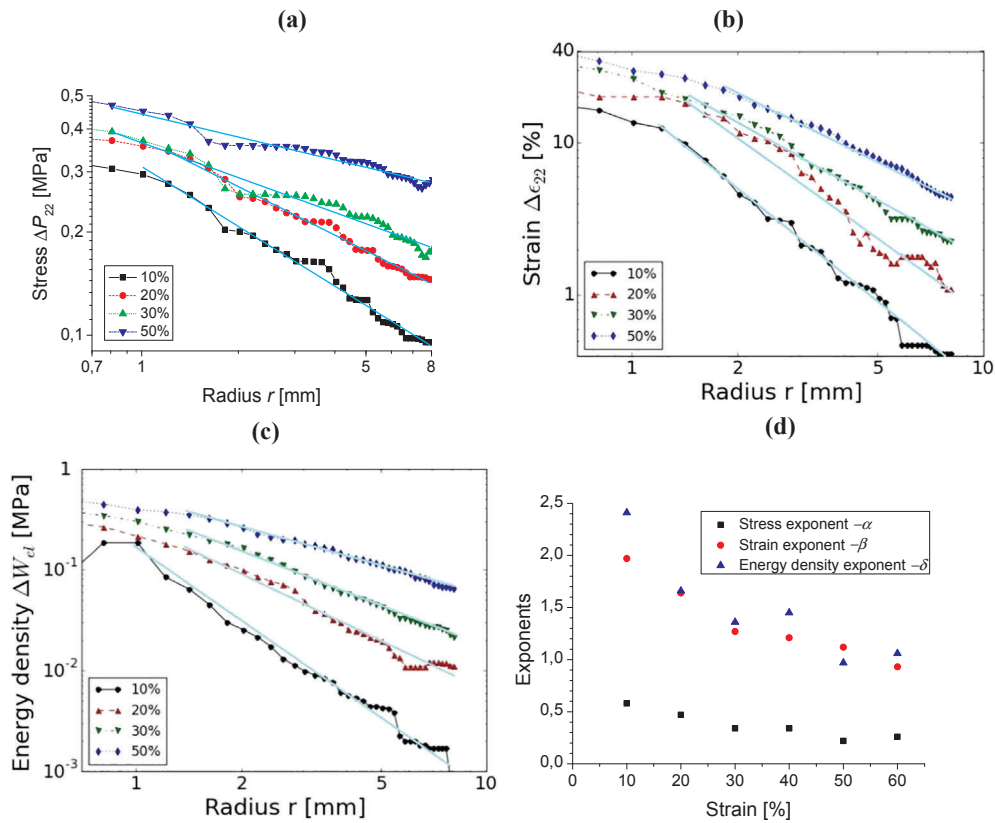


Fig. 4. Log-log plots of the stress increase  $\Delta P_{22} = P_{22} - P_{\infty}$  (a), strain increase  $\Delta \epsilon_{22} = \epsilon_{22} - \epsilon_{\infty}$  (b) and energy density increase  $\Delta W_{el} = W_{el} - W_{\infty}$  (c) while approaching the crack tip at  $X_2 = 0$ . The straight lines indicate power law behaviour with varying distance  $r$  from the crack tip with decreasing exponent for rising stretching from 10%, 20%, 30% to 50%. The changes of the three exponents with strain are summarized in (d).

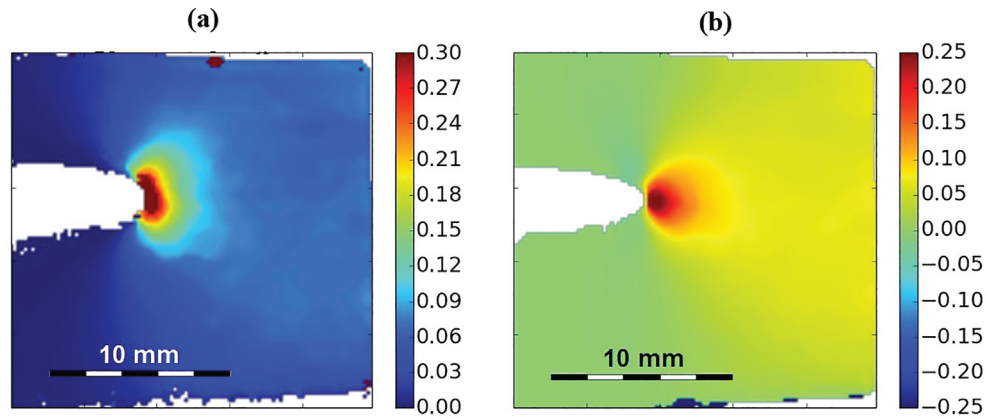


Fig. 5. Energy density  $W_{el}$  (a) and energy density component  $id_W = -W_{el} \cos(\varphi)$  (b) for the compound NR elongated by 20%.

direction of the crack) and vanishes for  $\theta = \pm \pi/2$  (perpendicular to the crack). Accordingly,  $id_W$  shown in Fig. 5b) is more confined toward the direction of crack growth compared to  $W_{el}$ . Far away in front of the crack tip  $W_{el}$  and also  $id_W$  take the value  $W_{\infty}$  on the whole height  $h$  of the sample. The term  $id_W$  is thus the origin of the value  $W_{\infty} h$  which appears as J-Integral of infinite long Pure Shear samples in agreement with the value of the tearing energy  $T$  for Pure Shear samples.

The stress component  $id_p = -P_{ij}N_j \partial U_i / \partial X_1$  consist of four contributions corresponding to the in-plane components  $P_{11}$ ,  $P_{12}$ ,  $P_{21}$  and  $P_{22}$ . The stress term  $P_{22}$  is the largest. The shear stress terms  $P_{12}$  and  $P_{21}$  are quite small and have only appreciable values perpendicular to the crack.  $P_{21}$  is multiplied with  $-N_1 = \cos(\theta)$  which vanishes perpendicular to the crack so that its contribution anywhere is quite moderate. The term  $\partial U_i / \partial X_1$  is comparatively small, especially close to the direction of crack growth. The terms  $P_{11}$  and  $P_{12}$  are multiplied with this term. The contribution of  $P_{11}$  is quite moderate because this stress term is largest close to the

direction of crack growth where  $\partial U_1/\partial X_1$  vanishes. The contribution of  $P_{12}$  is also quite moderate as neither of the factors is large. The stress term  $P_{22}$  on the contrary is large and it is multiplied by  $\partial U_2/\partial X_1$  which has significant contributions perpendicular to the crack tip (Fig. 6a) and b)). The term  $-N_2 = \sin(\theta)$  has its extremal values perpendicular to the crack. The negative values of  $\partial U_2/\partial X_1$  in the upper half plane are multiplied with the negative sinus so that the term  $id_{p22} = -P_{22}n_2\partial U_2/\partial X_1$  has no negative values (Fig. 6c)). Due to the sinus function the values close to the crack growth direction are small and  $id_{p22}$  is divided into an upper part and a lower part. The term  $id_{p22}$  is dominating the stress component to the integrand  $id_p$  (Fig. 6d)). Between  $id_{p22}$  and  $id_p$  there is hardly any difference recognizable.

The total integrand for NR stretched to 20% and to 50% is shown in Fig. 7a) and b), respectively. The more evenly yellowish colouring in the right side of the figures and the high values directly in front of the crack tip are mainly caused by the energy density component  $id_w$ . The high values at the sides of the crack tip come from the stress component  $id_p$ , which is rising faster with increasing straining than  $id_w$  so that the near field is more and more dominated by  $id_p$ . But in the far field is  $id_w$  is the only significant contribution.

#### 4.4. The J-Integral

Fig. 8 shows the obtained J-Integral values vs. contour radius for all compounds. It demonstrates that the J-Integral is not path-independent but increases for small radii until a plateau value is reached. These plateau values match fairly well with the global tearing energy  $T = W_\infty \cdot h$  especially for lower strain amplitudes. Naturally both  $J_1$  and  $T$  are expected to increase with rising strain amplitude. But at higher strains the increase of the plateau value of  $J_1$  is more pronounced so that the energy density component  $id_w$  is surmounting the global value  $T$ . The reason for this systematic deviation between  $J_1$  and  $T$  at higher strain amplitudes is not clearly understood, since the energy density  $W_\infty$  in a region far away from the crack tip is entering both quantities, implying that the energy density component  $id_w$  determines  $J_1$  and stress-softening can be neglected. For purely elastic materials one expects  $J_1 = W_\infty \cdot h$  [26], which should be fulfilled for all strain amplitudes. Mars et al. [19] showed that the factor  $k$  in the tearing energy of a single edge notched strip sample  $T = 2kW_{el}c$  depends on the Mullins effect describing the stress softening of elastomers. The larger the stress softening is implemented, the more the factor  $k$  surmounts the value  $\pi/\sqrt{\lambda}$ . A similar increase of tearing energy due to stress softening could explain that the J-Integral values at large strains exceed the global values given by  $T = W_{el}h$ . Also impacts due to the specimen borders or the clamping are possible.

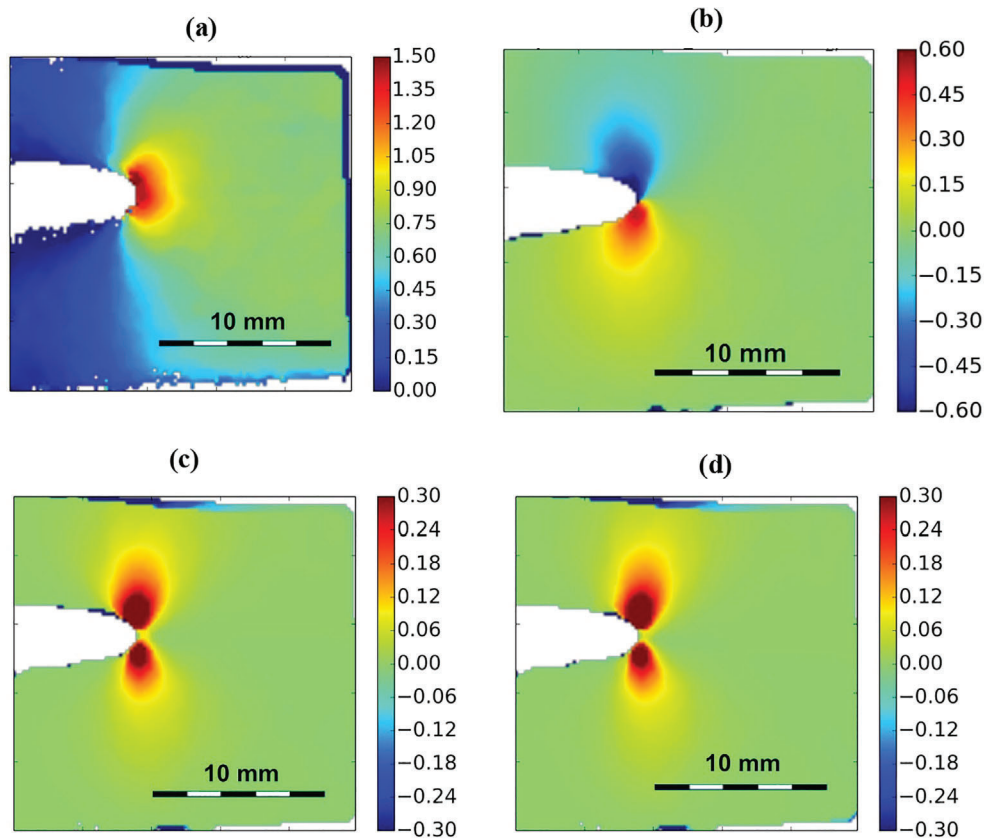


Fig. 6. Stress component  $P_{22}$  (a) and displacement gradient  $\partial U_2/\partial X_1$  (b) for the compound NR strained to 20%. Their multiplication with  $\sin(\varphi)$  yields  $id_{p22}$  (c), the dominant term in the stress component of the integrand  $id_p$  (d).

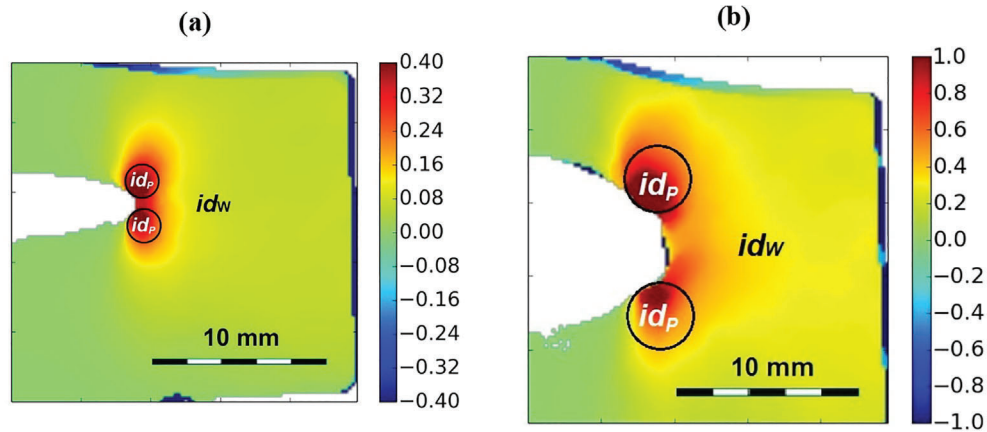


Fig. 7. Integrand of  $J_1$  for the compound NR elongated by 20% (a) and 50% (b). It is marked where the respective components are dominating.  $J_1$  follows as integral around circular paths  $\Gamma$ .

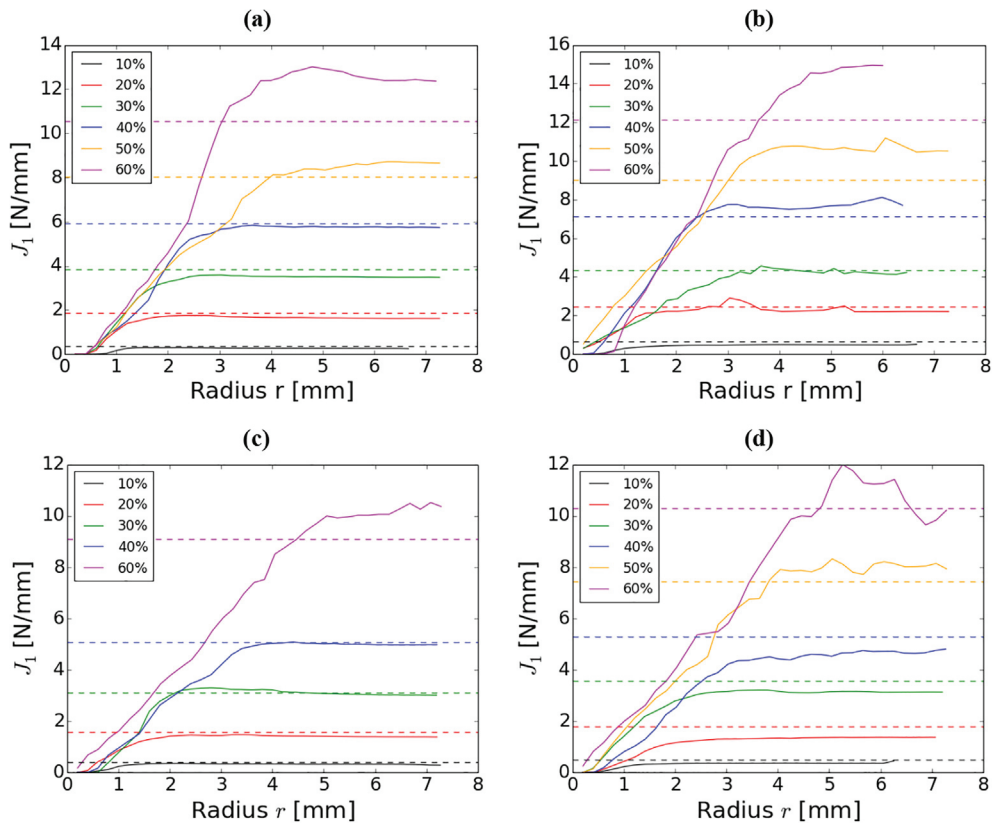


Fig. 8.  $J_1$  for strain amplitudes between 10% and 60% for NR (a), N55B45 (b), N55S45 (c), and N55BS23 (d). The global tearing energy  $T = W_\infty \cdot h$  for different strain amplitudes is shown as dashed lines for comparison.

A systematic decrease of the J-Integral occurs if the radius of the contour decreases and approaches zero. The difference of  $J_1$  for two different radii corresponds to the energy dissipated in the area between the two integration paths. In the case of invariant translation of the strain variable with a crack moving with constant velocity  $v$ , the energy dissipated between two circular contours  $\Gamma_1$  and  $\Gamma_2$  of different size  $r$  per unit time and sample thickness is given by the difference of the corresponding J-Integrals multiplied by  $v$  [4]. In this approach the crack velocity is considered to be constant, but in our investigations the crack velocity increases during stretching and decreases upon retraction. Therefore the amount of dissipated energy and the size of the dissipation regime are changing during a stretching cycle, implying that the J-Integral concept can't be applied in a strict sense. Although the crack velocity is not constant, but very small and its time dependency is unknown, we can evaluate the J-Integral in a short time interval at maximum strain by referring to an average crack velocity.

The observed increase of the J-Integral in Fig. 8 indicates that, in contrast to purely elastic materials, most of the elastic energy is dissipated in the region around the crack tip of filled elastomers and only a small amount is available for crack propagation. The increase of the J-Integral is due to the fact that the dissipating terms are not directly taken into account within the calculation of the J-Integral, though the differences for varying radii reflect the missing dissipated energy. The data indicate that more than 90% of the elastic energy is dissipated in the stress-softening area around the crack tip. A more exact evaluation how much of the energy is dissipated and how much is reaching the process zone cannot be quantified, as the behaviour of  $J_1$  closer to the crack tip is questionable. As discussed before, the J-Integral values below 0.5 mm contour radius are underrated due to insufficient resolution. Only finite strains being recorded yield  $J_1 \rightarrow 0$  for  $r \rightarrow 0$ . The exact progression of the  $J_1(r)$  curves towards zero contour radii depends also strongly on the positioning of the centres of the integration circles. From a theoretical point of view, the centres need to be placed at the crack tip, but the exact position of the crack tip is hard to determine. When the centre of the integration circle is moved slightly, highly strained areas can be included or excluded in the calculations of  $J_1$  for small circles so that the progression of the  $J_1(r)$  curves for small radii is changing. This uncertainty may also lead to the observed intersections of the J-Integrals for different strain amplitudes, which become apparent e.g. in Fig. 8b).

Fig. 9a) and b) compare  $J_1$  in dependence of the contour area  $A = \pi r^2$  for all compounds at 20% and 40% strain amplitude, respectively. The plateau values of  $J_1$  as well as  $T$  correlate with the stiffness of the different compounds, as reflected by the fitted values of the moduli  $G_c$  and  $G_e$  listed in Table 2. Accordingly, compound N55B45 is the stiffest and N55S45 is the least stiff compound. The difference of  $J_1$  integrated over two contours  $\Gamma_1$  and  $\Gamma_2$  is a linear measure of the dissipated energy in the cylindrical shell between  $\Gamma_1$  and  $\Gamma_2$ . Obviously, the slope of  $J_1(A)$  becomes larger close to the crack tip, indicating that the dissipated energy density is higher for the more strained regions close to the crack tip. We point out that the difference of  $J_1$  integrated over two contours  $\Gamma_1$  and  $\Gamma_2$  far away from the crack tip is vanishing. This shows that far away from the crack tip no significant energy dissipation occurs.

4.5. Crack deviation and strain-induced crystallization

The first component of the J-Integral (Eq. (1)) corresponds to the tearing energy for displacement of the crack tip in  $x_1$ -direction. This describes crack growth in direction of the crack. In contrast to that the second component of the J-Integral (Eq. (1))

$$J_2 = \oint_{\Gamma} \left[ W_{ei}N_2 - P_{ij}N_j \frac{\partial U_i}{\partial X_2} \right] d\Gamma \tag{13}$$

corresponds to a displacement of the crack tip in  $X_2$ -direction. In this case the whole crack is shifted in  $X_2$ -direction [15]. Nevertheless can the crack deflection angle of the crack in linear elastic fracture mechanics and for  $J_2 \ll J_1$  be connected to the ratio  $J_2/J_1$ . Integrating over circular paths and evaluating the line integral we obtain for  $J_2$  an equation analogous to Eq. (4):

$$J_2 = \int_0^1 \left[ -W_{ei} \sin(2\pi s) - P_{ij}N_j \frac{\partial U_i}{\partial X_2} \right] 2\pi r \, ds = \int_0^1 (id_w + id_p) 2\pi r \, ds \tag{14}$$

For this component  $id_w$  is calculated with the sinus and  $id_p$  uses the components  $\partial U_i / \partial X_2$  of the displacement gradient towards the second axis.  $id_w$  and  $id_p$  for the second component of the J-Integral are shown in Fig. 10a) and b), respectively. Both terms have a similar kind of dumbbell distribution at the sides of the crack tip.  $id_w$  is positive above the crack and negative below, but  $id_p$  is negative above the crack and positive below. Therefore the resulting integrand (Fig. 10c)) reaches lower absolute values. The second component of the J-Integral is comparatively small as the negative and positive values of the integrand above and below the crack, respectively, mainly counterbalance each other. The crack should therefore propagate preferentially perpendicular to the stretching direction. NR shows compared to the synthetic rubbers an increased tendency for the crack to deviate in stretching direction, which seems to be related to strain-induced crystallization of NR.

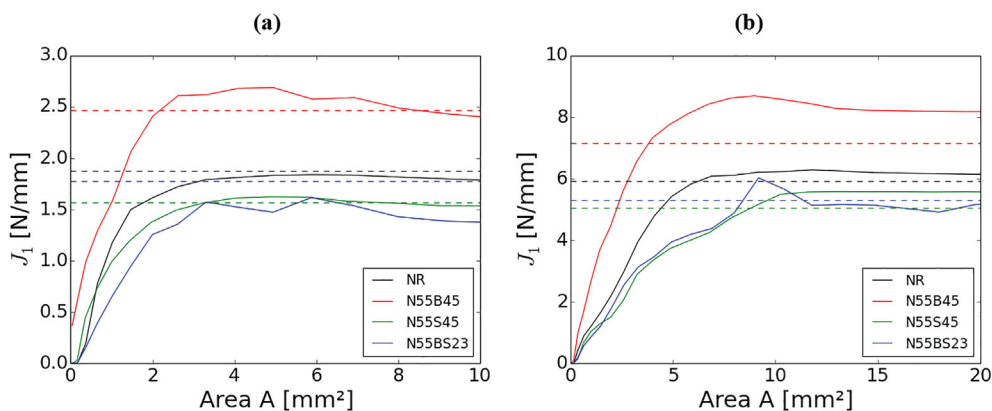


Fig. 9.  $J_1$  for the different compounds at 20% (a) and 40% (b) strain amplitude in dependence of the encircled area  $A = \pi r^2$  of the integration path  $\Gamma$ . The global tearing energies  $T = W_{\infty} \cdot h$  for the different compounds are shown as dashed lines for comparison.



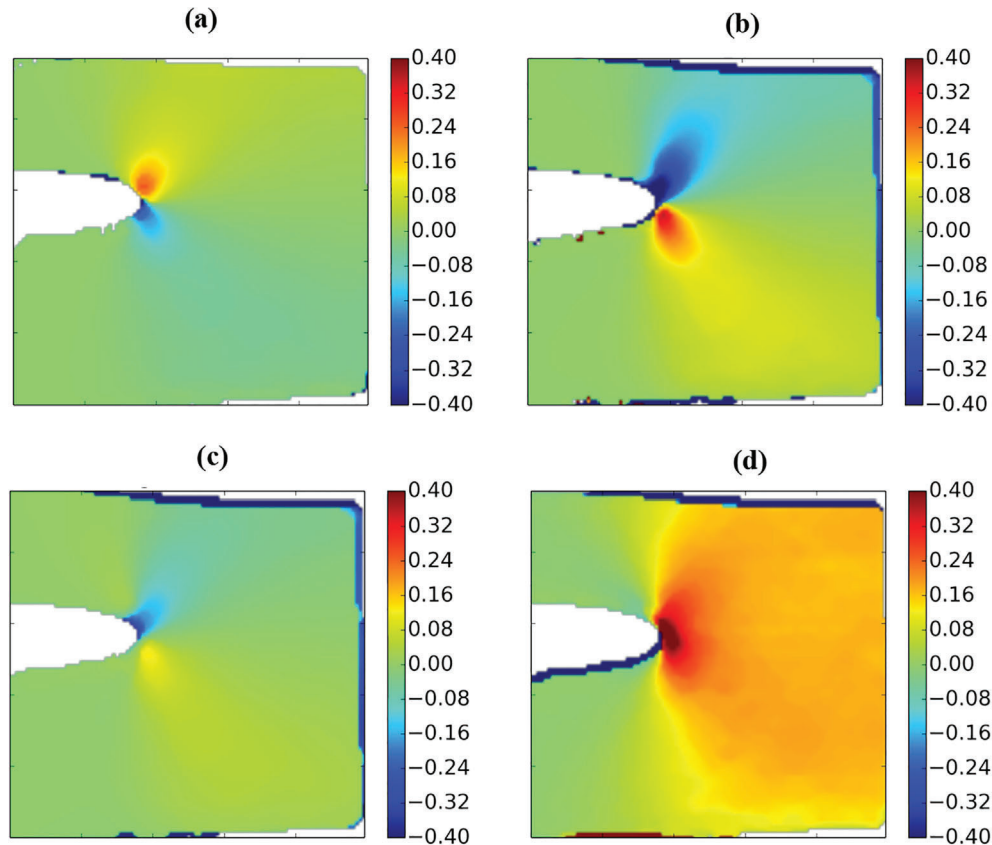


Fig. 10. Crack deviation: energy density component  $id_w = -W_{el} \sin(\varphi)$  (a), stress component  $id_p$  (b) and total integrand (c) of  $J_2$  and displacement gradient  $\partial U_2 / \partial X_2$  (d) for the NR compound elongated by 20%.

In filled NR sideways cracks are observed [18,5]: When stretching the rubber cracks start to grow in stretching direction instead of crack growth in direction of the crack. Such crack deviation needs a high anisotropy in strength. Ordered chains as they appear due to strain-induced crystallization increase the resistance against crack growth.

A possible explanation for crack deviation could be the distinct distribution of the stress components. The component of the displacement gradient  $\partial U_2 / \partial X_2$  in stretching direction is largest in front of the crack tip (Fig. 10d)). This strain leads to crystallization. The shear component  $\partial U_2 / \partial X_1$  is dominant laterally of the crack tip (Fig. 6b). Since strain-induced crystallization mainly results from chain stretching during uniaxial straining and is less sensitive to shear strain, this leads to a lower reinforcement by crystallization laterally of the crack tip so that crack deviation is increased compared to non-crystallizing rubbers.

## 5. Summary and conclusions

The effect of energy dissipation due to stress-softening of carbon-black filled truck tire tread compounds based on NR and blends of NR with BR and/or SBR on the available energy for crack propagation has been evaluated based on the J-Integral,  $J_1$ , pointing into crack growth direction perpendicular to the stretching direction. The J-Integral describes the tearing energy available for crack growth by integrating the energy flux into the crack tip through closed contours around the crack tip, here chosen as circular paths with varying radius  $r$ . Although the J-Integral concept can't be applied to experimental setups with cyclic loading and varying crack growth velocities in a strict sense, we have obtained reasonable results reflecting the energy dissipation around the crack tip. The path independence of the J-Integral as found for purely elastic materials is not obtained indicating that the differences can be related to viscoelastic effects of filled rubbers.

The J-Integral requires the elastic energy density, displacement gradient and stress field around the crack tip. Accordingly, the displacement fields around the crack tip are measured at notched Pure Shear samples by using the digital image correlation system ARAMIS. Up to around 0.5 mm from the crack tip reasonable resolution is achieved. A physically based model of stress softening is used to calculate the energy density and stress distribution surrounding the crack tip, which also enter into the J-Integral.

It is found that stress, strain and energy density values increase according to power laws when approaching the crack tip. The exponents differ significantly from the expectations from purely elastic material behaviour and depend on the applied strain. At small strain values, the obtained exponents for strain are almost four times larger than the elastic reference value  $-0.5$ , indicating a more pronounced singular behaviour due to strong stress softening effects. At higher strain amplitudes this is less pronounced since the

level of strain is larger far away from the crack tip, implying that less stress softening due to filler cluster breakdown can appear when approaching the crack tip. The singular behaviour can only be analysed as long the deformations can be recorded reasonably.

The components of  $J_1$  have been evaluated in some detail. The integrand of  $J_1$  is a sum of two contributions, the term  $id_W$  depending on the elastic energy density and the term  $id_p$  depending on stress and displacement gradient.  $id_W$  is responsible for contributions of  $J_1$  centrally in front of the crack tip and for the far field contribution. It is the dominant contribution to the value of  $J_1$  far away from the crack tip, i.e. the global value  $T$ .  $id_p$  is dominated by the stress component  $P_{22}$  and contributes significantly only laterally to the crack tip.

The J-Integral allows for the consideration of energy dissipation mechanisms close to the crack tip that lower the available energy for crack growth. The J-Integral, being path-independent for purely elastic materials, is found to increase significantly for circular paths around the crack tip with increasing size  $r$  until a plateau is reached. This indicates that most of the elastic energy is not available for crack growth since more than 90% is dissipated in the stress-softening area around the crack tip. The plateau value of  $J_1$  coincides with the global tearing energy  $T$  for smaller strain amplitudes. For strain amplitudes larger than 40%, the plateau value of  $J_1$  is found systematically larger than the global tearing energy  $T$  for all compounds.

### Acknowledgements

We would like to thank our project partners IPF Dresden and Continental AG for the very good cooperation. Continental is appreciated for mixing the compound in industrial scale. The Deutsche Forschungsgemeinschaft (DFG) is appreciated for financial support (grant KL 1409/9-1).

### References

- [1] Anderson TL. Fracture mechanics. Boca Raton, USA: CRC Press; 1995.
- [2] Cherepanov GP. Crack propagation in continuous media. *J Appl Math Mech* 1967;31:503–12.
- [3] El Yaagoubi M, Juhre D, Meier J, Alshuth T, Giese U. Prediction of tearing energy in mode III for filled elastomers. *Theor Appl Fract Mech* 2017;88:31–8.
- [4] Freund LB. Dynamic fracture mechanics. Cambridge University Press; 1998.
- [5] Gent AN, Razzaghi-Kashani M, Hamed GR. Why do cracks turn sideways? *Rubber Chem Technol* 2003;76:122–31.
- [6] Grellmann W, Reincke K, Lach R, Heinrich G. Characterization of crack toughness behaviour of unfilled and filled elastomers. *Kautsch Gummi Kunstst* 2001;54:387–93.
- [7] Griffith AA. The phenomena of rupture and flow in solids. *Philos Trans R Soc London A* 1921;221:163–98.
- [8] Harbour RJ, Fatemi A, Mars WV. The effect of a dwell period on fatigue crack growth rates in filled SBR and NR. *Rubber Chem Technol* 2007;80:838–53.
- [9] Heinrich G, Kaliske M. Theoretical and numerical formulation of a molecular based constitutive tube-model of rubber elasticity. *Comput Theor Polym Sci* 1997;7(3/4):227–41.
- [10] Horst T, Reincke K, Illisch S, Heinrich G, Grellmann W. Fracture surface statistics of filled elastomers. *Phys. Rev. E* 2009;80:046120.
- [11] Hess WM, Scott CE, Callan JE. Carbon black distribution in elastomer blends. *Rubber Chem Technol* 1967;40:371.
- [12] Holzapfel GA. Nonlinear solid mechanics. Hoboken, USA: Wiley; 2000.
- [13] Klüppel M. Evaluation of viscoelastic master curves of filled elastomers and applications to fracture mechanics. *J Phys Condens Matter* 2009;21. 035104 (10pp).
- [14] Klüppel M, Schramm J. A generalized tube model of rubber elasticity and stress softening of filler reinforced elastomer systems. *Macromol Theory Simul* 2000;9(9):742–54.
- [15] Kuna M. Finite elements in fracture mechanics. Dordrecht, Netherlands: Springer; 2013.
- [16] Liu C, Zhang L-Q, Zheng Q, Wu Y-P. Influence of strain amplification near crack tip on the fracture resistance of carbon black-filled SBR. *Rubber Chem Technol* 2015;88:276–88.
- [17] Lorenz H, Steinhauser D, Klüppel M. Morphology and micro-mechanics of filled elastomer blends: impact on dynamic crack propagation. In Grellmann W, Heinrich G, Kaliske M, Klüppel M, Schneider K, Vilgis TA, editor. *Fracture Mechanics and Statistical Mechanics of Reinforced Elastomeric Blends. Lecture Notes in Applied and Computational Mechanics* 2013;70:81–128 [Chapter 3].
- [18] Marano C, Boggio M, Cazzoni E, Rink M. Fracture phenomenology and toughness of filled natural rubber compounds via the pure shear test specimen. *Rubber Chem Technol* 2014;87:501–15.
- [19] Mars WV, Cheng XZ, Yang H, Zhang LQ. Influence of cyclic softening on the energy release rate of an edge crack under simple tension. *Constit Models Rubber* 2013;VIII:371.
- [20] Maugin GA. Material forces: concepts and applications. *Appl Mech Rev* 1995;48:213–45.
- [21] Meier JG, Klüppel M, Geisler H, Schuster RH. Kieselsäuregefüllte Elastomerblends durch Masterbatchtechnologie. *Kautsch Gummi Kunstst* 2005;58:587.
- [22] Persson BNJ, Brener EA. Crack propagation in viscoelastic solids. *Phys Rev E* 2005;71:036123.
- [23] Persson BNJ, Ahlbor O, Heinrich G, Ueba H. Crack propagation in rubber-like materials. *J Phys Condens Matter* 2005;17:R1071.
- [24] Plagge J, Klüppel M. A physically based model of stress softening and hysteresis of filled rubber including rate- and temperature dependency. *Int J Plast* 2017;89:173–96.
- [25] Plagge J, Klüppel M. A hyperelastic physically based model for filled elastomers including continuous damage effects and viscoelasticity. *Constit Models Rubber* 2017;X:559.
- [26] Rice JR. A path independent integral and the approximate analysis of strain concentration by notches and cracks. *J Appl Math Mech* 1968;35:379–86.
- [27] Rivlin RS, Thomas AG. Rupture of Rubber. I. Characteristic energy for tearing. *J Polym Sci* 1953;10:291–318.
- [28] Vilgis TA, Heinrich G, Klüppel M. Reinforcement of polymer nano-composites: theory, experiments and applications. Cambridge University Press; 2009.
- [29] Wunde M, Klüppel M. Influence of phase morphology and filler distribution in NR/BR and NR/SBR blends on fracture mechanical properties. *Rubber Chem Technol* 2016;89:588–607.
- [30] Wunde M, Klüppel M. Impact of mixing procedure on phase morphology and fracture mechanical properties of carbon black-filled NR/SBR blends. *Continuum Mech Thermodyn* 2017;29:1135–48.
- [31] Wunde M, Klüppel M. Viscoelastic response during crack propagation of unfilled and filled SBR. *Rubber Chem Technol* 2018:accepted.
- [32] Zehnder AT. Fracture mechanics. *Lect Notes Appl Comput Mech* 2012;62:33–54.

#### 4.4 Supplementary information

TIRE TESTS. Truck tire tests were performed for the tire compounds presented in the last publication and in chapter 3.5. For this reason tires of the dimension 205/ R17.5 CHS3 124 L were constructed and heated at 145°C for around 35 minutes. For the Chip & Cut test of each compound four tires are mounted on the rear axle of a truck. The tires are loaded by 1300 kg at a filling pressure of 7.5 bar at around 40 km/h. The test track consists of stones in the dimension between 10 and 30 mm. The stones are mostly sharp and hard rocks. The rating of the truck tire treads is based on the wear appearance after testing. These are shown exemplarily in Fig. 4.1. The rating of Chip & Cut resistance is: RNR, RN55S45, RN55B23S23 and RN55B45.[109] This rating of the tire tests is in agreement with the crack growth rates measured on the laboratory compounds for very high tearing energies  $>6$  N/mm (Fig. 4.2). The findings of the tire tests also correlate to the results of the instrumented Chip & Cut test explained in [108].[109]

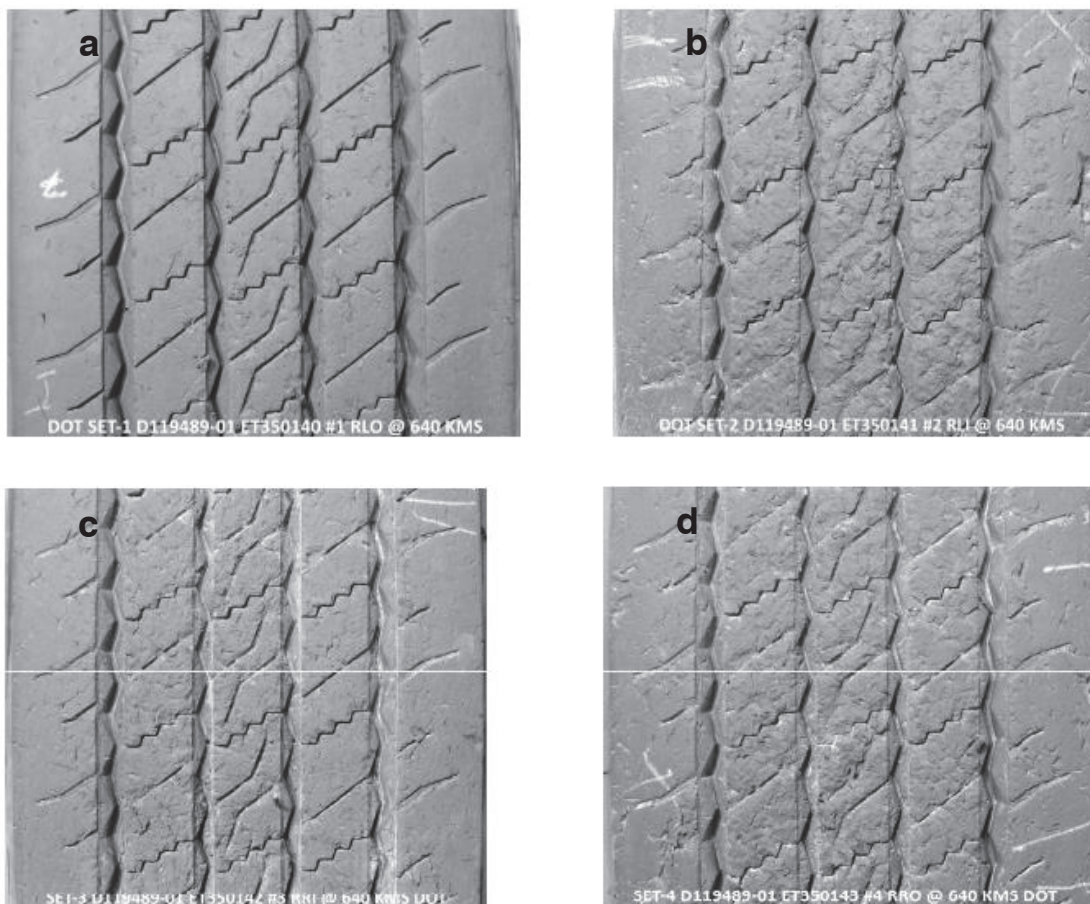


Fig. 4.1: Tire treads after Chip & Cut test: RNR (a), RN55B45 (b), RN55S45 (c) and RN55B23S23 (d). The ranking is: RNR, RN55S45, RN55B23S23 and RN55B45.[109]

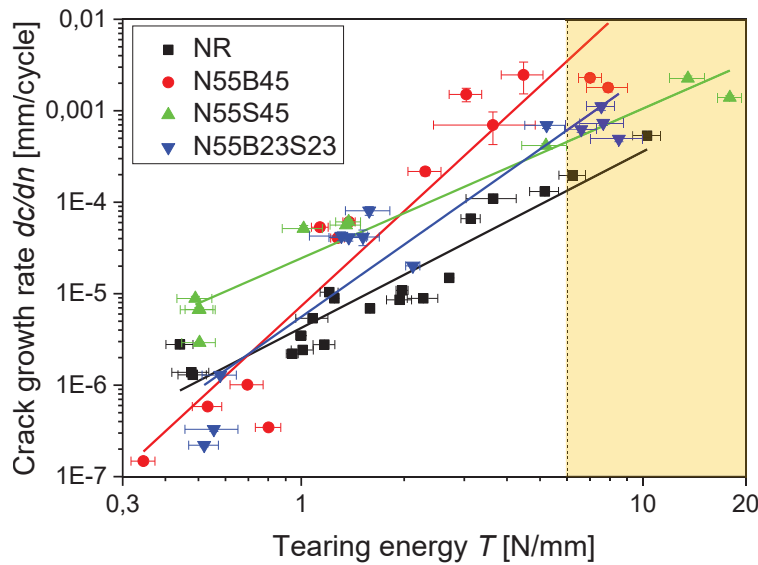


Fig. 4.2: Paris-plot of the laboratory compounds NR, N55B45, N55S45 and N55B23S23. In the colored area of very high tearing energies  $>6$  N/mm the same ranking as in the tire tests (Fig. 4.1) is obtained.[109]

MORE QUANTITIES DETERMINED IN THE CALCULATION OF THE J-INTEGRAL. The J-Integral in the last publication is calculated according to eq. (2.7). In the calculation procedure implemented in Python more quantities are determined than those presented in the publication. The following quantities are calculated for the NR strained to 20%: In Fig. 4.3 are shown the displacement gradients  $\partial U_i / \partial X_j$  not shown in the publication. Fig. 4.4 displays the square roots of the eigenvalues of the left Cauchy Green Tensor  $\mathbf{B}$ . In these images an undeformed sample would appear in green. Other colors show changed values in the deformed sample. In Fig. 4.5 are shown the first invariant  $\bar{I}_1 = \lambda_1^2 + \lambda_2^2 + \lambda_3^2 - 3$  and the generalized invariant  $\bar{I}^* = \lambda_1^{-1} + \lambda_2^{-1} + \lambda_3^{-1} - 3$ . Here, an undeformed sample would appear completely in blue.

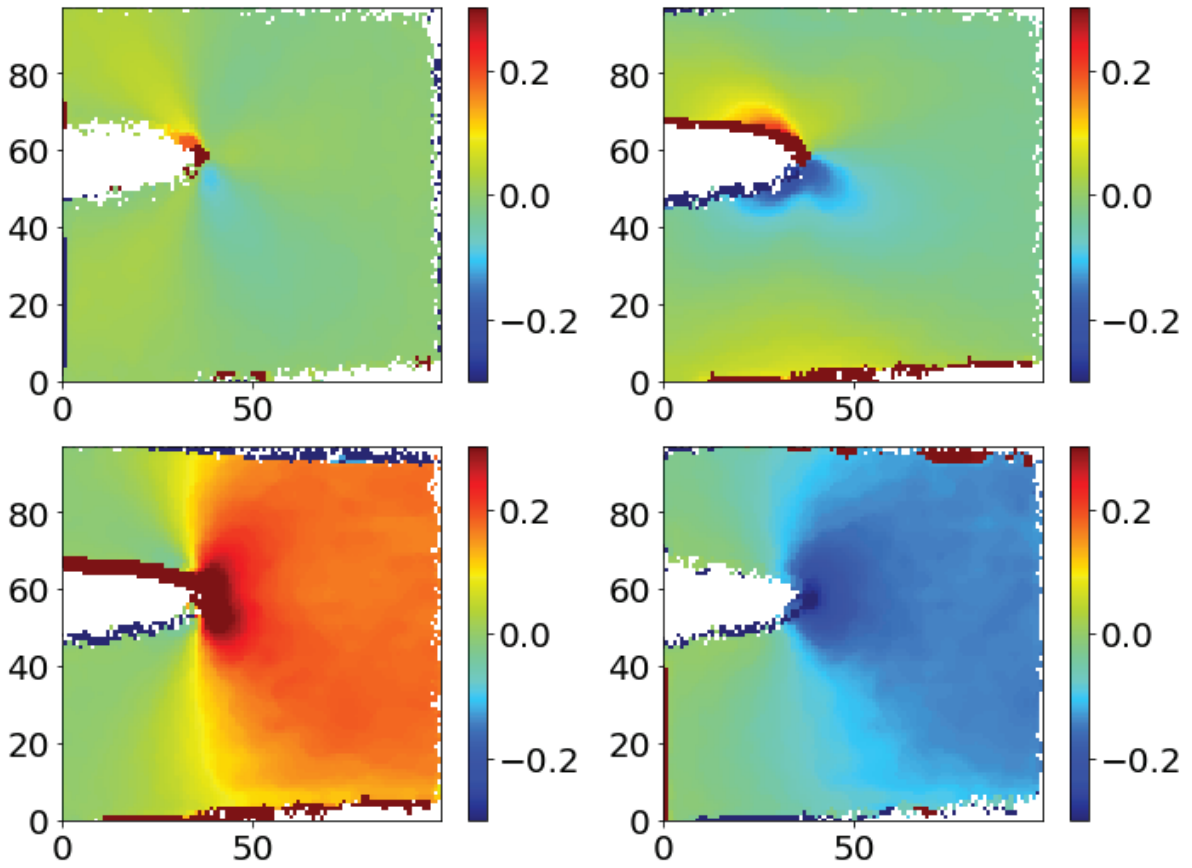


Fig. 4.3: Displacement gradients  $\partial U_1/\partial X_1$  (a),  $\partial U_1/\partial X_2$  (b),  $\partial U_2/\partial X_2$  (c) and  $\partial U_3/\partial X_3$  (d) of the NR strained to 20%. The displacement gradient  $\partial U_2/\partial X_1$  is shown in the last publication (chapter 4.3) as Fig. 6 (b).

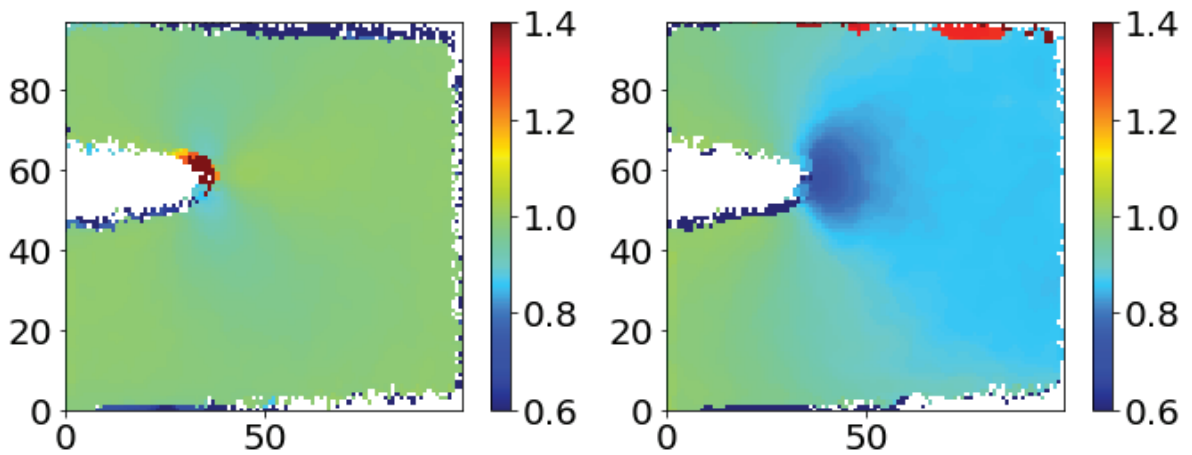


Fig. 4.4: Square roots of the eigenvalues of the left Cauchy Green Tensor  $\mathbf{B}$  of the NR strained to 20%.

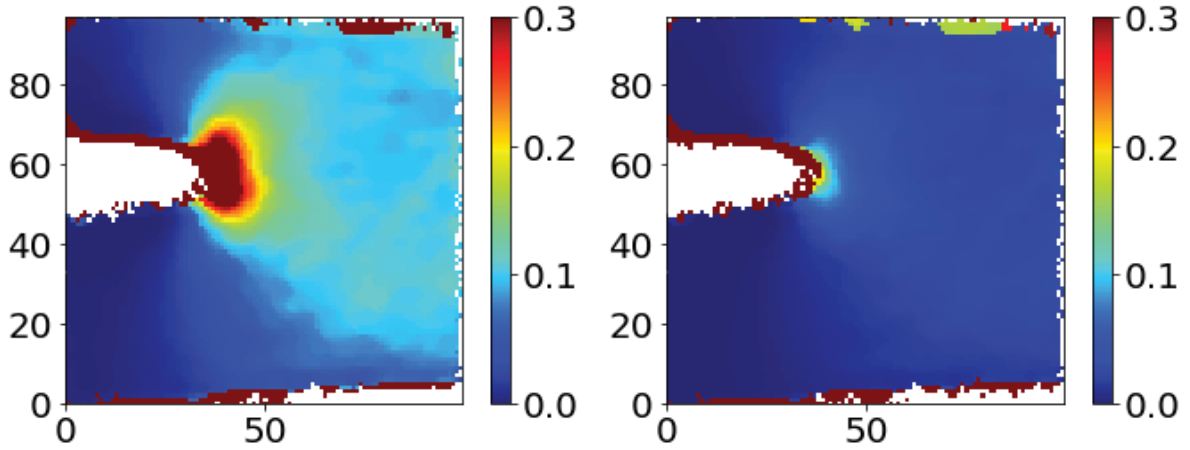


Fig. 4.5: First invariant  $\bar{I}_1 = \lambda_1^2 + \lambda_2^2 + \lambda_3^2 - 3$  and the generalized invariant  $\bar{I}^* = \lambda_1^{-1} + \lambda_2^{-1} + \lambda_3^{-1} - 3$  of the NR strained to 20%.

QUANTITIES DETERMINED FOR OTHER MEASUREMENTS. All these quantities presented in the last publication and the last paragraph are not only determined for the measurement of NR strained to 20% but for all measurements. Some of these quantities are shown for the NR strained to 50%: The displacement fields are shown in Fig. 4.6, the strain energy density  $W_{el}$  and its contribution to the integrand  $idw$  are shown in Fig. 4.7 and the stress component  $P_{22}$  and the stress contribution to the integrand  $idp$  is shown in Fig. 4.8. In all images values of zero correspond to the undeformed situation.

As found for all measurements the stress component  $P_{22}$  is the dominant contribution to  $idp$ . In the images obtained for the elongation to 50% the deviations from undeformed values are obviously largely enhanced compared to the elongation to 20% but many qualitative features within the images are similar.

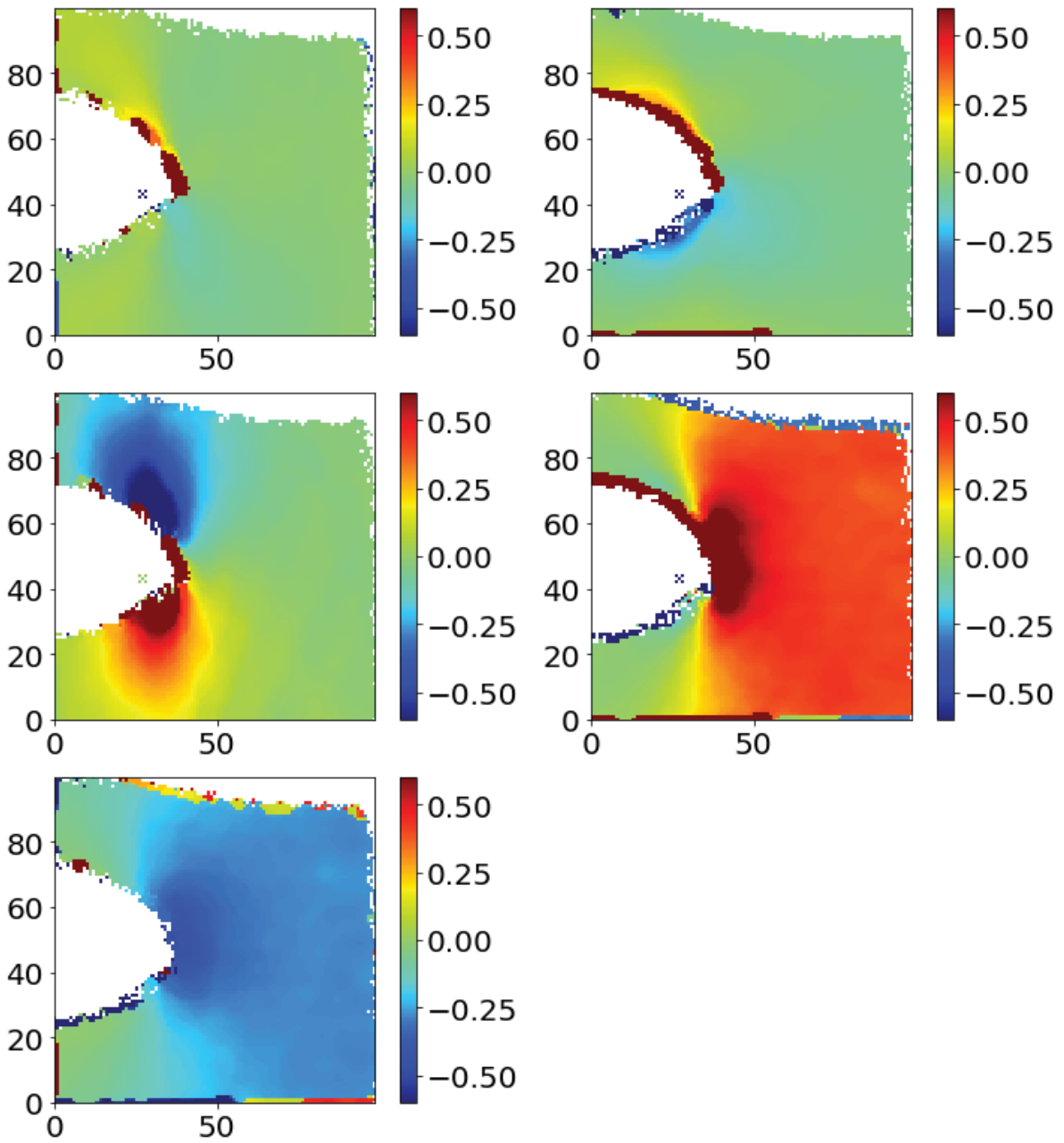


Fig. 4.6: Displacement gradients  $\partial U_1/\partial X_1$  (a),  $\partial U_1/\partial X_2$  (b),  $\partial U_2/\partial X_1$  (c),  $\partial U_2/\partial X_2$  (d) and  $\partial U_3/\partial X_3$  (e) for NR strained to 50%

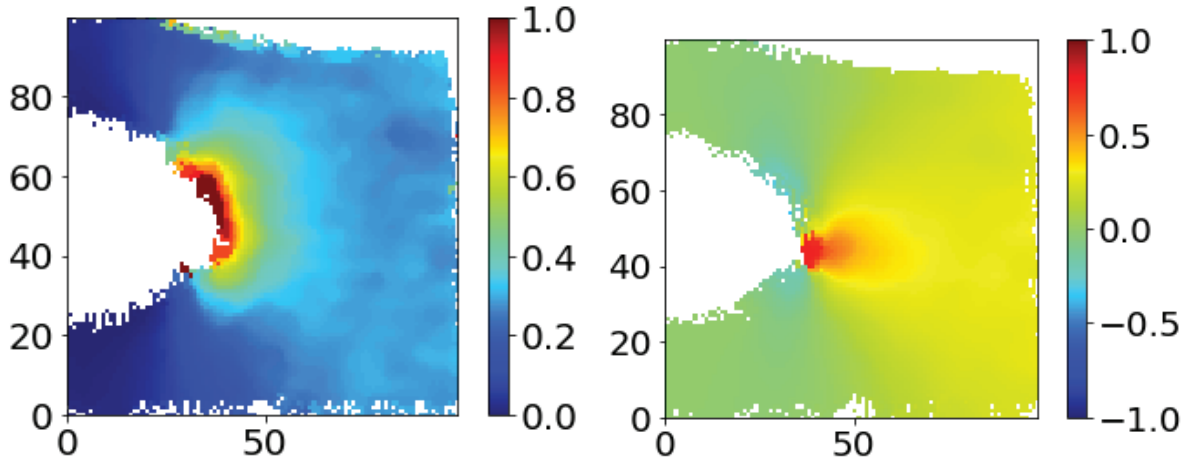


Fig. 4.7: Energy density  $W_{el}$  (a) and energy density component  $id_w = -W_{el} \cos(\varphi)$  (b) for the compound NR elongated by 50%.

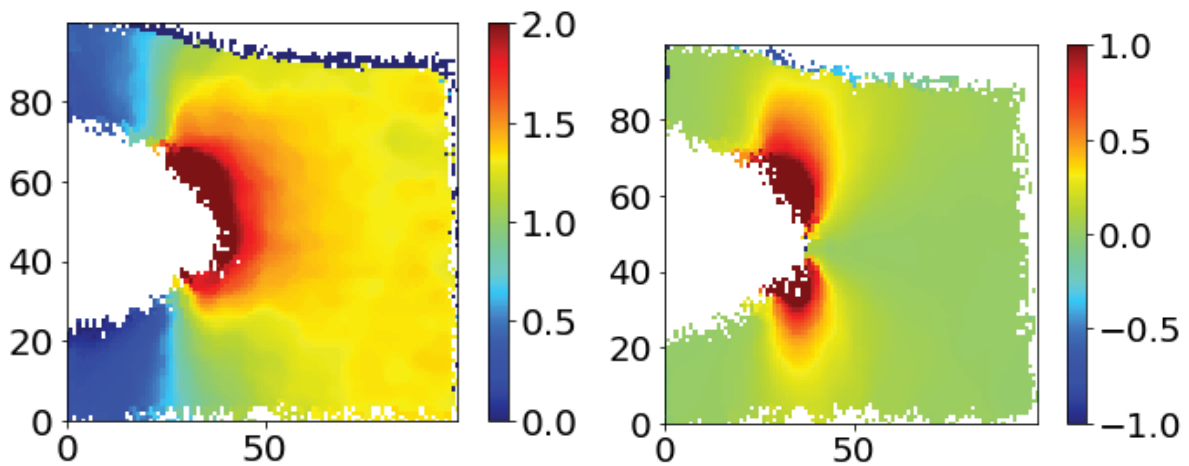


Fig. 4.8: Stress component  $P_{22}$  (a) stress component of the integrand  $id_p$  (b).

## 4.5 Outlook

Unfilled SBR shows a tearing behavior that is governed by its viscoelastic nature. This makes it possible to create master curves of the tearing energy. At high crack growth rates the tearing energy is influenced by flash temperature effects. It would be interesting to confirm that the flash temperature is responsible for the deviation. This could be done by measurements that avoid too high flash temperatures or by modeling which temperature is created and what effect this temperature increase has.

Steady tearing of filled SBR is not governed by the viscoelasticity of the rubber matrix. Especially at lower temperatures the filler network is affecting the tearing energy. Details on how the filler network is increasing the tearing energy and in modeling the dependency on crack growth velocity and temperature could be investigated.



Dynamic tearing of filled SBR seems to be governed by viscoelasticity, at least when only the dynamic part of the energy density is taken into account. By systematic variation of the preload it could be verified that only the dynamic energy density should be used to calculate the tearing energy in TFA measurements. These experiments should be done in a simple compound that shows little scattering in the crack growth rates.

The J-Integral is determined by calculating a line integral on a contour surrounding the crack tip. So far the determination of J-Integral is only reliable relatively far away from the crack tip. Therefore it is not possible to separate how much energy is dissipated in the process zone and how much energy is dissipated more or less close to the crack tip. In order to investigate this, high quality images in the direct vicinity of the crack tips are necessary. Possibly such images could be taken involving microscopic techniques.

Until now the calculation of the J-Integral does not include hysteresis. The implementation of hysteresis in the J-Integral not only gives a better parameter fitting but allows determining the evolution of the J-Integral during a stress-strain cycle.



## 5 Summary and conclusions

The crack growth behavior of elastomer compounds was analyzed. The measured crack growth rate in dynamic excitation depends on the tearing energy executed on the rubber sample and on the micro-mechanical structure in the compound. Large differences are obtained by reinforcement effects in the composite, as by strain induced-crystallization of natural rubber or through the impact of carbon black as active filler.

For steady tearing a viscoelastic crack growth theory exists. This theory could be applied on unfilled SBR measured at varying temperatures and crack growth velocities, while for carbon black filled SBR filler specific effects dominate. The crack growth theory could also be applied on dynamic tearing of unfilled and filled SBR. When a high preload is exerted a master curve is only obtained, when solely the dynamic part of tearing energy is chosen.

Dynamic crack growth measurements showed that the crack growth rate is lowest for the strain-crystallizing NR. Increasing the SBR portion in a NR/SBR blend leads to an increased crack growth for all tearing energies and increasing the BR portion in NR/BR blends yields strongly increased crack growth for higher tearing energies. This could be connected to the Chip & Cut behavior. Unfilled compounds, as shown with unfilled SBR, as well as increasing the temperature leads also to higher crack growth.

For the crack growth rate in viscoelastic materials not the tearing energy is the decisive energy, but the part of the tearing energy that reaches the process zone, which is in direct vicinity of the crack tip. The dissipative loss of energy further away from the crack could be determined with the J-Integral. The J-Integral is increasing from very low values for small integration radii around the crack tip towards a plateau for larger radii. The plateau value coincides at least for small strains to the value of tearing energy. The increase from low values into the plateau corresponds to the viscoelastic energy losses that do not directly affect crack growth.

The crack growth rate in elastomer blends is also affected by the blend morphology and filler distribution in the blend, which can be manipulated e.g. by the mixing procedure. Through a comparison of dynamical spectra from unfilled and filled blends the filler distribution can be calculated. This calculation yields high filler loadings in the SBR phase and the interphase in NR/SBR blends, but low filler loading in the BR phase in NR/BR blends. The determination

of filler distribution in blends containing NR and BR is hindered by thermally-induced crystallization of the BR that occurs at the same temperature range as the NR glass transition and is also leading to a peak in the loss modulus. The influence of BR crystallization on the DMA measurement is increased by carbon black and decreased by blending with SBR.

# Bibliography

- [1] J. Loadman, *Tears of the tree*. Oxford University Press Inc., New York, USA, 2005.
- [2] A. Behr and T. Seidensticker, *Einführung in die Chemie nachwachsender Rohstoffe*, Springer, Berlin, Germany, 2018.
- [3] F. Röthemeyer and F. Sommer, *Kautschuktechnologie*. Carl Hanser Verlag, München, Germany, 2001.
- [4] R. Hymann, <https://www.britannica.com/science/rubber-chemical-compound/Tapping-and-coagulation>
- [5] B. Tieke, *Makromolekulare Chemie*. Wiley-VCH GmbH & Co. KGaA, Weinheim, Germany, 2005.
- [6] H.-G. Elias, *An introduction in polymer science*. VCH Verlagsgesellschaft mbH, Weinheim, Germany, 1997.
- [7] H.-G. Elias, *Makromoleküle*. Hüthig & Wepf Verlag, Basel, Switzerland, 1975.
- [8] J. Schnetger, *Lexikon der Kautschuk-Technik*. Hüthig Buch Verlag GmbH, Heidelberg, Germany, 1991.
- [9] U. Eisele, *Introduction to polymer physics*. Springer Verlag, Berlin, Germany, 1990.
- [10] H. Takino, R. Nakayama and Y. Yamada, “Viscoelastic properties of elastomers and tire wet skid resistance”, *Rubber Chemistry and Technology*, vol. 70, pp. 584-594, 1997.
- [11] K. A. Grosch, “Visko-elastische Eigenschaften von Gummimischungen und deren Einfluß auf das Verhalten von Reifen”, *Kautschuk Gummi Kunststoffe*, vol. 42, no. 9, pp 745-751.
- [12] W. Baumann and M. Ismeier, *Kautschuk und Gummi*. Springer Verlag, Berlin, Germany, 1998.
- [13] J. L. White and N. S. Lee, “Optical, glass transition temperature and density characteristics of polybutadienes and butadiene-styrene copolymers”, *Kautschuk Gummi Kunststoffe*, vol. 43, no. 6, pp. 482-485, 1990.
- [14] D. Mangraj, “Elastomer blends”, *Rubber Chemistry and Technology*, vol. 75, no. 3, pp. 365-427, 2002.
- [15] H. J. Kim and G. R. Hamed, “On the reason that passenger tire sidewalls are based on blends of natural rubber and cis-polybutadiene”, *Rubber Chemistry and Technology*, vol. 73, no. 4, pp. 743-752, 2000.
- [16] B. E. Clapson and G. J. Lake, “Truck tire groove cracking - theory and practice”, *Rubber Journal* vol. 152, pp. 38-52, 1970 (Reprint: *Rubber Chemistry and Technology*, vol. 44, no. 5, pp. 1186-1202, 1971).

- [17] M. Rubinstein and R. H. Colby, *Polymer physics*. Oxford University Press Inc., New York, USA, 2003.
- [18] R. H. Schuster, “Verträglichkeit von Kautschuken. Ein altes und ein aktuelles Problem.”, *Die Angewandte Molekulare Chemie*, vol. 202/203, pp. 159-185, 1992.
- [19] R. H. Schuster, *Verträglichkeit von Kautschuken in Verschnitten. Teil 1. Theorie und Methoden*”, wdk Wirtschaftsverband der deutschen Kautschukindustrie e.V., Frankfurt, Germany, 1992.
- [20] R. H. Schuster, H. M. Issel and V. Peterseim, “Selective interactions in elastomers, a base for compatibility and polymer-filler interactions”, *Rubber Chemistry and Technology*, vol. 69, pp. 769, 1996.
- [21] A. Y. Coran, “Vulcanization”, in J. E. Mark, B. Erman, F. R. Eirich, Eds., *The science and technology of rubber*, Elsevier Academic Press, Burlington, USA, 2005.
- [22] B. Saville and A. A. Watson “Structural characterization of sulfur-vulcanized rubber networks”, *Rubber Chemistry and Technology*, vol. 40, pp. 100-148, 1967.
- [23] E. K. Peregi, “Thermisch-oxidative Alterungsvorgänge bei Dienkautschuken”, PhD Thesis, Hannover, Germany, 2008.
- [24] W. Hoffmann, *Vulkanisation & Vulkanisationshilfsmittel*. Farbenfabriken Bayer AG, Leverkusen, Germany, 1965.
- [25] J. D. Ferry, *Viscoelastic properties of polymers*. John Wiley & Sons, Inc., New York, USA, 1980.
- [26] M. L. Williams, R. F. Landel and J. D. Ferry, “The temperature dependence of relaxation mechanisms in amorphous polymers and other glass-forming liquids”, *Journal of the American Chemical Society*, vol. 77, no. 14, pp. 3701-3707, 1955.
- [27] W. B. Wiegand “The carbon reinforcement of rubber”, *Rubber Chemistry and Technology*, Vol. 10, No. 3, pp. 395-411, 1937.
- [28] W. Grellmann, K. Reincke, R. Lach and G. Heinrich, “Characterization of crack toughness behaviour of unfilled and filled elastomers”, *Kautschuk Gummi Kunststoffe*, vol. 54, no. 7-8, pp. 387-393, 2001.
- [29] T. A. Vilgis, G. Heinrich and M. Klüppel, *Reinforcement of polymer nano-composites*. Cambridge University Press, Cambridge, UK, 2009.
- [30] H. M. Smallwood, “Limiting law of the reinforcement of rubber”, *Journal of Applied Physics*, vol. 15, no. 11, pp. 758-766, 1944.
- [31] A. I. Medalia, “Elastic modulus of vulcanizates as related to carbon black structure”, *Rubber Chemistry and Technology*, vol. 46, no. 4, pp. 877, 1973.
- [32] A. I. Medalia, “Effective degree of immobilization of rubber occluded within carbon black aggregates”, *Rubber Chemistry and Technology*, vol. 45, no. 5, pp. 1171, 1972.
- [33] M. Klüppel, “The role of disorder in filler reinforcement of elastomers on various length scales”, *Advances in Polymer Science*, vol. 164, pp. 1-86, 2003.

- [34] J. G. Meier and M. Klüppel, “Carbon black networking in elastomers monitored by dynamic mechanical and dielectric spectroscopy”, *Macromolecular Materials and Engineering*, vol. 293, no. 1, pp. 12-38, 2008.
- [35] J. Fritsche and M. Klüppel, “Structural dynamics and interfacial properties of filler-reinforced elastomers”, *Journal of Physics: Condensed Matter*, vol. 23, pp. 035104, 2011.
- [36] A. R. Payne, “The dynamic properties of carbon black-loaded natural rubber vulcanizates. Part I”, *Journal of Applied Polymer Science*, vol. 6, no. 19, pp. 57-63, 1962.
- [37] R. Raghunath, D. Juhre and M. Klüppel, “A physically motivated model for filled elastomers including strain rate and amplitude dependency in finite viscoelasticity”, *International Journal of Plasticity*, vol. 78, pp. 223-241, 2016.
- [38] L. Mullins, “Softening of rubber by deformation”, *Rubber Chemistry and Technology*, vol. 42, no. 1, pp. 339-362, 1969.
- [39] U. Eisele, “Zum Einfluss der Mikrostruktur auf die Weiterreißenergie von Synthesekautschuken”, *Gummi Asbest Kunststoffe*, vol. 31, no. 10, pp. 724-730, 1978.
- [40] M. K. Kang, H.-J. Jeon, H. H. Song, and G. Kwag, “Strain-induced crystallization of blends of natural rubber and ultra high cis polybutadiene as studied by synchrotron x-ray diffraction”, *Macromolecular Research*, vol. 24, no. 1, pp. 31–36, 2016.
- [41] M. Tosaka, S. Kohjiya, S. Murakami, S. Poompradub, Y Ikeda, S. Toki, I. Sics and B. S. Hsiao, “Effect of network-chain length on strain-induced crystallization of NR and IR vulcanizates”, *Rubber Chemistry and Technology*, vol. 77, no. 4, pp. 711-723, 2004.
- [42] P.-A. Albouy, A. Vieyres, R. Pérez-Aparicio, O. Sanséau, and P. Sotta, “The impact of strain induced crystallization on strain during mechanical cycling of cross-linked natural rubber”, *Polymer*, vol. 55, no. 16, pp. 4022–4031, 2014.
- [43] S. Trabelsi, P.-A. Albouy and J. Rault, “Crystallization and melting processes in vulcanized stretched natural rubber”, *Macromolecules*, vol. 36, no. 20, pp. 7624-7639, 2003.
- [44] B. Huneau, “Strain-induced crystallization of natural rubber: a review of x-ray diffraction investigations”, *Rubber Chemistry and Technology*, vol. 84, no. 3, pp. 425-452, 2011.
- [45] S. Trabelsi, P.-A. Albouy and J. Rault, “Effective local deformation in stretched filled rubber”, *Macromolecules*, vol. 36, no. 24, pp. 9093-9099, 2003.
- [46] P.-A. Albouy, J. Marchal and J. Rault, “Chain orientation in natural rubber, Part I: The inverse yielding effect”, *European Physical Journal E: Soft matter and biological physics*, vol. 17, no. 3, pp. 247-259, 2005.

- [47] D. J. Lee and J. A. Donovan, “Microstructural changes in the crack tip region of carbon-black-filled natural rubber”, *Rubber Chemistry and Technology*, vol. 60, no. 5, pp. 910-923, 1987.
- [48] S. Trabelsi, P.-A. Albouy and J. Rault, “Stress-induced crystallization around a crack tip in NR”, *Macromolecules*, vol. 35, no. 27, pp. 10054-10061, 2002.
- [49] N. Bekkedahl and L. A. Wood, “Crystallization of vulcanized rubber”, *Industrial and Engineering Chemistry*, vol. 33, no. 3, pp. 381-384, 1941 (Reprint: *Rubber Chemistry and Technology*, vol. 14, no. 2, pp. 347-355, 1941).
- [50] L. A. Wood and N. Bekkedahl, “Crystallization of unvulcanized rubber at different temperatures”, *Journal of Applied Physics*, vol. 17, pp. 362-375, 1946.
- [51] M. F. Bukhina and S. K. Burlyand, *Low-Temperature Behaviour of Elastomers*, Koninklijke Brill NV, Leiden, The Netherlands, 2007.
- [52] G. A. Holzapfel, *Nonlinear solid mechanics*. John Wiley & Sons Ltd, Chichester, UK, 2001.
- [53] H. Lorenz, M. Klüppel and G. Heinrich, “Microstructure-based modelling and FE implementation of filler-induced stress softening and hysteresis of reinforced rubbers”, *Zeitschrift für Angewandte Mathematik und Mechanik*, vol. 92, no. 8, pp. 608–631, 2012.
- [54] F. Fleck, V. Froltsov and M. Klüppel, “Polymer-filler interphase dynamics and reinforcement of elastomer nanocomposites”, *Soft Materials*, vol. 12, pp. S121-S134, 2014.
- [55] J. Plagge and M. Klüppel, “A physically based model of stress softening and hysteresis of filled rubber including rate-and temperature dependency”, *International Journal of Plasticity*, vol. 89, pp. 173–196, 2017.
- [56] J. Plagge and M. Klüppel, “A hyperelastic physically based model for filled elastomers including continuous damage effects and viscoelasticity”, *Constitutive Models for Rubber X*, pp. 173-196, A. Lion, M. Jöhlich, Eds., Taylor & Francis, London, UK, 2017.
- [57] B. Huneau, I. Masquelier, Y. Marco, V. Le Saux, S. Noizet, C. Schiel and P. Charrier, “Fatigue crack initiation in a carbon black-filled natural rubber”, *Rubber Chemistry and Technology*, vol. 89, no. 1, pp. 126-141, 2016.
- [58] M. Ludwig, T. Alshuth, M. El Yaagoubi and D. Juhre, “Lifetime prediction of elastomers based on statistical occurrence of material defects”, *Constitutive Models for Rubber IX*, pp. 445-448, B. Marvalová, I. Petříková, Eds., Taylor & Francis, London, UK, 2015.
- [59] A. A. Griffith, “The phenomena of rupture and flow in solids”, *Philosophical Transactions of the Royal Society of London, Series A*, vol. 221, pp. 163-198, 1920.
- [60] T. L. Anderson, *Fracture mechanics*. CRC Press, Boca Raton, USA, 1995.



- [61] C. Liu, B. Dong, L.-Q. Zhang, Q. Zheng and Y.-P. Wu, "Influence of strain amplification near crack tip on the fracture resistance of carbon black-filled SBR", *Rubber Chemistry and Technology*, vol. 88, no. 2, pp. 276-288, 2015.
- [62] A. K. Bhowmick, A. N. Gent and C. T. R. Pulford, "Tear strength of elastomers under threshold conditions", *Rubber Chemistry and Technology*, vol. 56, pp. 226-232, 1983.
- [63] K. J. Mach, D. V. Nelson and M. W. Denny, "Techniques for predicting the lifetimes of wave-swept macroalgae: a primer on fracture mechanics and crack growth", *The Journal of Experimental Biology*, vol. 210, pp. 2213-2230, 2007.
- [64] B. P. Holownia, "Effect of carbon black on Poisson's ratio of elastomers", *Journal of the Institution of The Rubber Industry*, vol. 8, pp. 157ff, 1974 (Reprint: *Rubber Chemistry and Technology*, vol. 48, pp. 246-253, 1975).
- [65] H. P. Kugler, R. G. Stacer and C. Steimle, "Direct measurement of poisson's ratio in elastomers", *Rubber Chemistry and Technology*, vol. 63, no. 4, pp. 473-487, 1990.
- [66] R. S. Rivlin and A. G. Thomas, "Rupture of rubber. I. Characteristic energy for tearing", *Journal of Polymer Science*, vol. 10, no. 3, pp. 291-318, 1953.
- [67] A. G. Thomas, "The development of fracture mechanics of elastomers", *Rubber Chemistry and Technology*, vol. 67, no. 3, pp. 50-366, 1994.
- [68] G. R. Irwin, "Analysis of stresses and strain near the end of a crack traversing a plate", *Trans. ASME. Ser. E: J. Appl. Mech.*, vol. 24, no. 3, pp. 361-364, 1957.
- [69] A. N. Gent, P. B. Lindley and A. G. Thomas, "Cut growth and fatigue of rubbers. I. The relationship between cut growth and fatigue", *Journal of Applied Polymer Science*, vol. 8, pp. 455-466, 1964.
- [70] G. J. Lake and A. G. Thomas, "Physics of failure in rubber", *Kautschuk Gummi Kunststoffe*, vol. 20, no. 4, pp. 211-217, 1967.
- [71] P. C. Paris, M. P. Gomez and W. E. Anderson, "A rational analytic theory of failure", *The Trend in Engineering*, vol. 13, pp. 9-14, 1961.
- [72] P. Paris and F. Erdogan, "A critical analysis of crack propagation laws", *Journal of Basic Engineering*, vol. 85, no. 4, pp. 528-533, 1963.
- [73] U. Eisele, S. Kelbch and H.-W. Engels, "The Tear Analyzer - A new tool for quantitative measurements of the dynamic crack growth of elastomers", *Kautschuk Gummi Kunststoffe*, vol. 45, no. 12, pp. 1064-1069, 1992.
- [74] F. Abraham, "The influence of minimum stress on the fatigue life of non strain-crystallising elastomers", PhD Thesis, Hannover, Germany, 2002.
- [75] B. N. J. Persson, O. Albohr, G. Heinrich and H. Ueba, "Crack propagation in rubber-like materials", *Journal of Physics: Condensed Matter*, vol. 17, no. 44, R1071, 2005.
- [76] B. N. J. Persson and E. A. Brener, "Crack propagation in viscoelastic solids", *Physical Review E*, vol. 71, 036123, 2005.

- [77] G. Heinrich, M. Klüppel, T. Vilgis and T. Horst, “Wenn Gummi zu Bruch geht”, *Physik Journal*, vol. 11, no. 5, pp. 39-44, 2012.
- [78] M. Klüppel, “Evaluation of viscoelastic master curves of filled elastomers and application to fracture mechanics”, *Journal of Physics: Condensed Matter*, vol. 21, 035104, 2009.
- [79] P. G. de Gennes, “Soft adhesives”, *Langmuir*, vol. 12, pp. 4497-4500, 1996.
- [80] A. Le Gal and M. Klüppel, “Investigation and modeling of rubber stationary friction on rough surfaces”, *Journal of Physics: Condensed Matter*, vol. 20, 015007, 2008.
- [81] A. Le Gal and M. Klüppel, “Investigation and modeling of adhesion friction on rough surfaces”, *Kautschuk Gummi Kunststoffe*, vol. 59, pp. 308-315, 2006.
- [82] M. L. Williams and J. D. Ferry, “Second approximation calculations of mechanical and electrical relaxation and retardation distributions”, *Journal of Polymer Science*, vol. 11, no. 2, pp. 169-175, 1953.
- [83] J. R. Rice, “A path independent integral and the approximate analysis of strain concentration by notches and cracks”, *Journal of Applied Mechanics*, vol. 35, pp. 379-386, 1968.
- [84] G. P. Cherepanov, “Crack propagation in continuous media”, *Прикладная Математика и Механика (PMM)*, vol. 31, no. 3, pp. 476-488 (Translation: *Journal of Applied Mathematics and Mechanics*, vol. 31, no. 3, pp. 503-512, 1967).
- [85] G. A. Maugin, “Material forces: Concepts and applications”, *Applied Mechanics Reviews*, vol. 48, no. 5, pp. 213-245, 1995.
- [86] J. D. Eshelby, “The elastic energy-momentum tensor”, *Journal of Elasticity*, vol. 5, pp. 321-335, 1975.
- [87] L. B. Freund, *Dynamic fracture mechanics*. Cambridge University Press, Cambridge, UK, 1998.
- [88] A. T. Zehnder, “Fracture Mechanics”, *Lecture Notes in Applied and Computational Mechanics*, vol. 62, pp. 33-54, 2012.
- [89] T. Horst, G. Heinrich, M. Schneider, A. Schulze and M. Rennert, “Linking mesoscopic and macroscopic aspects of crack propagation in elastomers”, *Lecture Notes in Applied and Computational Mechanics*, vol. 70, pp. 129-165, 2013.
- [90] J. G. Meier, M. Klüppel, H. Geisler and R. H. Schuster, “Kieselsäuregefüllte Elastomerblends durch Masterbatchtechnologie”, *Kautschuk Gummi Kunststoffe*, vol. 58, pp. 587, 2005.
- [91] J. F. Meier, M. Klüppel and R. H. Schuster, “Steuerung der physikalischen Eigenschaften von Elastomeren”, *Kautschuk Gummi Kunststoffe*, vol. 58, pp. 82, 2005.
- [92] H. Lorenz, D. Steinhauser and M. Klüppel, “Morphology and micro-mechanics of filled elastomer blends: Impact on dynamic crack propagation”, *Lecture Notes in Applied and Computational Mechanics*, vol. 70, pp. 81-128, 2013.

- [93] M. Klüppel, R. H. Schuster and J. Schaper, "Carbon black distribution in rubber blends: A dynamic-mechanical analysis", *Rubber Chemistry and Technology*, vol. 72, pp. 91, 1999.
- [94] M. Klüppel, R. H. Schuster and J. Schaper, "Dynamischer Glasübergang in füllstoffverstärkten Kautschukblends", *GAK- Gummi Fasern Kunststoffe*, vol. 51, pp. 508, 1998.
- [95] R. H. Schuster, J. Meier and M. Klüppel, "The role of interphase in filler partition in rubber blends", *Kautschuk Gummi Kunststoffe*, vol. 53, pp. 663, 2000.
- [96] W. M. Hess, C. E. Scott and J. E. Callan, "Carbon black distribution in elastomer blends", *Rubber Chemistry and Technology*, vol. 40, pp. 371-383, 1967.
- [97] J. A. Ayala, W. M. Hess, F. D. Kistler and G. A. Joyce, "Carbon-black - elastomer interaction", *Rubber Chemistry and Technology*, vol. 64, no. 1, pp. 19-39, 1991.
- [98] J. E. Callan, W. M. Hess and C. E. Scott, "Elastomer blends. Compatibility and relative response to fillers", *Rubber Chemistry and Technology*, vol. 44, pp. 814, 1971.
- [99] H.H. Le, S. Ilisch, G.R. Kasaliwal and H.-J. Radusch, "Filler phase distribution in rubber blends characterized by thermogravimetric analysis of the rubber-filler gel", *Rubber Chemistry and Technology*, vol. 81, pp. 767-781, 2008.
- [100] G. R. Cotton and L. J. Murphy, "Mixing of Carbon black with rubber. Part 5. Analysis of BR/SBR blends", *Kautschuk Gummi Kunststoffe*, vol. 41, no. 1, pp. 54-58, 1988.
- [101] J. F. Meier, M. Klüppel and R. H. Schuster, "Steuerung der physikalischen Eigenschaften von Elastomeren", *Kautschuk Gummi Kunststoffe*, vol. 58, no. 3, pp. 82-89, 2005.
- [102] R. H. Schuster, "Beziehung zwischen Verschnittmorphologie und physikalischen Eigenschaften von Elastomeren", *GAK – Gummi Fasern Kunststoffe*, vol. 49, no. 12, pp. 966-974, 1996.
- [103] M. C. Morris, "Rates of crystallization of cis-1,4-polybutadiene in elastomer blends", *Rubber Chemistry and Technology*, vol. 40, pp. 341-349, 1967.
- [104] A. K. Sircar and T. G. Lamond, "Carbon black transfer in blends of cis-poly(butadiene) with other elastomers", *Rubber Chemistry and Technology*, vol. 45, pp. 178-191, 1972.
- [105] K. Reincke, W. Grellmann and M. Klüppel, "Investigations of fracture mechanical properties of filler-reinforced styrene-butadiene elastomers", *Kautschuk Gummi Kunststoffe*, vol. 62, pp. 246-251, 2009.
- [106] G. R. Hamed, H. J. Kim and A. N. Gent, "Cut growth in vulkanizates of natural rubber, cis-polybutadiene, and a 50/50 blend during single and repeated extension", *Rubber Chemistry and Technology*, vol. 69, pp. 807, 1996.
- [107] J. R. Beatty and B. J. Miksch, "A laboratory cutting and chipping tester for evaluating off-the-road and heavy-duty tire treads", *Rubber Chemistry and Technology*, vol. 55, pp. 1531-1546, 1982.

- [108] R. Stoczek, R. Kipscholl, E. Euchler and G. Heinrich “Study of the relationship between fatigue crack growth and dynamic chip & cut behavior of reinforced rubber materials”, *Kautschuk Gummi Kunststoffe*, vol. 67, no. 4, pp. 26-29, 2014.
- [109] M. Wunde, A. Schulze, C. Vatterott, J. Tschimmel, J. Lacayo-Pineda, G. Heinrich, and M. Klüppel, ”Verbesserung der Laborvorhersagen zum Risswachstum und Verschleiß von LKW-Reifenauflflächen”, *Kautschuk Gummi Kunststoffe*, vol. 72, no. 8 (October), pp. 72-78, 2019.
- [110] G. J. Lake and P. B. Lindley, “Ozone cracking, flex cracking and fatigue of rubber. Part one: Cut growth mechanisms and how they result in fatigue failure”, *Rubber Journal*, vol. 146, no. 10, pp. 24-30+79, 1964.
- [111] G. J. Lake and P. B. Lindley, “Ozone cracking, flex cracking and fatigue of rubber. Part two: Technological aspects”, *Rubber Journal*, vol. 146, no. 11, pp. 30-36+39, 1964.
- [112] A. N. Gent, “Adhesion and strength of viscoelastic solids. Is there a relationship between adhesion and bulk properties?”, *Langmuir*, vol. 12, no. 19, pp. 4492-4496, 1996.
- [113] A. N. Gent, S.-M. Lai, “Interfacial bonding, energy dissipation, and adhesion”, *Journal of Polymer Science: Part B: Polymer Physics*, vol. 32, pp. 1543-1555, 1994.
- [114] M. Ludwig, “Entwicklung eines Lebensdauer-Vorhersagekonzepts für Elastomerwerkstoffe unter Berücksichtigung der Fehlstellenstatistik”, PhD Thesis, Hannover, Germany, 2017.
- [115] M. Kuna, *Numerische Beanspruchungsanalyse von Rissen*. Vieweg+Teubner Verlag, Wiesbaden, Germany, 2010.
- [116] C. Marano, M. Boggio, E. Cazzoni and M. Rink, “Fracture phenomenology and toughness of filled natural rubber compounds via the pure shear test specimen”, *Rubber Chemistry and Technology*, vol. 87, no. 3, pp. 501-525, 2014.
- [117] A. N. Gent, M. Razzaghi-Kashani and G. R. Hamed, “Why do cracks turn sideways?”, *Rubber Chemistry and Technology*, vol. 76, no. 1, pp. 122-131, 2003.

# Index

- A**ccelerators 9
- Active filler 12
- Agglomerate 12
- Aggregate 12
- Allylic proton 8
- Amplification factor 17,18
- Amorphous state 14
- Approximation method of Ferry and Williams 30
  
- B**atch mixing procedure 33
- Blend 7
- Bound rubber 12
- Butadiene rubber 6
  
- C**arbon black 12
- Cauchy stress tensor 16
- Chip & Cut 36
- Cis-isomer 4
- Conventional system 10
- Crack initiation 21
- Crack opening modes 22
- Critical crack length 22
- Critical crack velocity 28
- Critical tearing energy 26
- Crosslinking 8
- Crosslink density 8
- Crystalline state 14
- Crystallization 14
- Crystallization half-life 15
  
- D**eformation gradient 30
- Determination of blend morphology 33
- Digital Image Correlation 89
- Displacement gradient 30
- Displacement vector 30
- Dynamic flocculation model 17
  
- E**ffective filler volume fraction 13
- Efficient system 10
- Elastomer 4
- Energy flux integral 31
- Entropy 14
- Equilibrium melting temperature 15
- Extended non-affine tube model 16
  
- F**atigue crack growth 25
- Flash temperature 90
- Filler 12
- Filler-filler bonds 13
- First Piola Kirchhoff stress tensor 16
- Fracture mechanics 21
- Free volume 4
  
- G**ibbs free energy 7
- Glass transition 4
- Glass transition temperature 4
- Griffith criterion 21
  
- H**orizontal shifting factor 11
- Hysteresis 12
  
- I**nactive filler 12
- Induction period 8
- Interaction parameter 7
- Interphase 7
- Intrinsic strength 26,27
  
- J**-Integral 30
  
- K**ramers-Kronig relations 10
  
- L**oss modulus 10
  
- M**aster curve 11
- Miscibility 7
- Monomer 4

Mullins effect 14

**N**atural rubber 5

**O**ccluded rubber 13

**P**aris-Erdogan law 26

Paris plot 26

Payne effect 13

Percolation threshold 13

Permanent set 12

Phase volume fraction 8

Physically based model of stress softening and hysteresis 18

Plane stress conditions 16

Poisson's ratio 23

Polybutadiene 6

Polyisoprene 5

Polymer 4

Polymerization 4

Pure Shear sample 23

**R**einforcement 12

Relaxation time spectrum 30

Rheological simple material 11

**S**emi-efficient system 10

Shear modulus 10

Single edge notched sample 23

Solubility parameter 7

Standard mixing procedure 33

Storage modulus 10

Strain-induced crystallization 15

Stress intensity factor 25

Stress softening 14

Styrene- butadiene rubber 6

Surface energy 21

**T**angent of the phase angle 10

Tear Fatigue Analyzer 27

Tearing energy 23

Thermally induced crystallization 15

Time-temperature superposition principle 11

Trans-isomer 4

Trousers sample 23

**U**niaxial deformation 23

**V**iscoelastic crack growth 27

Viscoelastic crack opening mechanism 29

Vulcameter curve 8

Vulcanization 8

**W**LF equation 11

**Y**oung's modulus 10

# Appendix

## A.1 Curriculum Vitae

### Personal Data

Name	Matthias Wunde
Date and place of birth	07.11.1984, Goslar
Nationality	German

### Work experience

05.2013 – 03.2019	Ph. D. research Deutsches Institut für Kautschuktechnologie e. V., department Material Concepts and Modeling
10.2011 – 10.2012	Diploma research Forschungszentrum Jülich, department PGI-3 Functional Nanostructures on Surfaces

### Education

10.2004 – 10.2012	Diploma in Physics, University of Cologne, Thesis: “Simulation von Ladungstransportmessungen mit einem Vierspitzen-Rastertunnelmikroskop”
08.2008 – 03.2009	Erasmus exchange program, University of Lund, Sweden
06.2004	Abitur, Abtei Gymnasium Brauweiler

### Honors and Awards

11.2014	2. Poster Prize, Kautschuk Herbst Kolloquium 2014, Hannover, Germany
---------	---

## A.2 Own Literature

### OWN LITERATURE INCLUDED IN THIS THESIS

1. M. Wunde and M. Klüppel, "Influence of phase morphology and filler distribution in NR/BR and NR/SBR blends on fracture mechanical properties", *Rubber Chemistry and Technology*, vol. 89, no. 4, pp. 588-607, 2016.
2. M. Wunde and M. Klüppel, "Impact of mixing procedure on phase morphology and fracture mechanical properties of carbon black-filled NR/SBR blends", *Continuum Mechanics and Thermodynamics*, vol. 29, pp. 1135-1148, 2017.
3. M. Wunde and M. Klüppel, "Effect of filler and blending with SBR and NR on thermally induced crystallization of high-cis BR as evaluated by dynamic mechanical analysis", *Express Polymer Letters*, accepted, 2020.
4. M. Wunde and M. Klüppel, "Viscoelastic response during crack propagation of unfilled and filled SBR", *Rubber Chemistry and Technology*, vol. 91, no. 4, pp. 668-682, 2018.
5. M. Wunde, J. Plagge and M. Wunde, "The role of stress softening in crack propagation of filler reinforced elastomers as evaluated by the J-Integral", *Engineering Fracture Mechanics*, vol. 214, pp. 520-533, 2019.

### OWN LITERATURE NOT INCLUDED IN THIS THESIS

1. M. Klüppel, M. Möwes, A. Lang, J. Plagge, M. Wunde, F. Fleck, and C. W. Karl, "Characterization and application of graphene nanoplatelets in elastomers," in *Designing of Elastomer Nanocomposites: From Theory to Applications*, Springer International Publishing, pp. 319-360, 2016.
2. T. Spratte, J. Plagge, M. Wunde, and M. Klüppel, "Investigation of strain-induced crystallization of carbon black and silica filled natural rubber composites based on mechanical and temperature measurements", *Polymer*, vol. 115, pp. 12-20, 2017.
3. M. Wunde, J. Plagge, and M. Klüppel, "Impact of stress softening on tearing energy of filled rubbers as evaluated by the J-Integral", in *Constitutive models for rubber*, Taylor & Francis Group, London, vol. 10, pp. 301-305, 2017.
4. M. Wunde, A. Schulze, C. Vatterott, J. Tschimmel, J. Lacayo-Pineda, G. Heinrich, and M. Klüppel, "Verbesserung der Laborvorhersagen zum Risswachstum und Verschleiß von LKW-Reifenaufläichen", *Kautschuk Gummi Kunststoffe*, vol. 72, no. 8 (October), pp. 72-78, 2019.



### A.3 Contributions to Conferences

1. M. Wunde and M. Klüppel, “Carbon black distribution in NR/BR and NR/SBR blends”, *International Seminar on Elastomers*, 08.2014, Bratislava, Slovakia.
2. M. Wunde, A. Schulze, J. Jungk, J. Tschimmel, J. Lacayo-Pineda, G. Heinrich and M. Klüppel, “Laboratory prediction of crack propagation in truck tire compounds”, *Tire Technology Expo*, 02.2015, Cologne, Germany.
3. M. Wunde and M. Klüppel, “Influence of carbon black distribution in NR/BR and NR/SBR blends on fracture mechanical properties”, *PhD Rubber Seminar*, 06.2015, Cologne, Germany.
4. M. Wunde and M. Klüppel, “Impact of phase morphology on mechanical and fracture mechanical properties of filled rubber blends”, *Deutsche Kautschuk Tagung*, 06-07.2015, Nürnberg, Germany.
5. M. Wunde and M. Klüppel, “Evaluation of blend morphology based on viscoelastic spectra and crack propagation of filled NR/BR and NR/SBR systems”, *PolyMerTec*, 06.2016, Merseburg, Germany.
6. M. Wunde and M. Klüppel, “Evaluation of tearing energy based on a micromechanical model for filler reinforced elastomers”, *Material Science and Engineering*, 09.2016, Darmstadt, Germany.
7. M. Wunde and M. Klüppel, “Tearing energy in filler reinforced elastomers for tire treads”, *Kautschuk Herbst Kolloquium*, 11.2016, Hannover, Germany.
8. M. Wunde, J. Plagge and M. Klüppel, “Impact of stress softening on tearing energy of filled rubbers as evaluated by the J-Integral”, *European Conference on Constitutive Models for Rubber*, 08.2017, Munich, Germany.
9. (Poster) M. Blab, M. Wunde, V. Cherepanov, P. Coenen and B. Voigtländer, “4-Tip STM Transport Measurements on Si(111)-7x7”, *DPG-Frühjahrstagung*, 03.2013, Regensburg, Germany.
10. (Poster) M. Wunde and M. Klüppel, “Distribution of carbon black in polymer blend systems”, *Kautschuk Herbst Kolloquium*, 11.2014, Hannover, Germany.

